NORTHWESTERN UNIVERSITY

Precision Rosenbluth Measurement of the Proton Elastic Electromagnetic Form Factors and Their Ratio at $Q^2 = $ 2.64, 3.20, and 4.10 GeV^2

A DISSERTATION

SUBMITTED TO THE GRADUATE SCHOOL
IN PARTIAL FULLFILLMENT OF THE REQUIREMENT

for the degree

DOCTOR OF PHILOSOPHY

Field of Physics and Astronomy

By

Issam A. Qattan

EVANSTON, ILLINOIS

December 2005

ii

Abstract

Precision Rosenbluth Measurement of the Proton Elastic Electromagnetic Form Factors and Their Ratio at Q^2 = 2.64, 3.20, and 4.10 GeV^2

Issam A. Qattan

Due to the inconsistency in the results of the $\frac{\mu_p G_{Ep}}{G_{Mp}}$ ratio of the proton, as extracted from the Rosenbluth and recoil polarization techniques, high precision measurements of the e-p elastic scattering cross sections were made at Q^2 = 2.64, 3.20, and 4.10 GeV^2. Protons were detected, in contrast to previous measurements where the scattered electrons were detected, which dramatically decreased ε dependent systematic uncertainties and corrections. A single spectrometer measured the scattered protons of interest while simultaneous measurements at Q^2 = 0.5 GeV^2 were carried out using another spectrometer which served as a luminosity monitor in order to remove any uncertainties due to beam charge and target density fluctuations. The absolute uncertainty in the measured cross sections is $\approx 3\%$ for both spectrometers and with relative uncertainties, random and slope, below 1% for the higher Q^2 protons, and below 1% random and 6% slope for the monitor spectrometer. The extracted electric and magnetic form factors were determined to 4%-7% for G_{Ep} and 1.5% for G_{Mp}. The ratio $\frac{\mu_p G_{Ep}}{G_{Mp}}$ was determined to 4%-7% and showed $\frac{\mu_p G_{Ep}}{G_{Mp}} \approx 1.0$. The results of this work are in agreement with the previous Rosenbluth data and inconsistent with high-Q^2 recoil polarization results, implying a systematic difference between the two techniques.

Acknowledgements

My most important acknowledgment is to my caring and loving family and in particular my mother and my father, for without their love and support none of this would have been possible. Their tremendous support all the time motivated, inspired, and kept me alive and helped keep my sane. No words can express my thanks and gratitude to my parents for all that they have gone through and done for me. **So, father and mother: this work is dedicated to you with great love and admiration.**

This thesis is a direct result of the dedication of a great number of people. In particular, I am greatly indebted to my Ph.D. and research advisors Professor Ralph E. Segel from Northwestern University and Dr. John R. Arrington from Argonne National Laboratory, for without their help, steady support, and encouragement this work would not have been possible as well. Their dedication to this work, patience, and "way" too many heated and rousing discussions guided me through too many dark days and tough times. **Ralph and John to you I say: I am extremely grateful for all you have done for me and in particular giving me the opportunity to work on a such high-profile experiment.** Also I like to thank Professors Heidi Schellman and David Buchholz for their enthusiasm for this work and being a committee members.

I gratefully acknowledge the staff of the Accelerator Division, the Hall A technical staff, the members of the survey and cryotarget groups at the Thomas Jefferson National Laboratory for their efforts in making this experiment possible. I like to acknowledge all of those "without going through the full list of names" who took shifts on the E01-001 experiment and kept the data flowing. In particular I would like to acknowledge the hard work and long hours on shifts put in by my fellow graduate

jeffy lab

"Beam in 30 minutes or it's free"

Contents

List of Figures

xviii

List of Tables

Chapter 1   Introduction

1.1   Overview

The modern concept of the atom as an object composed of a dense nucleus surrounded by an electron cloud came to life as a result of Rutherford's experiments in 1911. As time went on, it became clear that the nucleus itself is composed of even smaller objects or particles which we call nucleons. The fact that the proton's magnetic moment is $2.79\mu_N$ ($\mu_N = \frac{e\hbar}{2M_p c}$), rather than the $0.5\mu_N$ expected for a point-like spin $1/2$ charged particle demonstrates that the proton posses a structure. Similarly, the neutron's magnetic moment of $-1.91\mu_N$ is very different from the $0.0\mu_N$ that a point neutral particle would have. Thus, nucleons, protons and neutrons, which were once thought to be the fundamental building blocks of matter in fact are complex particles that turn out to be composed into even smaller objects which we call quarks and gluons. The whole picture boils down to electrons (leptons), quarks, and gluons as the fundamental types of building blocks.

Several challenging questions and issues arose when physicists tried to understand nucleons. For example, what are these particles made off, how do they interact, and, most importantly, how do they bind together? These are fundamental and complicated questions that must be addressed, answered, and resolved by the nuclear and particle physics communities. The strong force is the reason why protons and neutrons bind together to form the nuclei. It is the theory of Quantum Chromodynamics (QCD) that describes the strong interaction between the quarks and gluons, which in turn make up the protons and neutrons.

The strong coupling constant, α_s, as defined by the theory of Quantum Chromo-

dynamics [19], is a measure of the strength of the strong interaction between quarks and gluons and is a function of the four momentum transfer squared Q^2:

$$\alpha_s(Q^2) = \frac{12\pi}{(33 - 2N_f)\ln(\frac{Q^2}{\Lambda_{QCD}^2})} \; , \tag{1.1}$$

where N_f is the number of flavors active for QCD renormalization scale Λ_{QCD} [20, 21].

When Q^2 is large (short distance scale), equation (1.1) tells us that α_s is small. Therefore, at large momentum transfer, the quarks within a hadron (neutron or proton) are weakly interacting and behave almost as if they are free particles. On the other hand, when Q^2 is small (large distance scale), α_s is large and the quarks are strongly interacting particles and hence form hadronic matter.

1.2 Electron Scattering

In order to reveal the underlying structure of the nucleon, experimental techniques such as electron scattering have been developed. Electron scattering in particular has proven to be a powerful tool for studying the structure of the nucleus. The reason lies in the fact that the electron is a point-like particle and has no internal structure, making it a clean probe of the target nucleus. In this case, the information extracted such as the differential cross section reflects the structure of the target without any contribution from the projectile. The incident electron is scattered off a nuclear target (single particle in the target) by exchanging a virtual photon. The electron-photon scattering vertex is known and understood within the theory of QED.

In electron scattering experiments, highly relativistic electrons are used. At low energy transfers, the virtual photon interacts with the entire nucleus. The nucleus stays intact and the electron scatters elastically or excites nuclear states. In this case, the virtual photon is dominantly interacting with the nuclear target by coupling to a

vector meson resonance states or $q\bar{q}$ [22, 23].

As the energy transfer increases and becomes larger than the nuclear binding energy, we enter the quasi-elastic region. The virtual photon becomes more sensitive to the internal structure of the nuclear target and the scattering process is described in terms of photon-nucleon coupling rather than photon-meson coupling. In this case, the target is viewed by the virtual photon as a set of quasi-free nucleons. The electron scatters elastically from the nucleon which in turn is ejected from the nucleus.

By increasing Q^2 and the energy transfer further, we enter the resonance region. In this case, the virtual photon becomes sensitive to the internal structure of the nucleon. The quarks inside the nucleon absorb the virtual photons and form excited states which we refer to as nucleon-resonances.

If we increase Q^2 and the energy transfer even further, we enter the deep inelastic region. The virtual photon probes smaller distance scales and has enough energy to resolve the constituents of the nucleon, or partons. Perturbative QCD models (pQCD) [24, 25] seem to give the correct description of the scattering process at high Q^2.

In electron scattering experiments, see Figure 1.1, the initial electron's energy and momentum $k = (E, \vec{k})$ are known. Elastic electromagnetic scattering of the electron can be described, to lowest order in the electromagnetic coupling constant α, as the exchange of a single virtual photon γ^* of momentum $\vec{q}$ and energy ω. The virtual photon then interacts with the target. After the scattering, the final electron's energy and momentum $k' = (E', \vec{k'})$ are measured. This allows us to determine the energy $\omega = (E - E')$ and momentum $\vec{q} = (\vec{k} - \vec{k'})$ of the virtual photon. Usually we refer to the energy of the virtual photon, $\omega = (E - E')$, as the energy transfer.

We describe the scattering process using two main variables, the energy transfer to the virtual photon, $\omega = E - E'$, and the square of the 4-momentum transfer, $Q^2 = -q_\mu q^\mu = -q^2 = |\vec{k} - \vec{k'}|^2 - (E - E')^2$. We define the Bjorken variable $x = \frac{Q^2}{2M_p\omega}$,
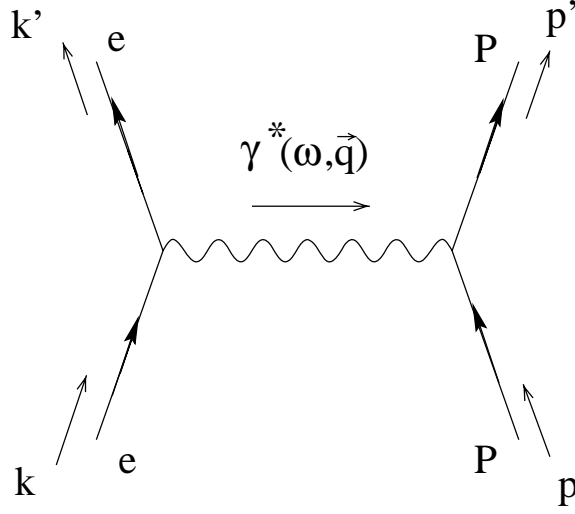
Figure 1.1: Feynman digram for electron-nucleus scattering.

where M_p is the mass of the nucleon. The Bjorken variable x varies between 0 and 1.0, where the $x = 1.0$ case corresponds to elastic scattering, and the $x < 1.0$ case corresponds to inelastic scattering.

The 4-momentum transfer $Q^2 = -q^2$ is given in terms of the electron's kinematics (initial energy E, final energy E', and the scattering angle θ_e) as:

$$Q^2 = 4EE' \sin^2 \frac{\theta_e}{2} \ . \tag{1.2}$$

We refer to the scattering as an exclusive scattering if the final state is fully identified. In this case we can also express the scattering kinematics in terms of the knocked out or recoil target (nucleon) rather than the electron. If the initial and the final four-momentum of the nucleon are defined as $P = (E_p, \vec{p})$ and $P' = (E'_p, \vec{p'})$, where E_p and E'_p are the initial and final energy of the nucleon and $\vec{p}$ and $\vec{p'}$ are the initial and final 3-momentum of the nucleon, we can write the the 4-momentum

transfer Q^2 as:

$$Q^2 = -q^2 = -(P' - P)^2 = \left((E'_p - E_p)^2 - (\vec{p'} - \vec{p})^2 \right) . \tag{1.3}$$

For the case where the final hadronic state contains a single nucleon only, the missing mass squared of the scattered hadron W^2 must equal the mass of the nucleon squared, M_p^2, where we define the missing mass squared as:

$$W^2 = M_p^2 + 2M_p\omega - Q^2 . \tag{1.4}$$

Examining equation (1.4), we see that if the final state contains only a single nucleon, then $W^2 = M_p^2$ and $Q^2 = 2M_p\omega$ yielding a value of $x = \frac{Q^2}{2M_p\omega} = 1$ for the Bjorken variable. So by choosing scattering kinematics where $x = 1$, we can isolate elastic scattering.

If the nucleus is knocked into an excited state, there is some additional energy transfer, and x will decrease as the energy transfer increases. At somewhat higher energy transfer, where quasielastic scattering is the dominant process, the electron knocks a single nucleon out of the nucleus. This corresponds to scattering near $x = 1$. At higher energy transfers, corresponding to $x < 1$, the scattering is inelastic and the struck nucleon is either excited into a higher energy state (resonance scattering), or temporarily fragmented (deep inelastic scattering). At very high energy transfers, where deep inelastic scattering dominates, the electron is primarily interacting with a single quark via the virtual photon γ^*. In this case, a short wavelength virtual photon γ^* is needed in order to resolve the quarks within the proton.

1.3   Elastic Electron-Proton Scattering

The electron-photon vertex as shown in Figure 1.1 is well understood and described by QED. On the other hand, the photon-proton vertex is complicated and the detail of such interaction, $\gamma^* + P(p) \rightarrow P(p')$, cannot be calculated from first principles. This is due to the fact that the proton is not a point-like particle but rather a particle with internal structure. We introduce two Q^2-dependent functions that contain all the information about the internal structure of the proton. We refer to these two functions as the proton electromagnetic form factors which parameterize the internal structure of the proton.

For the single-photon exchange diagram for the electron-proton elastic scattering shown in Figure 1.1, the Lorentz invariant transition matrix element is given by:

$$M_{fi} = \left(j_\mu(k, k') \frac{1}{q^2} J^\mu(p, p') \right) , \tag{1.5}$$

where j_μ and J^μ are the electromagnetic currents for the electron and proton, respectively: We can express the electromagnetic currents as:

$$j_\mu = -e\bar{u}(k')\gamma_\mu u(k) , \tag{1.6}$$

$$J^\mu = e\bar{v}(p')\Gamma^\mu v(p) , \tag{1.7}$$

where $u(k)$, $\bar{u}(k')$, $v(p)$, and $\bar{v}(p')$ are the four-component Dirac spinors for the initial and final electron and proton, respectively, which appear in the plane-wave solutions for Dirac equation, and Γ^μ and γ_μ are the Dirac 4x4 matrices. Therefore, the Lorentz invariant transition matrix element can be expressed as:

$$iM_{fi} = \frac{-i}{q^2} \left[ie\bar{v}(p')\Gamma^\mu(p, p')v(p) \right] \left[ie\bar{u}(k')\gamma_\mu u(k) \right] . \tag{1.8}$$

Because of the composite nature of the proton, Γ^μ rather than γ_μ is used to describe the proton current since Γ^μ contains all the information about the internal electromagnetic structure of the proton. It is worth mentioning that if the proton were to be treated as a point-like particle, then $\Gamma^\mu \to \gamma_\mu$ as in the case with the electron. The proton current J^μ is a Lorentz four-vector that is Lorentz invariant and satisfies both parity and current conservations in electromagnetic interactions, i.e. $\partial J^\mu = 0$. With this in mind, the proton current can be written as:

$$J^\mu = \bar{v}(p')\Big(F_1(q^2)\gamma_\mu + \frac{i\kappa_p}{2M_p}F_2(q^2)\sigma_{\mu\nu}q^\nu\Big)v(p) \; , \qquad (1.9)$$

where $\kappa_p = 1.793\mu_N$ is the proton anomalous magnetic moment and it is expressed in the unit of nuclear magneton (μ_N), M_p is the mass of the proton, $\sigma_{\mu\nu} = \frac{i}{2}[\gamma^\mu, \gamma^\nu]$, and the factor $\frac{i\kappa_p}{2M_p}$ has been included as a matter of convention. The functions $F_1(q^2)$ and $F_2(q^2)$ are functions of q^2 and known as Dirac and Pauli form factors, respectively. The Dirac form factor, $F_1(q^2)$, is used to describe the helicity-conserving scattering amplitude while the Pauli form factor, $F_2(q^2)$, describes the helicity-flip amplitude. In the limit that $q^2 \to 0$, the structure functions $F_1(q^2 = 0) = F_2(q^2 = 0) = 1.0$, and in this limit, the virtual photon becomes insensitive to the internal structure of the proton which is viewed as a point-like particle.

The elastic differential cross section in the lab frame for the $e(k) + P(p) \to e(k') + P'(p')$ reaction is given by:

$$\frac{d\sigma}{d\Omega} = \left[\frac{|M_{fi}|^2}{4\Big((k \cdot p)^2 - m_e^2 M_p^2\Big)}(2\pi)^4\delta^4\Big(k' + p - k - p'\Big)\frac{d^3k' d^3p'}{(2\pi)^3 2E'(2\pi)^3 2(M_p + \omega)}\right] \; .$$
$$(1.10)$$

By using the scattering amplitude M_{fi} expressed in terms of the electron and proton currents, integrating out the δ-function that imposes momentum conservation, and finally expressing the proton current in terms of the Dirac and Pauli form factors,

the differential cross section for an unpolarized beam and target can be written as:

$$
\begin{aligned}
\frac{d\sigma}{d\Omega dE'} \;=\;\; & \frac{\alpha^2}{4E^2 \sin^4(\frac{\theta_e}{2})} \frac{E'}{E} \left[\left(F_1^2 + \frac{\kappa_p^2 Q^2}{4M_p^2} F_2^2 \right) \cos^2(\frac{\theta_e}{2}) \right. \\
& \left. + \frac{Q^2}{4M_p^2} (F_1 + \kappa_p F_2)^2 \sin^2(\frac{\theta_e}{2}) \right] \delta(E - E' - \frac{Q^2}{2M_p}) \,,
\end{aligned}
\qquad (1.11)
$$

where we have averaged over initial spins and summed over final spins. It is understood that the δ-function is used to assure elastic scattering, that is, at a given energy E and angle θ_e, the elastic differential cross section is a δ-function in E' at $E' = E - \frac{Q^2}{2M_p}$. If we integrate over E' in equation (1.11) above and divide the numerator and denominator by $\cos^2(\frac{\theta_e}{2})$, we can write the elastic cross section as:

$$
\frac{d\sigma}{d\Omega} = \sigma_{ns} \left[\left(F_1^2 + \frac{\kappa_p^2 Q^2}{2M_p^2} F_2^2 \right) + \frac{Q^2}{2M_p^2} (F_1 + \kappa_p F_2)^2 \tan^2(\frac{\theta_e}{2}) \right] \,,
\qquad (1.12)
$$

where σ_{ns} in equation (1.12) above is known as the non-structure cross section and is given by:

$$
\sigma_{ns} = \frac{\alpha^2 \cos^2(\frac{\theta_e}{2})}{4E^2 \sin^4(\frac{\theta_e}{2})} \frac{E'}{E} \,,
\qquad (1.13)
$$

where α is the fine structure constant.

It is worth mentioning that σ_{ns}, equation (1.13), is nothing but the famous Rutherford formula for the elastic electron-proton scattering modified to account for the proton's recoil and the spin-orbit coupling effects:

1. The recoil effect: The term $\frac{E'}{E}$, which is relativistic in nature, is due to the recoil of the proton. Although the protons are massive, their recoil effect can not be neglected at high momentum transfer squared Q^2. We can write $\frac{E'}{E}$ in terms of the electron's kinematics as:

$$
\frac{E'}{E} = \frac{1}{1 + \frac{2E}{M_p} \sin^2(\frac{\theta_e}{2})} \,,
\qquad (1.14)
$$

where it should be clear that the term $(\frac{E'}{E}) \to 1.0$ as $Q^2 \to 0$.

2. The spin-orbit coupling: The electron is a spin-$\frac{1}{2}$ particle and has a magnetic moment μ_e which interacts with the magnetic field B_p of the proton as it is felt by the electron in its own frame of reference. This is referred to as the spin-orbit coupling effect which results in the $\cos^2(\frac{\theta_e}{2})$ term or more precisely, $1 - \beta^2 \sin^2(\frac{\theta_e}{2})$, with $\beta = (\frac{v}{c}) \to 1.0$ for extremely relativistic electrons.

We refer to the cross section without taking into account the recoil effect as the Mott cross section and it is given by:

$$\left(\frac{d\sigma}{d\Omega}\right)_{Mott} = \frac{(Z\alpha)^2 \left(1 - \beta^2 \sin^2(\frac{\theta_e}{2})\right)}{4k^2 \sin^4(\frac{\theta_e}{2})} \, , \tag{1.15}$$

where k is the initial momentum of the incident electron and Z is the atomic number. In the case of a high momentum electron scattered off a spin-1/2 point-like proton ($Z = 1$), we recover equation (1.13) without accounting for the recoil effect i.e. ($\frac{E'}{E} \to 1$).

In the non-relativistic limit where $\beta \to 0, E \to k$, and $\frac{E'}{E} \to 1$, equation (1.13) becomes:

$$\left(\frac{d\sigma}{d\Omega}\right)_{Rutherford} = \frac{\alpha^2}{4k^2 \sin^4(\frac{\theta_e}{2})} \, , \tag{1.16}$$

and this is the famous Rutherford cross section formula.

To put things in more perspective we can write:

$$\sigma_{ns} = \left(\frac{d\sigma}{d\Omega}\right)_{Rutherford} \left[1 - \beta^2 \sin^2(\frac{\theta_e}{2})\right] \left(\frac{E'}{E}\right) = \left(\frac{d\sigma}{d\Omega}\right)_{Mott} \left(\frac{E'}{E}\right) \, , \tag{1.17}$$

which describes the proton as a spin-1/2 point-like particle without any internal structure.

1.4   Form Factor Interpretations

As shown earlier the concept of the nucleus as a point-like particle with a static charge distribution $\varrho(\vec{r}) = Ze\delta(\vec{r})$ is not the correct one. This is due to the fact that the nucleus has an internal substructure in the form of electric charge and magnetic moment distribution. This substructure modifies the non-structure scattering cross section as given by equation (1.13) to:

$$\frac{d\sigma}{d\Omega} = \left(\frac{d\sigma}{d\Omega}\right)_{ns} |F(Q^2)|^2 \; , \tag{1.18}$$

where $F(Q^2)$ is the form factor which accounts for the fact that the target nucleon possess an internal structure. It should be mentioned that F is a function of Q^2 alone in the case of an elastic scattering.

It can be shown [19] that in the non-relativistic limit, the form factor $F(Q^2)$ can be expressed in terms of the charge distribution $\varrho(\vec{r})$ of the target nucleus as:

$$F_{NR}(Q^2) = \int \varrho(\vec{r}) e^{i\vec{Q}.\vec{r}} d^3\vec{r} \; , \tag{1.19}$$

where NR stands for Non-Relativistic. Equation (1.19) is the Fourier transform of the electric charge distribution of the target. In the case of the proton, $F_{NR}(Q^2)$ corresponds to the electric form factor, $G_{Ep}(Q^2)$. In the same way, if the target has an extended magnetic moment distribution, the magnetic form factor is the Fourier transform of the magnetic moment distribution of the target and is referred to as $G_{Mp}(Q^2)$.

If we scatter off a point-like particle with static charge distribution $\varrho(\vec{r}) = Ze\delta(\vec{r})$, equation (1.19) gives $F_{NR}(Q^2) = Z$, and in the case of an extended spatial charge distribution $\varrho(\vec{r}) = \rho_0 e^{-(\frac{r}{a})}$, equation (1.19) gives the well-known dipole form factor $F_{NR}(Q^2) = G_D(Q^2) = (1 + a^2 Q^2)^{-2}$ where a is the scale of the proton radius. Ex-

perimentally, it was observed that both the electric and magnetic form factors could be described to a good approximation by the dipole form factor $G_D(Q^2)$ with $a^2 = (0.71GeV^2)^{-1}$. Figures 1.2, 1.3, and 1.4 show the world data on the electric and magnetic form factors. Figure 1.4 also shows $\frac{G_{Mp}}{\mu p G_D}$ with the fits of Bosted [26] and Brash [27] to the proton magnetic form factor. The Bosted and the Brash fits will be discussed in detail in the next chapter.
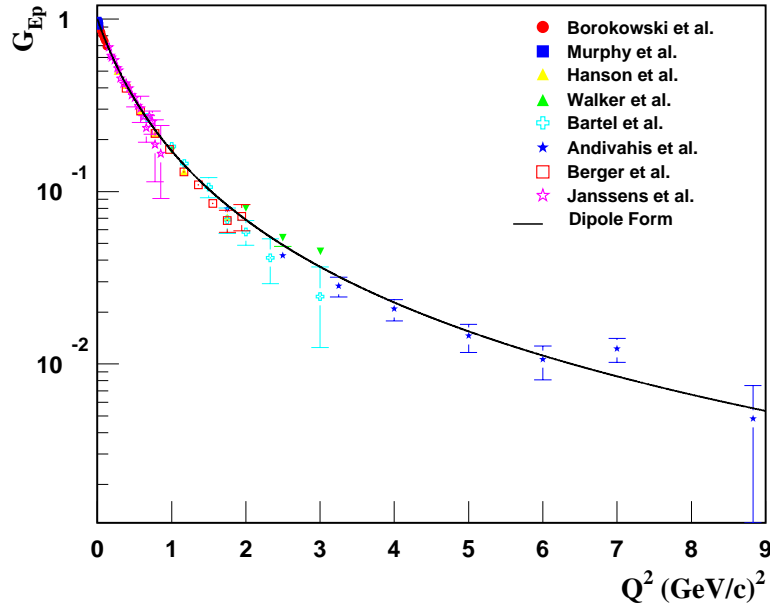
Figure 1.2: G_{Ep} world data. The black solid line is the dipole form factor fit to data. Data from references [6, 28, 29, 7, 5, 8, 4, 1].

If we assume that the magnetic moment of the proton has the same spatial dependence as the charge distribution, then the electric and magnetic form factors (in the non-relativistic limit) are related by $\mu_p \frac{G_{Ep}}{G_{Mp}} = 1.0$ and this is referred to as form factor scaling or:

$$G_{Ep}(Q^2) = \frac{G_{Mp}(Q^2)}{\mu_p} \ .$$
(1.20)

The electric and magnetic form factors seem to approximately follow the dipole
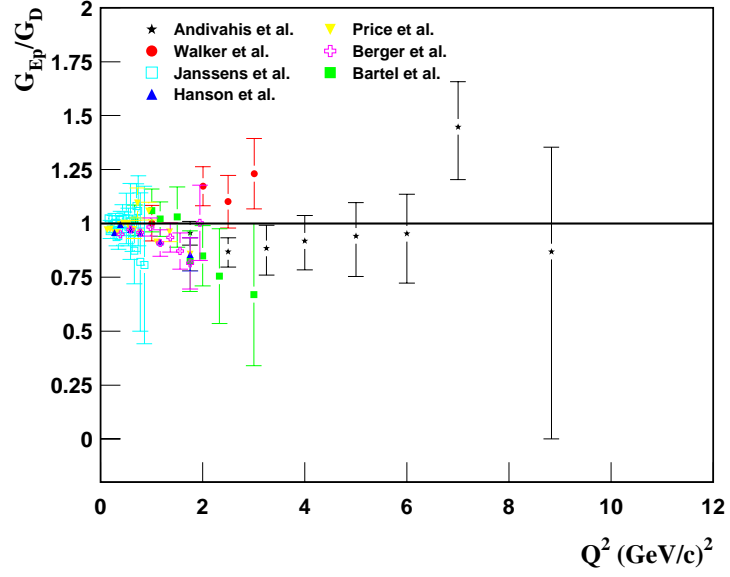
Figure 1.3: G_{Ep} world data normalized to the dipole form factor G_D. Data from references [28, 29, 7, 5, 8, 4, 1, 3].
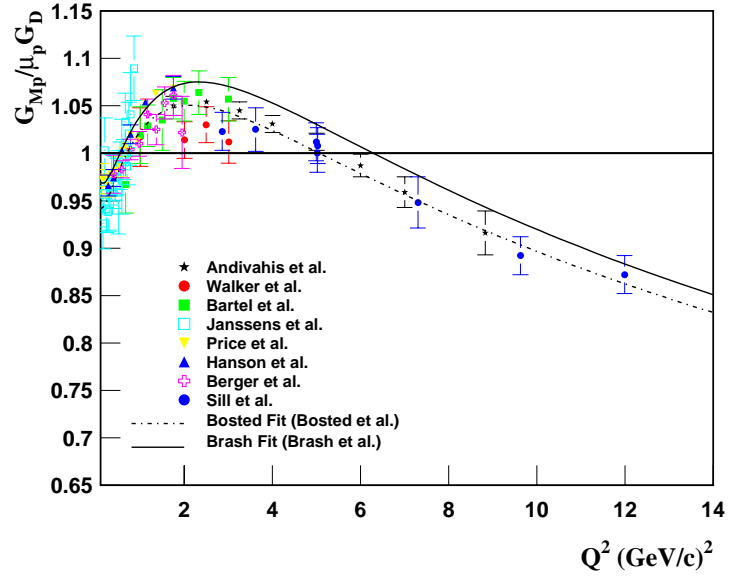
Figure 1.4: G_{Mp} world data normalized to the dipole form factor G_D. The solid and the dotted lines are the Bosted and Brash fits, respectively. Data from references [28, 29, 7, 5, 8, 4, 1, 3, 30].

form factor as shown in Figures 1.3 and 1.4. This indicates that both form factors have the same Q^2 dependence although G_{Mp} seems to significantly deviate from dipole form factor at high Q^2.

For $|\vec{Q}|r << 1$, equation (1.19) can be expanded in terms of the root-mean-square charge radius as [31]:

$$F_{NR}(Q^2) = 1 - \frac{|Q|^2 < r^2 >_{r.m.s}}{6} + \frac{|Q|^4 < r^4 >_{r.m.s}}{120} + \cdots ,$$

(1.21)

where the root-mean-square charge radius is given by:

$$< r^2 >_{r.m.s} = \int \varrho(\vec{r})r^2 d^3 r .$$

(1.22)

Finally, it is important to realize that the interpretation of the form factors (electric and magnetic) as the Fourier transform of the electric charge and magnetic moment distribution is only valid in the non-relativistic limit.

1.5   Rosenbluth Separations Technique

A linear combinations of the Dirac and Pauli form factors $F_1(q^2)$ and $F_2(q^2)$ can be used to define the Sachs form factors [32], G_{Ep} and G_{Mp}, the electric and magnetic form factors of the proton:

$$G_{Ep}(Q^2) = F_1(Q^2) - \kappa_p \tau F_2(Q^2) ,$$

(1.23)

$$G_{Mp}(Q^2) = F_1(Q^2) + \kappa_p F_2(Q^2) ,$$

(1.24)

where $\tau = \frac{Q^2}{4M_p^2}$. In the limit $Q^2 \to 0$, where the virtual photon becomes insensitive to the internal structure of the proton, equations (1.23) and (1.24) reduce to the

normalization conditions for the electric and magnetic form factors respectively:

$$G_{Ep}(0) = F_1(0) = 1 \; , \tag{1.25}$$

$$G_{Mp}(0) = \left[F_1(0) + \kappa_p F_2(0) \right] = \left(1 + \kappa_p \right) = \mu_p = 2.793 \mu_N \; , \tag{1.26}$$

where $\mu_p = 2.793$ is the proton magnetic moment in units of the nuclear magneton μ_N, $\mu_N = \frac{e\hbar}{2M_p c}$.

If we express $F_1(Q^2)$ and $F_2(Q^2)$ in terms of $G_{Ep}(Q^2)$ and $G_{Mp}(Q^2)$, we can write:

$$F_1(Q^2) = \left[\frac{G_{Ep}(Q^2) + \tau G_{Mp}(Q^2)}{1 + \tau} \right] \; , \tag{1.27}$$

$$F_2(Q^2) = \left[\frac{G_{Mp}(Q^2) - G_{Ep}(Q^2)}{\kappa_p (1 + \tau)} \right] \; . \tag{1.28}$$

By substituting for $F_1(Q^2)$ and $F_2(Q^2)$ in equation (1.12), and dropping the interference term between $G_{Ep}(Q^2)$ and $G_{Mp}(Q^2)$ (keeping leading order terms in perturbation theory with single-photon exchange), we can express the elastic electron-proton cross section in terms of the Sachs form factors as:

$$\frac{d\sigma}{d\Omega} = \sigma_{ns} \left(\frac{G_{Ep}^2(Q^2) + \tau G_{Mp}^2(Q^2)}{(1 + \tau)} + 2\tau G_{Mp}^2(Q^2) \tan^2(\frac{\theta_e}{2}) \right) \; . \tag{1.29}$$

If we express the non-structure cross section in terms of the Mott cross section, we can write equation (1.29) as:

$$\frac{d\sigma}{d\Omega} = \left(\frac{d\sigma}{d\Omega} \right)_{Mott} \left(\frac{E'}{E} \right) \frac{1}{1 + \tau} \left(G_{Ep}^2(Q^2) + \tau \left[1 + 2(1 + \tau) \tan^2(\frac{\theta_e}{2}) \right] G_{Mp}^2(Q^2) \right) \; . \tag{1.30}$$

The virtual photon longitudinal polarization parameter ε is defined as:

$$\varepsilon = \left[1 + 2(1 + \tau) \tan^2(\frac{\theta_e}{2}) \right]^{-1} \; , \tag{1.31}$$

which simplifies equation (1.30) to:

$$\frac{d\sigma}{d\Omega} = \left(\frac{d\sigma}{d\Omega}\right)_{Mott} \left(\frac{E'}{E}\right) \frac{1}{1+\tau} \left(G_{Ep}^2(Q^2) + \frac{\tau}{\varepsilon} G_{Mp}^2(Q^2)\right) , \qquad (1.32)$$

which is the Rosenbluth formula [33].

Due to the $\tau = \frac{Q^2}{4M_p^2}$ factor in equation (1.32) that multiplies $G_{Mp}^2(Q^2)$ but not $G_{Ep}^2(Q^2)$, two cases of interest arise:

1. Small Q^2 ($\tau << 1$): the magnetic form factor $G_{Mp}(Q^2)$ of the proton is suppressed and the cross section is dominated by the contribution of the electric form factor $G_{Ep}(Q^2)$ except as ε gets close to zero.

2. Large Q^2 ($\tau >> 1$): the electric form factor $G_{Ep}^2(Q^2)$ of the proton is suppressed and the cross section is dominated by the contribution of the magnetic form factor $G_{Mp}^2(Q^2)$. Figure 1.5 shows the fractional contribution of $G_{Ep}(Q^2)$ to the cross section as a function of ε for several Q^2 values assuming form factor scaling.

The fact that the magnetic form factor $G_{Mp}(Q^2)$ dominates at large Q^2 (small distances), makes it difficult to extract $G_{Ep}(Q^2)$ with high accuracy from the measured cross section at large Q^2. On the other hand, highly accurate $G_{Mp}(Q^2)$ at small Q^2 is also difficult to extract.

If we pull out the $\frac{\tau}{\varepsilon}$ factor in equation (1.32), we can write:

$$\frac{d\sigma}{d\Omega} = \left(\frac{d\sigma}{d\Omega}\right)_{Mott} \left(\frac{E'}{E}\right) \frac{1}{1+\tau} \frac{\tau}{\varepsilon} \left(\frac{\varepsilon}{\tau} G_{Ep}^2(Q^2) + G_{Mp}^2(Q^2)\right) . \qquad (1.33)$$

Finally, we can define the reduced cross section σ_R as:

$$\sigma_R = \frac{d\sigma}{d\Omega} \frac{(1+\tau)\varepsilon}{\sigma_{ns}} = \left(\tau G_{Mp}^2(Q^2) + \varepsilon G_{Ep}^2(Q^2)\right) , \qquad (1.34)$$

which is the measured cross section multiplied by a kinematic factor. By measuring the reduced cross section σ_R at several ε points for a fixed Q^2, a linear fit of σ_R to ε gives $\tau G_{Mp}^2(Q^2)$ as the intercept and $G_{Ep}^2(Q^2)$ as the slope.

This is known as the Rosenbluth separations method and an example is shown in Figure 1.6. Having extracted G_{Mp} and G_{Ep} for a fixed Q^2, the ratio of the electric to magnetic form factors of the proton $\frac{\mu_p G_{Ep}}{G_{Mp}}$ can be determined for that Q^2 point.
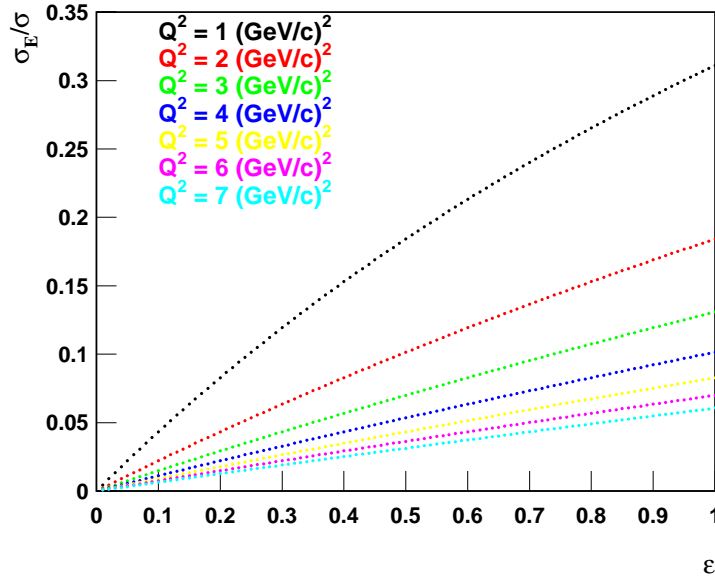
Figure 1.5: Fractional contribution of $G_{Ep}(Q^2)$ to the cross section $\frac{\sigma_E}{\sigma}$ as a function of the virtual photon polarization parameter ε for several Q^2 values assuming $\mu_p G_{Ep}(Q^2) = G_{Mp}(Q^2)$.

1.6 Recoil Polarization Technique

In recoil polarization experiments [11, 12, 14, 15], a longitudinally polarized beam of electrons is scattered by unpolarized protons. This results in a transfer of the polarization from the electrons to the recoil protons. It must be mentioned that any observed polarization of the struck proton was transfered from the electron since the
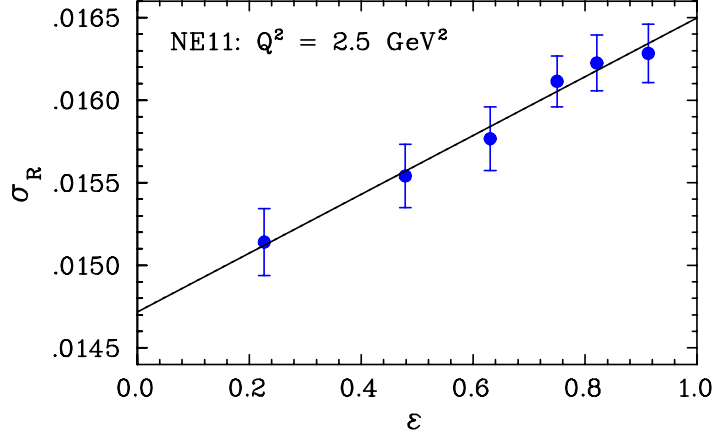
Figure 1.6: Reduced cross section σ_R as a function of the virtual photon polarization parameter ε at fixed $Q^2 = 2.5$ GeV^2. Data is taken from the SLAC NE11 experiment [8].

target is unpolarized. In elastic electromagnetic scattering in the single-photon exchange approximation, there is no induced polarization. In the $^1H(\vec{e}, e', \vec{p})$ reaction, see Figure 1.7, the only non vanishing polarization transfer observables are the transverse, P_t, and the longitudinal, P_l, components of the transfered polarization. The normal component, P_n, does not exist in elastic scattering in single-photon exchange.

In the single-photon exchange approximation, it can be shown [34, 35, 36] that the the transverse, P_t, and the longitudinal, P_l, components of the transfered polarization are related to the Sachs form factors by:

$$I_O P_l = \frac{(E + E')}{M_p} \sqrt{\tau(1 + \tau)} G_{Mp}^2(Q^2) \tan^2(\frac{\theta_e}{2}) \ , \tag{1.35}$$

$$I_O P_t = -2\sqrt{\tau(1 + \tau)} G_{Ep}(Q^2) G_{Mp}(Q^2) \tan(\frac{\theta_e}{2}) \ , \tag{1.36}$$

where E, E', and θ_e are the incident energy, final energy, and scattered angle of the
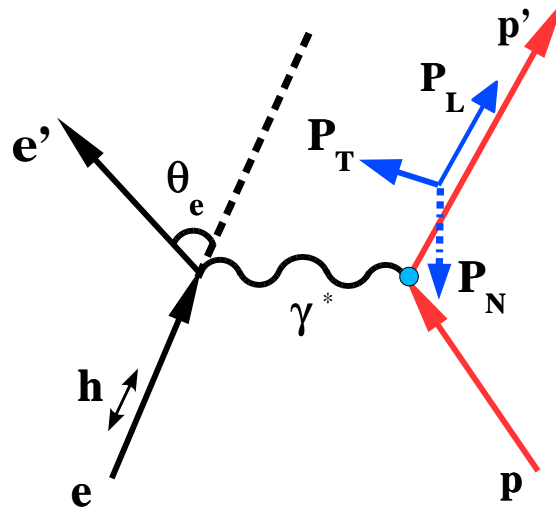
Figure 1.7: Schematic diagram for the recoil polarization spin transfer in the $^1H(\vec{e}, e', \vec{p})$ reaction.

electron, and I_O is defined as:

$$I_O = G_{Ep}^2(Q^2) + \frac{\tau}{\varepsilon}G_{Mp}^2(Q^2) \ . \tag{1.37}$$

In the recoil polarization experiments, a Focal Plane Polarimeter (FPP) [37] is used to simultaneously measure both the transverse and longitudinal polarization components P_t and P_l. By scattering the proton off a secondary target inside the FPP and measuring the azimuthal angular distribution, both P_t and P_l can be determined at the same time for a given Q^2 value.

By dividing equation (1.36) by (1.35) and solving for $\frac{G_{Ep}}{G_{Mp}}$ we can write:

$$\frac{G_{Ep}}{G_{Mp}} = \frac{P_t}{P_l}\frac{(E+E')}{2M_p}\tan(\frac{\theta_e}{2}) \ , \tag{1.38}$$

which is the ratio of the electric to magnetic form factors of the proton $\frac{G_{Ep}}{G_{Mp}}$ as ex-

tracted by direct and simultaneous measurement of the transverse and longitudinal polarization components of the recoiling proton. An interesting point is that while the Rosenbluth separations method measures absolute cross sections and then extracts G_{Ep} and G_{Mp} from these cross sections, the recoil polarization methods gives directly $\frac{G_{Ep}}{G_{Mp}}$ without any measurements of cross sections. The world data for $\frac{\mu_p G_{Ep}}{G_{Mp}}$ as extracted from the two techniques will be discussed in more detail in the next chapter.

Chapter 2   Previous Form Factor Data

2.1   Overview

Understanding the internal structure of the proton is a fundamental problem of strong-interaction physics. It was the famous experiment of Hofstadter and collaborators [38] at Stanford that first measured the internal structure of the proton. Since that time the structure of hadrons has become one of the most important topics in nuclear physics and received the attention of experimentalists and theorists worldwide. The virtual photon-proton vertex cannot be calculated from first principles. Therefore, the internal structure of the proton has been parameterized in terms of electric $G_{Ep}(Q^2)$ and magnetic $G_{Mp}(Q^2)$ form factors. The electromagnetic form factors of the protons are used to describe the deviations of the proton from a point-like particle in elastic electron-proton scattering. In the non-relativistic limit, the form factors are interpreted as the Fourier transform of the spatial distributions of the charge and magnetic moment.

2.2   Previous Measurements

Several experiments have been conducted over the last fifty years to measure the elastic electron-proton cross section. Some of these experiments were able to extract the electric and magnetic form factors of the proton, G_{Ep} and G_{Mp}, using the Rosenbluth separation technique. The form factor ratio $\frac{\mu_p G_{Ep}}{G_{Mp}}$ has also been measured using the recoil polarization technique where the elastic electron-proton cross section are not feasible. In this section I will briefly summarize the work done and the results quoted

by these two techniques in a chronological order. In particular, a brief description of the technique used, kinematics range covered, experimental details, radiative corrections applied (if applicable), and uncertainties quoted in the measured cross sections and in the overall normalization is presented. A comparison between the results of the two techniques will be made and a discussion of the global analyses and fits of the world data will be presented. Because the focus of the present work is on $\frac{\mu_p G_{Ep}}{G_{Mp}}$, the stress is placed on the values of this ratio obtained in the various experiments.

2.2.1 Elastic e-p Cross Sections Measurements

The following experiments measured the elastic e-p cross sections for different Q^2 range. Experiments are listed under the name of the first author:

- **_Janssens et al, 1966 [1]:_**

The Stanford Mark III linear accelerator was used to produce an incident electron beam of energies in the range of $0.25 < E_0 < 1.0$ GeV. A liquid hydrogen target 0.953 cm thick with 0.0254 mm stainless steel target walls was used to scatter electrons. The scattered electrons were detected using the 72 inch double focusing magnetic spectrometer. Elastic e-p cross sections were measured at 25 different Q^2 in the range of $0.15 < Q^2 < 0.86$ GeV^2 covering an angular range of $45^o < \theta < 145^o$ with uncertainty never more than 0.08^o. Of the 25 Q^2 measured, 20 Q^2 points had enough ε coverage to do an L-T separation (Rosenbluth separation). Typically 3-5 ε points per Q^2 value. Measurements for a single ε point at $Q^2 = 1.01$, 1.09, and 1.17 GeV^2 were made at constant spectrometer angle of $\theta = 145^o$, and that of $Q^2 = 0.49$, and 0.68 GeV^2 were made at constant spectrometer angle of $\theta = 75^o$. The internal radiative corrections were calculated using the method of Tsai [39] and the external radiative corrections (bremsstrahlung in the target) were calculated using the formulas of Schwinger [40] and Bethe [41]. The quoted uncertainty in the absolute elastic cross section was on

the 4.0% level with 1.6% as an overall normalization uncertainty. L-T extractions of the proton form factors were performed. Figure 2.1 shows the ratio of electric to magnetic form factor of the proton from this work.
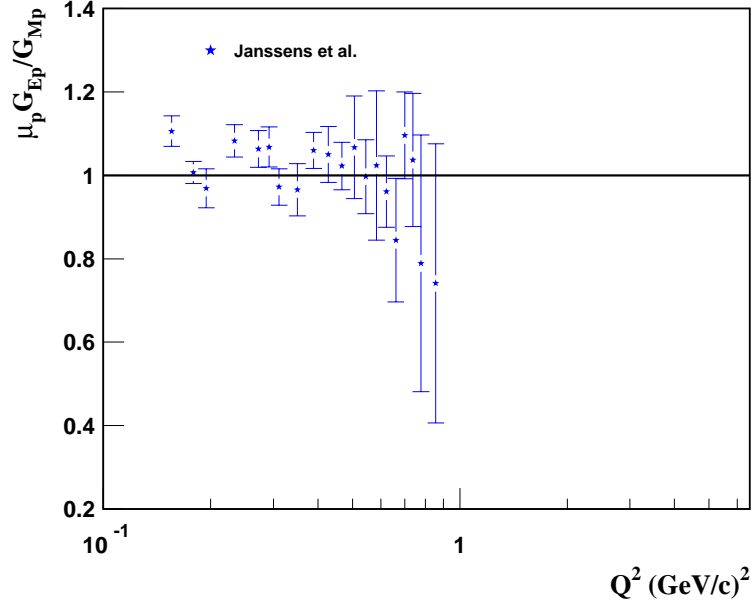
Figure 2.1: The ratio of electric to magnetic form factor $\mu_p G_{Ep}/G_{Mp}$ by Janssens et al [1].

- *Litt et al, 1970 [2]:*

An electron beam from the Stanford Linear Accelerator Center (SLAC) was produced in the range of $4.0 < E_0 < 10.0$ GeV. A liquid-hydrogen target 23 cm in length was used to scatter electrons. The scattered electrons were detected using the SLAC 8-GeV/c magnetic spectrometer. Six Q^2-values in the range of $1.0 < Q^2 < 3.75$ GeV^2, corresponding to a scattering angle in the range of $12.5^o < \theta < 41.4^o$, were covered. On the average, 3-5 ε points were taken for each Q^2 setting allowing for an L-T extraction of the proton form factors. Data was corrected for radiation loss due to straggling of

the electrons in the target using Eyges [42]. Internal radiative corrections were applied using Tsai [39]. Measured cross sections were determined to within a (1.5-2.0)% point-to-point uncertainty. An overall normalization uncertainty of 4.0% was quoted. Figure 2.2 shows the ratio of electric to magnetic form factor of the proton from this work.
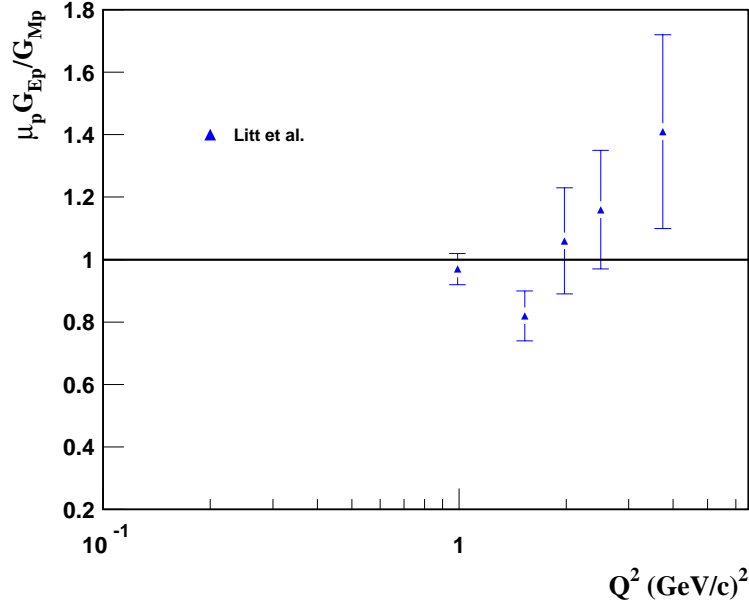
Figure 2.2: The ratio of electric to magnetic form factor $\mu_p G_{Ep}/G_{Mp}$ by Litt et al [2].

- ***Price et al, 1971 [3]:***

This experiment is an extension of the forward angle experiment done by Goitein et al [43]. Incident electron beams from the Cambridge Electron Accelerator (CEA) in the range of 0.45< E_0 <1.6 GeV were used and directed on a 3.3 cm liquid-hydrogen target in length. Electrons were scattered at large angle in the range of 80°< θ <90° and detected using the 14% total momentum acceptance and 0.83 msr solid angle magnetic spectrometer. Cross sections were measured in the range 0.25< Q^2 <1.75

GeV^2. Radiative corrections were applied using the equivalent radiators method of Mo and Tsai [44] with modifications added using Meister and Yennie [45]. The cross sections from the large angle measurements were known with uncertainties of (3.1-5.3)% including both statistical and systematic uncertainties. There is also an overall normalization uncertainty of 1.9%. It should be mentioned that the large angle data by itself was not sufficient to do an L-T extraction. Rather, elastic cross sections from this work were combined with several e-p scattering experiments and a correction for normalization difference between the several experiments was applied. Therefore, no estimation of the uncertainties in the cross sections was given due to the difference in the normalization procedures used. Global fits were performed using G_{Ep} and G_{Mp} as parameters of the fit. The results of combining e-p cross sections from several experiments showed deviations from form factor scaling. Figure 2.3 shows the ratio of electric to magnetic form factor of the proton from this work.
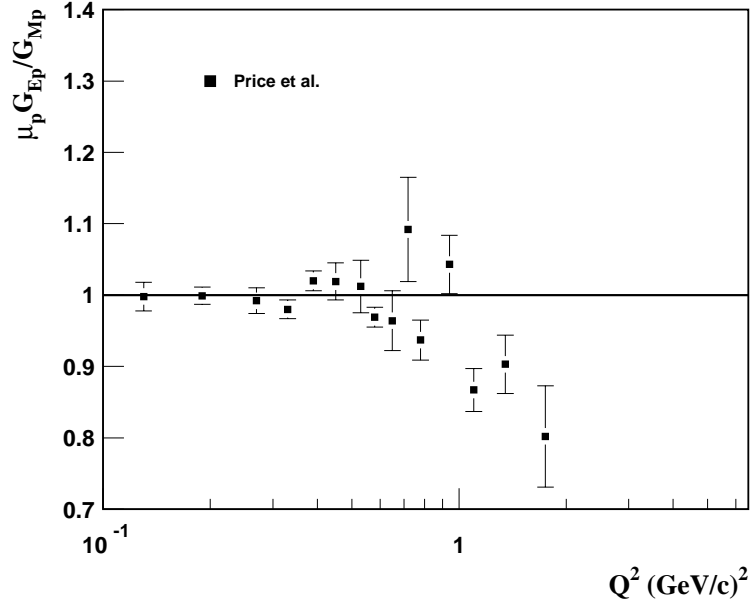
Figure 2.3: The ratio of electric to magnetic form factor $\mu_p G_{Ep}/G_{Mp}$ by Price et al [3].

- **Berger et al, 1971 [4]:**

Measurements of the elastic e-p cross sections were made at the Physikalisches Institute at the University of Bonn in Germany. Incident electron beams of energies in the range of $0.66 < E_0 < 1.91$ GeV were directed on a liquid-hydrogen target 5 cm in diameter. Cross sections measurements were made for $0.10 < Q^2 < 1.95$ GeV^2 covering angular range of $25^o < \theta < 111^o$ with low Q^2 data taken at $\theta = 30^o$ in order to normalize to other experiments (DESY, Bartel et al [46]). With the goal to combine the data and extract form factors, 3-14 ε data points were taken for each Q^2 value. Internal radiative correction were applied using the method of Meister and Yennie [45]. The external bremsstrahlung corrections were applied using Heitler [47]. Cross sections were determined to within (2-6)% with an overall normalization uncertainty of 4%. It was concluded that form factor scaling was not valid at least in the region of $0.39 < Q^2 < 1.95$ GeV^2. Figure 2.4 shows the ratio of electric to magnetic form factor of the proton from this work.

- **Kirk et al, 1972 [48]:**

Electron beams from the Stanford Linear Accelerator Center (SLAC) in the range of $4.0 < E_0 < 17.31$ GeV were directed on a five condensation-type liquid-hydrogen target cells of different sizes (8-32 cm diameter with 25-75-μ-thick stainless steel walls). The scattered electrons were detected using the SLAC 1.6-GeV/c and SLAC 8-GeV/c magnetic spectrometers. With the assumption that the electric form factor contribution to the elastic cross section is small, the experiment aimed to extract the magnetic form factors over a large Q^2 range of $1.0 < Q^2 < 25$ GeV^2, covering three main angular regions to a maximum of 180°. The 20-GeV/c spectrometer was used for small angle measurements $0^o < \theta < 20^o$, the 8-GeV/c spectrometer was used for intermediate angle measurements $12^o < \theta < 105^o$, and the 1.6-GeV/c spectrometer was used for backward angle measurements $25^o < \theta < 165^o$. The main data was taken in the
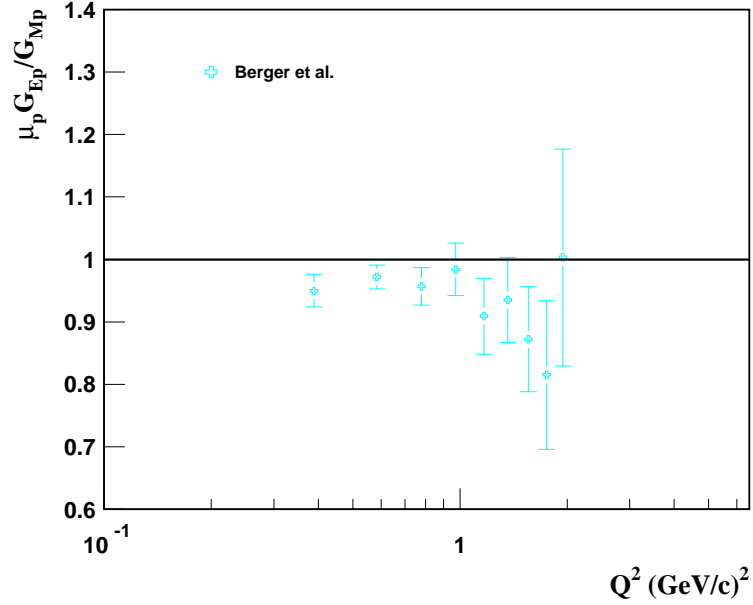
Figure 2.4: The ratio of electric to magnetic form factor $\mu_p G_{Ep}/G_{Mp}$ by Berger et al [4].

range of $12^o < \theta < 35^o$ while the data at low Q^2 was taken to provide cross calibration with other experiments. Some of the higher Q^2 data ($Q^2 = 5$ and 10 GeV^2) was taken to be combined with large angle measurements from different experiments to provide an upper limit value for G_{Ep}. Internal radiative corrections were applied using Tsai [39], and Eyges [42] for the external corrections. Cross sections were reported with uncertainties of 2.0% and with an overall normalization uncertainty of 4.0%. An L-T extraction was impossible since there were not enough ε data points taken. Although no plot of the ratio of electric to magnetic form factor of the proton from this work is possible, the cross sections measured in this experiment were combined with cross sections from other experiments for global extractions of the proton elastic form factors.

- *Murphy et al, 1974 [28]:*

The University of Saskatchewan Linear Accelerator was used to provide electron beams in the range of 0.057< E_0 <0.123 GeV. The beam was directed on a gaseous-hydrogen target in a circular cylinder 2.54 cm in radius and 3.50 cm in high. In this work, the recoil protons rather than the scattered electrons were detected by a double-focusing magnetic spectrometer. Measurements were made for 11-values of Q^2 in the range of 0.006< Q^2 <0.031 GeV^2 covering only two angles for the recoiled protons, $\theta_p = 30^o$ and 45°. Not enough ε data points were covered to perform an L-T extraction. Radiative corrections for the protons were applied using the method of Meister and Yennie [45]. The experiment extracted the values of G_{Ep} with total uncertainty in the range of (0.3-0.9)%. No plot of the ratio of electric to magnetic form factor of the proton from this work is possible. Cross sections measured in this experiment were combined with cross sections from other experiments for global extraction of the proton elastic form factors.

- *Bartel et al, 1973 [5]:*

Elastic e-p scattering cross sections were measured using the Deutsches Elecktronen-Synchrotron (DESY) in Hamburg Germany. An electron beams in the range of 0.8< E_0 <3.0 GeV were directed on a cylindrical vessel 5 cm in diameter and 6 cm long liquid-hydrogen target. Using the high resolution magnetic spectrometer (small angle spectrometer), measurements of cross sections were made at electron scattering angle in the range of 10°< θ_e <20° and by detecting protons at forward angles (corresponding to $\theta_e = 86^o$) using the recoil nucleon detector. Electrons scattered at large angle, $\theta_e = 86^o$, were measured using the large angle spectrometer. Cross sections were measured at 7-values of Q^2 in the range of 0.67< Q^2 <3.0 GeV^2 with uncertainty on the 2-4% level and an overall normalization uncertainty of 2.1%. Typically 2-3 ε points were taken per Q^2 value allowing for an L-T extraction. Internal radiative corrections were calculated using Meister and Yennie [45], and the external radiative contribution were calculated using Mo and Tsai [44]. Electron-proton cross

sections in this work and several other experiment were compiled and analyzed. A global fit was performed in order to extract the form factors. Deviations from form factor scaling were reported. Figure 2.5 shows the ratio of electric to magnetic form factor of the proton from this work.
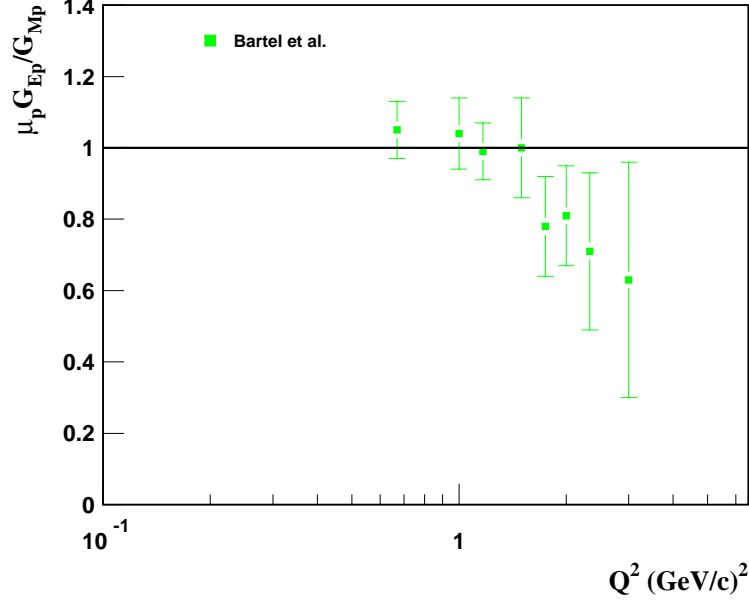
Figure 2.5: The ratio of electric to magnetic form factor $\mu_p G_{Ep}/G_{Mp}$ by Bartel et al [5].

- **_Stein et al, 1975 [49]:_**

The Stanford Linear Accelerator Center (SLAC) was used to produce an electron beams in the range of 4.5< E_0 <20.0 GeV. Elastic cross sections measurements were made in the range of 0.004< Q^2 <0.07 GeV^2 at a scattering angle of $\theta = 4^o$ providing one ε data point for each Q^2 value measured. Clearly not enough ε data points for an L-T extraction. The beam was directed on a vertical cylinder with 0.0076 cm aluminum walls liquid-hydrogen target. The scattered electrons were detected using the SLAC 20-GeV/c spectrometer. Radiative corrections were applied to the

measured cross sections using the procedure of Mo and Tsai [44]. The uncertainties in the cross sections are on the 3.1% level with an overall normalization uncertainty of 2.8%. No plot of the ratio of electric to magnetic form factor of the proton from this work is possible. Cross sections measured in this experiment were combined with cross sections from other experiments for global extractions of the proton elastic form factors.

- **Borkowski et al, 1975 [6]:**

Elastic e-p scattering cross sections have been measured using the 300 MeV Electron Linear Accelerator at Mainz. An electron beam was produced in the range of $0.15< E_0 <0.30$ GeV and was directed on a 10 mm diameter thin-walled cylindrical cell filled with liquid-hydrogen. Elastic cross sections measurements were made in the range of $0.005< Q^2 <0.183$ GeV^2 covering a scattering angle in the range of $28^o< \theta_e <150^o$. Measurements were made using two spectrometers. The first is the double-focusing 180° spectrometer and was set to different scattering angles. The second consisted of two quadrupoles and 12° bending-magnet spectrometer and was fixed at scattering angle of 28° as a monitor. Radiative corrections were applied using Mo and Tsai [44]. Random uncertainties in the cross sections were reported and were on the (1.0-2.0)% level. Figure 2.6 shows the ratio of electric to magnetic form factor of the proton from this work.

- **Bosted et al, 1990 [50]:**

The primary goal of this experiment was to measure the magnetic structure function $B(Q^2)$ of the deuteron to the largest Q^2-value possible. The elastic cross sections of the e-p scattering were measured near 180° and the value of the magnetic form factor G_{Mp} was determined assuming form factor scaling with small G_{Ep} contribution to the cross sections at high Q^2 points. Incident electron beam from the Stanford
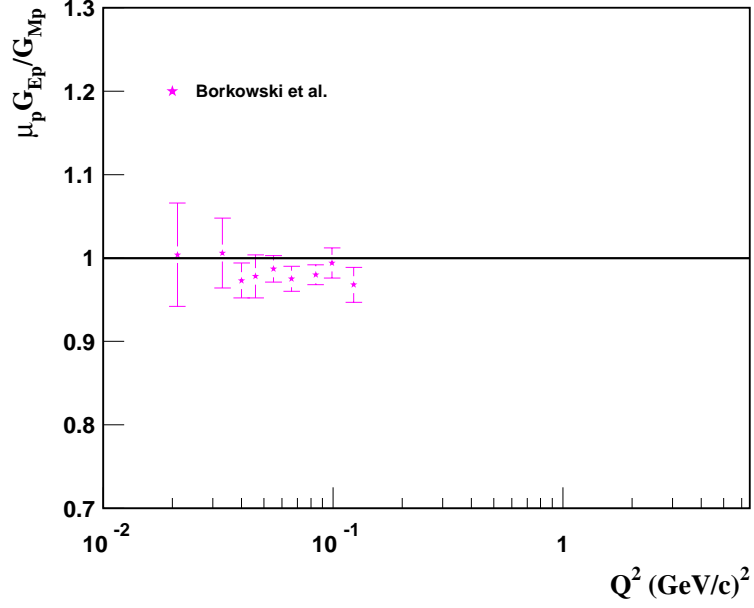
Figure 2.6: The ratio of electric to magnetic form factor $\mu_p G_{Ep}/G_{Mp}$ by Borkowski et al [6].

Linear Accelerator Center (SLAC) of energies in the range of 0.5< E_0 <1.3 GeV was directed on a liquid-hydrogen target with nominal lengths of 40, 20, 10, and 5 cm. Cross sections were measured at 11-values of Q^2 in the range of 0.49< Q^2 <1.75 GeV^2 for electrons backscattered near 180° in coincidence with protons recoiling near 0° in a large solid-angle double-arm spectrometer. An L-T extraction is impossible from these measurements. The equivalent radiator approximation method of Tsai [39] was used for the internal radiative corrections. The effect of the bremsstrahlung and Landau straggling in the target external radiative corrections were combined with that of the internal corrections. Cross sections with uncertainty of 3% were quoted with an overall normalization uncertainty of 1.8%. No plot of the ratio of electric to magnetic form factor of the proton from this work is possible. Cross sections measured in this experiment were combined with cross sections from other experiments for global extraction of the proton elastic form factors.

- ***Rock et al, 1992 [51]:***

The main goal of this experiment was to extract the elastic neutron cross sections but elastic e-p cross sections were also measured since they were needed for the analysis. The Stanford Linear Accelerator Center (SLAC) electron beam with energies in the range of $9.761 < E_0 < 21.0$ GeV was directed on a 30-cm long liquid-hydrogen cell. The elastic e-p cross sections were measured at 5 values of Q^2 in the range of $2.5 < Q^2 < 10.0$ GeV^2 at a fixed scattering angle of $\theta = 10^o$. An L-T extraction is impossible with this data. The scattered electrons were detected using the SLAC 20-GeV/c spectrometer. The cross sections were radiatively corrected using the method of Tsai [39]. The uncertainties in the cross sections were on the 1-4% level in addition to an overall normalization uncertainty of 3%. No plot of the ratio of electric to magnetic form factor of the proton from this work is possible. Cross sections measured in this experiment were combined with cross sections from other experiments for global extraction of the proton elastic form factors.

- ***Sill et al, 1993 [30]:***

Elastic e-p cross sections were measured using the beam line at the Stanford Linear Accelerator (SLAC). An electron beams of energies in the range of $5.0 < E_0 < 21.5$ GeV were directed on two liquid-hydrogen targets with different lengths. The 25-cm target was used for normalization of the acceptance of the 65-cm target and to provide a test for the low Q^2 data. The 65-cm target provided higher counting rate and was used to take the majority of the elastic data. The scattered electrons were detected using the SLAC 8-GeV/c spectrometer. Cross sections were measured for 13-values of Q^2 for the range of $2.9 < Q^2 < 31.3$ GeV^2 covering three-angle settings of $\theta_e = 21^o$, 25°, and 33°. Due to the limited angular range, an L-T extraction was impossible to perform. Radiative corrections were applied to the data using Mo and Tsai [44]. Cross sections uncertainties were on the 3-4% level with an overall normalization

uncertainty of 3.6%. No plot of the ratio of electric to magnetic form factor of the proton from this work is possible. Cross sections measured in this experiment were combined with cross sections from other experiments for global extraction of the proton elastic form factors.

- ***Walker et al, 1994 [7]:***

The Stanford Linear Accelerator Center beam line was used to produce incident electron beams of energies in the range of $1.594 < E_0 < 8.233$ GeV. The beam was directed on cylindrical liquid-hydrogen target 20-cm in length and 5.08-cm in diameter. The scattered electrons were detected using the SLAC 8-GeV/c spectrometer. Elastic e-p cross sections were measured for 4-values of Q^2 in the range of $1.0 < Q^2 < 3.007$ GeV^2 covering angular range of $11.714^o < \theta < 45.221^o$ with an average of 3-8 ε points per Q^2 point allowing for an L-T extraction. Internal radiative corrections were done using Mo and Tsai [44]. Also, improvements were made to the internal corrections using the equivalent radiator approximation. The external corrections were applied using the work of Tsai [39] to account for bremsstrahlung in the target material and the effects of the Landau tail of the ionization energy loss spectrum. Uncertainty in the cross sections was on the 1% level with an overall normalization of 1.9%. Figure 2.7 shows the ratio of electric to magnetic form factor of the proton from this work. Cross sections from several experiments including this work were combined and a fit for a global extraction of the form factors was performed. Results indicate good consistency between the different data sets. The form factors extracted from this work supported form factor scaling. See Figure 2.18 in section (2.4) for more detail.

- ***Andivahis et al, 1994 [8]:***

The primary goal of this experiment was to minimize both statistical and systematic uncertainties and extend the measurements of the form factors to a high Q^2
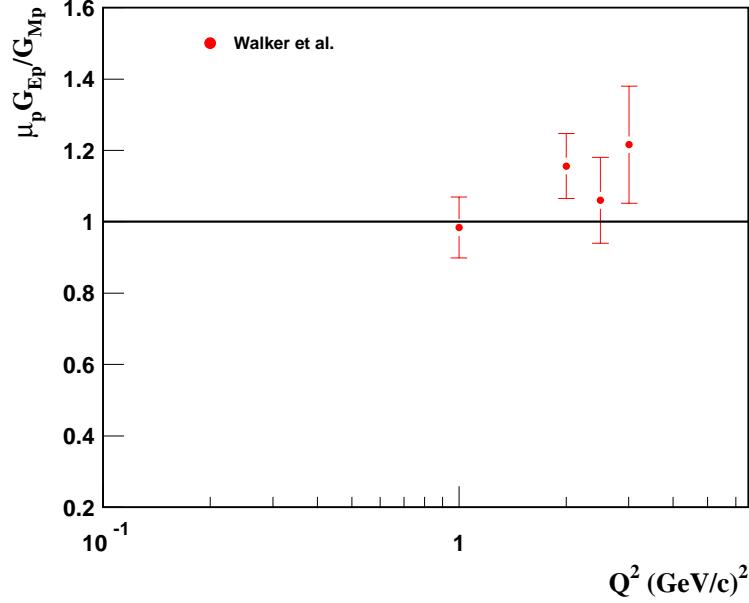
Figure 2.7: The ratio of electric to magnetic form factor $\mu_p G_{Ep}/G_{Mp}$ by Walker et al [7].

values. The Stanford Linear Accelerator Center (SLAC) was used to produce electron beams with energies in the range of $1.511< E_0 <9.8$ GeV. The beam was directed on a 15-cm liquid-hydrogen target. The scattered electrons were detected using both the SLAC 1.6 and 8-GeV/c spectrometers simultaneously. The 8-GeV/c spectrometer was used to measure 5-values of Q^2 in the range of $1.75< Q^2 <5.0$ GeV^2 where an L-T extraction is possible with an average of 3-6 ε points per Q^2. In addition, two extra points at $Q^2 = 6.0$ and 7.0 GeV^2 were measured as a single ε points. The angular range was $13.25^o< \theta <90.066^o$. The 1.6-GeV/c spectrometer was used to measure 8-single-points of ε at $Q^2 = 1.75, 2.50, 3.25, 4.0, 5.0, 6.0, 7.0,$ and 8.83 GeV^2 at a constant angle $\theta \approx 90^o$ so data could be combined with previous forward-angle cross sections [52, 30] collected at SLAC at the same Q^2. The 1.6-GeV/c cross sections were normalized to the 8-GeV/c results. The procedure of the radiative corrections applied was similar to the procedure introduced by Walker et al [7] reported above.

Average uncertainties in the cross sections were less than 2% with an overall normalization uncertainty of 1.77%. Figure 2.8 shows the ratio of electric to magnetic form factor of the proton from this work.
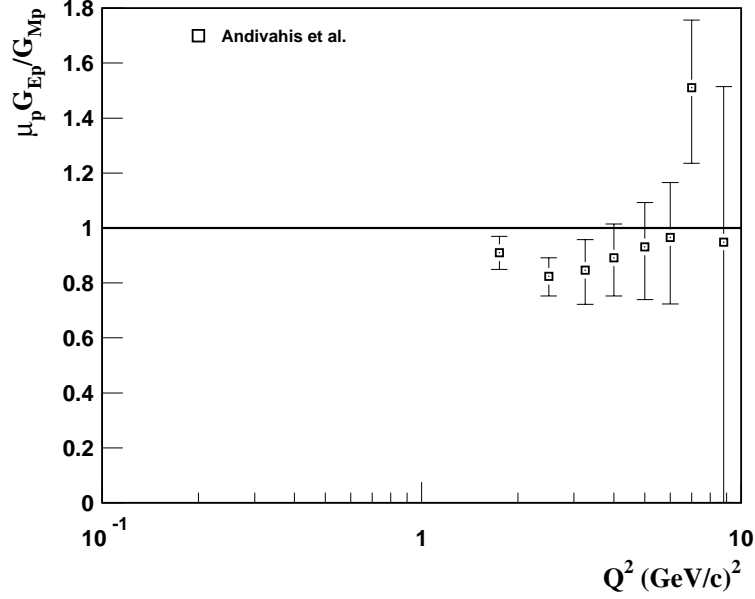
Figure 2.8: The ratio of electric to magnetic form factor $\mu_p G_{Ep}/G_{Mp}$ by Andivahis et al [8].

- *Christy et al, 2004 [9]:*

The focus of this experiment was to separate the longitudinal and transverse unpolarized proton structure functions in the resonance region using Rosenbluth separation technique, but elastic e-p cross sections were also measured at 28-values of Q^2 in the range of $0.4 < Q^2 < 5.5$ GeV^2 covering an angular range of $12.5^o < \theta_e < 80^o$. This range covered 3 ε points per Q^2 allowing for L-T separations at 7 Q^2-values. The experiment was done at the experimental Hall C of the Thomas Jefferson National Laboratory (JLAB) in Newport News Virginia. An electron beam in the range of $1.148 < E_0 < 5.494$ GeV was directed on a tuna-can shaped cryogen liquid hydrogen

cell. The cell has an inside diameter of 40.113 mm when warm and 39.932 mm when cold with cylindrical wall thickness of 0.125 mm. The scattered electrons were detected using the High Momentum Spectrometer. Radiative corrections were applied using the procedure described in Walker et al [7] and based on the prescription of Mo and Tsai [44]. Uncertainties in the cross sections were on the 1.96% level with an overall normalization uncertainty of 1.7%. The uncertainties in the $\frac{\mu_p G_{Ep}}{G_{Mp}}$ ratio in the Q^2 region of interest are quite large and do not represent an improvement in accuracy over previous L-T determinations. However, when the polarization transfer results became available and were at odds with the previously known Rosenbluth results, Christy et al carefully analyzed their elastic e-p data and concluded that their $\frac{\mu_p G_{Ep}}{G_{Mp}}$ were not consistent with the ratio reported by Jones et al. Figure 2.9 shows the ratio of electric to magnetic form factor of the proton from this work.
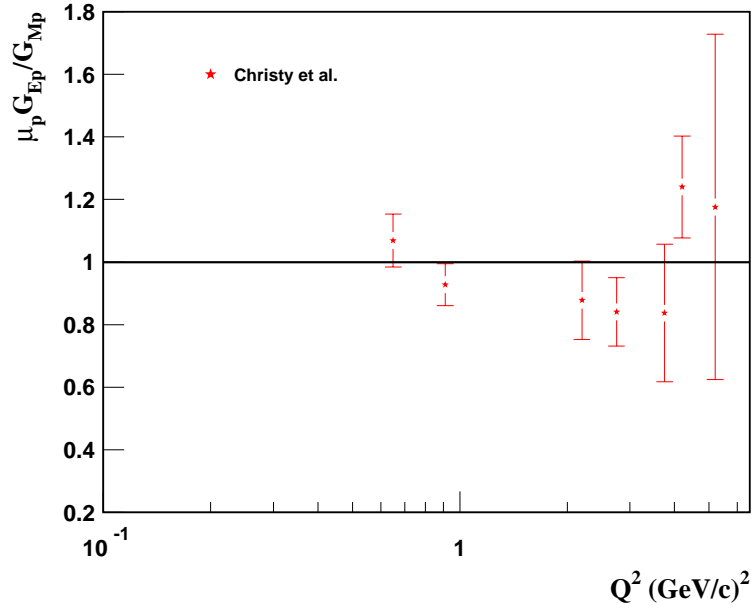
Figure 2.9: The ratio of electric to magnetic form factor $\mu_p G_{Ep}/G_{Mp}$ Christy et al [9].

2.2.2 Polarization Measurements

The following experiments represent the proton polarization measurements (recoil polarization and polarized target measurements) to date for different Q^2 range.

- **Alguard et al, 1976 [10]:**

  The main idea of this experiment was to measure the antiparallel-parallel asymmetry A in the differential cross section which in turn is related to the form factors of the proton. The polarized electron source (PEGGY) at the 20-GeV Stanford Linear Accelerator Center (SLAC) was used to produce a polarized electron beam which was directed on a polarized proton target polarized by the method of dynamic nuclear orientation in a butanol target doped with 1.4% porphyrexide. The scattered electrons were detected using the 8-GeV/c spectrometer. Data were taken at $Q^2 = 0.765$ GeV^2 with incident electron energy of $E_0 = 6.473$ GeV and scattering electron angle of θ_e = 8.005^o. The beam and target polarization P_e and P_p were measured. The experimental asymmetry Δ was determined in order to solve for the antiparallel-parallel cross section asymmetry A where $\Delta = P_e P_p F A$ and F is the fraction of the elastically scattered electrons within the elastic missing-mass region. Figure 2.10 shows the ratio of electric to magnetic form factor of the proton from this work.

- **Milbrath et al, 1998 [11]:**

  This is the first experiment to demonstrate the feasibility of the recoil polarization as a technique to extract the ratio of electric to magnetic form factors of the proton. Measurements of the recoil proton polarization observables in the reactions $p(\vec{e}, e'\vec{p})$ and $d(\vec{e}, e'\vec{p})n$ were made. The MIT-Bates Linear Accelerator Center was used to produce a longitudinally polarized electron beam of energy $E_0 = 0.58$ GeV. The beam was directed on an unpolarized cryogenic target of liquid hydrogen and deuterium cells of 5 and 3 cm in diameter respectively. The scattered electrons were

37
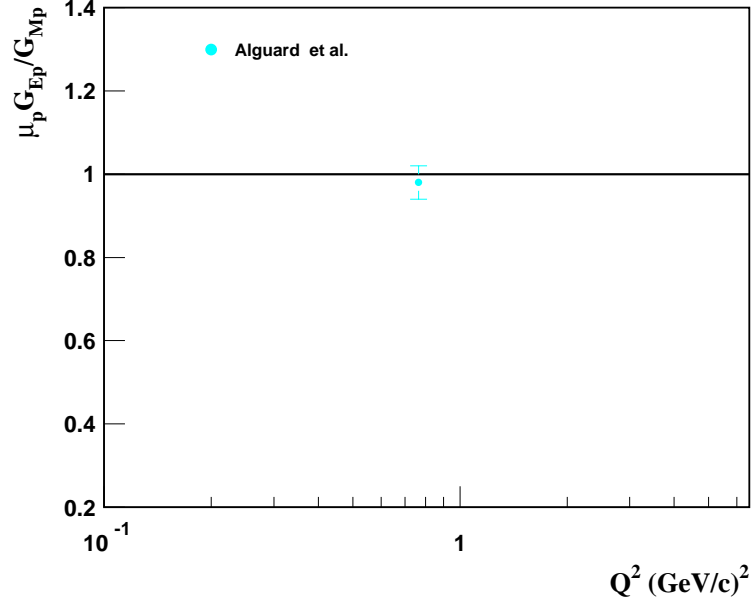
Figure 2.10: The ratio of electric to magnetic form factor $\mu_p G_{Ep}/G_{Mp}$ by Alguard et al [10].

detected using the Medium Energy Pion Spectrometer, and the scattered protons were detected using One-Hundred Inch Proton Spectrometer. Two Q^2-values of 0.38 and 0.5 GeV^2 were measured corresponding to electron-scattering angles of $\theta_e = 82.7^o$ and 113° respectively. The recoil proton polarization was measured in the focal plane polarimeter (FPP). Figure 2.11 shows the ratio of electric to magnetic form factor of the proton from this work.

- *Jones et al, 2000 [12]:*

Recoil proton polarization measurements were carried out at the experimental Hall A of Thomas Jefferson National Laboratory (JLAB) in Newport News Virginia. Polarized electron beam of energy in range of 0.934< E_0 <4.090 GeV was directed on a 15-cm-long unpolarized liquid hydrogen target. The elastically scattered electrons and protons were detected in coincidence using the two identical high resolution
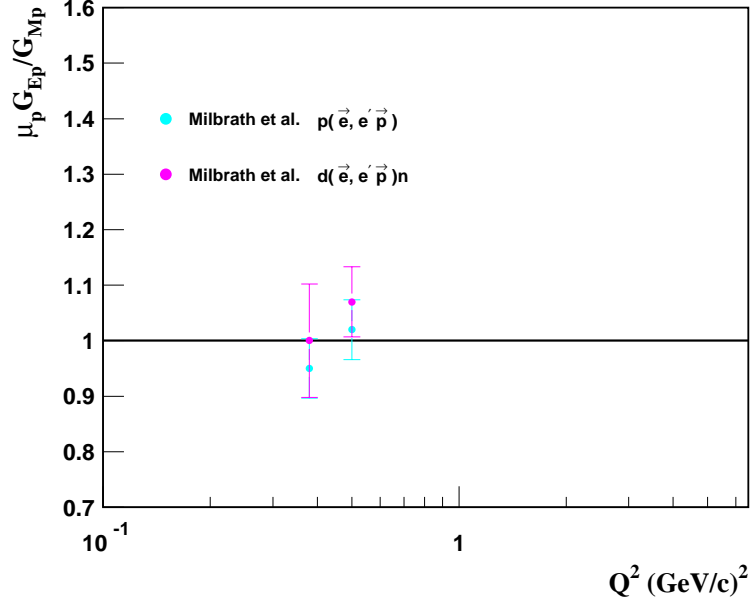
Figure 2.11: The ratio of electric to magnetic form factor $\mu_p G_{Ep}/G_{Mp}$ by Milbrath et al [11].

spectrometers (HRS) of Hall A. The ratio $\frac{\mu_p G_{EP}}{G_{MP}}$ was determined at 9 Q^2-values in the range of $0.49< Q^2 <3.47$ GeV^2 covering an angular range of $22.26^o< \theta_e <79.88^o$ for the electrons and $29.98^o< \theta_p <46.03^o$ for the protons. The recoil proton polarization was measured in the focal plane polarimeter (FPP). External radiative corrections were not applied. The internal radiative corrections such as the hard photon emission and higher order contributions were calculated [53] and found to be on the order of a few percent and were not applied. The results of this work showed the decline of $\frac{\mu_p G_{EP}}{G_{MP}}$ with increasing Q^2 deviating from form factor scaling and indicating for the first time a definite difference in the spatial distribution of charge and magnetization currents in the proton. Figure 2.12 shows the ratio of electric to magnetic form factor of the proton from this work.

- *Pospischil et al, 2001 [13]:*
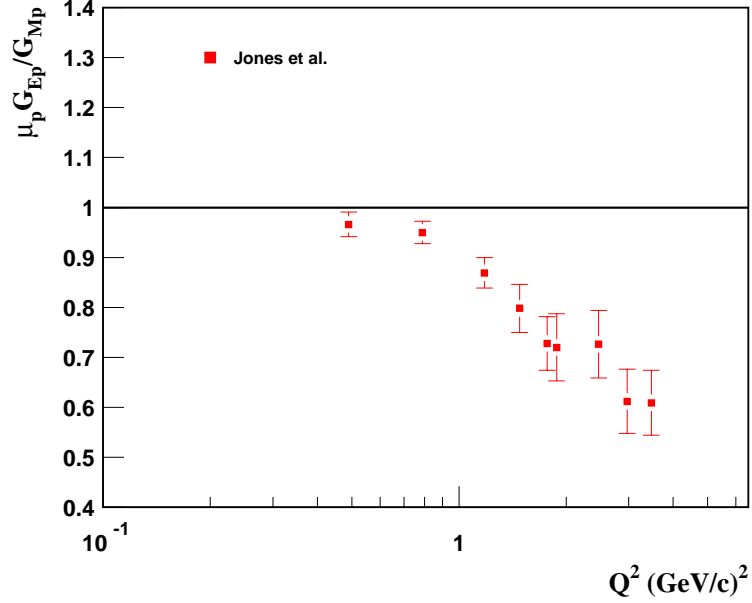
Figure 2.12: The ratio of electric to magnetic form factor $\mu_p G_{Ep}/G_{Mp}$ by Jones et al [12].

Recoil proton polarization measurements were carried at the 3-spectrometer setup of the A1-Collaboration at the Mainz microtron MAMI. Longitudinally polarized electron beam of energy $E_0 = 0.8544$ GeV was directed on a 49.5-mm-long Havar cell filled with unpolarized liquid hydrogen. Data were taken at 3 Q^2-values in the range of $0.373 < Q^2 < 0.441$ GeV^2 covering an angular range of $48.2^o < \theta_e < 54.4^o$ for the electrons and $45.5^o < \theta_p < 49.5^o$ for the protons. The recoil proton polarization was measured in the focal plane polarimeter (FPP). Radiative corrections were not applied. Figure 2.13 shows the ratio of electric to magnetic form factor of the proton from this work.

- **_Gayou et al, 2001 [14]:_**

Recoil proton polarization measurements were carried out at the experimental Hall A of Thomas Jefferson National Laboratory (JLAB) in Newport News Virginia using
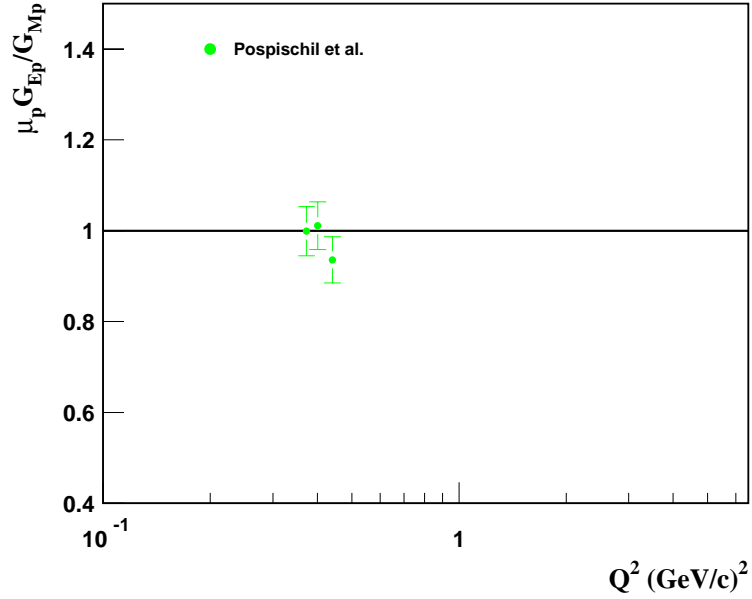
Figure 2.13: The ratio of electric to magnetic form factor $\mu_p G_{Ep}/G_{Mp}$ by Pospischil et al [13].

the same experimental hardware used by Jones et al [12]. Polarized electron beam of energy in range of $1.0 < E_0 < 4.11$ GeV was directed on a 15-cm-long unpolarized liquid hydrogen target. The elastically scattered electrons and protons were detected in coincidence using the two identical high resolution spectrometers (HRS) of Hall A. Although the goal of this experiment was to study the $D(\vec{\gamma}, p)n$ and $H(\vec{\gamma}, p)\pi^0$ reactions, 13 measurements of coincidence $ep \to ep$ polarizations were performed to calibrate the focal plane polarimeter (FPP) used to study the reactions defined above. Data were taken in the range of $0.32 < Q^2 < 1.76$ GeV^2 covering an angular range of $18.012^o < \theta_e < 48.65^o$ for the electrons and $37.446^o < \theta_p < 55.984^o$ for the protons. The recoil proton polarization was measured in the focal plane polarimeter. Radiative corrections were not applied. Figure 2.14 shows the ratio of electric to magnetic form factor of the proton from this work.
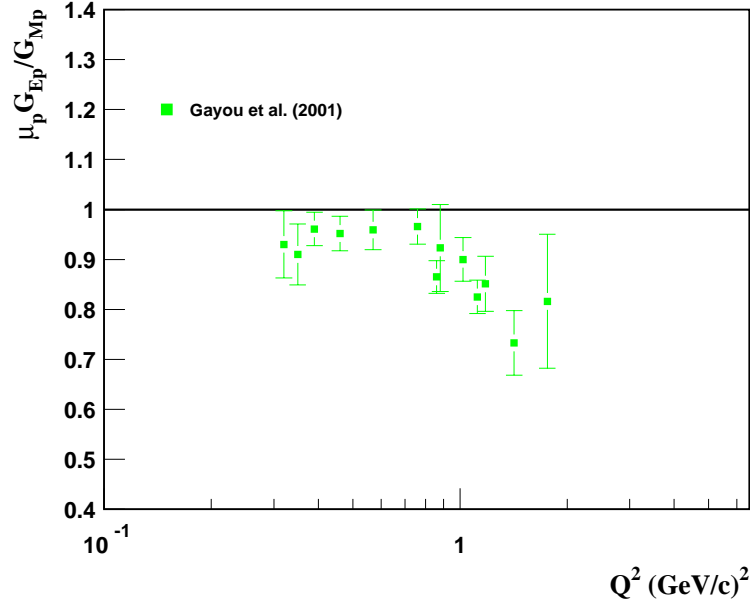
Figure 2.14: The ratio of electric to magnetic form factor $\mu_p G_{Ep}/G_{Mp}$ by Gayou et al [14] (first measurements).

- **_Gayou et al, 2002 [15]:_**

This work in an extension of that of Jones et al [12] where measurements were taken to higher Q^2 value of 5.54 GeV^2. Recoil proton polarization measurements were carried out at the experimental Hall A of Thomas Jefferson National Laboratory (JLAB) in Newport News Virginia also using the same experimental hardware used by Jones et al. Polarized electron beam of energy in range of 4.59< E_0 <4.607 GeV was directed on a 15-cm-long unpolarized liquid hydrogen target. Data were taken in the range of 3.5< Q^2 <5.54 GeV^2. At $Q^2 = 3.5$ GeV^2, the elastically scattered electrons and protons were detected in coincidence using the two identical high resolution spectrometers (HRS) of Hall A with fixed angles of $\theta_e = 30.6^o$ for the electrons and $\theta_p = 31.785^o$ for the protons. At higher Q^2 values of 3.97, 4.75, and 5.54 GeV^2 and at a fixed beam energy $E_0 = 4.607$ GeV, the electrons scattered at a

higher angles than the protons and were detected using a calorimeter in coincidence with the protons covering an angular range of $19.275^o < \theta_e < 28.587^o$ for the electrons and $34.5^o < \theta_p < 51.44^o$ for the protons. The recoil proton polarization was measured using a focal plane polarimeter. Radiative corrections were not applied. Figure 2.15 shows the ratio of electric to magnetic form factor of the proton from this work.
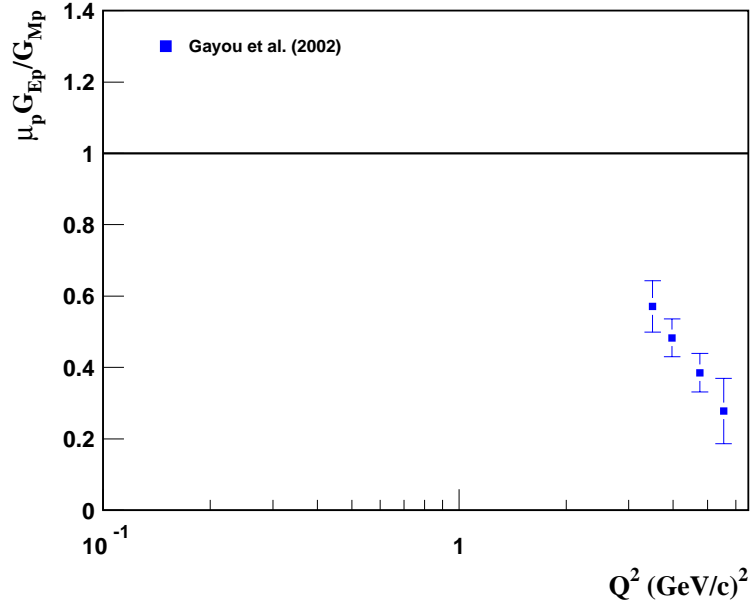
Figure 2.15: The ratio of electric to magnetic form factor $\mu_p G_{Ep}/G_{Mp}$ by Gayou et al [15] (second measurements).

2.3   Summary of Previous e-p Measurements

A summary of section 2.2 for the world's data on elastic e-p scattering cross section measurements is given in Table 2.1. Experiments are listed under the principal author's name, laboratory at which they were performed, energy, Q^2, number of ε points measured at each Q^2 value N_ε, cross section uncertainty $\Delta\sigma$, and the overall normalization uncertainty in the cross section $\Delta\sigma_N$.

Author	Laboratory	Energy (GeV)	Q^2 (GeV^2)	N_ε	$\Delta\sigma$ %	$\Delta\sigma_N$ %
Janssens[1]	Mark III	0.250-1.00	0.15-0.86	3-5	4	1.6
Litt[2]	SLAC	4.00-10.00	1.00-3.75	3-5	1.5-2.0	4
Price[3]	CEA	0.45-1.60	0.25-1.75	1	3.1-5.3	1.9
Berger[4]	Bonn	0.66-1.91	0.10-1.95	3-14	2-6	4
Kirk[48]	SLAC	4.00-17.31	1.00-25.00	1	2	4
Murphy[28]	Saskatchewan	0.057-0.123	0.006-0.031	1	-	-
Bartel[5]	DESY	0.80-3.00	0.67-3.00	2-3	2-4	2.1
Stein[49]	SLAC	4.50-20.00	0.004-0.07	1	3.1	2.8
Borkowski[6]	Mainz	0.15-0.30	0.005-0.183	-	1-2	-
Bosted[50]	SLAC	0.50-1.30	0.49-1.75	2-7	3	1.8
Rock[51]	SLAC	9.761-21.00	2.50-10.00	1	1-4	3
Sill[30]	SLAC	5.00-21.50	2.90-31.30	1	3-4	3.6
Walker[7]	SLAC	1.594-8.233	1.00-3.007	3-8	1	1.9
Andivahis[8]	SLAC	1.511-9.80	1.75-5.00	3-6	< 2	1.77
Christy[9]	JLAB	1.148-5.50	0.40-5.50	3	1.96	1.7

Table 2.1: Summary of selected world data on e-p elastic scattering cross section measurements.

2.4 Discussion

The world data on the ratio of electric to magnetic form factor of the proton as extracted from elastic e-p cross sections (Rosenbluth separation) and recoil polarization measurements in the single-photon exchange approximation have been summarized in section 2.2. Figure 2.16 shows the $\frac{\mu_p G_{Ep}}{G_{Mp}}$ world data as determined by the Rosenbluth separation method (notice the logarithmic scale for the Q^2 axis). With the exception of the data of Berger [4] and Bartel [5], which show a decrease in the ratio with increasing Q^2 especially for the $Q^2 > 1.0$ GeV^2, the data show approximate form factor scaling or $\frac{\mu_p G_{Ep}}{G_{Mp}} = 1.0$ with some fluctuation at high Q^2 points where the uncertainties become large. This is due to the fact that the experimental cross section is small and dominated by G_{Mp} which makes it difficult to extract G_{Ep} with high precision. The difficulty in extracting G_{Ep} at high Q^2 values with high precision using the Rosenbluth separation technique was the motivation behind developing the recoil polarization technique, which is more sensitive to G_{Ep} at large Q^2.

Figure 2.17 shows the world data on $\frac{\mu_p G_{Ep}}{G_{Mp}}$ as determined by recoil polarization technique. The data agree with form factor scaling for the region $Q^2 < 1.0$ GeV^2. However, for the region $Q^2 \geq 1.0$ GeV^2, the data decrease with increasing Q^2 (notice the logarithmic scale for the Q^2 axis) deviating significantly from form factor scaling as suggested by Rosenbluth separation. The data from recoil polarization measurements are more precise at high Q^2 and maybe less sensitive to systematic uncertainties than the Rosenbluth data. The dashed line in Figure 2.17 is the recoil polarization fit to the data [15] or:

$$\frac{\mu_p G_{Ep}}{G_{Mp}} = 1 - 0.13(Q^2 - 0.04) \ . \tag{2.1}$$

We can see from Figures 2.16 and 2.17 that the two techniques give different results in the region $Q^2 \geq 1.0$ GeV^2. The values of $\frac{\mu_p G_{Ep}}{G_{Mp}}$ from the two techniques
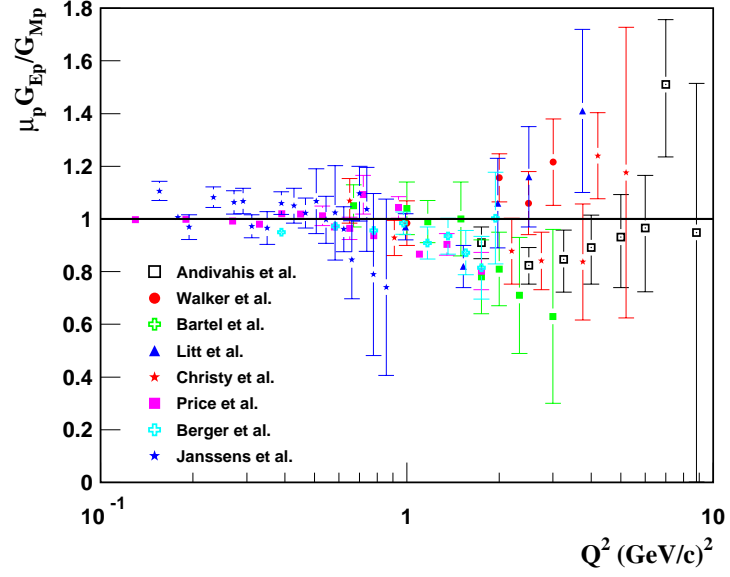
Figure 2.16: The world data on the ratio of electric to magnetic form factor $\mu_p G_{Ep}/G_{Mp}$ by Rosenbluth separation.
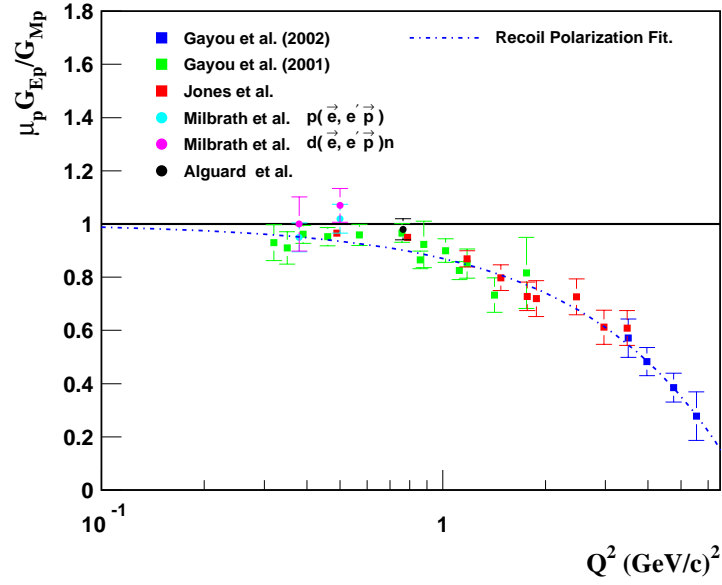
Figure 2.17: The world data on the ratio of electric to magnetic form factors $\mu_p G_{Ep}/G_{Mp}$ by recoil polarization. The dashed line is the recoil polarization published fit.

differ almost by a factor of three at the high Q^2 points. This discrepancy between the results of the two techniques is becoming to be known as the G_E^p crisis. This difference implies uncertainties in our knowledge of the form factors of the proton and raises several questions that must be answered. For example, the high precision data provided by the recoil polarization technique and the larger uncertainties in the L-T data (small G_{Ep} contribution at high Q^2) have led people to believe that the previous Rosenbluth extractions are inconsistent. If this is the case, then all the form factors extracted using Rosenbluth separation technique which are supposed to parameterize the deviation of the proton's structure from point-like particle are unreliable. Also, if there is a significant error in the elastic e-p cross section measurements ($Q^2 \geq 1.0$ GeV^2), then there could be errors in all previous experiments that require normalization to elastic e-p cross sections, or require the use of the elastic cross sections [54, 55] or form factors [56] as an input to the analysis. If the cross section measurements and hence the Rosenbluth extractions are incorrect, that still will not solve the problem since the recoil polarization technique provides the ratio of G_{Ep} to G_{Mp} and not the actual values for the individual form factors.

At this point, the following questions are paramount:

1. *Why do the two techniques disagree?*

   - *Is there a missing correction (radiative corrections or normalization uncertainties) or something wrong in the analysis of the previous Rosenbluth separations data?*

   - *Is there a missing correction (radiative corrections or proton spin precession determination) or something wrong in the analysis of the previous recoil polarization data?*

2. *Which form factors are the correct ones to use?*

- *Is there something fundamentally wrong in the physics of one or both techniques?*

3. *What about all the conclusions based on the old and new theoretical models and calculations concerning the proton form factors?*

In order to provide a check on the consistency of the world's cross section measurements, several global analysis have been done. Walker [7, 57] combined cross sections from different experiments and performed a global extraction of the elastic form factors in the range of $0.1 < Q^2 < 10.0$ GeV^2. The result of the global fit supported the ansatz of form factor scaling as shown in Figure 2.18.

An empirical fit to the world data of the proton form factors was made by Bosted [26] for the region $0.0 < Q^2 < 30.0$ GeV^2. The data of both $\frac{G_{Ep}}{G_D}$ and $\frac{G_{Mp}}{\mu_p G_D}$ in the region $Q^2 \leq 7.0$ GeV^2 are from the global analysis of Walker [7], while for $Q^2 > 9.0$ GeV^2, form factor scaling was assumed to extract G_{Mp}. A good fit to the data was achieved when the form factors were described as an inverse polynomial in Q:

$$G_{Ep}(Q^2) = \frac{1.0}{1.0 + 0.62Q + 0.68Q^2 + 2.80Q^3 + 0.83Q^4} , \qquad (2.2)$$

$$\frac{G_{Mp}(Q^2)}{\mu_p} = \frac{1.0}{1.0 + 0.35Q + 2.44Q^2 + 0.50Q^3 + 1.04Q^4 + 0.34Q^5} . \qquad (2.3)$$

An extensive examination of the form factors extractions from cross section measurements was done by Arrington [55, 58]. A similar global analysis to that of Walker was performed. The fit included two extra data sets from Stein [49] and Rock [51] in addition to the data sets used in Walker's analysis. Also, the final published cross sections in the work of Sill [30] and Andivahis [8] were used which were not available for Walker's analysis. Some recent measurements of elastic scattering at Jefferson Lab by Dutta [54], Niculescu [59], and Christy [9] were added. Also, the results of Borkowski [6], Murphy [28], and Simon [60] were added to constrain the low Q^2

behavior. In addition, all the high Q^2 data up to 30 GeV^2 were included in the fit.

For each dataset, an overall normalization uncertainty was determined. The normalization uncertainties were taken either from the original published work or from Walker's global analysis. Independent normalization uncertainties were assigned to data taken by different detectors in the same experiment. In the work of Bartel [46], data were taken using three different spectrometers, so the data were divided into three sets with different normalization uncertainty factor assigned to each data set. Higher order terms such as the Schwinger term [40] and additional corrections for vacuum polarization contributions from muon and quark loops were added to the radiative corrections applied to the work of Janssens [1], Bartel [46, 61, 5], Albercht [62], Litt [2], Goitein [43], Berger [4], and Price [3]. Finally, the small-angle ($< 20^o$) data from Walker [7] were excluded since an error was identified in that data. The form factors are parameterized as:

$$G_{Ep}(Q^2), \frac{G_{Mp}(Q^2)}{\mu_p} = \frac{1.0}{1.0 + p_2 Q^2 + p_4 Q^4 + \ldots + p_{2N} Q^{2N}} \ , \qquad (2.4)$$

where the parameters of the fit are listed in Table 2.2.

Parameter	G_{Ep}	$\frac{G_{Mp}}{\mu_p}$
p$_2$	3.226	3.19
p$_4$	1.508	1.355
p$_6$	-0.3773	0.151
p$_8$	0.611	-1.14×10^{-2}
p$_{10}$	-0.1853	5.33×10^{-4}
p$_{12}$	1.596×10^{-2}	-9.0×10^{-6}

Table 2.2: Form factors parameters, equation (2.4), as extracted by Arrington fit to σ.

It was hypothesized that the discrepancy between the Rosenbluth and the polarization data was coming from a common systematic error in the cross section

measurements and a (5-8)% ε-dependent systematic error in the cross sections could resolve the discrepancy (see section 6.4 for more detail). Therefore, a combined analysis was done by Arrington [55] where an ε-dependent correction of 6% was applied to all cross sections:

$$\sigma_c = \sigma_o \left(1.0 - 0.06(\varepsilon - 1.0) \right) , \qquad (2.5)$$

and then the recoil polarization data were included in the fit. Here σ_c and σ_o are the corrected and uncorrected cross sections respectively. The form factors were parameterized using the same form as in equation (2.4). The parameters of the fit are listed in Table 2.3.

Parameter	G_{Ep}	$\frac{G_{Mp}}{\mu_p}$
p_2	2.94	3.00
p_4	3.04	1.39
p_6	-2.255	0.122
p_8	2.002	-8.34×10^{-3}
p_{10}	-0.5338	4.25×10^{-4}
p_{12}	4.875×10^{-2}	-7.79×10^{-6}

Table 2.3: Form factors parameters as extracted from Arrington combined fit to cross sections and recoil polarization data.

The ratio of the electric to magnetic form factor of the proton as extracted from the Arrington's global fit to the world's elastic cross section data supports the results of previous Rosenbluth extractions. The result indicated a good consistency between all different data sets and ruled out any possibility for a single or two bad data sets or incorrect normalization in the combined Rosenbluth analysis.

An empirical fit to the proton form factors was done by Brash [27] where most of the higher-Q^2 elastic e-p cross sections data were reanalyzed by using the ratio between the proton form factors $r = \frac{\mu_p G_{Ep}}{G_{Mp}}$ as provided by the recoil polarization

data as a constraint:

$$r(Q^2) = \frac{\mu_p G_{Ep}}{G_{Mp}} = \begin{cases} 1 & : \text{if } Q^2 \leq 0.04 \text{ GeV}^2 \text{ ,} \\ 1 - 0.130(Q^2 - 0.04) & : \text{if } 0.04 < Q^2 < 7.7 \text{ GeV}^2 \text{ ,} \\ 0 & : \text{if } Q^2 \geq 7.7 \text{ GeV}^2 \text{ ,} \end{cases} \qquad (2.6)$$

that way, $r(Q^2)$ fixes the ratio between the intercept $(a = \tau G_{Mp}^2)$ and the slope $(b = G_{Ep}^2)$ from the linear fit of the reduced cross section σ_R to ε. The form factors are associated with the parameters of the linear fit, $\sigma_R = a(1 + b\varepsilon)$, where $a = \frac{\mu_p^2 b\tau}{r^2} = bR$ and $R = \frac{\tau \mu_p^2}{r^2}$. A new parameterization of the proton magnetic form factor G_{Mp} was obtained and the electric form factor was then calculated using the recoil polarization constrained ratio:

$$\frac{G_{Mp}(Q^2)}{\mu_p} = \frac{1}{1.0 + 0.116Q + 2.874Q^2 + 0.241Q^3 + 1.006Q^4 + 0.345Q^5} \text{ ,} \qquad (2.7)$$

$$G_{Ep}(Q^2) = r(Q^2)\frac{G_{Mp}(Q^2)}{\mu_p} \text{ .} \qquad (2.8)$$

The magnetic form factor of the proton as parameterized by Brash [27] was shown previously in Figure 1.4 in section 1.4. In Figures 2.18, 2.19, and 2.20, the fits of Arrington, Bosted, and recoil polarization are shown along with the world data on proton form factors in addition to Walker's global analysis.
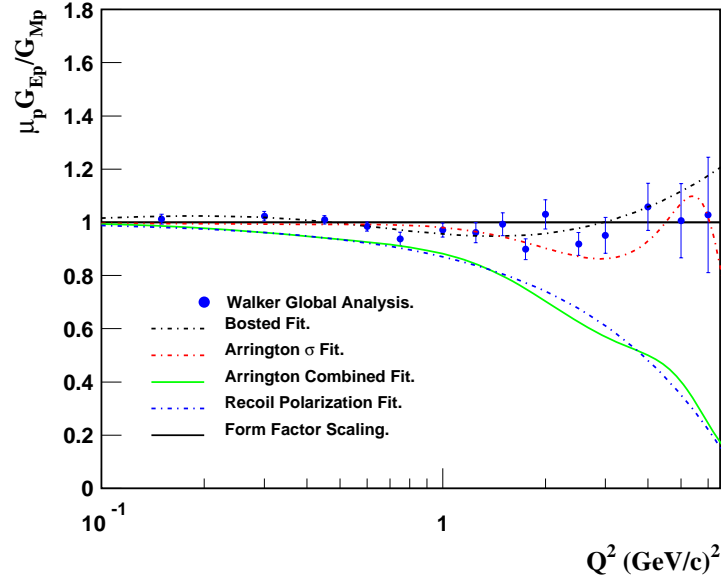
Figure 2.18: Global analysis of the proton form factors ratio $\mu_p G_{Ep}/G_{Mp}$ by Walker. In addition, the fits of Arrington, Bosted, and recoil polarization are also shown.
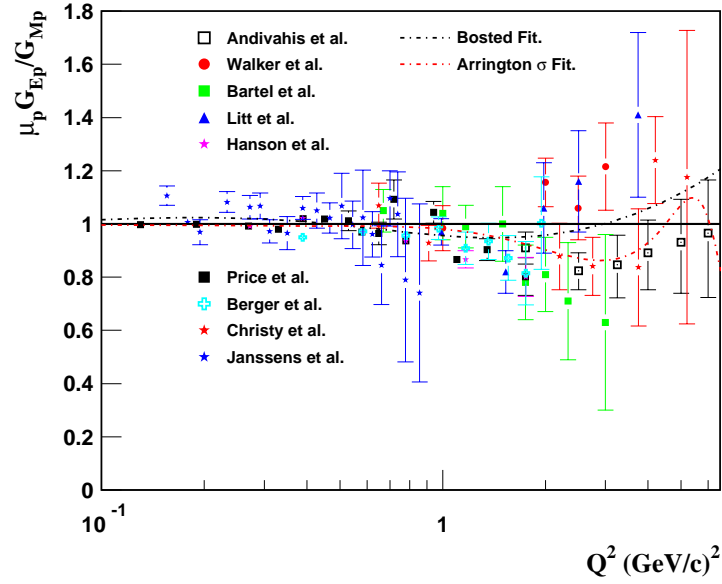
Figure 2.19: Proton form factors ratio $\mu_p G_{Ep}/G_{Mp}$ by Rosenbluth separations. In addition, the fits of Arrington and Bosted are also shown.
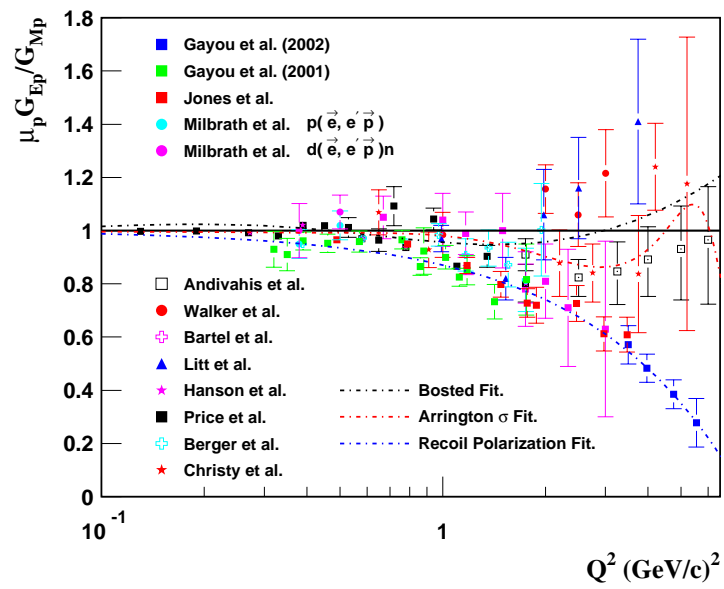
Figure 2.20: Proton form factors ratio $\mu_p G_{Ep}/G_{Mp}$ by Rosenbluth separations and recoil polarization. In addition, the fits of Arrington, Bosted, and recoil polarization are also shown.

Chapter 3   Experimental Setup

3.1   Overview

Due to the inconsistency in the results of the ratio of the electric to magnetic form factors of the proton, $\frac{\mu_p G_{Ep}}{G_{Mp}}$, as extracted from the Rosenbluth and recoil polarization techniques, and due to the fact that the reported uncertainties in $\frac{\mu_p G_{Ep}}{G_{Mp}}$ in the various Rosenbluth determinations are much larger than those quoted for the polarization transfer measurements, a high-precision measurement of $\frac{\mu_p G_{Ep}}{G_{Mp}}$ using the L-T separation technique in the $Q^2 > 1.0$ GeV^2 region is important to:

- *Provide a comparison between the two techniques in the region where both can extract the value of $\frac{\mu_p G_{Ep}}{G_{Mp}}$ with high precision.*

- *Achieve uncertainties comparable to or better than the uncertainties quoted by the recoil polarization measurements.*

- *Provide a check on any possibility of additional and unaccounted for systematic uncertainties in the L-T or recoil polarization measurements.*

Experiment E01-001 sought to achieve these goals. It ran in May 2002 and was carried out in Hall A of the Thomas Jefferson National Accelerator Facility (formerly known as Continuous Electron Beam Accelerator Facility, or CEBAF) which is located in Newport News Virginia in the U.S.A. An incident electron beam of energies in the range of 1.912< E_0 <4.702 GeV was directed on a 4-cm-long unpolarized liquid hydrogen target. High precision measurements of the elastic e-p cross sections

were made to allow for an L-T separation of the proton electric and magnetic form factors. Protons were detected simultaneously using the two identical high resolution spectrometers (HRS) or what is known by the left and right arm spectrometers of Hall A. The left arm spectrometer was used to measure three Q^2 points of 2.64, 3.20, and 4.10 GeV^2. Simultaneously, measurements at $Q^2 = 0.5$ GeV^2 were carried out using the right arm spectrometer which served as a monitor of beam charge, current, and target density fluctuations.

A total of 12 points (5 ε points for $Q^2 = 2.64$ GeV^2, 4 ε points for $Q^2 = 3.20$ GeV^2, and 3 ε points for $Q^2 = 4.10$ GeV^2) were measured covering an angular range of $12.52^o < \theta_L < 38.26^o$ for the left arm, while the right arm was at $Q^2 = 0.5$ GeV^2, and used to simultaneously measure 5 ε points covering an angular range of $58.29^o < \theta_R < 64.98^o$. Here, θ_L and θ_R are the nominal angle of the struck proton with respect to the beam electron for the left and right spectrometer, respectively. Figure 3.1 and Table 3.1 show and list the nominal kinematics covered in the E01-001 experiment and their settings. Small offsets were determined and applied to the energy and scattering angles. See section 4.4 for details. The final kinematics used in the analysis are listed in Table 4.2.

The final momentum of the scattered protons, $P_{measured}$, measured using the high resolution spectrometer, was compared to the final momentum of the scattered protons, $P_{calculated}(\theta_p)$, calculated from two-body kinematics using the measured scattering angle of the protons θ_p (see equation (5.8)):

$$P_{calculated}(\theta_p) = \frac{2E_{beam}(M_p^2 + E_{beam}M_p)\cos\theta_p}{M_p^2 + E_{beam}^2 + 2E_{beam}M_p - E_{beam}^2\cos^2\theta_p} \ , \tag{3.1}$$

and the difference in momentum ΔP was then constructed:

$$\Delta P = P_{measured} - P_{calculated}(\theta_p) \ , \tag{3.2}$$

where M_p is the mass of the proton and E_{beam} is the incident electron energy.
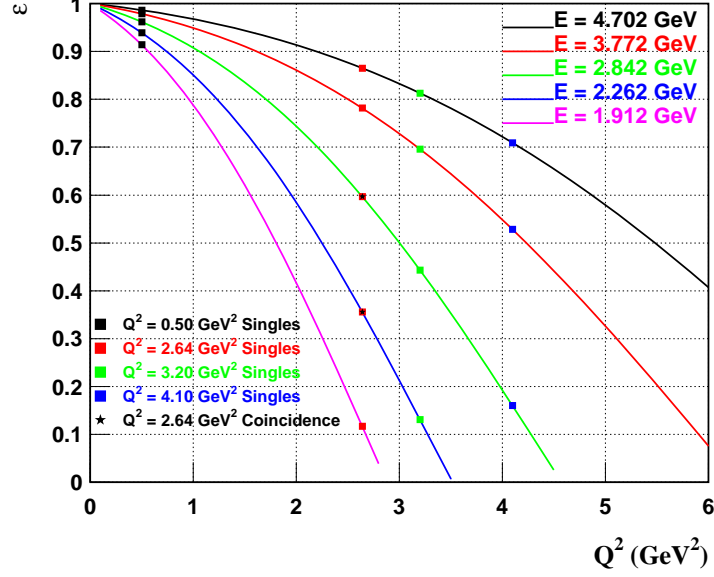
Figure 3.1: Plot of ε vs Q^2 showing the kinematics covered.

The ΔP spectrum is made of several contributions. The main contributions come from the elastic peak which is due to the elastic $ep \rightarrow ep$ scattering and the radiative tail. In addition there are backgrounds due to quasi-elastic scattering from the aluminum target windows and high energy protons generated from photoreactions ($\gamma p \rightarrow \pi^0 p$ and $\gamma p \rightarrow \gamma p$) that contribute to the ΔP spectrum. For each of the kinematics covered, data were taken with the dummy target to subtract away the endcaps contribution from the spectrum. The photoproduction of π^0 or $\gamma p \rightarrow \pi^0 p$ events were simulated using a calculated bremsstrahlung spectrum and $\frac{d\sigma}{dt} \propto s^{-7}$ and then subtracted away from the spectrum as well.

The net number of elastic events from data is then compared to the number of elastic events in the e-p peak as simulated using the Monte Carlo simulation program SIMC [63, 64], under the same conditions (cuts), for a given narrow window cut on the ΔP spectrum. The ratio of the number of events from the data to that of

Setting	E_{beam} (GeV)	ε_L	Q_L^2 (GeV^2)	θ_L (^{o})	P_L (GeV/c)	ε_R	θ_R (^{o})	P_R (GeV/c)
o	1.912	0.117	2.64	12.631	+ 2.149	0.914	58.288	+ 0.756
a	2.262	0.356	2.64	22.166	+ 2.149	0.939	60.075	+ 0.756
i	2.842	0.597	2.64	29.462	+ 2.149	0.962	62.029	+ 0.756
q	3.772	0.782	2.64	35.174	+ 2.149	0.979	63.876	+ 0.756
l	4.702	0.865	2.64	38.261	+ 2.149	0.986	64.978	+ 0.756
b	2.262	0.131	3.20	12.525	+ 2.471	0.939	60.075	+ 0.756
j	2.842	0.443	3.20	23.395	+ 2.471	0.962	62.029	+ 0.756
p	3.772	0.696	3.20	30.501	+ 2.471	0.979	63.876	+ 0.756
m	4.702	0.813	3.20	34.139	+ 2.471	0.986	64.978	+ 0.756
k	2.842	0.160	4.10	12.682	+ 2.979	0.962	62.029	+ 0.756
r	3.772	0.528	4.10	23.665	+ 2.979	0.979	63.876	+ 0.756
n	4.702	0.709	4.10	28.380	+ 2.979	0.986	64.978	+ 0.756
$coin1$	2.262	0.356	2.64	22.166	+ 2.149	0.356	71.481	- 0.855
$coin2$	2.842	0.597	2.64	29.462	+ 2.149	0.597	47.439	- 1.435
$coin3$	3.362	0.398	4.10	20.257	+ 2.185	0.398	61.184	- 1.177

Table 3.1: The nominal kinematics setting for the E01-001 experiment. For each setting, E_{beam} is the nominal electron beam energy, ε_L (ε_R) is the virtual photon polarization parameter for the left (right) arm spectrometer, Q_L^2 is the four-momentum transfer squared for the left arm spectrometer, θ_L (θ_R) is the spectrometer nominal scattering angle for the left (right) arm spectrometer, and P_L (P_R) is the central momentum for the left (right) arm spectrometer. Note that the four-momentum transfer squared for the right arm Q_R^2 (not listed) was at 0.50 GeV^2 for all the settings except for the coincidence kinematics settings $coin1$, $coin2$, and $coin3$ where $Q_R^2 = Q_L^2$. Small offsets were determined and applied to the energy and scattering angles. See section 4.4 for details. The final kinematics used in the analysis are listed in table 4.2.

the simulation normalized to input e-p cross section is then determined for that ΔP window cut.

In addition, three coincidence kinematics were taken in order to allow for a separation of the elastic events from background events. Such separations helped us test our calculations of the lineshapes of the ΔP spectrum. The left arm was used to detect protons while electrons scattered in coincidence with protons were detected using the right arm spectrometer. The coincidence data were also used to provide a check on the scattering kinematics and to measure the proton detection efficiency and absorption.

3.2 Why Detect Protons?

The majority of the previous elastic e-p cross section measurements were made by detecting electrons rather than protons. However, proton detection has several advantages over electron detection:

1. *Protons at moderately large angles correspond to electrons scattered at small angles. Detecting protons allows us to go to lower values of electron scattering angles (down to $\sim 7^o$) than would normally be possible.*

2. *Detecting protons reduces the variation of the cross section with the scattering angle. The cross section for the forward angle electrons varies rapidly with the scattering angle, while such variation for the corresponding protons is much smaller. The reverse is true for the backwards angle electrons where the variation of the cross section with the scattering angle is greater for the corresponding forward angle protons, however, it is still a smaller effect than that for the forward angle electrons.*

3. *Detecting protons reduces the variation of the cross section with the beam energy.*

4. *Detecting backwards angle electrons results in a reduced cross section within the angular acceptance of the spectrometer. On the other hand, the corresponding protons fall within a narrow angular window resulting in higher counting rates in less running time. That is, electrons are cross section limited at large angles (small ε), while protons cross section is 10-20 times larger for small ε.*

5. *The proton momentum is constant for all ε values for a given Q^2.*

6. *The linear ε dependence of the radiative corrections is smaller for the protons than for the electrons.*

Because of these advantages, detecting protons greatly reduces the ε-dependent systematic corrections and associated uncertainties applied to the measured cross sections as compared to detecting electrons. Figure 3.2 shows the momentum of the proton and electron as a function of the virtual photon polarization parameter ε for $Q^2 = 2.64$ GeV^2. The momentum is constant for the proton, while it varies by a factor of ~ 20 for the electron. The fact that the proton momentum is the same for all ε values at a given Q^2 point means that there is no ε dependence due to any momentum-dependent corrections due to detector efficiency, particle identification, and multiple scattering. It should be mentioned that any momentum-dependent correction will introduce an uncertainty in the reduced cross sections at a given Q^2 point which in turn introduces an uncertainty in both G_{Ep} and G_{Mp} but not in the ratio.

Figure 3.3 shows the cross section for both the proton, $\frac{d\sigma}{d\Omega_p}$, and electron, $\frac{d\sigma}{d\Omega_e}$, as a function of ε for $Q^2 = 2.64$ GeV^2. The cross section, and thus rate for fixed conditions, is nearly constant for the proton and that will reduce the effect of rate-dependent uncertainties dramatically. Also, the low ε cross sections are no longer rate limited for the proton as it is the case for the electron which will require more running time for comparable statistics.
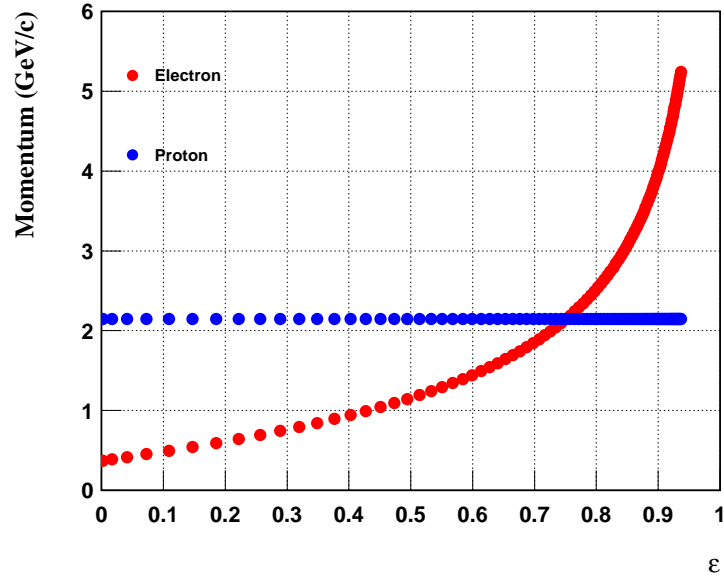
Figure 3.2: Plot of the proton and electron momentum as a function of ε at $Q^2 = 2.64$ GeV^2.
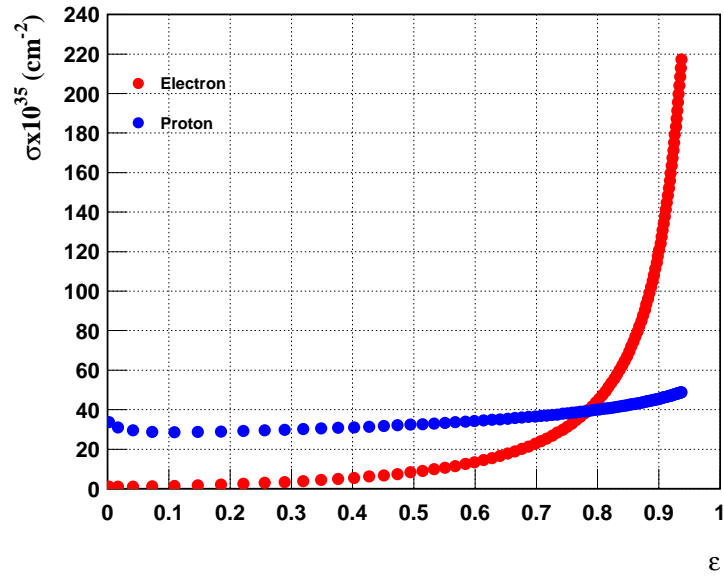
Figure 3.3: Plot of the proton and electron cross section $(\sigma \times 10^{35})$ (cm^{-2}) as a function of ε at $Q^2 = 2.64$ GeV^2.

Figures 3.4 and 3.5 show the sensitivity of the cross section to the beam energy (percentage change in the cross section per one percent change in the beam energy) and scattering angle (percentage change in the cross section per one degree change in the scattering angle) for both particles as a function of ε for $Q^2 = 2.64$ GeV^2. The variation of the cross section with beam energy and especially with scattering angle as a function of ε is less for the proton than that of the electron.

Figure 3.4 shows the sensitivity of the electron and proton cross section to a 1% change in the beam energy. For the electron, the maximum variation of the cross section is $\sim 7\%$ and for the proton it is 4%. If a 0.5% measurement in the cross section is desired, then the beam energy must be known with a precision of 7.14×10^{-4} for the electron and 1.25×10^{-3} for the proton. Such high precision is achievable for both particles knowing that energy measurements at JLAB can performed with precision as high as $\frac{\delta E_o}{E_o} = 2 \times 10^{-4}$.

Looking at Figure 3.5 it can be seen that the biggest variation of the cross section of the electron for a one degree change in the scattering angle is $\sim 55\%$. If we want to achieve a 0.5% measurement in the cross section, we need to know the scattering angle to within ~ 0.158 mrad which is very difficult to achieve. On the other hand, for the proton, over the same ε range, the variation is a factor of 3 less and the scattering angle need only to be known to within ~ 0.476 mrad which is much more readily achievable.

Finally, Figure 3.6 shows the radiative correction factor (internal corrections only) as a function of ε for $Q^2 = 2.64$ GeV^2 based on calculations done by Afanasev et al [53]. While the magnitude of the corrections is similar and both show an approximately linear dependence on ε the dependence is much smaller for protons, $\sim -8\%$, than for the electron $\sim 17\%$. Note that the radiative corrections have an ε dependence that is comparable to the slope brought about by the form factors. It is therefore extremely important that the radiative corrections (section 5.6) are correctly handled.
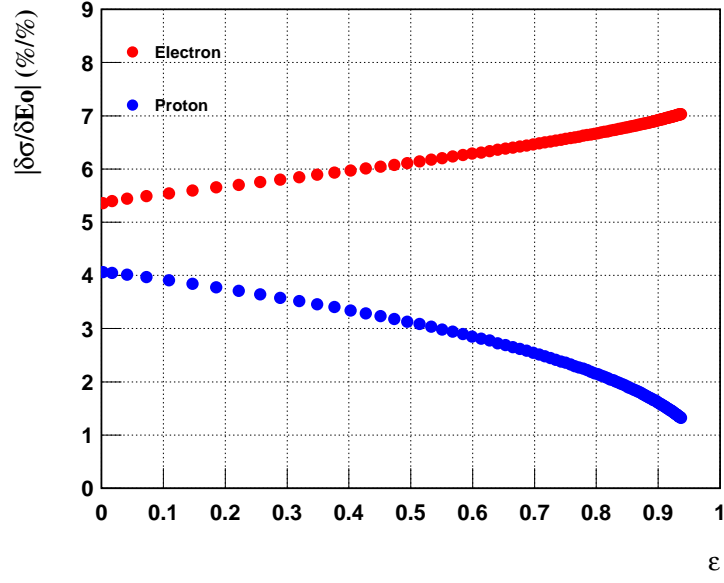
Figure 3.4: Plot of the proton and electron cross section sensitivity to the electron beam energy offset $\left(\frac{\delta\sigma}{\delta E_o}\right)$ (%/%) as a function of ε at $Q^2 = 2.64$ GeV^2.
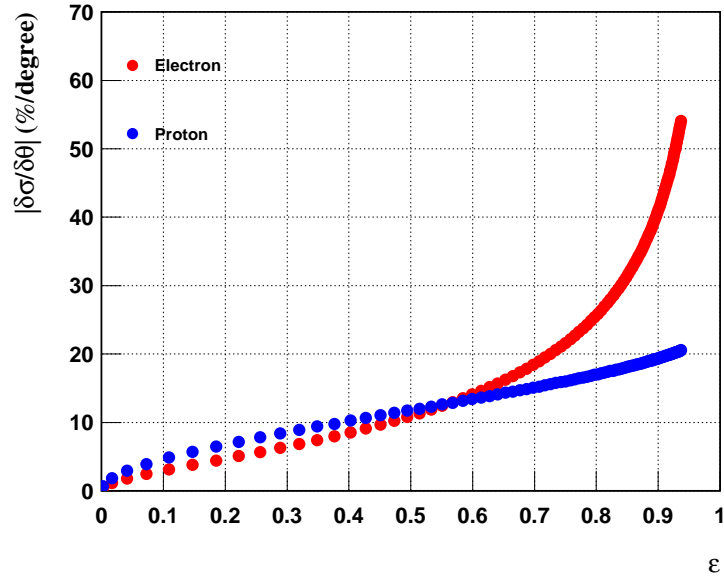
Figure 3.5: Plot of the proton and electron cross section sensitivity to the scattering angle offset $\left(\frac{\delta\sigma}{\delta\theta}\right)$ (%/degree) as a function of ε at $Q^2 = 2.64$ GeV^2.
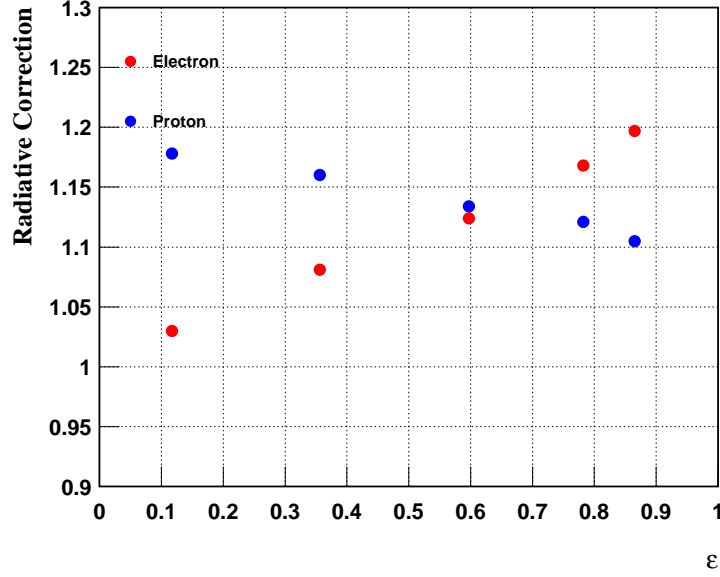
Figure 3.6: Plot of the proton and electron radiative correction factor (internal corrections only) as a function of ε at $Q^2 = 2.64$ GeV^2.

3.3 The Continuous Electron Beam Accelerator Facility (CEBAF)

During the run of the E01-001 experiment, the Continuous Electron Beam Accelerator Facility of the Thomas Jefferson National Accelerator Facility [65] provided an unpolarized electron beam in the range of 1.912< E_0 <4.702 GeV with beam currents up to 70 μA. Figure 3.7 shows the layout of the Jefferson Lab accelerator.

Using a state-of-the-art strained GaAs photocathode gun system with maximum current of ($I \sim 200$ μA) and polarization above 70%, continuous-wave (CW) beams of high current and polarization are delivered to both Hall A and Hall C ($I \sim 100$ μA). Meanwhile, a high polarization and low current beam is delivered to Hall B ($I \sim$ 100 nA).

First, electrons from the photocathode gun is accelerated to 50 MeV, and then
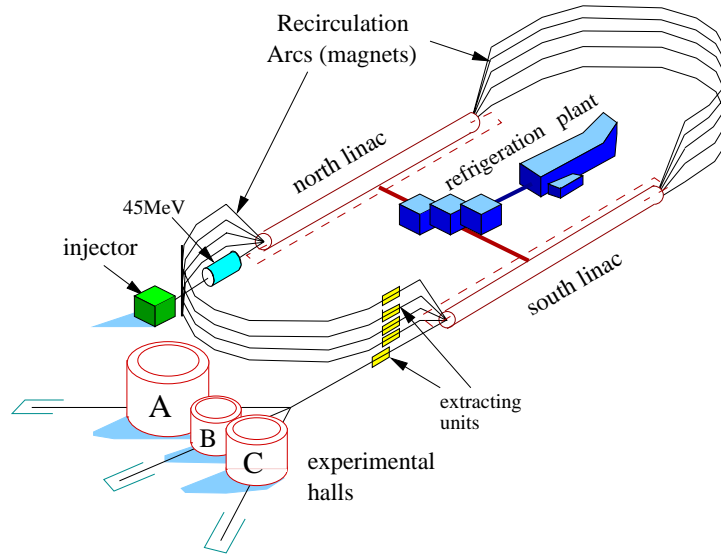
Figure 3.7: Schematic layout of the Thomas Jefferson National Accelerator Facility.

injected into the north-linac. The north-linac consists of 20 Radio Frequency (RF) cryomodules. Each cryomodule has eight accelerating superconducting niobium cavities kept at a temperature of 2 K using liquid helium coolant form the Central Helium Liquefier. By the time the electrons reach the end of the north-linac, they could have been accelerated up to 600 MeV by the 160 cavities. At the end of the north-linac, 180° bending arcs (east arc) with a radius of 80 meters join the north-linac to the identical and antiparallel superconducting south-linac forming a recirculating beamline. The beam through each arc is focused and steered using quadrupole and dipole magnets located inside each arc. The east arc has a total of 5 arcs on top of each other each with different bending field. The beam is steered through the east arc and passed on to the south-linac where it gets accelerated again and gain up to 600 MeV. At the end of the south-linac, the beam can be sent through the west arc for another pass or it can be sent to the Beam Switch Yard with a microstructure that consists

of short (1.67 ps) bursts of beam coming at 1497 MHz. Each hall receives one third of these bursts, giving a pulse train of 499 MHz in each hall.

If another beam pass is desired for higher energy, the beam can be sent through the west recirculating linac for additional acceleration in the linacs, up to 5 passes through the accelerator. At the west recirculating linac, there are 4 different arcs on top of each other each with different bending field. It must be mentioned that the energy of the extracted beam is always a multiple of the combined linac energies $E_{linacs} = E_{north\ linac} + E_{south\ linac}$, plus the initial injector energy $E_{injector}$ or $(E_{injector} + nE_{linacs})$ where n is the number of passes.

3.4 Hall A Beam Energy Measurements

Precise measurements of the beam energy are required in order to extract the form factors of the protons from the elastic e-p cross sections. There are two different measurements that can be performed to determine the energy of incident electron beam with precision as high as $\frac{\delta E_o}{E_o} = 2 \times 10^{-4}$. These measurements are known as the arc and ep measurements.

3.4.1 The Arc Beam Energy Measurement

In the arc measurement [66, 67, 68], the momentum p of the incident electrons is determined by knowing the net bend angle θ of the electrons and the integral of the magnetic field along the arc section (electron path) of the beam line:

$$p = c\frac{\int B\,dl}{\theta} \ , \tag{3.3}$$

where c is the speed of light. Equation (3.3) is derived based on the fact that when an electron moves in a circular motion with velocity $\vec{v}$ in region of magnetic field $\vec{B}$,

where the magnetic force on the electron $\frac{e}{c}\vec{v} \times \vec{B}$ provides the central force $\frac{mv^2}{r}$. Here, e is the charge of the electron, m is the mass of the electron, and r is the radius of circular path which is related to the net bend angle and linear electron path l as $l = r\theta$.

In the arc measurements, simultaneous measurements of the bend angle and the magnetic field integral of the 8 bending dipoles (based on the measurement of the 9th dipole as a reference) in the arc section of the beamline are made. The bend angle is determined by measuring the beam position and profile at the entrance and exist of the arc using four wire scanners or superharps. During the bend angle measurement, the quadruples are turned off (dispersive mode). The nominal bend angle of the beam in the arc section of the beamline is $\phi = 34.3^o$.

A superharp consists of three wires, two vertical wires for the horizontal beam profile measurement and one horizontal wire for the vertical beam profile. The signal from the wires gets picked up by an analog-to-digital converter (ADC). In addition, a position encoder measures the position of the ladder as the wires pass through the beam. The signal from the ADC and the position of the ladder determines the position and profile of the beam. Figures 3.8 and 3.9 show the superharp system and the arc section of the beamline.
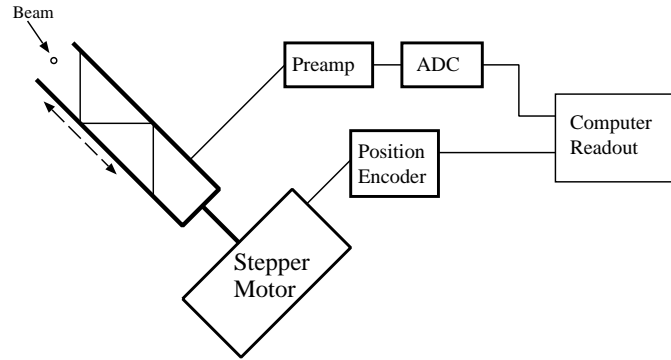
Figure 3.8: Schematic of the superharp system.
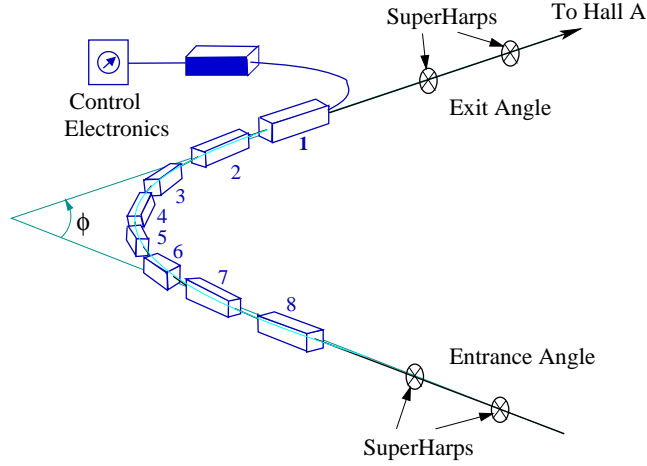
Figure 3.9: Schematic Layout of the Arc Section of the Beamline.

3.4.2   The ep Beam Energy Measurement

The second method of measuring the beam energy is the ep measurement [67, 69, 68]. A stand-alone device along the beamline located 17 m upstream of the target is used for the ep measurement. Based on the two-body kinematics in the elastic $^1H(\vec{e}, e'\vec{p})$ reaction, an incident electron is scattered by a CH_2 film target enclosed by an aluminum cover. The scattered electron and recoiled proton are detected using two identical arms, each of which has a detector package as shown in Figure 3.10. The angles of the scattered electron θ_e and recoiled proton θ_p are measured, and the incident electron energy E_o is then determined from the two-body kinematic equation:

$$E_o = M_p \left(\frac{\cos\theta_e + (\sin\theta_e / \tan\theta_p) - 1}{1 - cos\theta_e} \right) + O(\frac{m_e^2}{E}) \ , \tag{3.4}$$

where M_p is the mass of the proton, m_e is the mass of the electron, and E is the final energy of the scattered electron. The energy measurements by the arc and ep methods show an excellent agreement with each other within an experimental

uncertainty of $\leq 3 \times 10^{-4}$. During the run of the E01-001 experiment, three arc and two ep measurements were made to determine the beam energy.
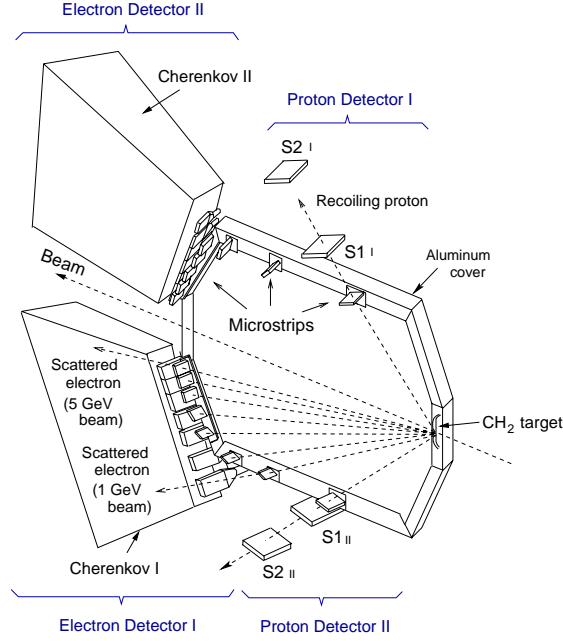
Figure 3.10: Schematic Layout of the ep energy measuring system.

Table 3.2 lists all of the beam energy measurements for the E01-001 experiment. The Tiefenback energy measurement is similar to the arc measurement but is determined using Hall A arc beam position monitors (BPMs) instead of the superharps to calculate the beam energy. The Tiefenback value for the beam energy, which is consistent with the arc measurements, is used in the analysis of the E01-001 experiment.

Random (point-to-point) and scale uncertainties of 0.01% and 0.05% have been reported on the non-invasive arc measurements (the Tiefenback energy), respectively, and a 0.02% random uncertainty in the full invasive arc measurement or the ep measurement [67]. Since the Tiefenback results were consistent with the full arc and ep measurements where we took them, we can assume that the absolute uncertainty

Pass	E(Tiefenback) (MeV)	ΔE (MeV)	Arc (MeV)	ep (MeV)	Arc/Tiefenback	ep/Arc
2	1912.94	0.69	-	-	-	-
2	2260.00	0.81	2260.20	2260.83	1.000088	1.000279
3	2844.71	1.03	-	-	-	-
4	3772.80	1.36	3773.10	3775.23	1.000080	1.000565
5	4702.52	1.70	-	-	-	-
5	5554.60	2.00	5555.17	-	1.000103	-

Table 3.2: Tiefenback, Tiefenback quoted uncertainty ΔE, arc, and ep beam energy measurements of the E01-001 experiment. Tiefenback energy was used for the analysis with final uncertainty of 0.03% offset combined with 0.02% point-to-point uncertainty.

in the Tiefenback is closer to the 0.02%. Therefore, an overall scale and random uncertainties of 0.03% and 0.02% are estimated on Tiefenback energy, respectively.

The classification of the uncertainty into a slope, random, and scale will be discussed in detail in section 4.1. The sensitivity of the cross sections to a 0.02% beam energy offset has been studied. Figures 3.11 and 3.12 show the relative difference between the nominal cross sections, determined at the nominal scattering angle and energy, and cross sections with a 0.02% shift in the beam energy for the right and left arms and at all kinematics. A 0.02% energy fluctuation changes the cross section by 0.01-0.03% for the right arm and 0.04-0.08% for the left arm. Such change in the cross sections was applied as a random uncertainty to each ε point.

Similarly, the sensitivity of the cross sections to an overall 0.03% beam energy offset has been studied. Figures 3.13 and 3.14 show the relative difference between the nominal cross sections and cross sections with a 0.03% beam energy offset for the right and left arms and at all kinematics. In order to determine the slope uncertainty in the cross sections due to a 0.03% beam energy offset, a fit of the relative difference in the cross sections to a straight line was performed at each Q^2 value. The average slope was used as the overall slope uncertainty. On the other hand, the deviation of

the relative difference in the cross sections from the data and fit was then used as a measure of the random uncertainty in each ε point, while the average of the relative difference in the cross sections was used as an overall scale uncertainty. The right arm results show an average scale, random, and slope uncertainties of 0.034%, 0.01%, and 0.29%, respectively. The left arm results show an average scale, random, and slope uncertainties of 0.13%, 0.02%, and 0.073%, respectively. It should be mentioned that the same procedure of estimating the scale, random, and slope uncertainties in the sensitivity of the cross sections to a 0.10 mrad and 0.18 mrad angle offset will be used in section 4.4.
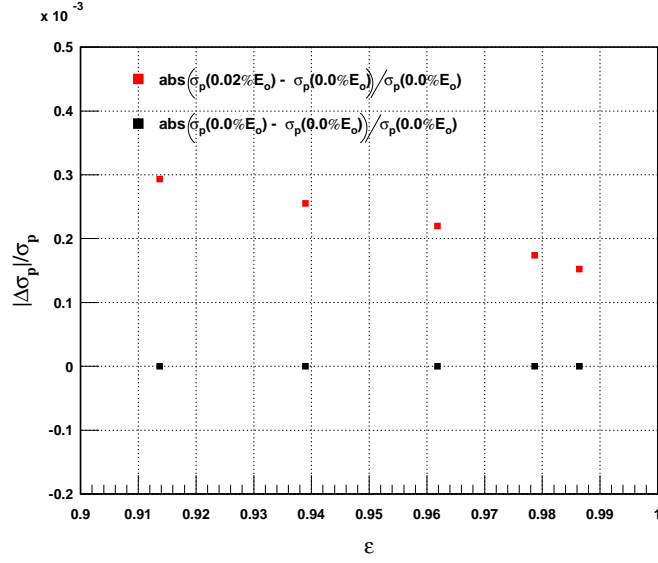
Figure 3.11: The relative difference between the right arm nominal cross sections and cross sections with a 0.02% beam energy offset (red squares) as a function of ε at all 5 incident energies. The black squares are the nominal cross sections relative to themselves.
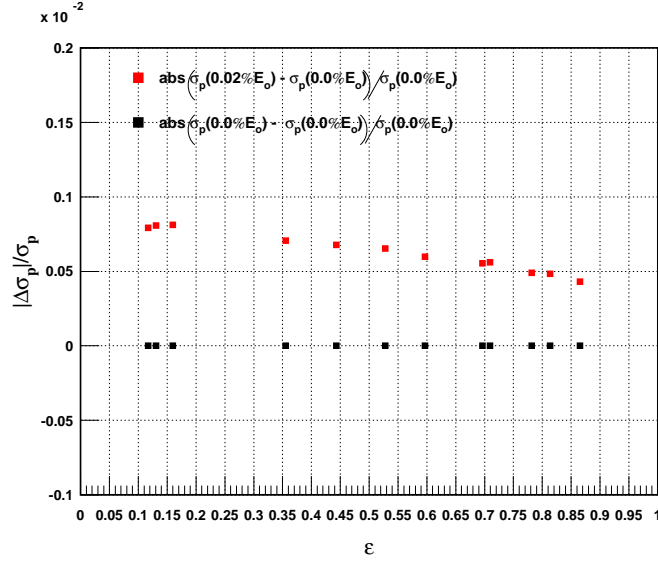
Figure 3.12: The relative difference between the left arm nominal cross sections and cross sections with a 0.02% beam energy offset (red squares) as a function of ε. The black squares are the nominal cross sections relative to themselves.
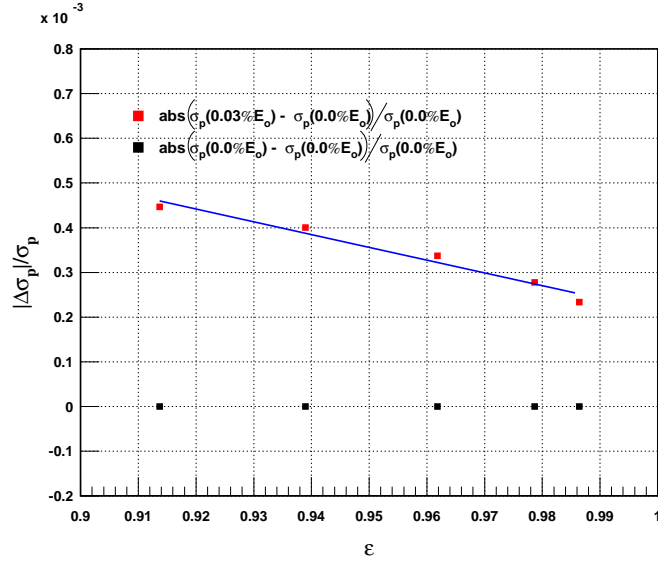
Figure 3.13: The relative difference between the right arm nominal cross sections and cross sections with a 0.03% beam energy offset (red squares) as a function of ε at all 5 incident energies. The solid blue line is a linear fit to the data.
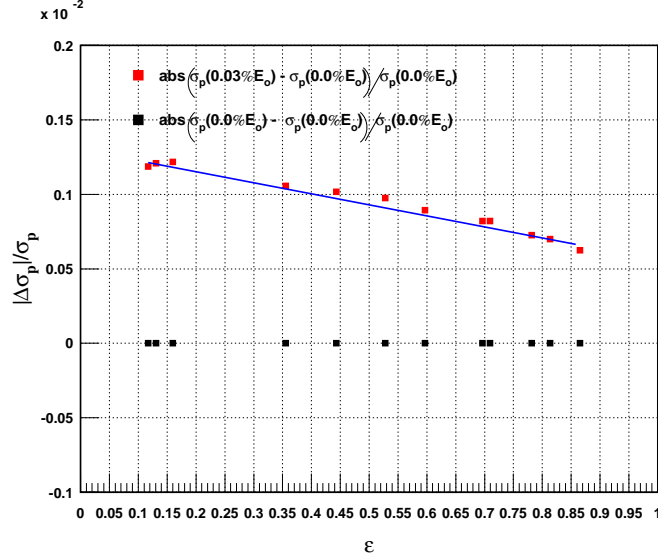
Figure 3.14: The relative difference between the left arm nominal cross sections and cross sections with a 0.03% beam energy offset (red squares) as a function of ε. The solid blue line is a linear fit to the data.

3.5 Beam Position Measurements

Knowing the position and direction of the beam on the target is crucial since any beam offset could be translated into an uncertainty in the effective target length used in the analysis. During the E01-001 experiment, the beam first was rastered using a rectangular raster [67] producing a ~ 2 mm $\times$ 2 mm spot size at the target to prevent any damage to the target by overheating it or local density fluctuations.

In order to determine the beam position and direction at the target, two beam position monitors (BPMs), BPMA and BPMB, [67, 68, 70] located 7.516 and 2.378 m upstream from the target were used. The BPM is a cavity with 4-wire antenna in one plane with frequency tuned to match the RF frequency of the beam (1497 MHz). The absolute position of the beam is determined by the BPMs by calibrating the BPMs with respect to wire scanners (superharps) located adjacent to each BPM

at 7.345 and 2.214 m upstream of the target.

The standard difference-over-sum method is used to determine the relative position of the beam to the wires. The position of the beam averaged over 0.3 sec, as read from the BPMs, is written into a data stream system on a event-by-event basis. The actual beam position and angle at the target can be reconstructed as:

$$x_{beam} = \frac{1}{a_3} \left(x_{bpma} z_{bpmb} - x_{bpmb} z_{bpma} \right) , \tag{3.5}$$

$$y_{beam} = \frac{1}{a_3} \left(y_{bpma} z_{bpmb} - y_{bpmb} z_{bpma} \right) , \tag{3.6}$$

$$\theta_{beam} = \frac{a_1}{a_3} , \tag{3.7}$$

$$\phi_{beam} = \frac{a_2}{\sqrt{a_1^2 + a_3^2}} , \tag{3.8}$$

where $a_1 = x_{bpmb} - x_{bpma}$, $a_2 = y_{bpmb} - y_{bpma}$, and $a_3 = z_{bpmb} - z_{bpma}$. Also, x_{bpma}, y_{bpma}, x_{bpmb}, and y_{bpmb} are the x and y coordinates of the beam as determined by beam position monitor a and b (BPMA and BPMB). Finally, z_{bpma} and z_{bpmb} are the locations of the superharps for both BPMA and BPMB and have a value of -2.214 and -7.345 m, respectively. The values of z_{bpma} and z_{bpmb} are negative because the superharps are located upstream with respect to the target.

Using the above equations, the position of the beam on the target was reconstructed. Figure 3.15 top(bottom) shows the $x(y)$ coordinate of the beam at the target for all the runs in order of increasing ε and Q^2. For example, the point Q^2 = 2.64 GeV^2 has 5 ε points and a different color is given for each ε value starting with black for the lowest ε point and then red for the next and higher ε point and so on. See Table 3.1 for kinematics description. The beam was well focused on the target with an average (x,y) position of (-0.20,-0.10) mm, and an average beam drift of ±0.30 mm. The position uncertainties of 0.30 mm in two BPMs a $\sim$ 5 m apart yield a $\sim$ 0.07 mrad angle uncertainty in the beam angle.
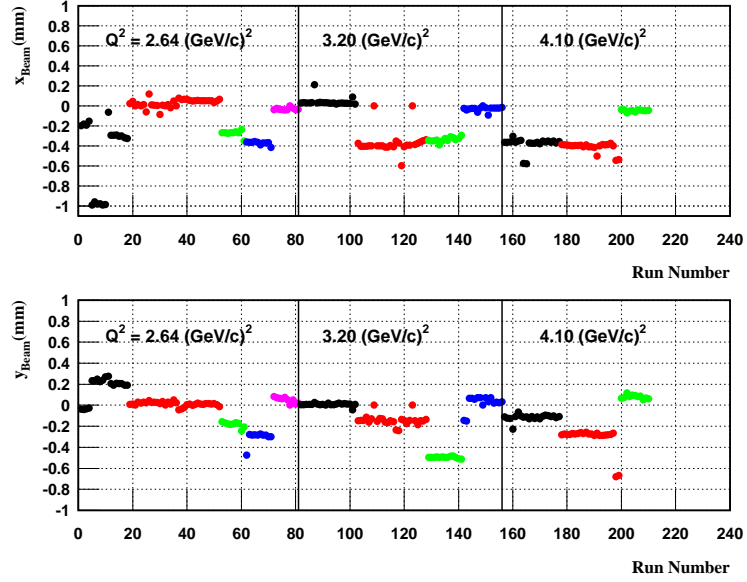
Figure 3.15: The top(bottom) plot shows the x(y) coordinate of the beam at the target.

3.6   Beam Current Measurements

In order to measure the current used and therefore the total charge accumulated during each run in each kinematics, two identical beam current monitors (BCMs) located $\sim$ 25 m upstream from the target are used. The two BCMs are calibrated at several beam currents relative to a parametric current transformer or Unser monitor. The Unser monitor is located halfway between the two BCMs and is calibrated by passing a precisely known current through it. Hall A beam current monitors [67] are designed to provide a non-invasive continuous measurements for the beam current. The Hall A BCM is a stainless steel cylindrical cavity 15.24 cm in length and 15.48 cm in diameter. The cylindrical axis of the cavity coincides with the beam direction. When the electron beam enters the cavity, it excites the transverse magnetic mode of the cavity. The resonant frequency of the cavity is tuned to the frequency of the

electron beam (1497 MHz) and hence an output signal from one of the two antennas inside the cavity is produced. The output signal is then amplified and split into two components, one of which is sent to an AC Voltmeter which measures the beam current averaged over 1.0 sec period. The second signal is then converted into an analog DC voltage level by using an RMS-to-DC converter. The analog DC voltage level is then converted to a frequency signal using a voltage-to-frequency converter. Scalers gated by the start and end of each run receive the frequency signal and then provide a measurement of the accumulated charge during the runs. Figure 3.16 shows the schematic layout of the BCM readout block.
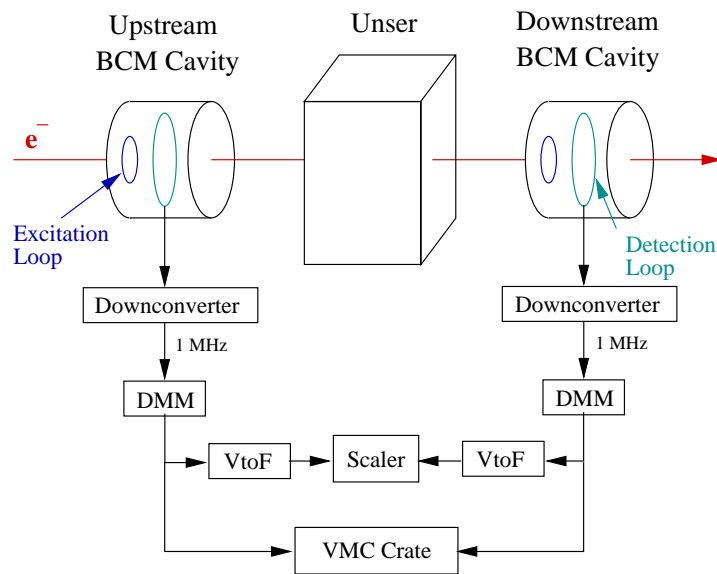
Figure 3.16: Schematic layout of the Hall A Beam Current Monitors readout block.

3.7 Hall A Target System

The target system of Hall A [67, 71] consists of the scattering vacuum chamber and the cryogenic targets. The 4-cm long liquid hydrogen target was used in this experiment.

3.7.1 The Scattering Chamber

The scattering vacuum chamber of Hall A consists of three main sections or rings. The first section, the base ring, is fixed on the pivot of the hall and made of stainless-steel. It contains a vacuum pump-out port and several viewing and electrical ports. The middle section, middle ring, is located at the beam height and is made of aluminum. It has a 104 cm inner diameter and 5 cm thick aluminum wall. Also a 15.2 cm vertical cutout on each of the beam side over the whole angular range of $12.5^o < \theta < 167.5^o$ has been introduced. A 0.38 mm thin aluminum foil covers the vertical cutout on both side of the beam. The middle section has beam entrance and exit ports which are vacuum coupled to the electron beamline to prevent the beam from interacting with any material except the target. The third section, the upper ring, houses the cryogenic targets system.

3.7.2 The Cryogenic Target

The cryogenic target system of Hall A is mounted on a ladder inside the scattering vacuum chamber. The ladder contains sub-systems for cooling, gas handling, temperature and pressure monitoring, and target control and motion. The ladder also contains a selection of solid targets such as dummy target for background measurements and BeO, ^{12}C, and optics targets for beam viewing and calibration. The desired target can be selected from the control room (counting house) by moving the ladder vertically up and down until the target is aligned with the beam.

The cryogenic target has three independent loops. Two loops were configured to

hold liquid hydrogen (LH_2) or liquid deuterium (LD_2), and one for a gaseous helium. Fans are used to circulate the liquid or the gas through each loop. Each of the LH_2 and LD_2 loops has two aluminum cylindrical target cells of either 4 or 15 cm in length and 6.35 cm in diameter. The sidewalls of the cells are 0.178 mm thick with entrance (upstream) and exit (downstream) windows of 0.071 and 0.102 mm thick, respectively.

During the E01-001 experiment, the 4-cm LH_2 target was used and operated at a constant temperature of 19 K and pressure of 25 psi with a density of 0.0723 g/cm^3. The temperature of the target was stabilized using a high-power heater to compensate for the effect of any beam intensity variation on the target's temperature. The target was cooled using a target coolant (liquid helium) at 15 K supplied by the End Station Refrigerator (ESR). Because of the small spot size of the beam, the beam was rastered using a rectangular raster producing a $\sim$ 2 mm $\times$ 2 mm spot size at the target to prevent any damage to the target by overheating it.

3.8   Hall A High Resolution Spectrometers

Protons were detected simultaneously using the two identical high resolution spectrometers (HRS), also called the left and right arm spectrometers of Hall A. The left arm spectrometer was used to measure three Q^2 points of 2.64, 3.20, and 4.10 GeV^2. Simultaneously, measurements at $Q^2 = 0.5$ GeV^2 were carried out using the right arm spectrometer which served as a luminosity monitor to remove any uncertainties due to beam charge, current, and target density fluctuations.

The two spectrometers are identical in their design [67]. They can provide a maximum central momentum of $\sim$ 4 GeV/c with momentum resolution better than 2×10^{-4} and a horizontal angular resolution better than 2 mrad. Figure 3.17 shows the basic layout of the high resolution spectrometer, as well as the detector hut which will be discussed later on in more detail. Table 3.3 lists some of the characteristics of the
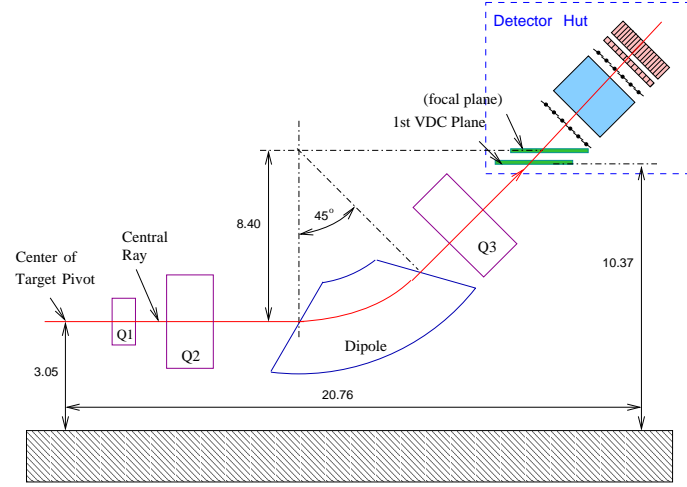
Figure 3.17: Schematic layout of the Hall A high resolution spectrometer (HRS) and the detector hut. Dimension are in meters.

Configuration	$QQDQ$
Momentum Range p (GeV/c)	0.30 - 4.0
Bend Angle (^{o})	45
Optical Length (m)	23.4
Momentum Acceptance $\delta p/p$ (%)	$\pm$ 4.50
Dispersion (D) (cm/%)	12.4
Radial Linear Magnification (M)	2.5
D/M	5.0
Momentum Resolution (FWHM) $\delta p/p$	1×10^{-4}
Angular Acceptance (Horizontal) (mrad)	$\pm$ 28
Angular Acceptance (Vertical) (mrad)	$\pm$ 60
Solid Angle $\Delta\Omega$ (msr)	$\sim$ 6.7
Angular Resolution (FWHM) Horizontal ϕ (mrad)	0.6
Angular Resolution (FWHM) Vertical θ (mrad)	2.0
Transverse Length Acceptance (cm)	$\pm$ 5.0
Transverse Position Resolution (FWHM) (mm)	1.50
Spectrometer Angle Determination Accuracy (mrad)	0.10

Table 3.3: Characteristics of the Hall A high resolution spectrometer.

Hall A high resolution spectrometer. A detailed description of the spectrometer design can be found in [67, 72] and references therein. Each high resolution spectrometer uses a $QQDQ$ configuration of super-conducting magnets to focus charged particles onto their focal planes. Each spectrometer consists of two super-conducting quadrupoles followed by a 6.6 m long indexed dipole magnet for bending with focusing entrance and exit windows. Due to the trapezoidal cross sectional shape of the dipole, the bending field inside the dipole is not radially uniform. The first quadrupole is used to focus in the vertical plane, while the second and the third quadrupoles are used to focus in the horizontal plane. The net effect of the $QQDQ$ configuration is to provide a vertical bending with nominal bending angle of 45°.

3.9   Detector Package

The detector package of each HRS is located in a large steel and concrete detector hut after the magnet system. The purpose of these detectors is to select and identify the charged particles coming through the spectrometers. During the E01-001 experiment, the two spectrometers (arms) included similar detector packages with a slight difference between the two arms. A detailed description of the detector package on each arm can be found in [67, 73] and references therein. The following detectors were used on each arm:

- **A set of two Vertical Drift Chambers (VDC's) for tracking purposes.**

- **Two scintillator planes, S_1 and S_2, for trigger activation and time-of-flight determination. In addition, an extra plane S_0 was added to the left arm for efficiency determination.**

- **Aerogel Cerenkov detectors A_1 for the left arm and A_2 for the right arm for particle identification (p and π^+ separation).**

- **A gas Cerenkov detector for particle identification. The right arm gas Cerenkov detector was used during the coincidence runs for e^- and π^- separation.**

In addition, the right and left arm detector packages included some extra detectors that were not used during the E01-001. The right arm had a mirror aerogel detector and calorimeter. The left arm included a gas Cerenkov, pion rejector (two layers), and focal plane polarimeter (FPP) (rear straw chambers). Although these extra detectors were not used during the E01-001 experiment, they do contribute to proton absorption (absorption in the material of each detector) if they were located before the scintillator plane S_2. The mirror aerogel detector and the gas Cerenkov detector are the most relevant in this case and their contribution to proton absorption should be taken into an account. On the other hand, both layers of the pion rejector and the two rear straw chambers of the FPP were located behind the S_2 scintillator and were not relevant for the proton absorption determination. Figures 3.18 and 3.19 show a schematic layout of the detector package used with each arm during the E01-001 experiment.

3.9.1 Vertical Drift Chambers

Vertical drift chambers (VDCs) [67, 74] are used for tracking (position and slope of the particle trajectory) of the scattered particles. Each spectrometer of Hall A has two vertical drift chambers. The first VDC is located at the focal plane of the spectrometer, and the second VDC is positioned parallel to and 23 cm away from the first VDC. Both VDCs intersect the spectrometer central ray at an angle of 45° which is the approximate nominal angle at which the particle trajectory crosses the wire planes of each VDC. Each VDC has two wire planes known as the U and V planes. Each wire plane contains 368 parallel 20μm-diameter gold-coated tungsten wires sandwiched in between gold-coated mylar planes. The wires of the U plane are
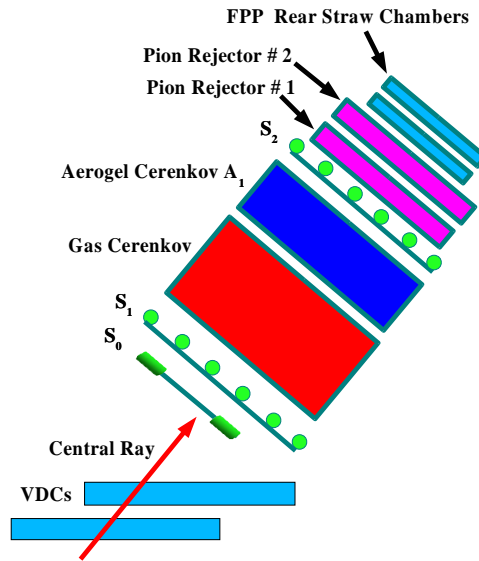
Figure 3.18: Schematic layout of the left arm detector package used during the E01-001 experiment.
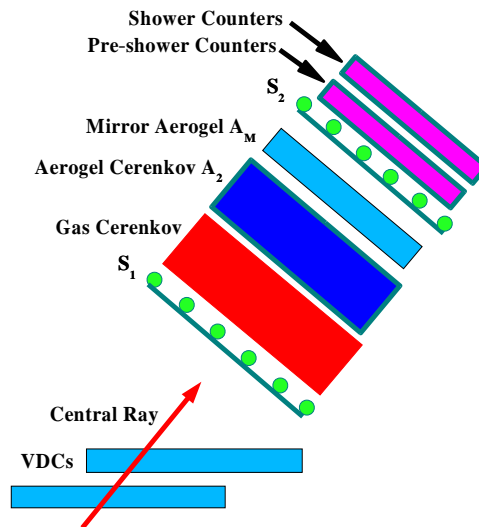
Figure 3.19: Schematic layout of the right arm detector package used during the E01-001 experiment.

perpendicular to that of the V plane and they are oriented with an angle of 45° (-45°) with respect to the dispersive (transverse) direction. We refer to the U and V planes as U$_1$ and V$_1$ planes in the first VDC and U$_2$ and V$_2$ planes in the second. Figures 3.20 and 3.21 show a pair of vertical drift chambers and a side view of a nominal 45° particle trajectory crosses the planes of the VDCs. To operate the VDCs, a gas
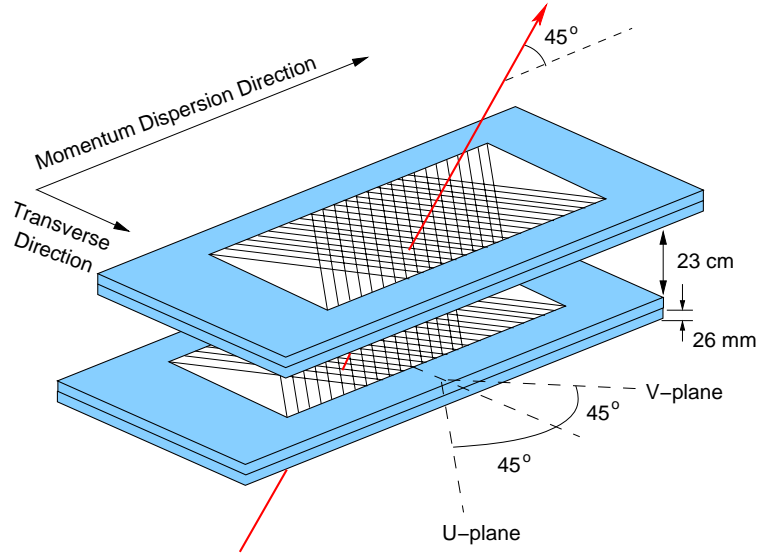
Figure 3.20: Schematic layout of the Hall A vertical drift chambers.

mixture of argon (62%) and ethane (38%) (C$_2$H$_6$) fills the area between the mylar planes. The mylar planes are kept at negative potential of 4KV, while the tungsten wires are grounded. When a charged particle crosses the VDC planes, it ionizes the atoms in the gas mixture. The released electrons are accelerated (drift) due to the potential difference between the mylar planes and the tungsten wires taking the path of least time (also known as the geodetic path). Once the electrons are close to the sense wires where the electric field is the strongest, the drifting electrons create an electron avalanche. This avalanche of electrons hits the sense wire and then generates a signal which gets amplified, discriminated, and then sent to a multihit time-to-
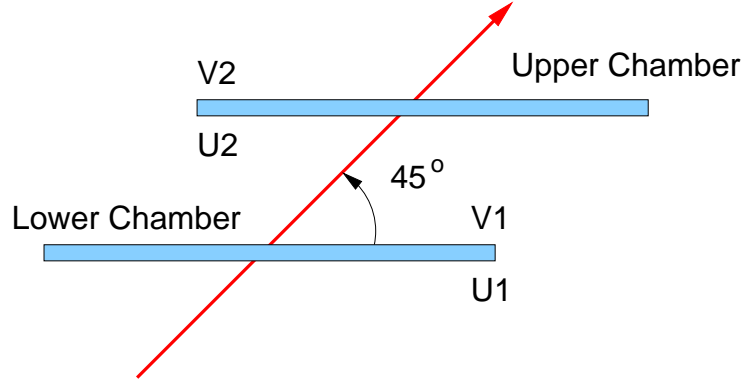
Figure 3.21: Side view of the Hall A vertical drift chambers planes. The red arrow is the nominal 45° particle trajectory crosses the planes of the VDCs.

digital converter (TDC) to measure the time for the least path defined above. The TDC is started by the signal from the sense wire and stopped by the event trigger supervisor.

In order to get the tracking information or the drift distance of the charged particle from each fired wire, we use the drift velocity of the ionized electrons in the C_2H_6 gas mixture (known to be 50 μm/ns), and the output of the TDC signal (time). Having calculated the drift distance of the charged particle from each fired wire, the trajectory (track) of the charged particle can be reconstructed. A 45° nominal trajectory (track) typically triggers five wires. Figure 3.22 shows the reconstruction of the charged particle track in the VDC planes.

3.9.2   Scintillators and Triggers

For most of the data taking, proton singles events were detected. In addition, co-incidence runs at $Q^2 = 2.64$ and 4.10 GeV^2 were taken. Electrons in coincidence with protons were detected using the right arm spectrometer while the protons were detected using the left arm. Triggering of such events was made possible by the use
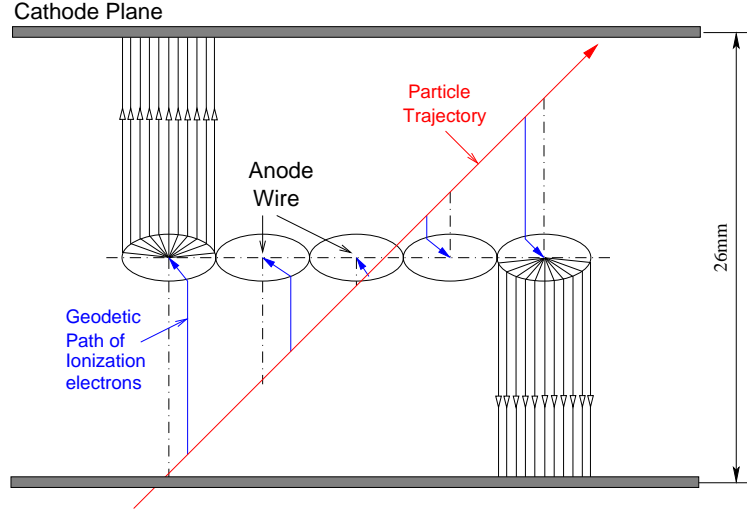
Figure 3.22: The avalanche process in the VDC and the reconstruction of the charged particle track.

of the Hall A scintillators and trigger system [67, 75].

For each spectrometer in Hall A, there are two scintillators planes labeled S_1 and S_2. The two planes are parallel to each other and both are perpendicular to the nominal central ray of the spectrometer. The two scintillators planes are ~ 2 meters apart. Each scintillator plane has 6 identical overlapping scintillators paddles made of thin plastic (0.5 cm thick BICON 408) to minimize hadron absorption. A photo-multiplier tube (PMT) is attached to each end of each scintillator paddle to collect the photons produced by particles passing through scintillator. We refer to these PMTs as the left and right PMT of the scintillator paddle. Figure 3.23 shows the scintillator configuration.

The active area of S_1 is ~ 170 cm $\times$ 36 cm (30 cm $\times$ 36 cm for each paddle) and ~ 220 cm $\times$ 60 cm (37 cm $\times$ 60 cm for each paddle) for S_2. The time resolution for each scintillator plane is ~ 0.30 ns. For the E01-001 experiment, an additional scintillator counter , S_0, was added to the left arm trigger system for a more accurate

measurement of the efficiency. S_0 was installed before the S_1 scintillator plane and it is a 1 cm thick scintillator paddle with an active area of $\sim$ 190 cm $\times$ 40 cm. The S_0 paddle has 2 PMTs labeled top and bottom. The analog signals from the PMTs
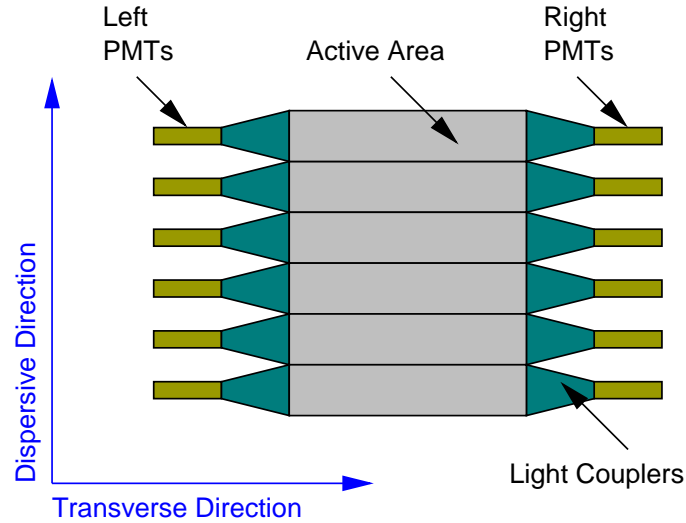
Figure 3.23: Scintillator plane configuration. Each scintillator plane is perpendicular to the nominal central ray of the spectrometer.

are first sent to a discriminator (LeCroy model 4413/200) providing both digitized and analog outputs. The analog signals are sent to ADCs and the digitized signal are split into three signals. One signal is sent to TDCs, the second is sent to a scalers gated by the start and the end of each run, and the third is sent to a logical unit called the AND unit to make a coincidence between the pairs of PMTs viewing the same paddle. For each of the spectrometers, the 12 outputs of the logical AND unit are fed into the Memory Lookup unit (MLU) which takes in a combination of logical signals at its input and gives out a combination of logical signals at its output.

There are five basic triggers (event types) generated from the scintillators timing information. They are classified as main physics triggers and loose (auxiliary) physics

triggers. The conventional triggers types used for the left arm are the main singles trigger T_3 and the loose singles trigger T_4. For the right arm, we refer to the main singles trigger by T_1 and the loose singles trigger by T_2. Finally, there is the coincidence trigger T_5 which is the coincidence of T_1 and T_3 implying that the two events T_1 and T_3 were produced at the target simultaneously. The loose triggers are usually used to determine the efficiencies of the main triggers and the scintillators planes in general.

The output of each ADC is proportional to the number of photons produced inside the scintillator and in turn represents the ionization energy loss of the particle, or equivalently, the energy deposition in the scintillator. For low momenta, the heavier the particle, the more energy it deposits in the scintillator. The TDC signal provides timing information for the different type triggers used. By determining the time-of-flight of the particle between the scintillator planes form the TDC signals, and by knowing the distance between the two scintillator planes, the velocity of the particle v or $\beta = v/c$ can be determined. Usually β is used for particle identification (PID) since different charged particles of a known momentum can be separated by knowing their velocity and hence β. Figure 3.24 shows the ADC and TDC spectrum from one of the PMTs from the second scintillator plane S_2 for the low-momentum setting spectrometer (right arm). A β spectrum where different particles are clearly separated is also shown.

The left and right arm MLUs were programmed to generate a logical signal which defines and assigns the trigger (event type) $T_1(T_3)$ to an event (particle) if the event satisfies the following:

- The main $T_1(T_3)$ event type is generated if:

    1. A scintillator paddle is said to have fired if and only if a signal from both the right and left PMT in that paddle is generated. The logic AND is then
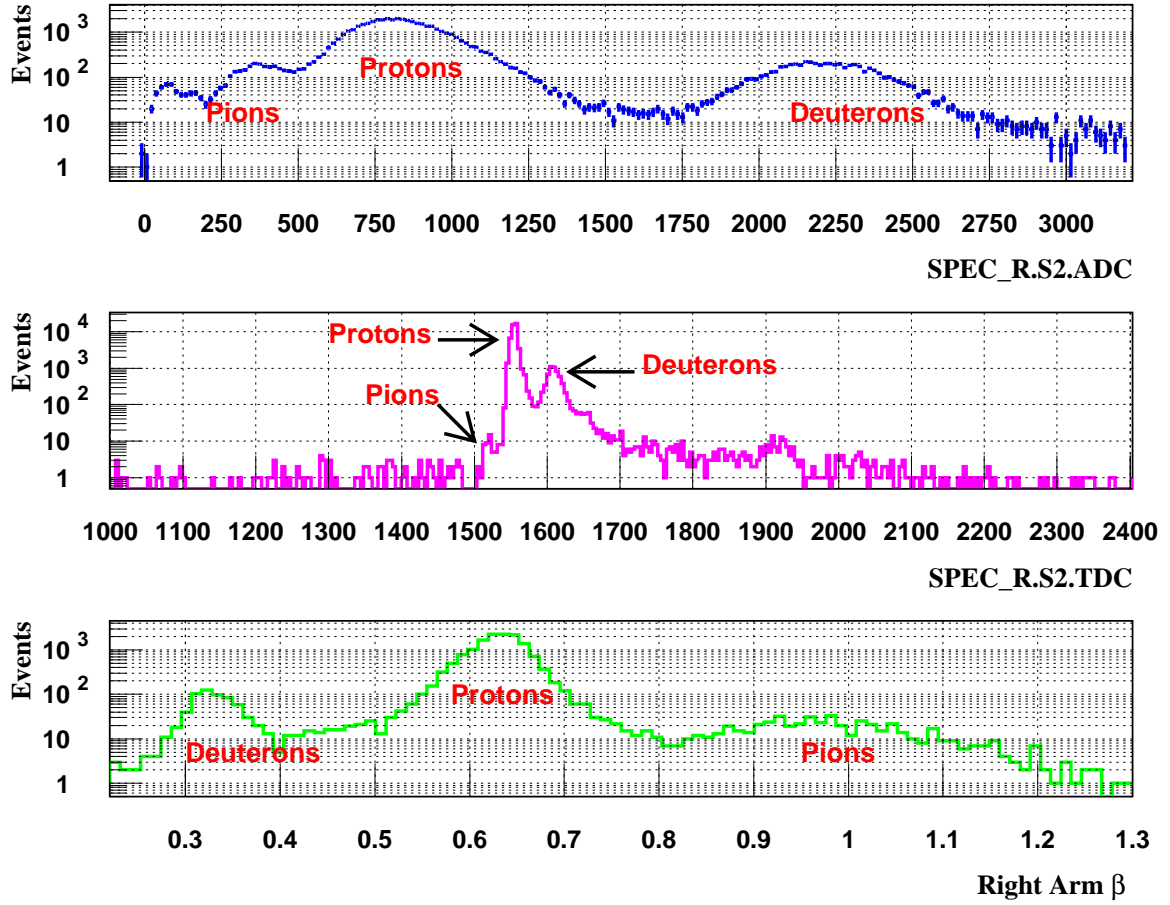
Figure 3.24: Typical ADC and TDC spectra from a scintillator PMT (upper two plots) from the low-momentum setting spectrometer. Different particles have been identified using the ADC spectrum based on the amount of the energy deposited in the scintillator. Pions show first (time wise) in the TDC spectrum since they are lighter than the protons and therefore have smaller time-of-flight (larger β). The calculated β spectrum based on the TDC timing information and distance between the two scintillators planes is also shown (lower plot). The β spectrum is used for particle identification.

formed between the right and left PMT's signal to generate that paddle's signal.

2. Each scintillator plane will have 6 signals (one signal from each paddle in each plane).

3. The logic OR of the 6 signals in that plane generate the main signal for that plane (one main signal for each scintillator plane).

4. The right arm main trigger (T_1) is defined as:

    (S_1 main signal) AND (S_2 main signal).

5. A third scintillator S_0 was added to the left arm only. Therefore, the left arm main trigger (T_3) is defined as:

    (S_0 main signal) AND (S_1 main signal) AND (S_2 main signal).

- The loose T_2(T_4) event type is generated if:

1. T_2 is the same as T_1 defined above except the AND in point number 4 is replaced with an OR:

    (S_1 main signal) OR (S_2 main signal).

2. T_4 is the same as T_3 defined above except the AND between S_1 and S_2 in point number 5 is replaced with an OR:

    (S_0 main signal) AND $\Big(($S_1$ main signal) OR (S_2 main signal)$\Big)$.

- The coincidence trigger T_5 is generated as the coincidence between T_1 and T_3.

3.9.3   Gas Cerenkov

Coincidence kinematics were taken at $Q^2 = 2.64$ and 4.10 GeV^2. Electrons were detected using the right arm and protons using the left arm. See Table 3.1 for more details. In order to separate electrons from background particles such as the

negatively charged pions, a Cerenkov detector was used in the right arm for particle identification.

The gas Cerenkov detector used in Hall A [67, 76] was installed between the scintillator S_1 and S_2 planes. It is a rectangular chamber filled with CO_2 gas at atmospheric pressure. When a high energy charged particle travels through a material of index of refraction n with velocity v larger than the velocity of light in that material (c/n) where c is the speed of light, electromagnetic radiation (light) is emitted. This is known as the Cerenkov effect. For the Hall A Cerenkov detector, 10 spherical mirrors at the back wall focus the Cerenkov radiation on 10 PMT photocathodes.

A charged particle can emit Cerenkov radiation only when its velocity is larger than a threshold velocity set by the index of refraction of that material:

$$v_{th} = \frac{c}{n} \ ,$$

(3.9)

and therefore a threshold momentum:

$$p_{th} = \frac{m v_{th}}{\sqrt{1 - \frac{v_{th}^2}{c^2}}} \ .$$

(3.10)

For the CO_2 gas used, the index of refraction is $n = 1.00041$. Equation (3.10) then gives a momentum threshold of $p_{th} \sim 17$ MeV/c for electrons and $p_{th} \sim 4.8$ GeV/c for pions which is larger than the momentum range of the Hall A HRS which is $0.30-4.0$ GeV/c. So, only electrons give a signal in the analog-to-digital (ADC) of the Cerenkov detector. Figure 3.25 shows the distribution of the sum of the 10 ADCs signals of the gas Cerenkov PMTs.
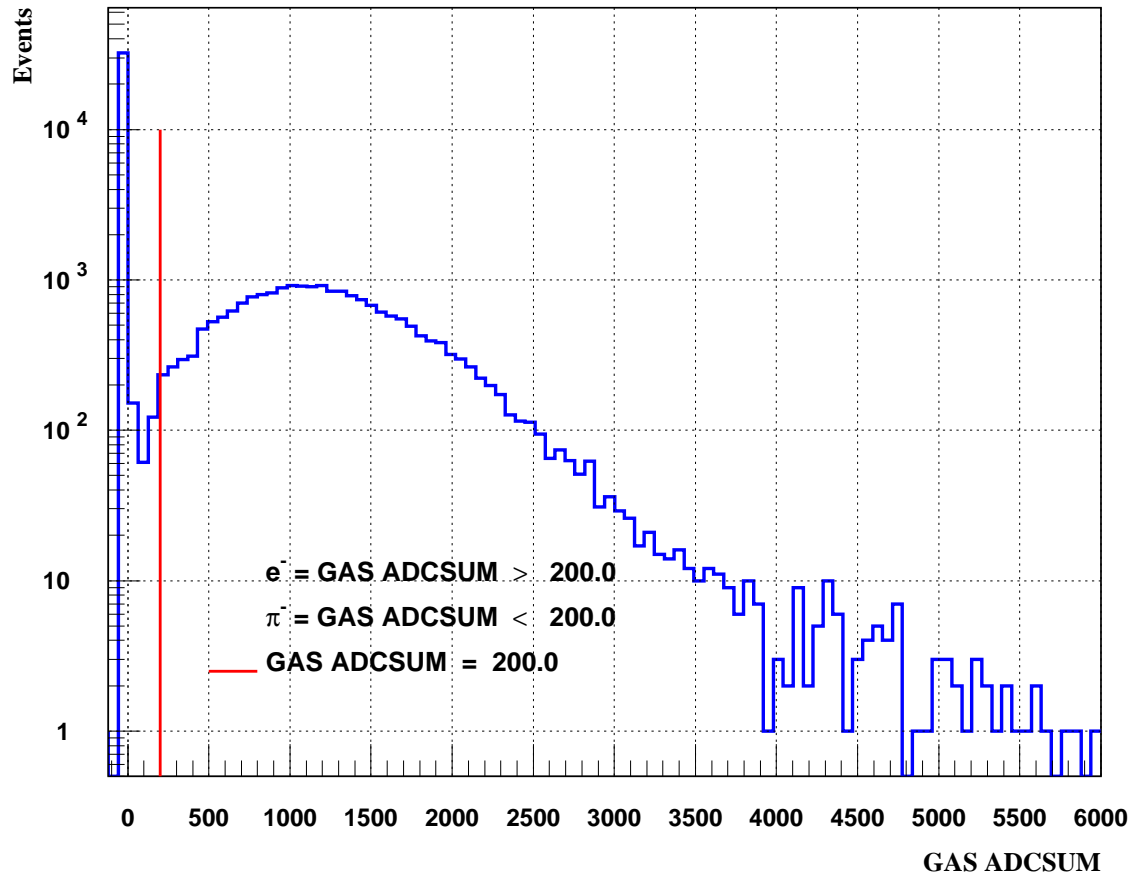
Figure 3.25: Gas Cerenkov ADCs sum signal. The peak at GAS ADCSUM = zero represents the π^- which did not fire the gas Cerenkov. GAS ADCSUM > 200 represents the e^- signal which fired the gas Cerenkov. The red solid line is the boundary between the π^- region (GAS ADCSUM < 200) and e^- region (GAS ADCSUM > 200).

3.9.4   Aerogel Cerenkov

Two Aerogel Cerenkov detectors A_1 and A_2 [67, 77, 78] were used for particle identification where protons and positively charged pions could be separated based on the Cerenkov radiation effect discussed above. The A_2 aerogel detector was used with the right arm, while the A_1 aerogel was used with the left arm. In addition, a mirror aerogel, A_M, was installed on the right arm between the S_1 and S_2 scintillators but was never used. The A_M Aerogel contributes to the proton absorption in the right arm.

The two aerogel detectors A_1 and A_2 are designed in the same way. The A_1 aerogel has a 9 cm aerogel radiator with index of refraction $n_{A_1} = 1.015$ while A_2 has a 5 cm aerogel radiator with index of refraction $n_{A_2} = 1.055$. There are 24 PMTs installed in A_1 and 26 PMTs in A_2.

For the A_1 aerogel ($n_{A_1} = 1.015$), equation (3.10) gives a momentum threshold of $p_{th} \sim 5.4$ GeV/c for protons and $p_{th} \sim 0.8$ GeV/c for positive pions, while, for the A_2 aerogel ($n_{A_1} = 1.055$), equation (3.10) gives a momentum threshold of $p_{th} \sim 2.8$ GeV/c for protons and $p_{th} \sim 0.40$ GeV/c for positive pions. For the A_1 aerogel (left arm), the momentum threshold for the protons is larger even than the momentum range of the Hall A HRS ($0.30-4.0$ GeV/c) and that makes it impossible for the protons to fire the aerogel Cerenkov detector. On the other hand, the momentum threshold for the positive pions is within the momentum range of the Hall A HRS and hence pions above 0.8 GeV/c should produce a signal in the analog-to-digital (ADC) of the A_1 aerogel Cerenkov detector. For the right arm where A_2 aerogel was used, only positive pions could trigger the analog-to-digital and fire the aerogel Cerenkov detector since the central momentum for the right arm spectrometer was always set to 0.756 GeV/c which is less than the threshold momentum needed for the protons to trigger the aerogel Cerenkov detector. Figure 3.26 shows the distribution of the sum of the ADCs signals of the $A_2(A_1)$ aerogel Cerenkov PMTs.
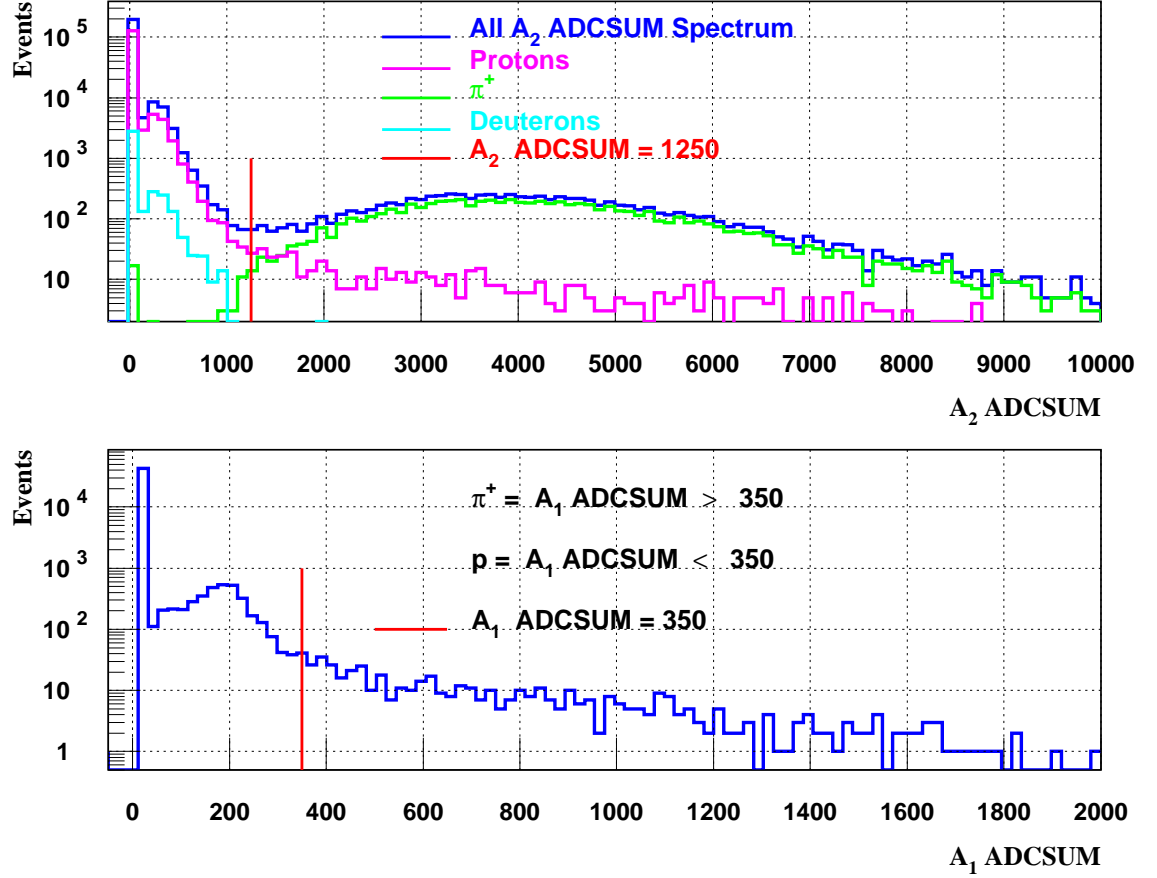
Figure 3.26: $A_2(A_1)$ aerogel Cerenkov ADCs sum signal top(bottom) in blue. The peak at $A_2(A_1)$ ADCSUM = zero represents the protons which did not fire the aerogel Cerenkov. The contribution of protons, π^+, and deuterons to A_2 ADCSUM (selected by cuts on the time-of-flight and amount of energy deposited in the S_1 scintillator) is shown. The contribution of protons, π^+, and deuterons to A_1 ADCSUM is not shown since they cannot be separated using any other detector and it will be discussed in the next chapter in more detail. The $A_2(A_1)$ ADCSUM $> 1250(350)$ represents the cut we use to separate the π^+ signal which fired the aerogel Cerenkov. Notice the leakage of protons into the π^+ area and the small contamination of the protons area with π^+ and deuterons as can be seen form A_2 ADCSUM spectrum.

3.10   Data Acquisition System

The data acquisition system in Hall A (DAQ) was used during the run of experiment E01-001. The data acquisition system is controlled by CEBAF On-line Data Acquisition system (CODA) [67, 79] which is developed by the JLAB data acquisition group and designed for nuclear physics experiments. CODA is a toolkit that is composed of a set of software and hardware packages from which DAQ can be built to manage the acquisition, monitoring, and storage of data.

Data acquisition in Hall A takes the following steps:

- The data is read out from Read-Out Controllers (ROCs). The ROCs are CPUs in Fastbus and VME crates in the hall and in the electronics room. These crates contain the ADCs, TDCs, and scalers that contain the event information.

- The Trigger Supervisor controls the state of the run, and generates the triggers that cause the ROCs to be read out.

- The Event Builder subsystem (EB) is the part of CODA that reads in the data fragments from the ROCs and puts the data together into an event, incorporating all of the necessary CODA header information needed to describe and label the event and the data fragments.

- CODA manages the data acquisition system, and takes care of handling the data from the events.

- After the event is built by the EB, it is placed into a buffer, after which it can be tested and recorded using the event recorder or rejected if desired.

- The accepted events (data) are written to a local disk and then transferred to the Mass Storage System.

- Data from various control systems and scalers are injected into the data stream every few seconds using the event transfer.

- In addition to running the data acquisition, CODA also includes a graphical user interface (RunControl) which allows the user to start and stop runs, as well as define run parameters.

- Events are classified as physics events which come from the spectrometers (detectors) and beamline information (Beam position monitors, beam loss monitors, and beam raster readback values recorded for each event), or EPICS events [80] such as the readout of hardware (spectrometers magnets settings, angles, and target controls).

Chapter 4   Data Analysis I: Efficiencies and Corrections

4.1   Analysis Introduction

In this chapter a description of the event reconstruction procedure and the corrections and efficiencies applied to the measured beam charge, Q, will be presented. These corrections and efficiencies include the computer and electronics livetimes , CLT, and ELT, respectively, VDCs tracking efficiency, ϵ_{VDC}, VDCs hardware cuts efficiency ϵ_{VDCH}, scintillators efficiency (product of the two scintillators efficiency or $\epsilon_{S_1} \times \epsilon_{S_2}$), particle identification (PID) efficiency, ϵ_{PID}, proton absorption correction, $C_{Absorption}$, target boiling correction, C_{TB}, and target length correction, C_{TL}. In addition, a brief description of the spectrometer optics calibration and spectrometer mispointing measurements will be given. Having applied these corrections and efficiencies to the beam charge, we refer to the corrected charge as the effective charge or Q_{eff} and it is defined as:

$$Q_{eff} = \frac{1}{ps}\Big(Q \times ELT \times CLT \times \epsilon_{VDC} \times \epsilon_{VDCH} \times \epsilon_{S_1} \times \epsilon_{S_2} \times \epsilon_{PID} \times C_{Absorption}$$
$$\times C_{TB} \times C_{TL} \Big) , \tag{4.1}$$

where ps is the prescale factor. The prescale factor n for the trigger type T_i ($i = 1, \cdots, 5$) means that the Trigger Supervisor will read out every nth event of type T_i.

The advantages of detecting protons as against electrons were discussed in section 3.2. Because of these advantages, the E01-001 experiment was able to greatly reduce

any ε-dependent systematic corrections and associated uncertainties applied to the measured cross sections. In addition, measurements at $Q^2 = 0.5$ GeV^2 using the right arm spectrometer which served as a luminosity monitor will check the uncertainties due to beam charge, current, and target density fluctuations.

The systematic uncertainties in these efficiencies and corrections will be discussed. These systematic uncertainties are a measure of how accurately we know the various efficiencies and corrections. The systematic uncertainties are classified into three types, based on how they contribute to the quantities we want to extract:

- Scale Uncertainty: Sometimes referred to as normalization uncertainty as it has the same effect on all ε points at a given Q^2. An example would be the uncertainty in the target length. Such uncertainty would affect both G_{Ep} and G_{Mp} the same way but not the ratio.

- Random Uncertainty: Sometimes referred to as point-to-point uncertainty. It has an uncorrelated effect on each ε point at a given Q^2. Two examples are the statistical uncertainty and the uncorrelated shifts in the beam energy and scattering angle for different kinematics. Such uncertainties affect the extraction of G_{Ep}, G_{Mp}, and the ratio.

- Slope Uncertainty: Refers to a correlated uncertainty in a correction that varies linearly with ε. An example would be the effect of a fixed scattering angle or beam energy offset for all kinematics which also leads to a scale uncertainty. Such an uncertainty will modify the slope of the reduced cross section verses ε, and thus G_{Ep} and $\frac{G_{Ep}}{G_{Mp}}$, but will not spoil the expected linearity.

It must be mentioned that in some cases it is unclear whether the uncertainty is scale, random, or slope. In these cases, the worst case of the three uncertainties is assumed. Table 4.1 indicates whether the different types of uncertainties effect the individual form factors, their ratio, and the linearity of the L-T plots. Note that the

slope uncertainty is the change in slope between $\varepsilon = 0.0$ and $\varepsilon = 1.0$. So the value for the slope uncertainty is the change over the actual ε range in data divided by $\Delta\varepsilon$. Since $\Delta\varepsilon \sim 0.70$ for the left arm and $\Delta\varepsilon \sim 0.07$ for the right arm, the slope uncertainty is much larger for the right arm.

Uncertainty Type	G_{Ep}	G_{Mp}	$\mu_p G_{Ep}/G_{Mp}$	Linearity
Scale	Yes	Yes	No	No
Random	Yes	Yes	Yes	Yes
Slope	Yes	Yes	Yes	No

Table 4.1: The effect of the scale, random, and scale uncertainties on the individual form factors, their ratio, and the linearity of the L-T plots.

4.2 Event Reconstruction

The raw data files imported from the DAQ system were replayed using the standard Hall A event processing software ESPACE (Event Scanning Program for Hall A Collaboration Experiments) [81]. The multipurpose ESPACE reads the raw events and then decodes, filters, calibrates, and reconstructs physical variables of interest for the analysis on an event-by-event basis. These physical variables can be detector hits, tracks and particle identification (PID) signals, or the coordinates of the reaction vertex in the target. The outputs of ESPACE are histograms and ntuples (multidimensional matrices of the physical quantities of interest) saved in HBOOK formated files [82]. An HBOOK file is generated for each production run. These HBOOKs are read using the Physics Analysis Workstation (PAW) software [83] where cuts can be applied on these physical quantities.

4.3 Optics

There are different coordinate systems used in Jefferson Lab Hall A. These coordinate systems are described in detail in [81, 84] and can be classified as: the hall coordinate system, the target coordinate system (spectrometer reconstructed coordinate system), the detector coordinate system, the transport coordinate system, and finally the focal plane coordinate system. The hall and target coordinate systems are commonly used to define and calculate the physical quantities of interest for data analysis (see Figures 4.1 and 4.2), while the detector, transport, and focal plane coordinate systems are used for Monte Carlo simulations and optics calibrations.
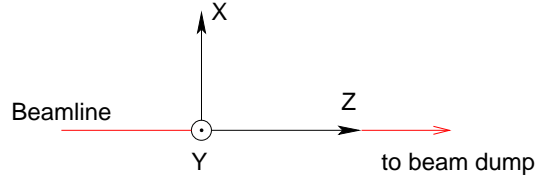
Figure 4.1: The hall coordinate system viewed from above: Z is the beam direction, Y is vertically pointing up, and X is to the left of the beam direction and perpendicular to both Z and Y.

For event reconstruction, ESPACE starts by reconstructing the event at the focal plane of the spectrometer (passing through the center of the U_1 plane of the first VDC). That includes determination of the electrons drift times in the wire chambers and the drift distances (see section 3.9.1), reconstruction of the particle trajectories, and calculation of $\beta = v/c$ and positions and angles of the track in the focal plane coordinate system. The detector coordinate system, the transport coordinate system, and the focal plane coordinate system all share the same origin defined as the intersection of central wire 184 of the VDC U_1 plane and the central wire projection of the VDC V_1 plane.
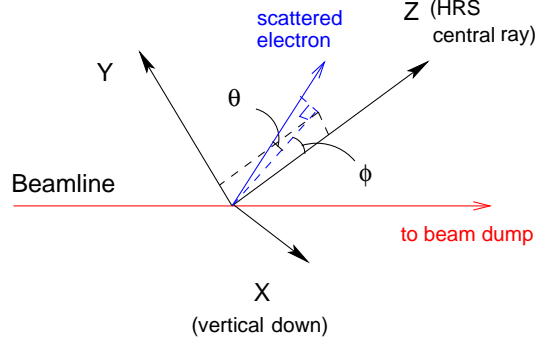
Figure 4.2: The target coordinate system: Z is the spectrometer central ray direction, X is pointing down (dispersive direction), and Y is perpendicular to both Z and X (transverse direction), ϕ and θ (usually called ϕ_{tg} and θ_{tg} where tg is short for target) are the in-plane and out-of-plane scattering angles, respectively, as measured with respect to the spectrometer central ray.

Having reconstructed the focal plane variables, the reconstruction of the target variables or reconstruction of the trajectories at the target can be done by using the optics database or transformation matrix between the focal plane and target variables [84]. These reconstructed target variables are the in-plane and out-of-plane scattering angles ϕ or ϕ_{tg}, and θ or θ_{tg} where tg is short for target, the y-coordinate of the extended target length y_{tg}, and the deviation from the central momentum $\delta = \frac{p-p_o}{p_o}$.

In order to study the optical properties of the spectrometer, sieve slits collimators [67, 85] positioned 1.184±0.005 and 1.176±0.005 m from the target on the left and right arm spectrometers, respectively, are used. The sieve slit is a 5 mm thick stainless steel sheet with a pattern of 49 holes (7 x 7), spaced 12.5 mm apart horizontally and 25 mm apart vertically. Two of the holes, one in the center and one displaced two rows vertically and one horizontally, are 4 mm in diameter, while the rest are 2 mm in diameter. Figures 4.3 and 4.4 show the reconstruction of the sieve slit image due to electrons scattering from a thin ^{12}C target as seen by the right and left arm spectrometers, respectively. The fact that the optics database used by ESPACE

during the E01-001 analysis produces the correct position of the holes in the sieve slit for both spectrometers indicates that the optics database is well calibrated and no further calibration is needed. The calibration procedure is documented in detail in [84].
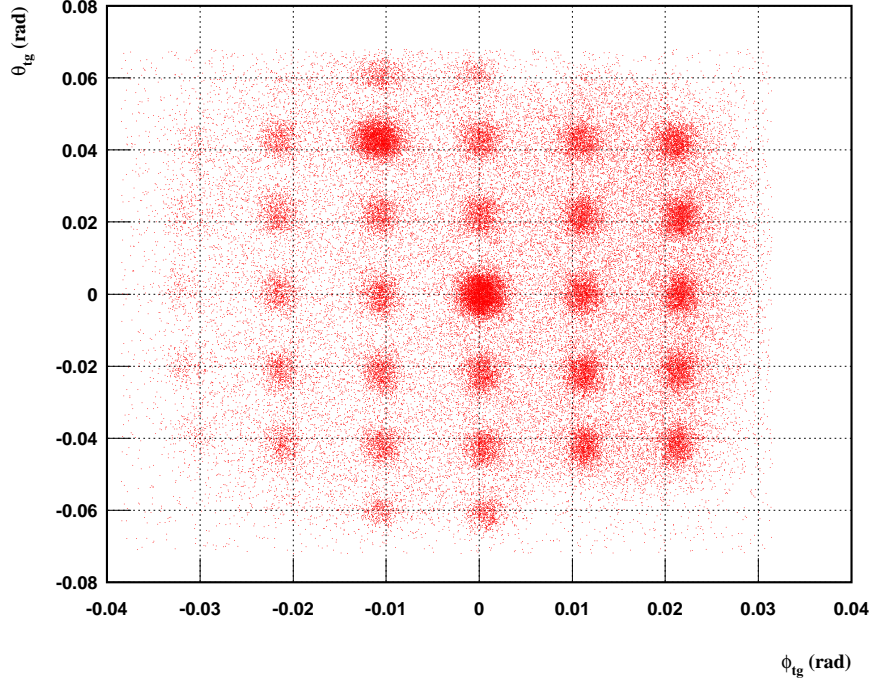
Figure 4.3: The reconstruction of the sieve slit image into the right arm spectrometer due to electrons scattered from a thin ^{12}C target.

During the analysis of the E01-001 experiment, a 1.6 msr solid angle software cut was applied. This cut corresponds to an out-of-plane angle of -40.0$< \theta_{tg} <$40.0 mrad and in-plane angle of -10.0$< \phi_{tg} <$10.0 mrad. See section 5.2 and Table 5.2 for a full description of the cuts applied during the analysis. We estimate that we know the edge of the θ_{tg} and ϕ_{tg} cuts from looking at the adjacent hole separation in the vertical and horizontal directions to within 0.20 mrad. This translates into a 2.0% scale uncertainty in the in-plane angle (0.2 mrad/10 mrad), and 0.5% scale

uncertainty in the out-of-plane angle (0.2 mrad/40 mrad). The sum in quadrature of the two angle scale uncertainties was used to determine the final estimated scale uncertainty in the 1.6 msr solid angle cut of 2.06%. Because the 1.6 msr solid angle cut is identical for all kinematics, the uncertainty in the solid angle only contributes to the scale uncertainty.
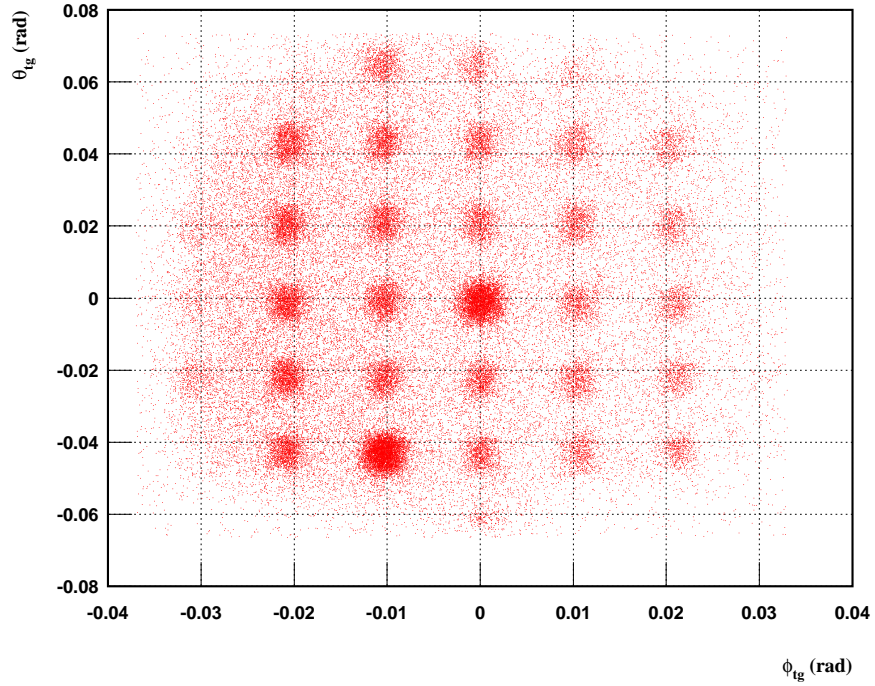
Figure 4.4: The reconstruction of the sieve slit image into the left arm spectrometer due to electrons scattered from a thin ^{12}C target.

4.4   Spectrometer Mispointing

Experiment E01-001 requires a precise knowledge of the e-p reduced cross sections. In order to achieve that, an accurate knowledge of the scattering angle is required. Knowing the scattering angle accurately requires accurate knowledge of the spec-

trometer optics and offsets, target position, and beam position. Figure 4.2 shows the coordinate system of the spectrometer. Ideally, the target center coincides with the hall center. Due to translational movements of the spectrometer around the hall center, the central ray of the spectrometer can miss the hall center in both the horizontal and vertical directions. The horizontal offset or the horizontal distance between the hall center and the central ray of the spectrometer is referred to as the spectrometer mispointing.

There are two different and reliable methods by which the horizontal and vertical offsets can be measured and hence the spectrometer angle: the survey method and the carbon-pointing method. The survey method is the most precise. The two spectrometers used during the E01-001 experiment were surveyed at several kinematics settings by the JLAB survey group.

For the right arm spectrometer, the spectrometer angle was surveyed and determined at all 5 ε points, and the survey angles were used in the analysis. For the left arm, there were several spectrometer settings where a survey was not performed, and so the carbon-pointing method was used. In the carbon pointing method, the spectrometer mispointing, Δh, and spectrometer angle, θ_s, are determined using carbon-pointing runs where electrons are scattered by a thin carbon foil. By knowing the spectrometer central angle, θ_o, (defined as the spectrometer angle with no mispointing), as determined from the hall floor marks, target position as reconstructed by the spectrometer, y_{tg}, and the target offset along the beam direction, z_{off}, as measured by the target survey group, Δh can be determined as:

$$\Delta h = \pm y_{tg} + z_{off} \sin(\theta_o) \; , \tag{4.2}$$

and hence the spectrometer scattering angle (angle setting) can be calculated as:

$$\theta_s = \theta_o + \frac{\Delta h}{L} \; , \tag{4.3}$$

where the plus(minus) sign in front of y_{tg} in equation (4.2) is used with the right(left) arm and L is the distance between the hall center and the floor marks where the angles are scripted and has a value of 8.458 m. Note that $\frac{\Delta h}{L} = \Delta\theta_o$ in equation (4.2) above represents the correction to the central scattering angle of the spectrometer, $\theta_s = \theta_o \pm \Delta\theta_o$. The spectrometer is said to be mispointed downstream(upstream) if Δh is positive(negative).

We can test the nominal kinematics by looking at the reconstructed kinematics for elastic scattering. The reconstruction of the ΔP spectrum is discussed in section 5.2. The elastic peak position should be near $\Delta P = 0.0$ MeV, but there are small corrections due to energy loss and radiative corrections, which are modeled in the Monte Carlo simulation program SIMC. See section 5.5.1 for details. The elastic peak position in the ΔP spectrum from data, δ_P RIGHT(LEFT), is compared to that in simulations δ_P SIMC. This comparison was done for the right and left arms and at all kinematics. For the left arm, an overall angular offset of 0.19 mrad was applied to the pointing angles to best center the elastic peak position from data to that of simulations at each kinematics. Note that an offset of 0.28 mrad is needed to match the carbon angles to the survey ones. The two offsets are consistent taking into account the 0.18 mrad scale uncertainty assigned in the scattering angle (discussed below). For the right arm, the survey angles are used and yielded a good ΔP peak position. Therefore, no additional offset was needed. Figures 4.5 and 4.6 show the difference in the elastic peak position from data and that of simulations after applying the angular offset and for both arms. The error bars assume random uncertainties of 0.10 mrad for the angle (see discussion below) and 0.02% for the beam energy (see section 3.4). With these uncertainties, the values of δ_P from data are in good agreement with those of simulations. In fact, the difference is zero to better than the error bars, indicating that we might be slightly overestimating the random uncertainties, but we will stick with these uncertainties to be conservative.
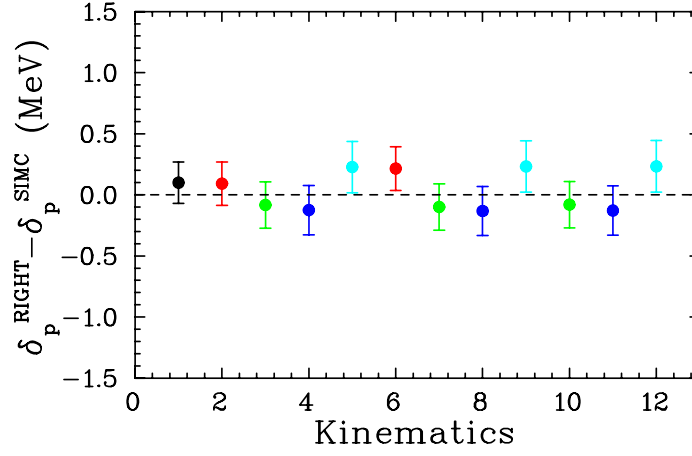
Figure 4.5: The right arm difference in the elastic peak position from data (δ_P RIGHT) and that of simulations (δ_P SIMC) after applying the angular offset. The points are sorted according to the kinematics of the left arm. Kinematics 1-5 correspond to $Q^2 = 2.64$ GeV^2, while kinematics 6-9 (10-12) correspond to 3.20 (4.10) GeV^2. For each Q^2 value, the points are sorted by ε (low to high). Note that for the right arm only the first five measurements are truly independent. The later points are repeats at the same kinematics.
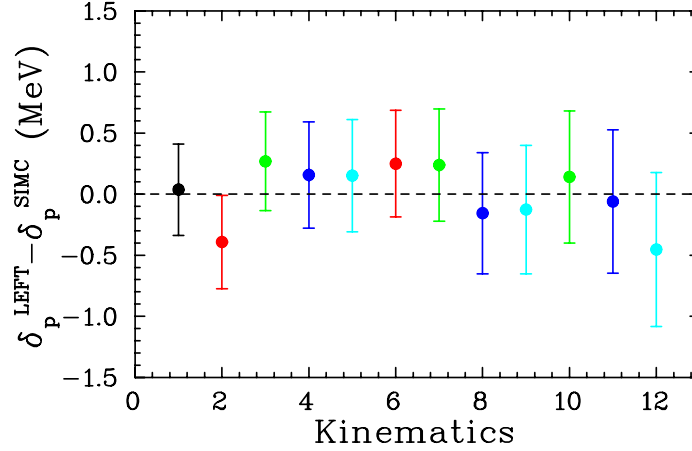
Figure 4.6: The left arm difference in the elastic peak position from data (δ_P LEFT) and that of simulations (δ_P SIMC) after applying the angular offset. Kinematics 1-5 correspond to $Q^2 = 2.64$ GeV^2, while kinematics 6-9 (10-12) correspond to 3.20 (4.10) GeV^2. For each Q^2 value, the points are sorted by ε (low to high).

A 0.10 mrad random uncertainty in the angular offset is assigned. This is based on the following contributions combined in quadrature: 0.07 mrad due to drifts in the beam angle as determined from the BPMs, ~ 0.05 mrad uncertainty that comes from the ~ 0.1 MeV uncertainties in determining the peak position, and the ~ 0.05 mrad uncertainty from the pointing determination (run to run scatter and uncertainty in determining the target position). Table 4.2 shows the Tiefenback energy and the spectrometer settings used for the left and right arms.

Kinematics	Tiefenback Energy (MeV)	θ_L (^{o})	θ_R (^{o})
o	1912.94	12.6311	58.3090
a	2260.00	22.1592	60.0700
i	2844.71	29.4590	62.0380
q	3772.80	35.1512	63.8710
l	4702.52	38.2512	64.9810
b	2260.00	12.5226	60.0700
j	2844.71	23.3896	62.0380
p	3772.80	30.4802	63.8710
m	4702.52	34.1225	64.9810
k	2844.71	12.6807	62.0380
r	3772.80	23.6586	63.8710
n	4702.52	28.3735	64.9810

Table 4.2: The Tiefenback energy and spectrometer settings used in the actual analysis of the E01-001 kinematics. The right arm spectrometer settings θ_R are the survey angles, while the left arm spectrometer settings θ_L are the angles as determined by carbon-pointing runs measurements corrected by 0.19 mrad to center the elastic peak.

A 0.18 mrad scale uncertainty in the angular offset is assigned. The scale uncertainty is determined based on the following contributions combined in quadrature: 0.13 mrad uncertainty due to uncertainty in modeling the energy loss and radiative effects on the elastic peak (if we shift the peak centers by 0.2 MeV due to error in SIMC energy loss, or small errors in the smearing we use, the angle offset varies by

0.13 mrad), 0.07 mrad uncertainty for possible beam angle offset, and 0.10 mrad uncertainty coming from the fact that a small shift in the beam energy can give a solution with the wrong angle offset (if we shift the beam energy by 0.03%, we still get decent elastic peak positions by shifting the angle by 0.1 mrad. The χ^2 is worse, but not totally unreasonable).
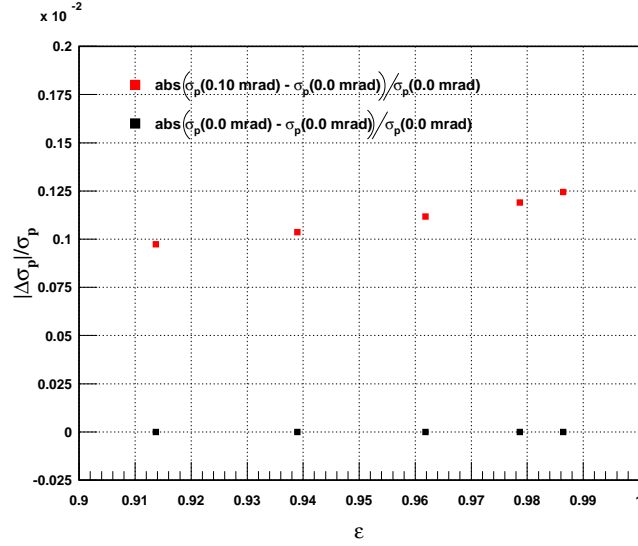
Figure 4.7: The relative difference between the right arm nominal cross sections and cross sections with a 0.10 mrad offset in the scattering angle (red squares) as a function of ε at all 5 incident energies. The black squares are the nominal cross sections relative to themselves.

In estimating the scale, random, and slope uncertainties in the sensitivity of the cross sections to a 0.10 mrad and 0.18 mrad angle offset, the same procedure described in section 3.4.2 is used. The sensitivity of the cross sections to a 0.10 mrad offset in the scattering angle has been studied. Figures 4.7 and 4.8 show the relative difference between the nominal cross sections, determined at the nominal scattering angle and energy, and the cross sections with a 0.10 mrad change in the scattering angle for the right and left arms at all kinematics. A 0.10 mrad angle fluctuation changes the cross section by (0.10-0.12)% for the right arm and (0.02-0.10)% for the left arm. Such
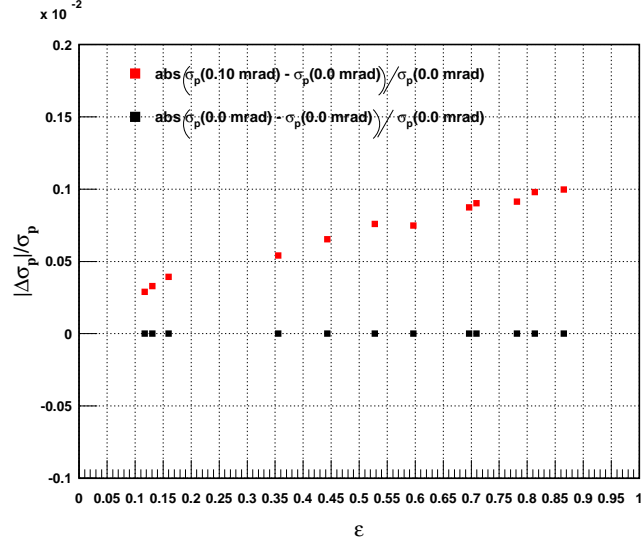
Figure 4.8: The relative difference between the left arm nominal cross sections and cross sections with a 0.10 mrad offset in the scattering angle (red squares) as a function of ε.

change in the cross sections was applied as a random uncertainty to each ε point.

Similarly, the sensitivity of the cross sections to a 0.18 mrad offset in the scattering angle has been studied. Figures 4.9 and 4.10 show the relative difference between the nominal cross sections and the cross sections with a 0.18 mrad angle offset for the right and left arms and at all kinematics. The right arm results show an average scale, random, and slope uncertainties of 0.20%, 0.02%, and 0.67%, respectively. While, the left arm results show an average scale, random, and slope uncertainties of 0.13%, 0.01%, and 0.18%, respectively.

4.5   VDC Tracking Efficiency

The VDC tracking inefficiency is defined as the fraction of good events where we do not reconstruct a track in the VDCs. It is determined by taking the fraction of the
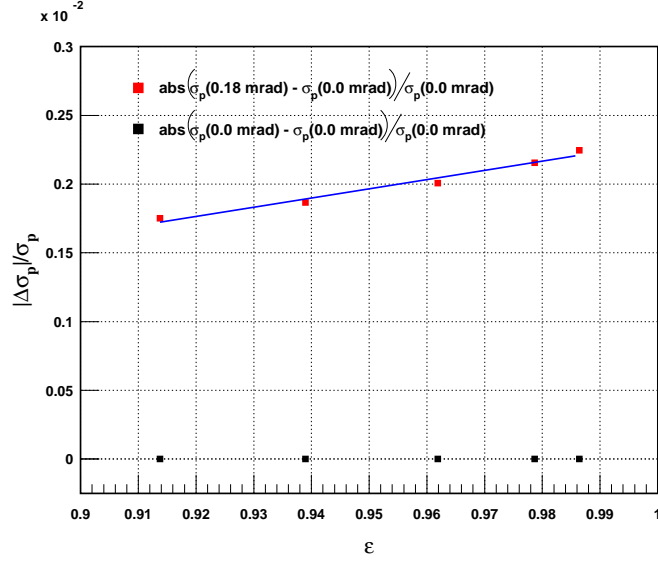
Figure 4.9: The relative difference between the right arm nominal cross sections and cross sections with a 0.18 mrad offset in the scattering angle (red squares) as a function of ε at all 5 incident energies. The solid blue line is a linear fit to the data.
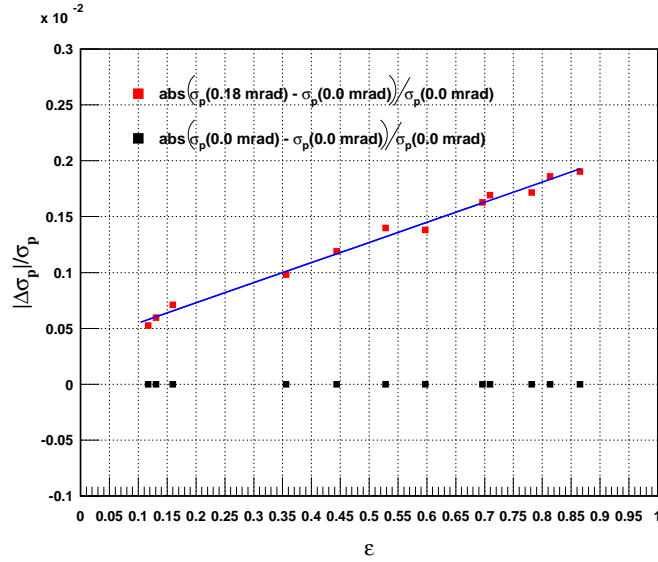
Figure 4.10: The relative difference between the left arm nominal cross sections and cross sections with a 0.18 mrad offset in the scattering angle (red squares) as a function of ε. The solid blue line is a linear fit to the data.

zero- and multiple-track events that passed through both planes of the two VDCs and caused a trigger in the scintillators planes: $(N_{zero} + N_{multiple})/N_{total}$ where N_{zero} and $N_{multiple}$ are the number of events with zero- and multiple-track, respectively, and N_{total} is the total number of good events. That in turn defines the VDC tracking efficiency ϵ_{VDC} as the fraction of one track events N_{one}/N_{total}. In the analysis of E01-001, we require only one-track events. Therefore, we reject multi-track events and correct for lost events. A good-track event is defined as a one-track event that fired both VDCs planes and was in the the fiducial area, i.e, hit the central paddles of the S_1 and S_2 scintillator planes. That requires a hit in paddle 3 or 4 of each scintillator plane. In addition, tracks with zero or many hits (hits per plane >30) are excluded. In addition on both arms, particle identification (PID) cuts using A_1 and A_2 aerogels were applied to exclude π^+. See section 4.7 for a more detailed description of the PID cuts. Figure 4.11 shows the distribution of the number of reconstructed tracks that
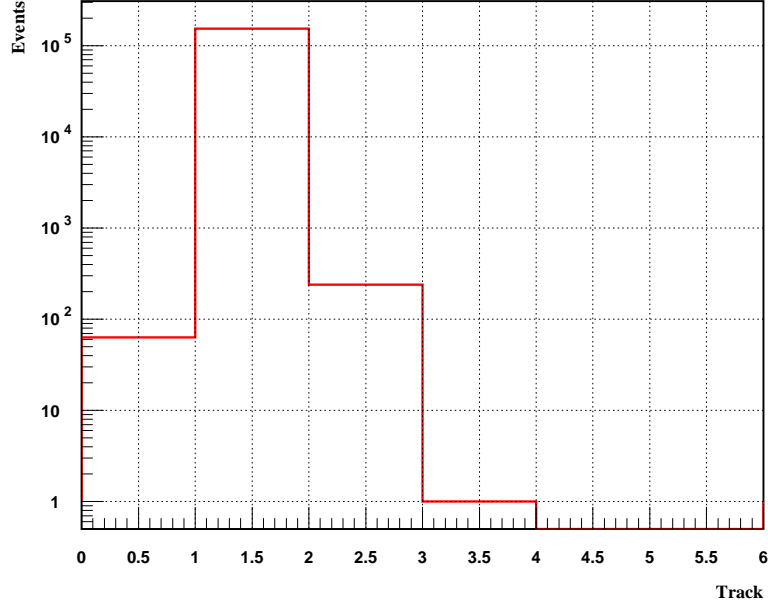
Figure 4.11: Track multiplicity in the left arm spectrometer for run 1597, kinematics i.

109

satisfy the good-track event condition defined above for the left arm spectrometer. Although events with one track are desired, events with zero- or multiple-track are also present. Table 4.3 shows the number of zero-, one-, multiple-track events, and the VDC tracking efficiency for the right and left arm spectrometers as determined for a single run. The efficiency is calculated and applied to each run separately. The zero- and multiple-track inefficiencies for the left arm are $\leq 0.21\%$ and $\leq 0.38\%$, respectively, and $\leq 0.017\%$ and $\leq 1.26\%$ for the right arm, respectively.

In order to determine the uncertainty in the VDC tracking efficiency, the average zero- and multiple-track inefficiencies for all the runs in all the kinematics were determined by applying several cuts. These cuts include: cut1 = fiducial cut, cut2 = fiducial plus no zero-hit cut, cut3 = fiducial plus no multi-hit cut, and cut4 = fiducial plus no zero-hit plus no multi-hit cut. Figures 4.12, 4.13, 4.14, and 4.15 show the average zero- and multiple-track inefficiencies as determined under these cuts for the right and left arms, respectively. For the zero-track inefficiency, Figures 4.12 and 4.14 show that cut1 and cut3 produce similar results as do cut2 and cut4. Clearly, exclusion of the no multi-hit cut does not alter the results and suggests the importance of the fiducial and no zero-hit cut applied only. Therefore, in the analysis of the E01-001, cut4 was used to determine the zero- and multiple-track inefficiencies. Clearly the zero-track inefficiency for the left arm is larger than that for the right arm and has a range of $(0.05\text{-}0.20)\%$ with Q^2 dependence but not any ε dependence. There is an estimated random or point-to-point uncertainty (fluctuation) of $\leq 0.01\%$ in the average zero-track inefficiency for both arms. Therefore, the random uncertainty will be set to 0.0%. The average zero-track inefficiency on the right arm does not have any significant ε dependence or scale offset. Therefore, a scale and slope uncertainties of 0.0% are assigned. On the other hand, a scale and slope uncertainties of 0.1% and 0.0% are assigned for the left arm.

As for the multiple-track inefficiency, Figures 4.13 and 4.15 show that the differ-

ent cuts seem to produce relatively close results. The multiple-track inefficiency for the right arm has a range of (0.60-1.30)% mainly rate dependence with an average inefficiency of $\sim 1.0\%$ and shows an ε dependence of 0.05%. If a 10% measurement is assumed, this will yield a 0.10% scale uncertainty. A slope uncertainty of 0.05%/0.07 $\approx 0.70\%$ is assigned when we consider the $\Delta\varepsilon$ range of 0.07. On the other hand, the multiple-track inefficiency for left arm has a range of (0.15-0.30)% which varies with Q^2. A scale uncertainty of $\sim 0.10\%$ will be assigned as well. The multiple-track inefficiency shows insignificant ε dependence and a slope uncertainty of 0.0% is assigned. In order to determine the random uncertainty in the multiple-track inefficiency for both arms, the average multiple-track inefficiency from all the cuts (cut1-cut4) were plotted relative to cut4 and in order of increasing ε. This was done for the average zero-track inefficiency as well. Figure 4.16 and 4.17 show the results. Again, the multiple-track inefficiency for the left arm is larger than that for the right arm and has some Q^2 dependence as well. The average multiple-track inefficiency for the right arm has on the average a random fluctuation of 0.01% (set to 0.0%), while the left arm average multiple-track inefficiency shows a random fluctuation of 0.02%.

Number of Tracks	Right Arm	Left Arm
Zero	10	63
One	198563	154028
Two	2231	240
Three	16	1
Four	0	0
Five	0	0
Total	200820	154332
Zero-track fraction (%)	0.00498	0.0408
Multiple-track fraction (%)	1.119	0.156
ϵ_{VDC}	0.988	0.998

Table 4.3: The number of zero-, one-, multiple-track events, and the VDC tracking efficiency for the right and left arm spectrometers for run number 1597, kinematics i.
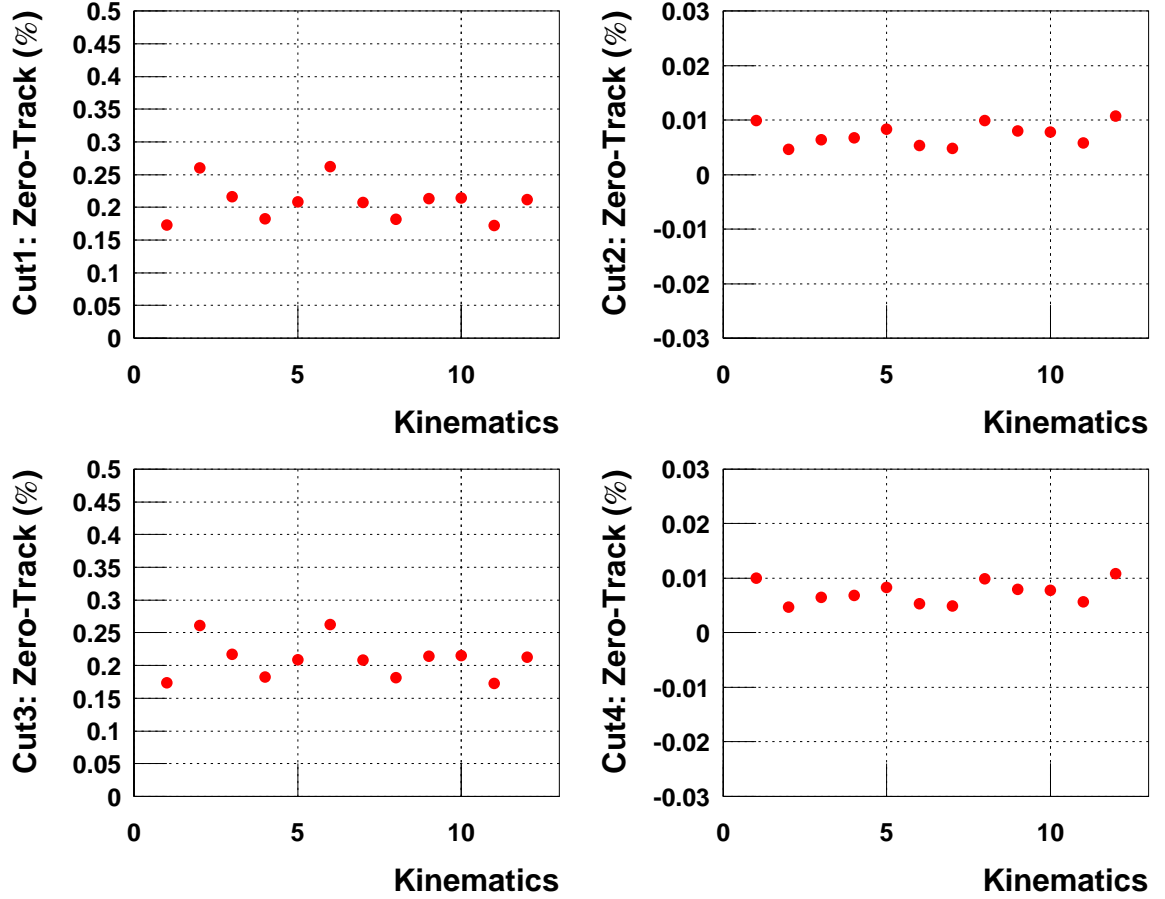
Figure 4.12: The average zero-track inefficiency for the right arm with several cuts applied plotted as a function of kinematics. The points are sorted according to the kinematics of the left arm. Kinematics 1-5 correspond to $Q^2 = 2.64$ GeV^2, while kinematics 6-9 (10-12) correspond to 3.20 (4.10) GeV^2. For each Q^2 value, the points are sorted by ε (low to high). See Table 3.1 for detail. Note that cut4 was used in the analysis.
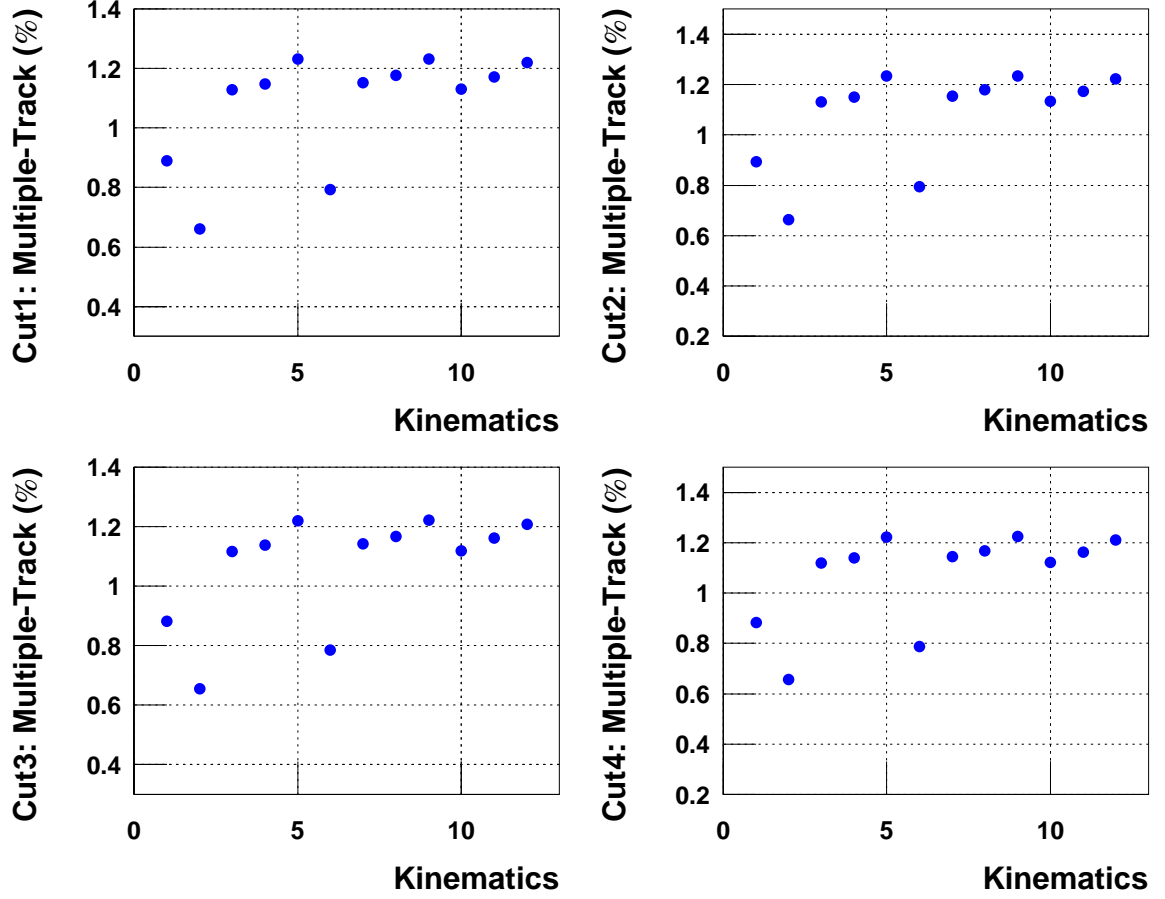
Figure 4.13: The average multiple-track inefficiency for the right arm with several cuts applied plotted as a function of kinematics. The points are sorted according to the kinematics of the left arm. Kinematics 1-5 correspond to $Q^2 = 2.64$ GeV^2, while kinematics 6-9 (10-12) correspond to 3.20 (4.10) GeV^2. For each Q^2 value, the points are sorted by ε (low to high). See Table 3.1 for detail. Note that cut4 was used in the analysis.
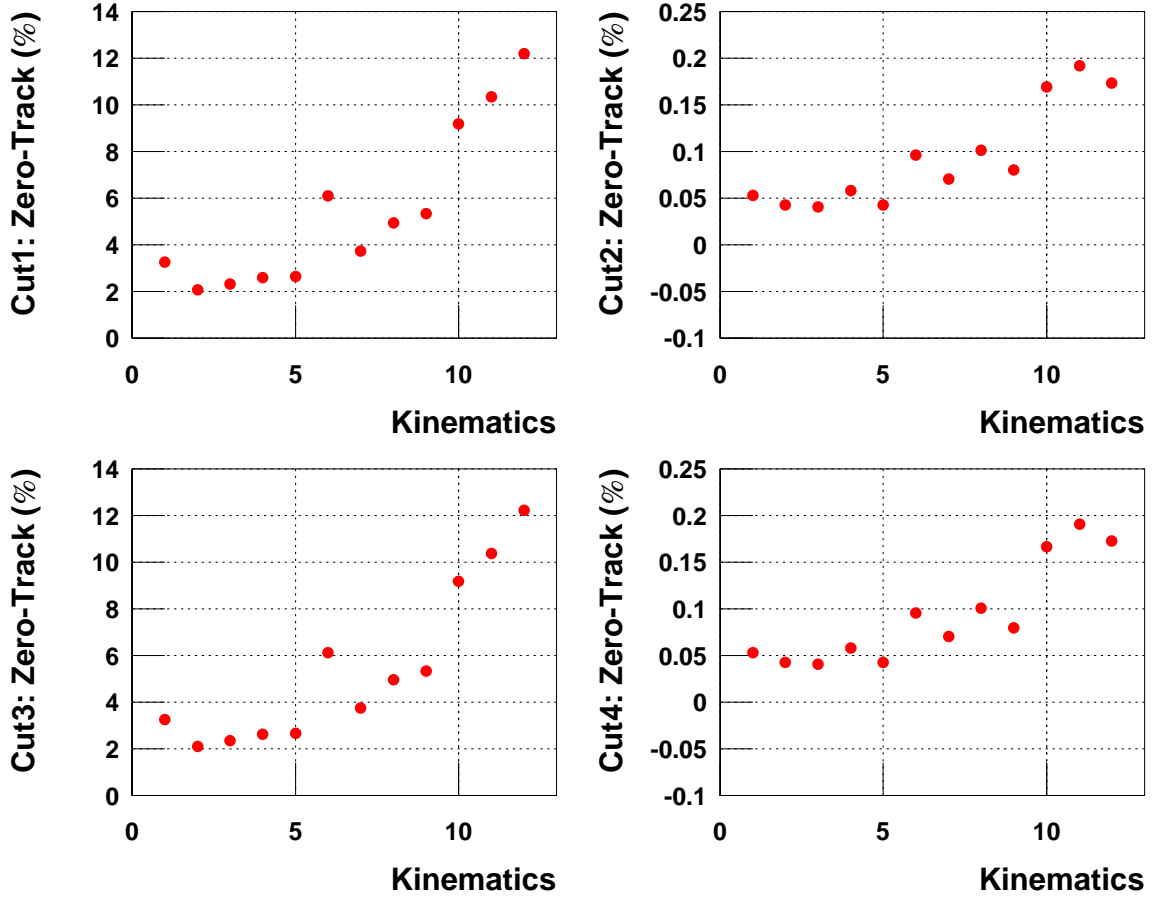
Figure 4.14: The average zero-track inefficiency for the left arm with several cuts applied plotted as a function of kinematics. Kinematics 1-5 correspond to $Q^2 = 2.64$ GeV^2, while kinematics 6-9 (10-12) correspond to 3.20 (4.10) GeV^2. For each Q^2 value, the points are sorted by ε (low to high). See Table 3.1 for detail. Note that cut4 was used in the analysis.
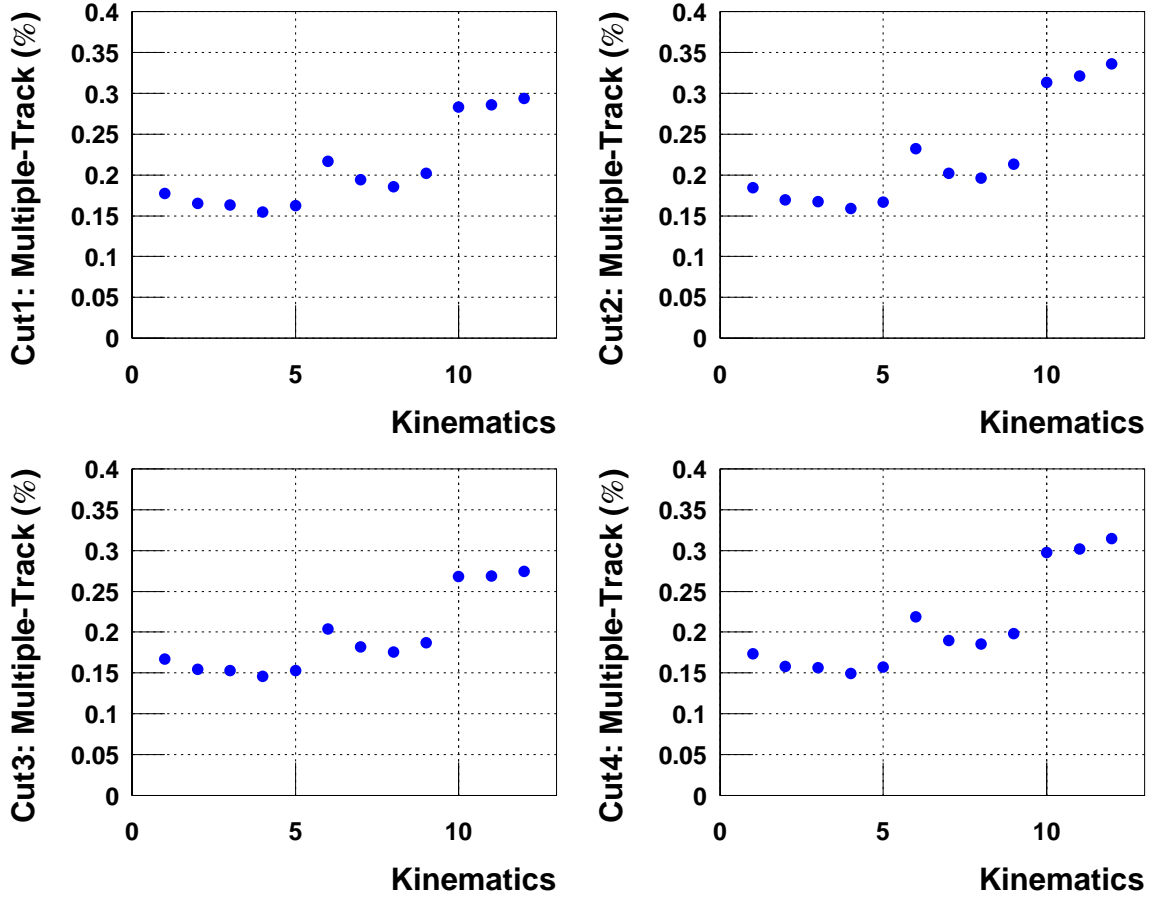
Figure 4.15: The average multiple-track inefficiency for the left arm with several cuts applied plotted as a function of kinematics. Kinematics 1-5 correspond to $Q^2 = 2.64$ GeV^2, while kinematics 6-9 (10-12) correspond to 3.20 (4.10) GeV^2. For each Q^2 value, the points are sorted by ε (low to high). See Table 3.1 for detail. Note that cut4 was used in the analysis.
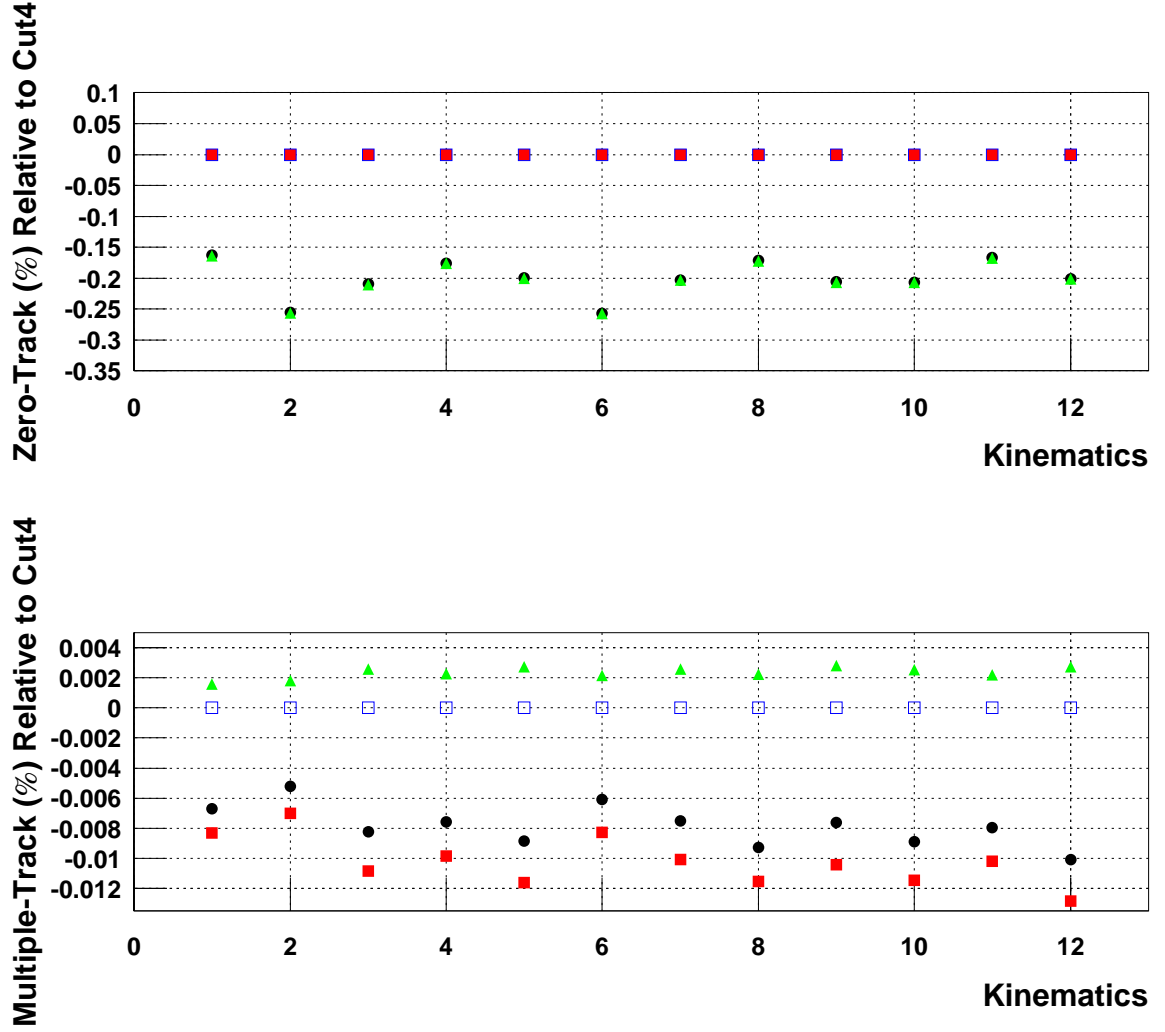
Figure 4.16: Top: The right arm average zero-track inefficiency with several cuts applied (cut1 = solid black circles, cut2 = solid red squares, cut3 = solid green triangles) relative to cut4 (open blue squares) plotted as a function of kinematics. Note that the open blue squares are the average zero-track inefficiency from cut4 relative to itself. The points are sorted according to the kinematics of the left arm. Kinematics 1-5 correspond to $Q^2 = 2.64$ GeV^2, while kinematics 6-9 (10-12) correspond to 3.20 (4.10) GeV^2. For each Q^2 value, the points are sorted by ε (low to high). See Table 3.1 for detail. Bottom: The right arm average multiple-track inefficiency with several cuts applied (cut1 = solid black circles, cut2 = solid red squares, cut3 = solid green triangles) relative to cut4 (open blue squares) plotted as a function of kinematics. The points are sorted according to the kinematics of the left arm as discussed in top caption above.
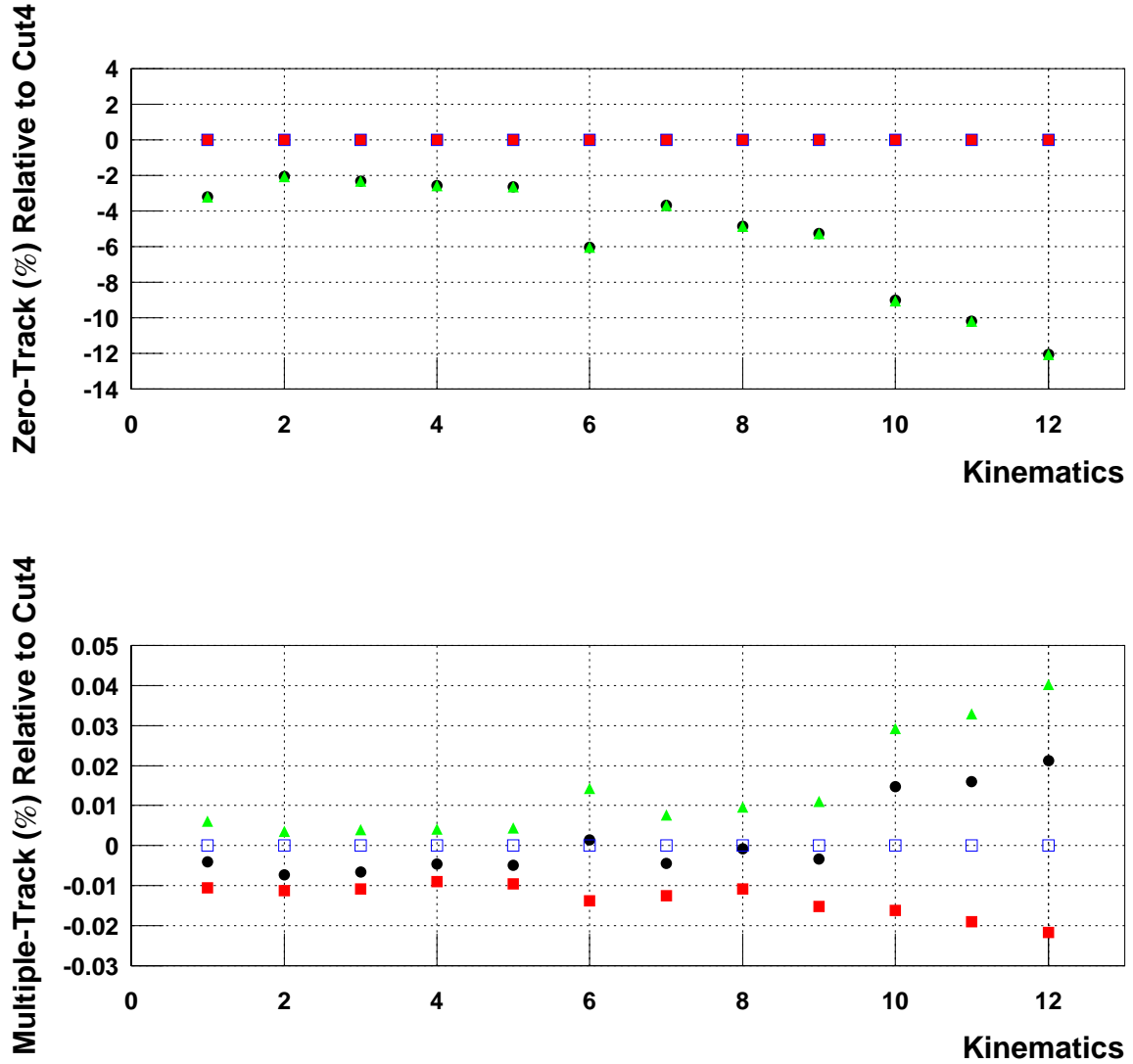
Figure 4.17: Top: The left arm average zero-track inefficiency with several cuts applied (cut1 = solid black circles, cut2 = solid red squares, cut3 = solid green triangles) relative to cut4 (open blue squares) plotted as a function of kinematics. Note that the open blue squares are the average zero-track inefficiency from cut4 relative to itself. Kinematics 1-5 correspond to $Q^2 = 2.64$ GeV^2, while kinematics 6-9 (10-12) correspond to 3.20 (4.10) GeV^2. For each Q^2 value, the points are sorted by ε (low to high). See Table 3.1 for detail. Bottom: The left arm average multiple-track inefficiency with several cuts applied (cut1 = solid black circles, cut2 = solid red squares, cut3 = solid green triangles) relative to cut4 (open blue squares) plotted as a function of kinematics. The points are sorted according to the kinematics of the left arm as discussed in top caption above.

4.5.1   VDC Hardware Cuts Inefficiency

In the previous section we discussed the VDC tracking efficiency. Even after selecting single-track event, not every reconstructed track corresponds to the true particle trajectory . A typical single-track event making an angle of 45° with the VDC surface has a multiplicity, number of hit wires in the cluster that were fired by the event, of 4-6 [81, 74]. Some of the good single-track events do not have enough hits in the VDC cluster or have noise hits not associated with the true particles. This can lead to tracks that do not reproduce the true particle trajectory. Such tracks lead to a long tails in the distribution of the reconstructed physical quantities.

In order to eliminate these long tails, we apply a VDC hardware cuts. These cuts require that the number of clusters for each VDC plane = 1, minimum number of hits per cluster in each VDC plane = 3, maximum number of hits per cluster in each VDC plane = 6. However, removing these long tails comes at the expense of loosing good events which must be accounted for. We account for such loss by multiplying the beam charge Q with the efficiency of the VDC hardware cuts ϵ_{VDCH}.

Figure 4.18 shows the inefficiency of the VDC hardware cuts applied for the right arm as a function of ε for all 5 incidents energies. This inefficiency represents the fraction of good events that were lost after applying the VDC hardware cuts to remove the long tails seen in the distribution of the reconstructed physical quantities. In determining the inefficiency, we applied a set of physics/data quality cuts to get rid of junk events (see section 5.2 for a full list of cuts applied) and the results have some cut dependence. The results show an average inefficiency of 11.35% giving $\epsilon_{VDCH} = 0.8865$. We do not expect this efficiency to depend on ε and the results are consistent with no slope. Therefore a slope uncertainty of 0.0% is assigned. The results also suggest a scale and random uncertainties of 0.5% and 0.1%, respectively, due to the dependence on the quality cuts applied.

Figure 4.19 shows the inefficiency of the VDCs hardware cuts applied as a function
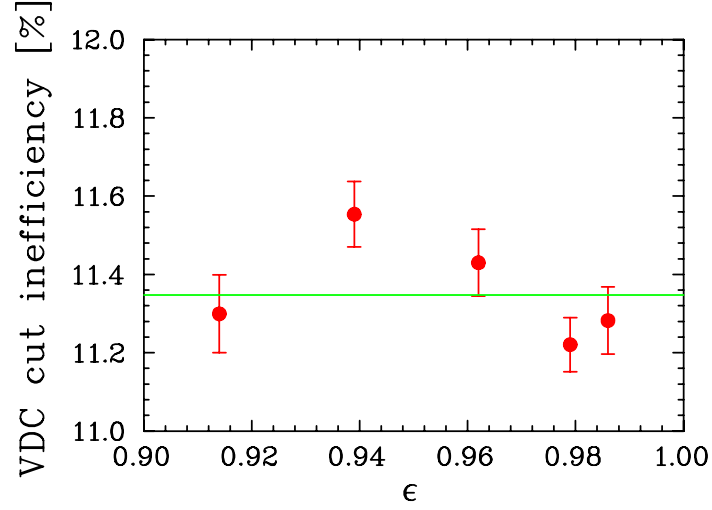
Figure 4.18: The right arm VDCs hardware cuts inefficiency as a function of ε at all 5 incident energies (solid red circles). The solid green line is the average inefficiency of 11.35% used in the analysis.
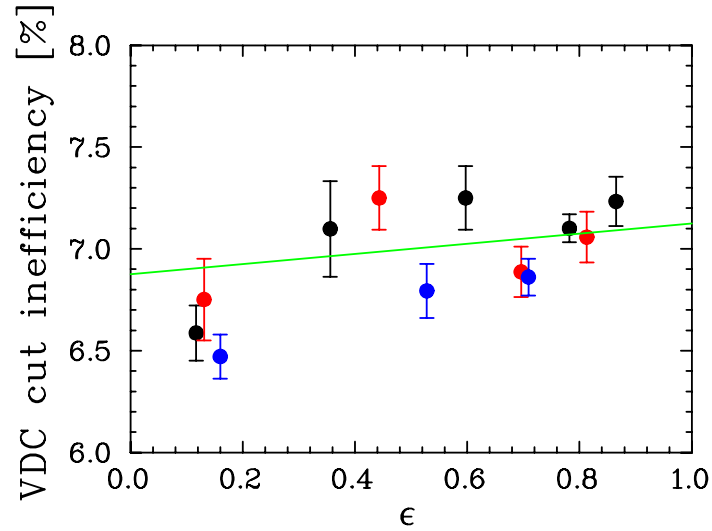
Figure 4.19: The left arm VDCs hardware cuts inefficiency as a function of ε for all kinematics. The $Q^2 = 2.64$ GeV^2 kinematics are shown as solid black circles, $Q^2 = 3.20$ GeV^2 as solid red circles, and $Q^2 = 4.10$ GeV^2 as solid blue circles. For each Q^2 value, the points are sorted by ε (low to high). The solid green line is the inefficiency we use in the analysis as given by 7.0%+0.25%(ε-0.50). See text for details.

of ε for all kinematics for the left arm. Each of the three Q^2 values gives a small slope. If we average the three slopes we get an average slope of $(0.60 \pm 0.14)\%$. However, most of the slope comes from the lowest ε point. If we remove the lowest point for each Q^2, the result is consistent with zero slope. We do not know of any reason why the efficiency of the VDCs hardware cuts should depend on ε. However, we do know of reasons why our estimate of the efficiency might have an ε dependence and that is because of the overlap of the VDCs cuts with some of our physics/data quality cuts. So we take our best set of cuts, and apply a correction that has a large enough uncertainty to be consistent with no ε dependence. Therefore, we apply a small slope with a large uncertainty of $(0.25 \pm 0.25)\%$ to try and cover both possibilities. The green line shown in Figure 4.19 is the inefficiency or correction we apply to each kinematics and is given by: $7.0\% + 0.25\%(\varepsilon\text{-}0.5)$. The results also suggest a scale and random uncertainties of 0.5% and 0.1%, respectively.

4.6   Scintillator Efficiency

The scintillator planes and trigger system are described in detail in section 3.9.2. Too little or no energy deposited by the charged particles in the scintillator paddles, the inefficient transmission of light emitted by the charged particle inside the scintillators paddles to the PMTs, or inefficiencies of the PMTs used, will result in scintillator inefficiency and hence trigger inefficiency. Trigger inefficiency is estimated by taking the fraction of good events that were not counted by the main physics trigger $T_1(T_3)$ in the right(left) arm but still caused a trigger as a $T_2(T_4)$ event type in the right(left) arm.

In calculating the scintillator efficiency, single-track events that fell inside the scintillator boundaries were kept by projecting the track to the scintillator plane and excluding events that missed the detectors. This is done by applying cuts on the VDCs

planes multiplicity and focal plane x and y axes, xfp and yfp, and angles, $xpfp$ and $ypfp$. PID cuts were used to separate π^+ background from protons. Photomultiplier hits in the left and right side of each scintillators plane were required and software solid angle cut of 1.6 msr was applied to assure that these protons within the desired spectrometer's angular acceptance.

Each scintillator plane efficiency $\epsilon_{S1,S2}$ was calculated using:

$$\epsilon_{S1,S2} = \frac{N_{1(3)} + N_5}{N_{1(3)} + N_5 + N_{2(4)}} \ , \tag{4.4}$$

where N_i $(i = 1, \cdots, 5)$ is the number of events of trigger type i corrected for prescaling factor and electronic and computer deadtimes that fell inside the scintillators boundaries as defined by Table 4.4. It must be clear that event type $T_{2(4)}$ requires a hit in S_1 or S_2 but not both. In determining the efficiency of S_1, $N_{2(4)}$ in equation (4.4) is the number of events that fired S_2 scintillator plane but not necessarily S_1. Similarly, if the efficiency of S_2 is desired, $N_{2(4)}$ will be the number of events that fired S_1 scintillator plane but not necessarily S_2.

Arm	S_1 plane boundary	S_2 plane boundary
Right	$-1.05 < xfp + 1.381xpfp < 0.90$ $-0.18 < yfp + 1.381ypfp < 0.18$	$-1.30 < xfp + 3.314xpfp < 1.00$ $-0.32 < yfp + 3.314ypfp < 0.32$
Left	$-1.05 < xfp + 1.287xpfp < 0.90$ $-0.18 < yfp + 1.287ypfp < 0.18$	$-1.30 < xfp + 3.141xpfp < 1.00$ $-0.32 < yfp + 3.141ypfp < 0.32$

Table 4.4: Track projected from the focal plane to the location of S_1 and S_2 scintillators and required to be inside of the scintillator plane. The focal plane variables used are the x and y axis coordinates, xfp and yfp (measured in meter), and angles, $xpfp$ and $ypfp$.

Figure 4.20 shows how the efficiency for the two scintillators planes ϵ_{S_1} and ϵ_{S_2}, as defined by equation (4.4), for the right arm spectrometer is calculated. Similar plots (not shown) were generated for the left arm spectrometer and for each run. The
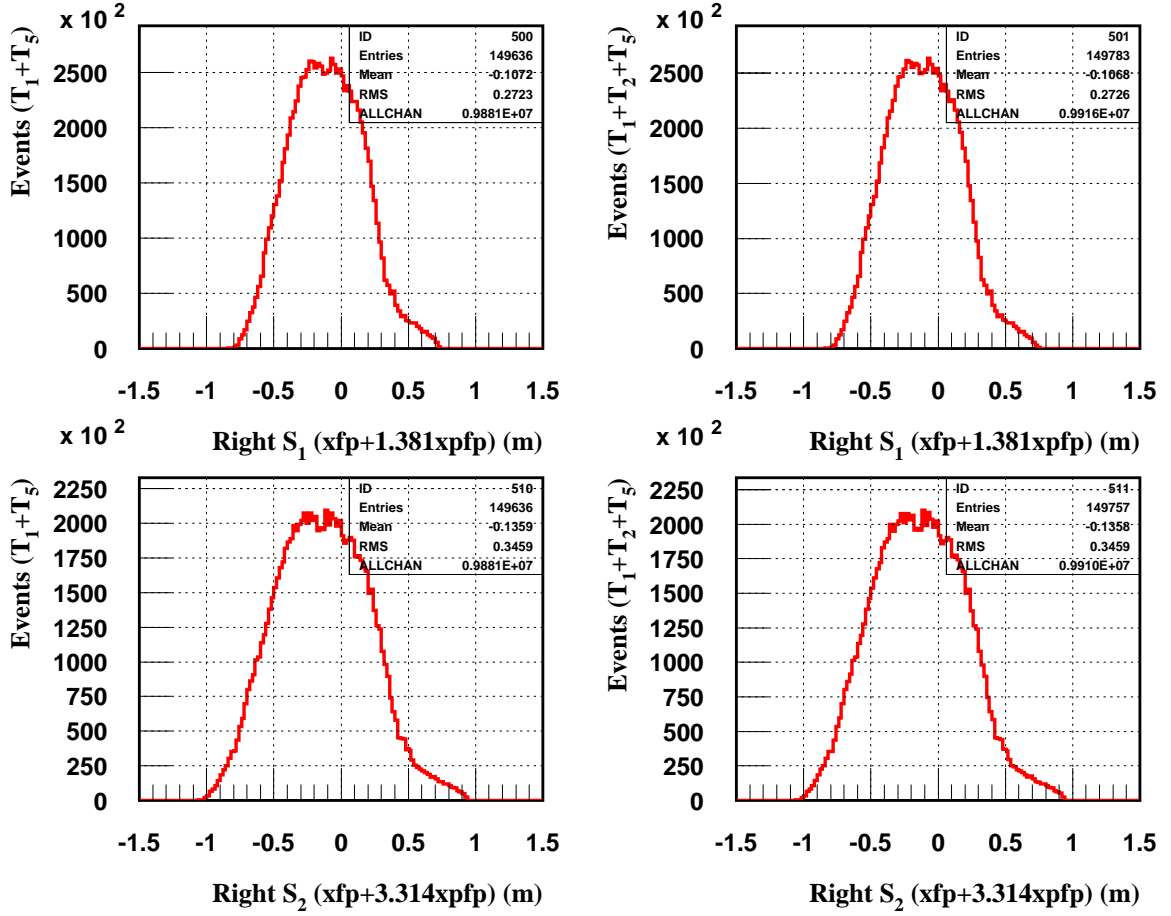
Figure 4.20: Events that fell within the scintillators boundaries as defined by Table 4.4 and needed for determination of S_1 and S_2 scintillators efficiencies for run 1597, kinematic i. Top left: Events of type $(T_1 + T_5)$ that fell within the right arm S_1 scintillator boundary as projected from the focal plane (xfp+1.381xpfp). Top right: Events of type $(T_1 + T_2 + T_5)$ that fell within the right arm S_1 scintillator boundary as projected from the focal plane (xfp+1.381xpfp). The S_1 scintillator efficiency is ratio of events in the two plots. Bottom left: Events of type $(T_1 + T_5)$ that fell within the right arm S_2 scintillator boundary as projected from the focal plane (xfp+3.314xpfp). Bottom right: Events of type $(T_1 + T_2 + T_5)$ that fell within the right arm S_2 scintillator boundary as projected from the focal plane (xfp+3.314xpfp). The S_2 scintillator efficiency is ratio of events in the two plots. Similar plots can be generated for the left arm scintillators with $T_{1(2)} \rightarrow T_{3(4)}$.

final and total scintillators efficiency for any run is the product of the two scintillators efficiencies or $\epsilon_{S_1}\epsilon_{S_2}$. Table 4.5 lists the results for ϵ_{S_1}, ϵ_{S_2}, and $\epsilon_{S_1}\epsilon_{S_2}$ for both the right and left arm spectrometers for a selected run. The scintillators efficiencies were typically $\geq 99.5\%$ and $\geq 99.6\%$ for S_1 and S_2, respectively, and were calculated and applied to each run separately.

Arm	ϵ_{S1}	ϵ_{S2}	$\epsilon_{S_1}\epsilon_{S_2}$
Right	0.996	0.997	0.994
Left	0.999	0.999	0.998

Table 4.5: The S_1 and S_2 efficiencies, ϵ_{S_1} and ϵ_{S_2}, and total scintillators efficiency, $\epsilon_{S_1}\epsilon_{S_2}$, for the right and left arm spectrometers as determined for run 1597, kinematics i.

Figures 4.21 and 4.22 show the efficiency of the two scintillators planes, ϵ_{S_1} and ϵ_{S_2}, for all the LH$_2$ and dummy data runs for both arms. For the both arms, we estimate the random and scale uncertainties to be 0.05% and 0.10%, respectively. There is not any significant ε dependence observed in the results, therefore a 0.0% slope uncertainty is assigned.

4.7   Particle Identification Efficiency

Particle identification (PID) cuts are needed in order to obtain a clean proton sample and the efficiency of these cuts must be accurately determined as well as any misidentification of other particles as protons. Two spectrometers were used, the low Q^2 spectrometer (right arm) and the high Q^2 spectrometer (left arm), and PID cuts and their efficiencies are needed for both.
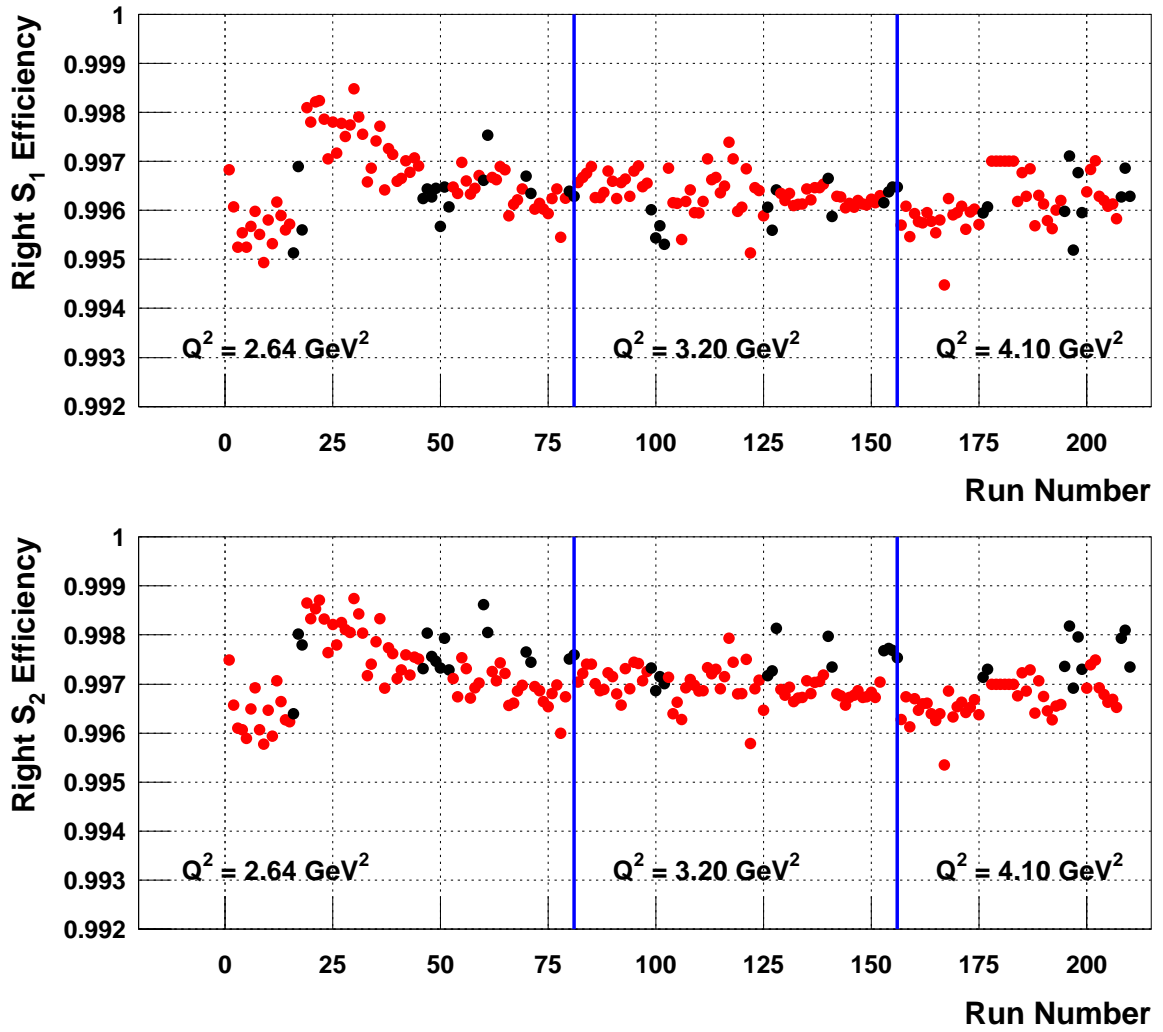
Figure 4.21: The right arm S_1 and S_2 scintillators efficiency for both LH_2 (red) and dummy (black) for all of the elastic kinematics. The efficiency is plotted as a function of run number. The run number is sorted according to the kinematics of the left arm and by increasing Q^2. For each Q^2, the kinematics are sorted by ε (low to high). See Table 3.1 for details.
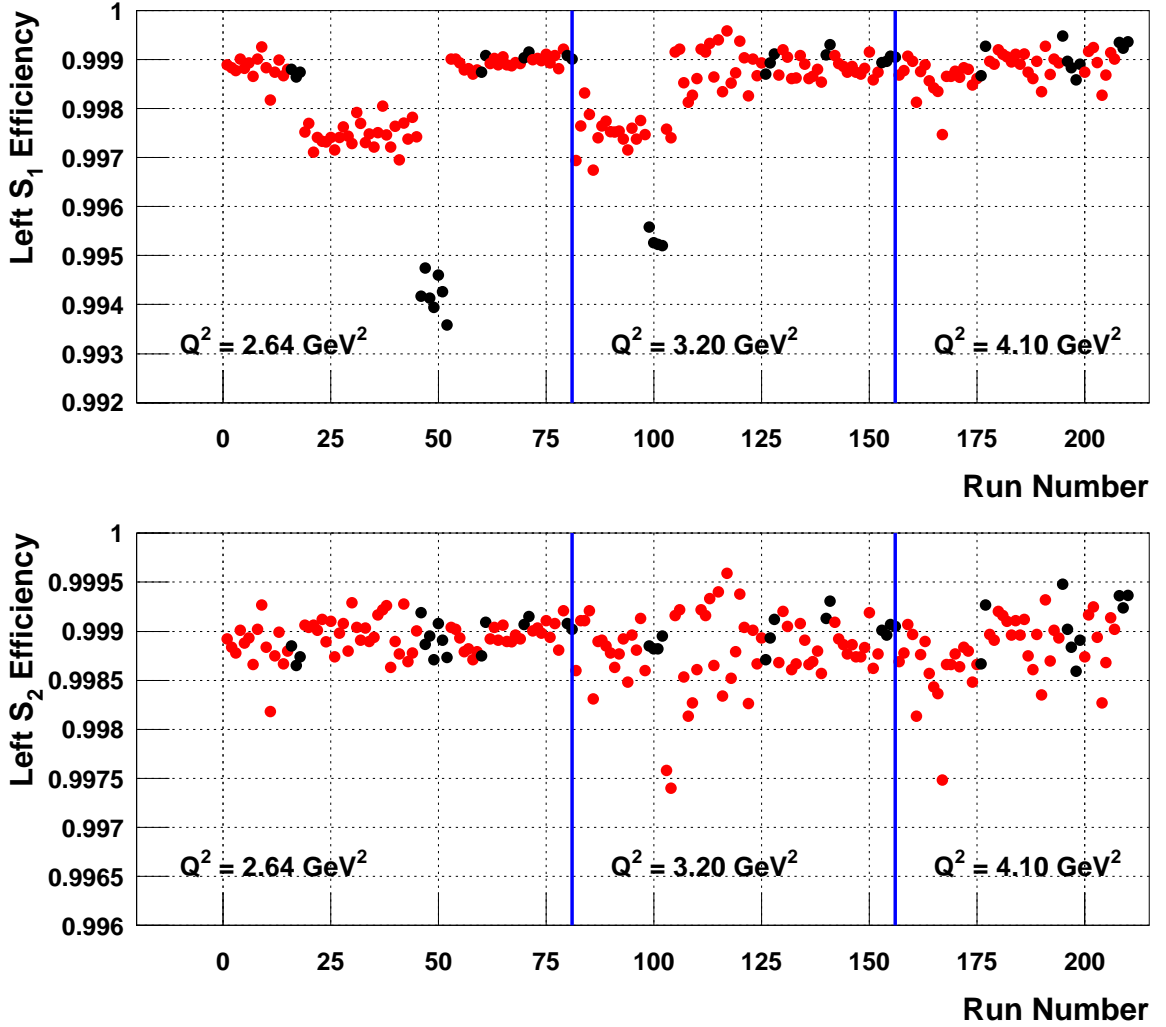
Figure 4.22: The left arm S_1 and S_2 scintillators efficiency for both LH_2 (red) and dummy (black) for all of the elastic kinematics. The efficiency is plotted as a function of run number. The run number is sorted by increasing Q^2 and for each Q^2 by ε (low to high). Kinematics a and b have lower S_1 scintillator efficiency for their LH_2 and dummy runs compared to the rest of the kinematics because one of the six paddles in the S_1 scintillator plane was tilted at the time of the run forming a gap with the adjacent paddle. Because the gap was far from the elastic acceptance, we increased the efficiency of the S_1 scintillator by 0.15% for all the runs in kinematics a and b.

4.7.1 The efficiency of the right arm β cut

In order to determine the efficiency of the β cut, ϵ_β, that we are applying, a two-dimensional plot of the sum of the ADC signals for the A_2 aerogel, A_2 ADCSUM, and the energy deposited in the first right arm scintillator, $S_1\ dE/dx$, was generated. Figure 4.23 shows such a plot. In Figure 4.23, deuterons, protons, and pions have been identified and separated from each other by applying two-dimensional cuts on A_2 ADCSUM vs S_1dE/dx. A plot of the right arm β for the three particle types was then generated using two-dimensional cuts shown in Figure 4.23. Figure 4.24
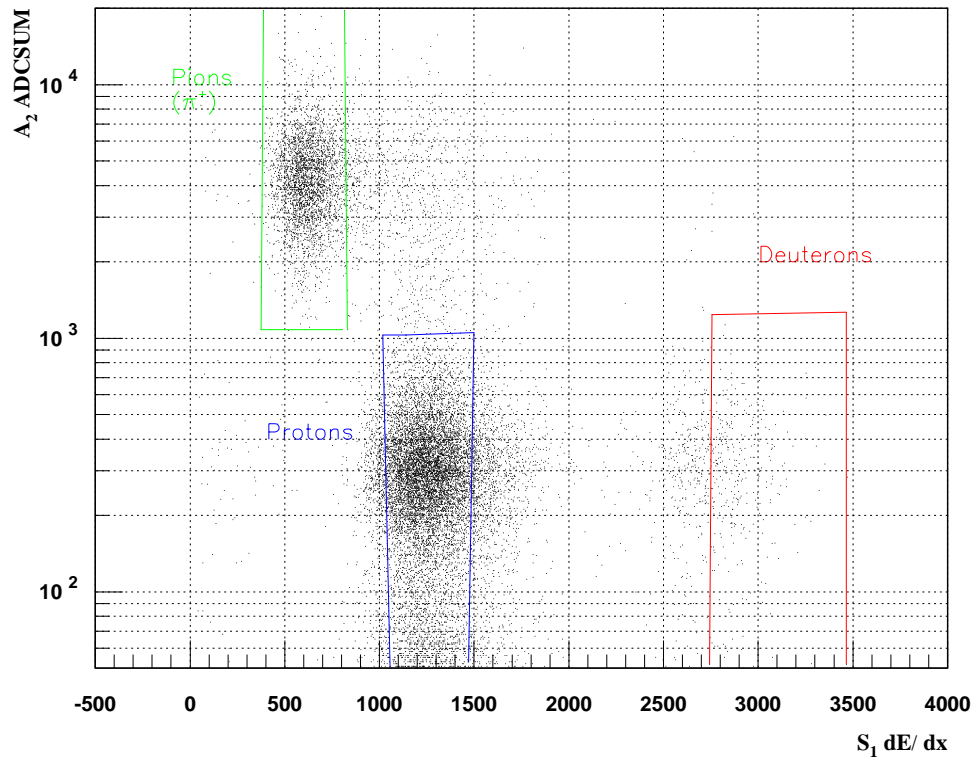
Figure 4.23: Two-dimensional plot of A_2 ADCSUM vs $S_1\ dE/dx$ for run 1730 from kinematics n. Deuterons (red boundary), protons (blue boundary), and pions (π^+) (green boundary) have been identified and separated from each other using the tight two-dimensional cuts shown. The cut for deuterons is offset to reduce proton contamination since the efficiency of this cut is not important.

shows the contribution of each particle to the full β spectrum. Pions (which usually measure 0.85< β <1.20) and deuterons (usually 0.02< β <0.45) leak into the protons area with 0.45< β <0.85. Although the tails of the distributions (tails of the pions, deuterons, and protons distributions) with β < zero and β > 1.0 are unphysical and are due to finite timing resolution of the PMTs, we account for the events in these tails when we calculate the pion and deuteron contaminations as well as the proton loss.
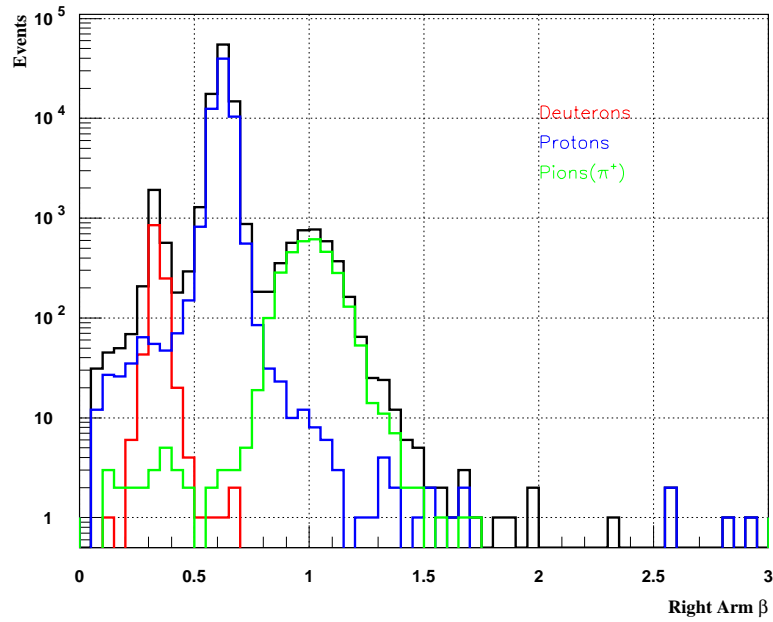
Figure 4.24: The contribution of pions (green), deuterons (red), and protons (blue) to the full right arm β spectrum (solid black line).

Based on Figure 4.24, the deuteron and pion contamination and proton loss were determined to be:

- Total number of deuterons = 1185

- Number of deuterons into protons area = 9

- Number of deuterons into pions area = 0

- Total number of pions = 3051

- Number of pions into protons area = 132

- Number of pions into deuterons area = 14

- Total number of protons = 64587

- Number of protons into pions area = 62

- Number of protons into deuterons area = 271

- Number of protons into protons area = 64089

- Deuteron Contamination = (Number of deuterons into protons area/Number of protons into protons area)×100% = (9/64089)×100% = 0.014%

- Pion Contamination = (Number of pions into protons area/Number of protons into protons area)×100% = (132/64089)×100% = 0.206%

- Proton Efficiency (ϵ_β) = (Number of protons into protons area/Total number of protons) = (64089/64587) = 0.99243

This analysis was done at all 5 incident energies and for multiple runs. Table 4.6 summarizes the results. The deuteron contamination is clearly negligible while the pion contamination is small and is negligible after applying the aerogel A_2 ADCSUM cut.

Figure 4.25 shows the deuteron contamination, pion contamination, proton loss, and the efficiency of the β cut, ϵ_β, for a multiple runs from all the kinematics. The results are plotted in order of increasing ε. The efficiency of the β cut is typically $\geq 99.2\%$ with an average random fluctuation of 0.05% and without any noticeable ε dependence.

128
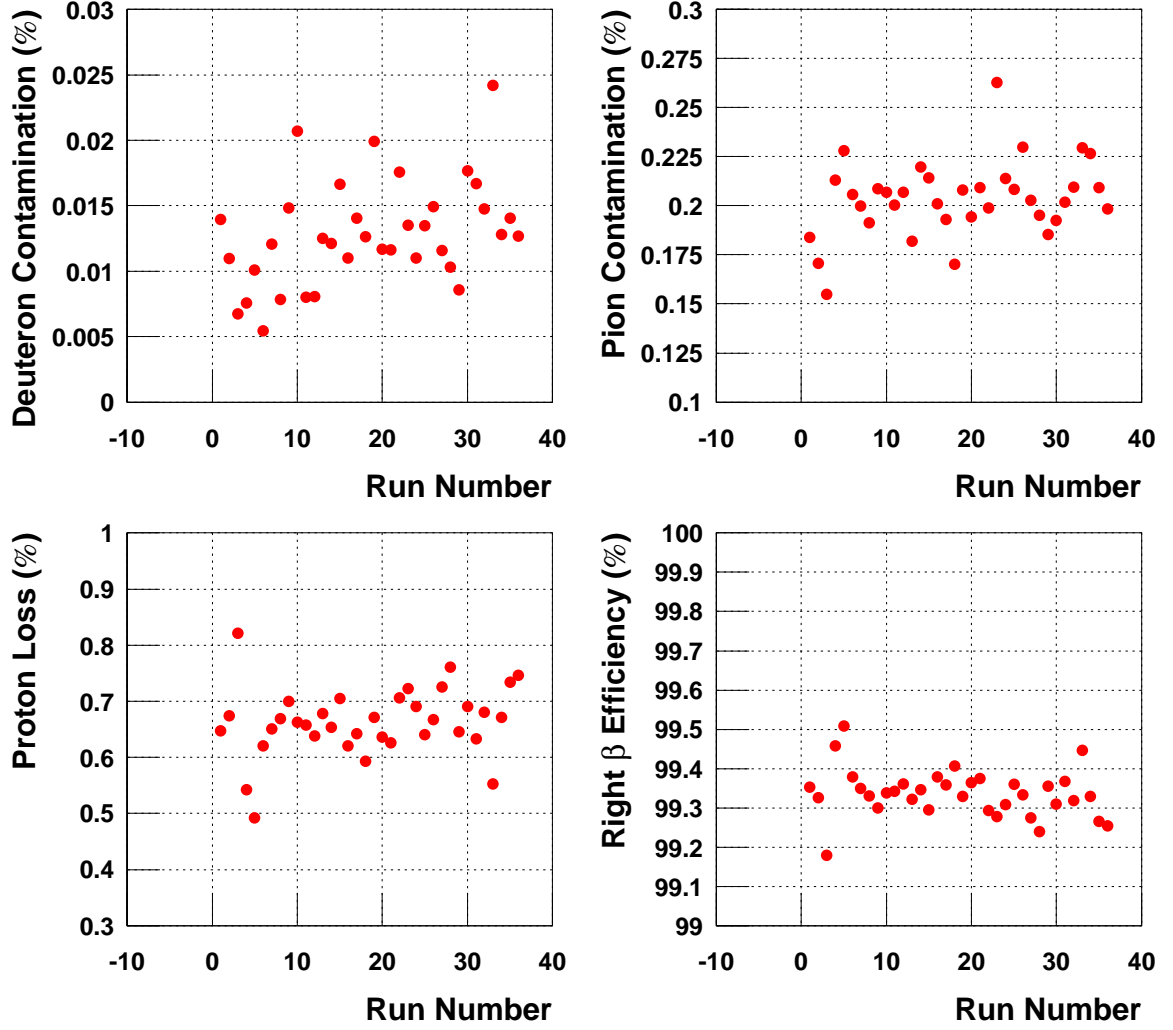
Figure 4.25: The right arm deuteron contamination (top left), pion contamination (top right), proton loss (bottom left), and efficiency of the β cut, ϵ_β, (bottom right) for sample runs from all kinematics. The points are sorted according to the kinematics of the left arm, with three runs shown for each kinematics setting. Runs 1-15 correspond to $Q^2 = 2.64$ GeV^2, while 16-27 (28-36) correspond to 3.20 (4.10) GeV^2. For each Q^2 value, the points are sorted by ε (low to high). See Table 3.1 for details.

Run Number	Incident Energy (MeV)	Maximum Deuteron Contamination (%)	Maximum Pion Contamination (%)	Proton Efficiency (ϵ_β)
1252	2260.00	0.0100	0.1886	0.9943
1653	2844.71	0.0086	0.1827	0.9932
1730	4702.52	0.0140	0.2060	0.9924
1772	1912.94	0.0000	0.2290	0.9934
1823	3772.80	0.0120	0.1937	0.9925

Table 4.6: The incident energy, deuteron contamination, pion contamination, and proton efficiency for the β cut.

Having determined the proton efficiency from the β cut, ϵ_β, we would like to determine the uncertainty in ϵ_β. Note that ϵ_β was determined assuming a pure proton sample. However, this is not the case since any pion and deuteron contamination will change the value of ϵ_β. In order to determine the size of possible pions/deuterons contamination, the β spectrum is used and the number of deuterons and pions which can be misidentified as protons determined. This was done for multiple runs at all 5 incident energies. First, the maximum number of deuterons (maximum bin content) in the deuterons area is determined. Then the maximum number of protons which leaked into the deuterons area is determined. This is an upper limit estimate and based on the content of the bin directly below the bin that contained the maximum number of deuterons. This procedure is illustrated below for run number 1250 as in Figure 4.24 and for deuterons:

- Total number of deuterons in all β spectrum = 1326.

- Maximum deuterons bin content in deuterons area = 506.

- Maximum protons into deuterons area (upper limit estimate)= 65.

- Ratio of protons to deuterons in deuterons area = α = 12.85%.

- Number of deuterons misidentified as protons $= N_{Deuterons} = \alpha$(total number of deuterons) ≈ 170.

- Total number of protons in all β spectrum $= N_{proton} = 161019$.

The same procedure used to determine the uncertainty in ϵ_β is used to determine the uncertainty in ϵ_{A_2}. Similarly the number of pions (in the pions area) which are misidentified as protons are determined. The ratio of protons to pions is estimated to be $\gamma = 0.69\%$, giving the number of pions misidentified as protons $= N_{\pi+} = \gamma$(total number of pions) ≈ 47. The scale uncertainty is determined as $(N_{Deuterons} + N_{\pi+}) \times 100\% / N_{proton} = 0.135\%$. The scale uncertainty in the efficiency of the β cut as determined at all the incident energies was fairly constant and an overall scale uncertainty of 0.15% was assigned.

4.7.2 The efficiency of the right arm A_2 Aerogel (A_2 ADC-SUM) cut

We looked at the A_2 ADCSUM for each of the five runs listed in Table 4.6. For each run, we overlayed the contribution from each of the three particles to the A_2 ADCSUM spectrum using tight cuts on β and S_1 dE/dx as shown in Table 4.7. Figure 4.26 shows the full A_2 ADCSUM spectrum and its constituents. In addition, the PID boundary cut used in the analysis is also shown.

Particle	β range	S_1 dE/dx range
Deuterons	$0.20 < \beta < 0.40$	$2500 < S_1\ dE/dx < 3500$
Protons	$0.60 < \beta < 0.70$	$1000 < S_1\ dE/dx < 1800$
Pions	$0.80 < \beta < 1.20$	$400 < S_1\ dE/dx < 900$

Table 4.7: The tight β and S_1 dE/dx cuts range.
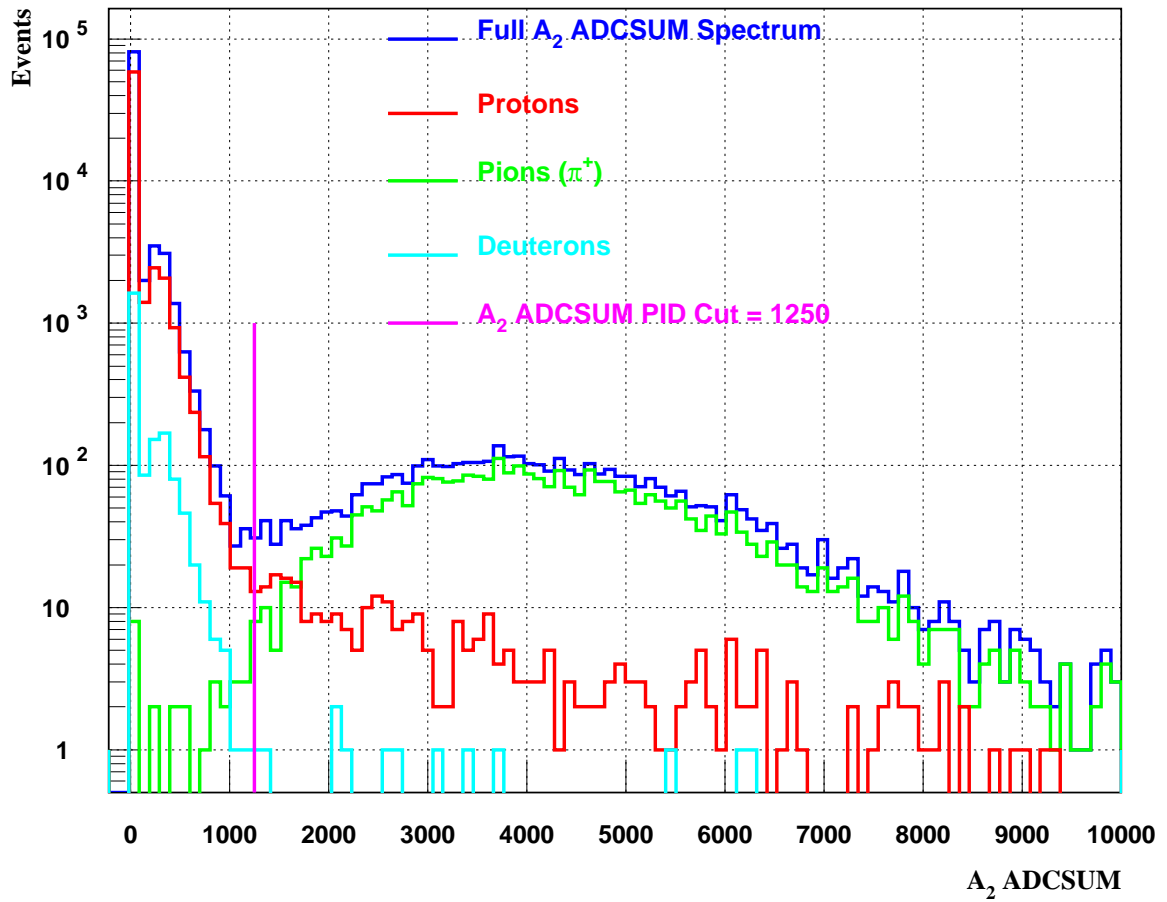
Figure 4.26: The full A_2 ADCSUM spectrum (blue). Also shown the deuterons (cyan), protons (red), and pions (π^+) (green) contribution to the full A_2 ADCSUM signal for run 1730 from kinematics n. The magenta line at A_2 ADCSUM = 1250 is the PID cut used.

It can be seen that some of the protons leak into the pion area, A_2 ADCSUM > 1250. Similarly, some pions make it into the proton region, A_2 ADCSUM < 1250. Only events with A_2 ADCSUM < 1250 are kept knowing that these good protons are definitely contaminated with some pions and deuterons while events with A_2 ADCSUM > 1250 will be rejected with some good protons lost.

The contamination of pions and the protons efficiency were determined for the data shown in Figure 4.26 as the following:

- Total Protons = 66503

- Protons greater than 1250 = 322

- Protons less than 1250 = 66181

- Total Pions = 3208

- Pions greater than 1250 = 3176

- Pions less than 1250 = 32

- Pion Contamination = (Number of pions less than 1250/Number of protons less than 1250)×100% = (32/66181)×100% = 0.05%

- Proton Efficiency (ϵ_{A_2}) = (Number of protons less than 1250/Total number of protons) = (66181/66503) = 0.99516

Similar analyses were done on runs taken at the other four incident energies. Table 4.8 summarizes the results. The final proton efficiency for each of the 5 ε points is defined as the product of the proton efficiency as determined from the β cut and the proton efficiency as determined from the A_2 ADCSUM cut or $\epsilon_\beta \epsilon_{A_2}$. As can be seen from Table 4.9, the final proton efficiency as determined for all of the 5 ε points is fairly constant as expected since all data are taken at a fixed proton momentum. The

particle identification efficiency, ϵ_{PID}, for the right arm is taken as the product of the average value of ϵ_β and ϵ_{A_2} or $\epsilon_{PID} = <\epsilon_\beta><\epsilon_{A_2}> = 0.9886$. Table 4.9 summarizes the results. It can be seen from Table 4.8 that the pion contamination is $< 0.1\%$ and can be reduced by applying the β cut. Such contamination can be reduced further by kinematics cuts and endcaps subtraction and it is taken to be negligible in the analysis.

Run Number	Incident Energy (MeV)	Pion Contamination (%)	Proton Efficiency (ϵ_{A_2})
1252	2260.00	0.0410	0.9960
1653	2844.71	0.0353	0.9950
1730	4702.52	0.0500	0.9952
1772	1912.94	0.0404	0.9960
1823	3772.80	0.0397	0.9950

Table 4.8: The pion contamination and proton efficiency as determined using the A_2 ADCSUM cut.

Figure 4.27 shows the deuteron contamination, pion contamination, proton loss, and the efficiency of the A_2 ADCSUM cut, ϵ_{A_2}, for multiple runs from all the kinematics. Again, the results are plotted in order of increasing ε and the efficiency of the A_2 ADCSUM cut is typically $\geq 99.4\%$ with an average random fluctuation of 0.05% and without any significant ε dependence. Similarly, and based on the same procedure used earlier with the β cut efficiency, the scale offset uncertainty was determined by looking at the A_2 ADCSUM spectrum and determining the number of deuterons and pions which can be misidentified as protons. The scale uncertainty in the efficiency of the A_2 ADCSUM cut as determined at all the incident energies was fairly close and an overall scale uncertainty of 0.25% was assigned. Therefore, a scale uncertainty of $\sim 0.30\%$ (adding in quadrature the scale uncertainty from ϵ_β and ϵ_{A_2}) on the right arm particle identification efficiency ϵ_{PID} is assigned.
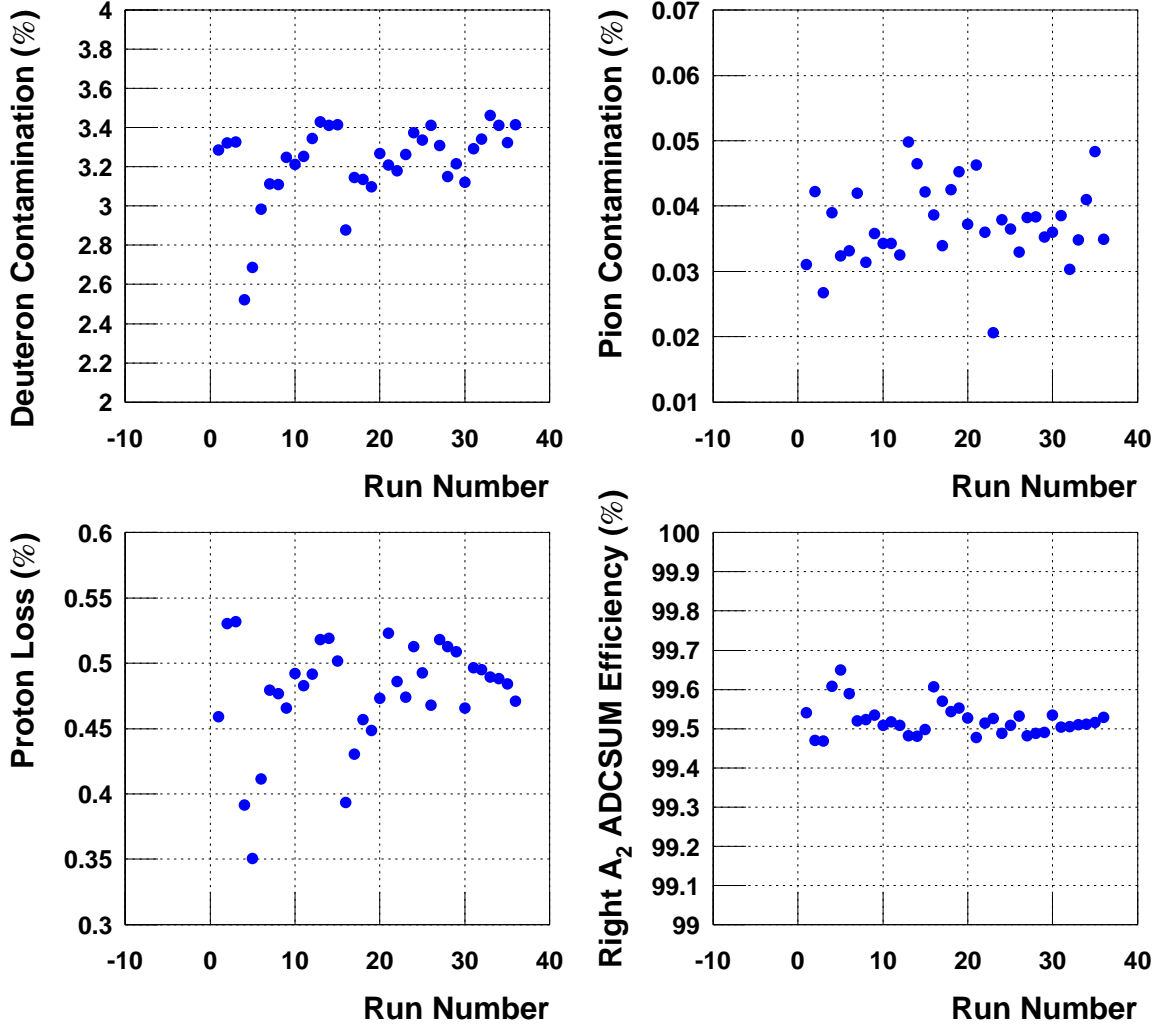
Figure 4.27: The right arm deuteron contamination (top left), pion contamination (top right), proton loss (bottom left), and efficiency of the A_2 ADCSUM cut, ϵ_{A_2}, (bottom right) for sample runs from all kinematics. The points are sorted according to the kinematics of the left arm, with three runs shown for each kinematics setting. Runs 1-15 correspond to $Q^2 = 2.64$ GeV^2, while 16-27 (28-36) correspond to 3.20 (4.10) GeV^2. For each Q^2 value, the points are sorted by ε (low to high). See Table 3.1 for details.

Run Number	Energy (MeV)	Proton Efficiency ϵ_β	Proton Efficiency ϵ_{A_2}	Final Proton Efficiency $\epsilon_\beta \epsilon_{A_2}$
1252	2260.00	0.9943	0.9960	0.9903
1653	2844.71	0.9932	0.9950	0.9882
1730	4702.52	0.9924	0.9952	0.9876
1772	1912.94	0.9934	0.9960	0.9894
1823	3772.80	0.9925	0.9950	0.9875
		$< \epsilon_\beta > = 0.9932$	$< \epsilon_{A_2} > = 0.9954$	$\epsilon_{PID} = 0.9886$

Table 4.9: The final proton efficiency as determined from the efficiency of the β and A_2 ADCSUM cuts.

4.7.3 The efficiency of the left arm A_1 Aerogel (A_1 ADCSUM) cut

Understanding the PID cuts and efficiencies for the left arm is not as straightforward as it is for the right arm. In the right arm, we had a good separation of particles using β, dE/dx, and the A_2 ADCSUM cuts. For the left arm, using the A_1 aerogel to separate the protons from pions works well, however, the β cut cannot be used because at such high Q^2 protons and pions have almost the same value for β.

The coincidence runs with protons in the left spectrometer and electrons in the right spectrometer were used to generate a pure proton spectrum. First, all the runs in each of the three coincidence kinematics were added. A plot of $\log_{10}(A_1)$ for each coincidence kinematics was generated. For simplicity, I will refer to $\log_{10}(A_1)$ by A_1 ADCSUM throughout this section. The total number of events under the A_1 ADCSUM spectrum as well as the number below and above A_1 ADCSUM = 2.544, which is the PID cut used for A_1 ADCSUM and is represented by the blue line in Figure 4.28, was determined for pure proton sample. A pure proton sample was generated by applying cuts on the elastic peak ΔP and/or y-coordinate of the extended target length y_{tg}. The results were insensitive to the exact cuts applied.

This allowed for determination of the fraction of protons (proton inefficiency) that leaked into A_1 ADCSUM > 2.544 which was fairly constant regardless of the various cuts applied. The two $Q^2 = 2.64$ GeV^2 spectra yield consistent proton inefficiencies, $(1.037\pm0.029)\%$ and $(1.030\pm0.013)\%$, while the $Q^2 = 4.1$ GeV^2 has a higher proton inefficiency of $(1.940\pm0.054)\%$. Figure 4.28 shows the A_1 ADCSUM spectrum for kinematics coin1 (see Table 3.1). We do not have any coincidence kinematics with $Q^2 = 3.2$ GeV^2 to extract clean proton sample. Instead, we take the A_1 ADCSUM spectrum for each of the kinematics at this Q^2 value, and get clean proton sample by applying kinematics cuts on the elastic peak ΔP, $-15.5< \Delta P <30.5$ MeV, and y_{tg}, $-0.0044< y_{tg} <-0.001$ m, to eliminate the endcaps contribution. The same procedure applied above was used and gave a value of $(1.550\pm0.049)\%$ for the proton inefficiency.
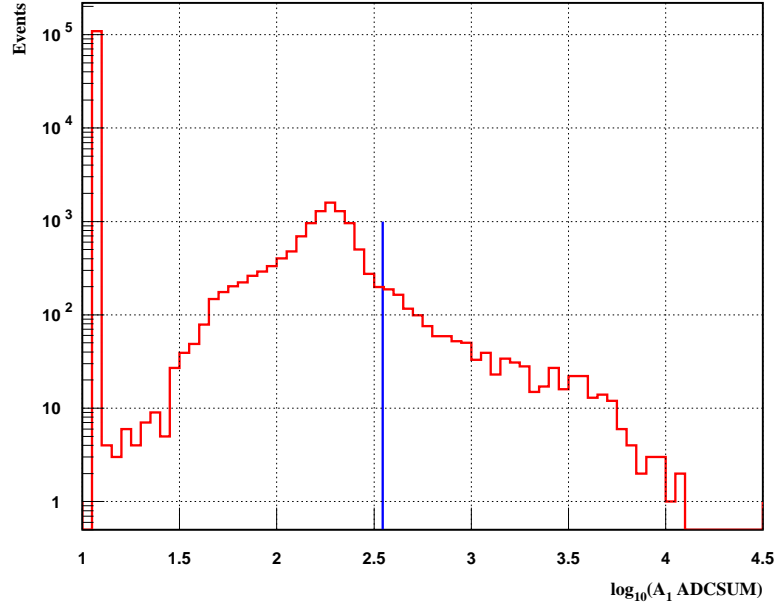
Figure 4.28: The A_1 ADCSUM spectrum for a pure proton sample from coincidence kinematics coin1. The blue line is the PID cut used.

We also need to determine the π^+ contamination. To do that, we need the number of π^+ and fraction of π^+ that are identified as protons (π^+ efficiency). We compared
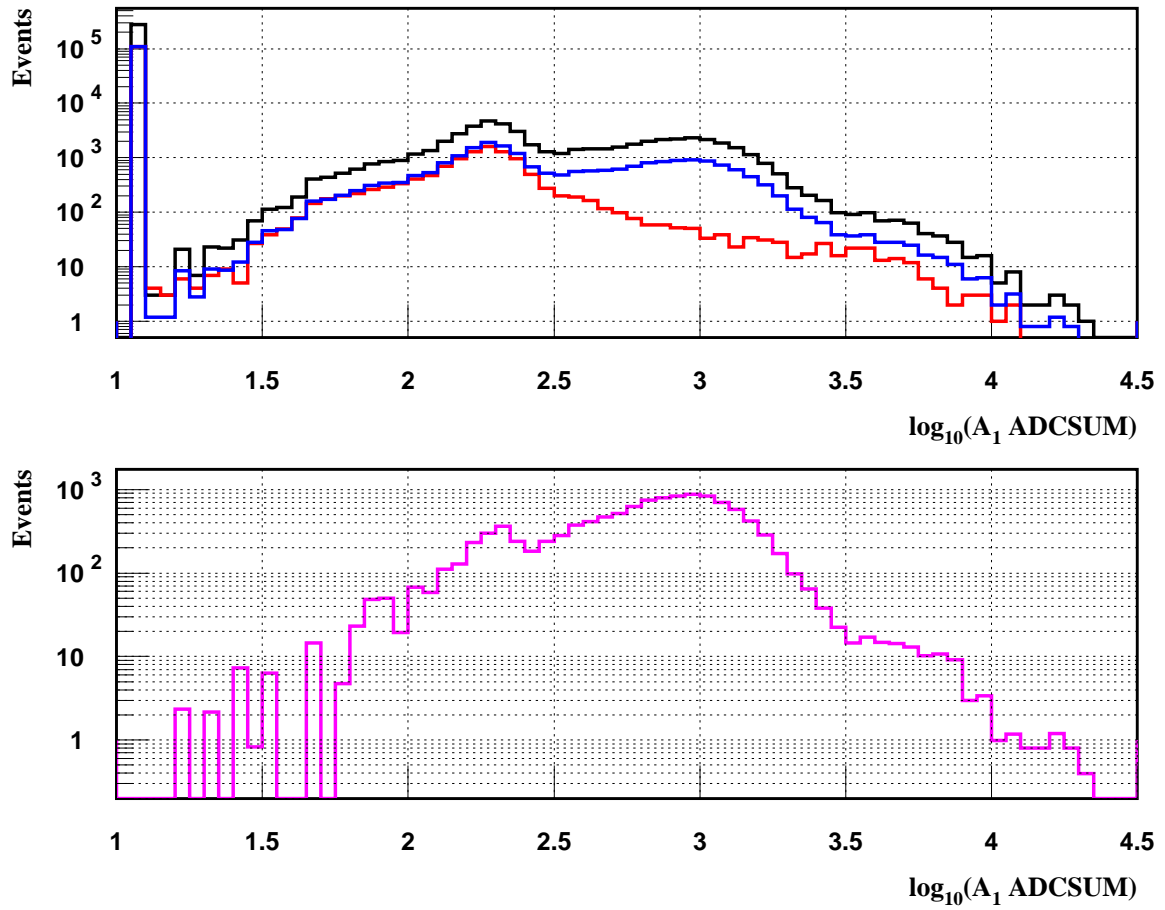
Figure 4.29: The A_1 ADCSUM spectra from singles kinematics n (top black), coincidence kinematics coin1 (top red), scaled kinematics n (top blue). The difference between the A_1 ADCSUM spectrum from the scaled kinematics n and the coin1 spectrum (blue minus red) is the pions spectrum (bottom magenta).

the A_1 ADCSUM spectrum from trigger type T_3 events (LH$_2$ singles events, which include both protons and π^+) with that of the trigger type T_5 events (LH$_2$ coincidence events, which have only protons). The difference in the spectra should represent the A_1 ADCSUM spectrum for the background π^+. When we compare the two A_1 ADCSUM spectra, we scale the A_1 ADCSUM spectrum for the singles events so that the two peaks match. Figure 4.29 illustrates this procedure where the A_1 ADCSUM spectrum with trigger type T_3 events is compared with that of trigger type T_5 events. The peak of the A_1 ADCSUM spectrum from singles was scaled to match that of coincidence. The difference between the A_1 ADCSUM spectrum from the scaled singles and the coincidence spectrum should represent the A_1 ADCSUM spectrum for pions. The total number of pions under the A_1 ADCSUM spectrum and the number of pions below and above A_1 ADCSUM $= 2.544$ are determined. The pion efficiency is defined as (number of pions below A_1 ADCSUM $= 2.544$)/(total number of pions).

Having determined the pion efficiency and proton inefficiency, the pion contamination is then calculated for each kinematics based on the A_1 ADCSUM spectrum and without applying any kinematics cuts or subtracting off the yield from the aluminum endcaps using the following procedure:

- Total number of protons $\approx$ number of events < 2.544.

- Total number of pions $\approx$ number of events > 2.544 - (total number of protons)$\times$ (proton inefficiency).

- Number of pions $< 2.544 =$ (pion efficiency)$\times$(total number of pions).

- Pion contamination $=$ (number of pions < 2.544)/(total number of protons).

For the proton inefficiency we considered the average weight of $(1.031\pm0.012)\%$ for $Q^2 = 2.64$ GeV^2, while for $Q^2 = 4.10$ GeV^2, a value of 1.88% was used. For $Q^2 =$

3.20 GeV^2, the average value of the proton inefficiency for $Q^2 = 2.64$ and 4.10 GeV^2 or 1.45% was finally used. Figure 4.30 shows the results for the proton inefficiency as determined by applying cuts on the elastic peak ΔP and y_{tg} for multiple runs selected at the three Q^2 values. For $Q^2 = 2.64$ GeV^2, the proton inefficiency seems to have, on the average, a random fluctuation and scale offset uncertainties of $\leq 0.1\%$ each, and no significant ε dependence. For $Q^2 = 3.20$ GeV^2, the proton inefficiency shows, on the average, a random fluctuation and scale offset uncertainties of $\leq 0.1\%$ and (0.10-0.20)% respectively, and does not show any significant ε dependence based on the data centered around the 1.5% proton inefficiency. Finally, for $Q^2 = 4.10$ GeV^2, the proton inefficiency shows a random fluctuation and scale offset uncertainties of $\leq 0.1\%$ and 0.10% respectively, and does not show any significant ε dependence. Therefore, and mainly based on the results of the $Q^2 = 3.20$ GeV^2 point, a scale, random, and slope uncertainties of 0.20%, 0.10%, and 0.0%, respectively, will be assigned for the A_1 PID efficiency at all three Q^2 points.

To estimate the pion contamination, we also need the pion efficiency. We take the worst case estimate to give a conservative limit on the pion contamination. The pion efficiency for $Q^2 = 2.64$ and 4.10 GeV^2 was found to be $(4.230\pm1.32)\%$ or 5.5% as a worst case (defined as the maximum value) and $(8.935\pm1.93)\%$ or 11% as a worst case, respectively. For $Q^2 = 3.20$ GeV^2, pion efficiency value of 11% was used as a worst case. Table 4.10 summarizes the results for the pion efficiency, proton inefficiency, pion contamination at the three Q^2 values. The proton efficiency ϵ_{A_1}, ϵ_{A_1} $= 1.0 -$ proton inefficiency, or the efficiency of the A_1 ADCSUM cut is also listed. The pion contamination is always $\leq 1.0\%$. Applying kinematics cuts and subtracting the target endcaps reduces the pions contaminations as most of the pions are generated by bremsstrahlung scattering in the endcaps. Thus, pion contamination in the final results, after the dummy subtraction, is always $\leq 0.1\%$.
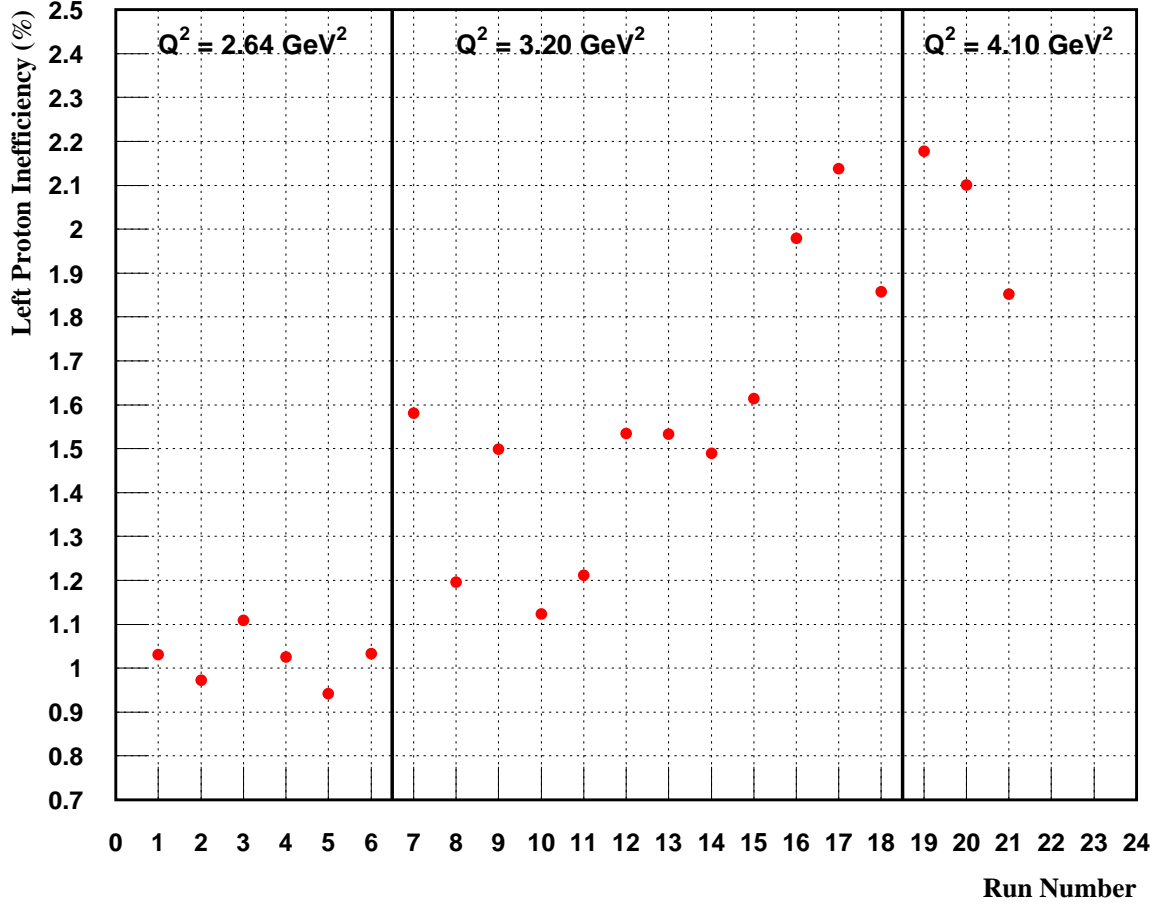
Figure 4.30: The left arm proton inefficiency for sample runs. Runs 1-6 correspond to the two coincidence kinematics with $Q^2 = 2.64$ GeV^2, 7-18 correspond to singles kinematics with $Q^2 = 3.20$ GeV^2, and 19-21 correspond to coincidence kinematics with $Q^2 = 4.10$ GeV^2. For each Q^2 value, the points are sorted by ε (low to high). See Table 3.1 for details. Note that for $Q^2 = 3.20$ GeV^2, we do not have a direct measurements, and so the scatter of the results shown in the plot is due to uncertainty in the procedure used rather than an actual variation in the proton inefficiency.

Kinematics	Q^2 (GeV^2) (%)	Pion Efficiency (%)	Proton Inefficiency (%)	Pion Contamination (%)	Proton Efficiency (ϵ_{A_1})
o	2.64	5.5	1.02	1.012E-02	0.9898
a	2.64	5.5	1.02	1.590E-02	0.9898
i	2.64	5.5	1.02	1.585E-01	0.9898
q	2.64	5.5	1.02	2.230E-01	0.9898
l	2.64	5.5	1.02	2.155E-01	0.9898
b	3.20	11.0	1.45	9.153E-02	0.9855
j	3.20	11.0	1.45	3.100E-01	0.9855
p	3.20	11.0	1.45	6.216E-01	0.9855
m	3.20	11.0	1.45	6.098E-01	0.9855
k	4.10	11.0	1.88	7.630E-02	0.9812
r	4.10	11.0	1.88	7.944E-01	0.9812
n	4.10	11.0	1.88	8.065E-01	0.9812

Table 4.10: The pion efficiency as determined using the A_1 ADCSUM cut. In addition, the proton inefficiency, pion contamination, and proton efficiency are also listed.

4.8   Proton Absorption

Once the protons are struck, they have to travel through material in the target, spectrometer, and the detector stack before they can cause a trigger in the scintillators. While traveling, some protons undergo nuclear interaction in these materials and hence get absorbed or scattered. Such loss due to the nuclear interaction is called nuclear absorption. In order to determine the proton absorption for each arm, we have to account for all the target materials the protons have to pass through on their way to the scintillators. Also the thickness [67, 86, 87, 88, 89] and density of each absorber [90, 91, 86, 87], and the mean free path between nuclear collision $\bar{\lambda}$ (effective absorption length) are needed in order to calculate the absorption.

To determine $\bar{\lambda}$, the mean free path between nuclear collision (total interaction length), λ_T, and the mean free path between inelastic interactions (inelastic interaction length), λ_I, must be known [90, 91] . In the analysis of the E01-001 experiment, $\bar{\lambda}$

was determined using two different definitions. The first definition, $\bar{\lambda}$ is estimated as $2\lambda_T\lambda_I/(\lambda_T + \lambda_I)$ assuming that half of the elastic and inelastic scattering contribute to the absorption. The second definition, $\bar{\lambda}$ is estimated as the average of two lengths or $(\lambda_T + \lambda_I)/2$ since we cannot determine exactly the full contribution from the elastic scattering to the absorption. I will refer to $\bar{\lambda}$ estimated by the first(second) definition as $\lambda_{act}(\lambda_{avg})$ where act and avg stand for actual and average.

The ratio of $X/\bar{\lambda}$ is calculated for each absorber first using λ_{act} and then λ_{avg}. Here X is the product of the absorber's density and thickness. The ratios are then added, i.e, $\sum_{i=1}^{n}(X_i/\bar{\lambda}_i)$ where i runs over all absorbers n. The proton absorption is given by:

$$\text{proton absorption} = 1.0 - e^{-\sum_{i=1}^{n}(X_i/\bar{\lambda}_i)} , \tag{4.5}$$

where $e^{-\sum_{i=1}^{n}(X_i/\bar{\lambda}_i)}$ defines the proton transmission. The final proton absorption used is the average value of the calculated proton absorption from the two definitions or 5.19% for the right arm and 4.91% for the left arm giving a proton absorption correction of $C_{Absorption} = 0.948$ and 0.951 for the right arm and left arm, respectively. Tables 4.11 and 4.12 list the absorbers used and their properties for both arms. Uncertainty in the final proton absorption used rise due to our lack of precise knowledge of the actual thickness of each absorber used and the use of different cross sections in determining the mean free path lengths discussed above. Therefore, a scale offset of 1% is assigned. Due to the fact that the scattered proton will have to travel different path length inside the LH_2 target at each kinematics, calculations of the proton absorption inside the LH_2 target at different scattering angles for both arms show an ε dependence uncertainty of 0.03% and 0.10% for the left and right arm, respectively. Random uncertainty of 0.0% is assigned.

Target	Density (gm/cm^3)	Thickness (cm)	X (gm/cm^2)
LH_2 Target	0.708E-01	1.69934	0.1203
Al Target	2.70	0.164484E-01	0.444E-01
Al Chamber	2.70	0.33E-01	0.891E-01
Kapton	1.42	0.254E-01	0.361E-01
Titanium	4.54	0.10E-01	0.454E-01
Air (Spectrometer exist to VDC1)	0.121E-02	80.00	0.968E-01
Mylar (Wire Chamber)	1.39	0.12E-01	0.167E-01
Wire VDC (effective)	19.30	0.40E-04	0.772E-03
Ar/Ethan	0.107E-02	20.00	0.214E-01
S_1 Scintillator	1.032	0.507	0.523
A_2 Aerogel	0.22	5.00	1.100
AM Aerogel	0.10	9.00	0.900
Short Gas Cerenkov(CO_2)	0.1977E-02	100.00	0.197
S_2 Scintillator	1.032	0.52	0.536
Air (VDC1 to S_2 Scintillator)	0.121E-02	220.20	0.266

λ_T (gm/cm^2)	λ_I (gm/cm^2)	X/λ_{avg}	X/λ_{act}
43.30	50.80	0.2557E-02	0.2573E-02
70.60	106.40	0.5018E-03	0.5232E-03
70.60	106.40	0.1006E-02	0.1049E-02
60.30	85.80	0.4937E-03	0.5092E-03
79.90	124.90	0.4433E-03	0.4658E-03
62.00	90.00	0.1273E-02	0.1318E-02
62.50	85.70	0.2251E-03	0.2307E-03
110.30	185.00	0.5228E-05	0.5586E-05
68.572	101.43	0.2517E-03	0.2615E-03
58.50	81.90	0.7453E-02	0.7666E-02
66.30	96.90	0.1348E-01	0.1397E-01
66.30	96.90	0.1102E-01	0.1143E-01
62.40	89.70	0.2599E-02	0.2686E-02
58.50	81.90	0.7644E-02	0.7862E-02
62.00	90.00	0.3505E-02	0.3628E-02
$\sum_{i=1}^{n}(X/\lambda)$	-	0.0525	0.0542
Transmission	-	0.9488	0.9472
Absorption (%)	-	5.114	5.275

Table 4.11: The absorbers used and their properties for the right arm spectrometer.

Target	Density (gm/cm^3)	Thickness (cm)	X (gm/cm^2)
LH$_2$ Target	0.708E-01	1.94808	0.1379
Al Target	2.70	0.147682E-01	0.3987E-01
Al Chamber	2.70	0.33E-01	0.891E-01
Kapton	1.42	0.254E-01	0.360E-01
Titanium	4.54	0.10E-01	0.454E-01
Air (Spectrometer exist to VDC1)	0.121E-02	80.00	0.968E-01
Mylar (Wire Chamber)	1.39	0.12E-01	0.166E-01
Wire VDC (effective)	19.30	0.40E-04	0.772E-03
Ar/Ethan	0.107E-02	20.00	0.214E-01
S$_0$ Scintillator	1.032	1.00	1.032
S$_1$ Scintillator	1.032	0.507	0.523
A$_1$ Aerogel	0.60E-01	9.00	0.540
Short Gas Cerenkov (CO$_2$)	0.1977E-02	100.00	0.197
S$_2$ Scintillator	1.032	0.52	0.536
Air (VDC1 to S$_2$ Scintillator)	0.121E-02	220.20	0.266

λ_T (gm/cm^2)	λ_I (gm/cm^2)	X/λ_{avg}	X/λ_{act}
43.30	50.80	0.2931E-02	0.2950E-02
70.60	106.40	0.4505E-03	0.4697E-03
70.60	106.40	0.1006E-02	0.1049E-02
60.30	85.80	0.4937E-03	0.5092E-03
79.90	124.90	0.4433E-03	0.465E-03
62.00	90.00	0.1273E-02	0.1318E-02
62.50	85.70	0.2251E-03	0.2307E-03
110.30	185.00	0.5228E-05	0.5586E-05
68.572	101.43	0.2517E-03	0.2615E-03
58.50	81.90	0.1470E-01	0.1512E-01
58.50	81.90	0.7453E-02	0.7666E-02
66.30	96.90	0.6617E-02	0.6858E-02
62.40	89.70	0.2599E-02	0.2686E-02
58.50	81.90	0.7644E-02	0.7862E-02
62.00	90.00	0.3505E-02	0.3628E-02
$\sum_{i=1}^{n}$(X/λ)	-	0.0496	0.0510
Transmission	-	0.9516	0.9502
Absorption (%)	-	4.839	4.980

Table 4.12: The absorbers used and their properties for the left arm spectrometer.

4.9   Target Length Correction

Figure 4.31 shows the geometry of the 4 cm LH_2 cell used in the experiment. The cell wall is made of 0.14 mm Al. The cell has two endcaps. The upstream endcap (not shown) is the beam entrance window and it is made of Al 7075 T6 with 0.142 mm thickness, while the downstream endcap window is uniformly machined Al in the shape of a hemisphere and has a thickness of 0.15 mm and radius R = 20.33 mm. The length of the central axis of the cell is 40.18 mm (black dashed line) [92, 93, 94, 89].

The 4 cm dummy target used is made of Al 6061 T6 with density 2.85 g/cm^3. The thickness is 0.2052 g/cm^2 for the upstream foil and 0.2062 g/cm^2 for the downstream one. The distance between the two foils is (40±0.13) mm [92, 93, 94, 89].
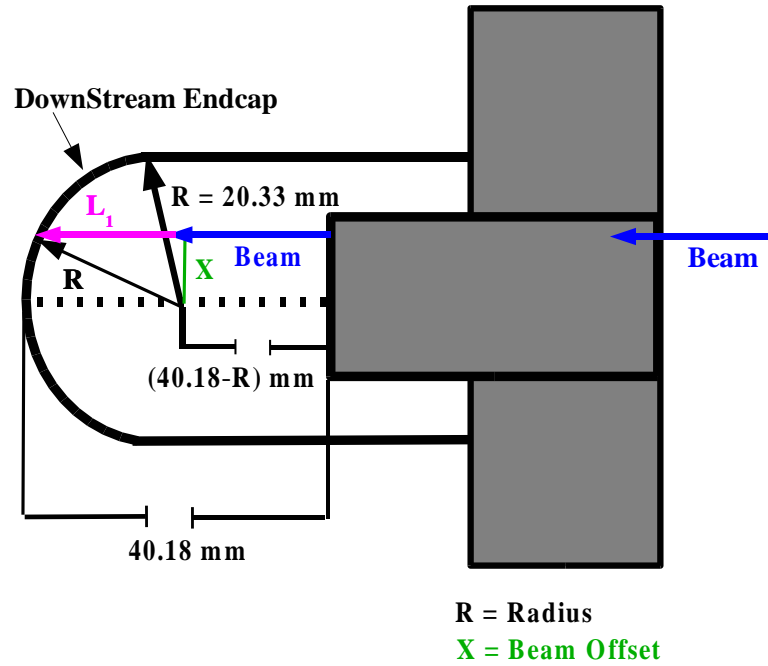
Figure 4.31: Geometry of the 4 cm LH_2 cell. The electron beam (blue arrow) is going from the right to the left side with an offset X (green line) from the central axis of the cell (black dashed line).

If the beam (the blue arrow going from left to right) is displaced a distance X (green line) from the central axis, then the length that the beam will travel in the target is L = L_1 + (40.18 - R) mm where L_1 < R and is shown as a magenta arrow. This length is effectively the new target length. A survey showed that the target was displaced down (2.0±0.5) mm relative to the center of the beam. Furthermore, the beam was rastered to produce an ~ 2 mm × 2 mm spot. Therefore, the average beam path length in the target (new target length) is then L = <L_1> + (40.18 - R) where <L_1> is given by:

$$< L_1 > \quad = \frac{\int_{X_{min}}^{X_{max}} \sqrt{R^2 - X^2}\, dX}{\int_{X_{min}}^{X_{max}} dX} \ , \tag{4.6}$$

and X_{min} and X_{max} are the minimum and maximum beam displacement.

The target length correction needed is defined as δL = (40.18-L)×100%/40.18. Table 4.13 lists the results of the calculations. The nominal value of δL, δL = 0.266%, gives a target length correction to Q_{eff} of C_{TL} = 0.9973, which changes by ~ 0.12% (average difference from the nominal value) for a 0.50 mm beam shift. Therefore, a scale uncertainty in the target length of 0.12% is assigned for both arms.

The beam position measurements are discussed in detail in section 3.5. Figure 3.15 shows the x and y coordinates of the beam at the target. The beam was well focused on the target with an average beam drift of 0.30 mm. This drift in the beam position translates into an uncertainty in the effective target length and introduces a correction to Q_{eff}. Table 4.14 lists the results. The target length correction δL changes by ~ 0.074% (average difference from the nominal value) for a 0.30 mm beam drift. Therefore, a random uncertainty in the target length of 0.074% is assigned for both arms.

X_{min} (mm)	X_{max} (mm)	$<L_1>$ (mm)	L (mm)	δL (%)
0.5	2.5	20.2663	40.1163	0.158540
1.0	3.0	20.2231	40.0731	0.266053
1.5	3.5	20.1673	40.0173	0.404930
Average	-	-	-	0.27651

Table 4.13: The target length correction δL as determined for several beam offset ranges.

X_{min} (mm)	X_{max} (mm)	$<L_1>$ (mm)	L (mm)	δL (%)
0.7	2.7	20.2505	40.1005	0.197860
1.0	3.0	20.2231	40.0731	0.266053
1.3	3.3	20.1911	40.0411	0.345694
Average	-	-	-	0.26987

Table 4.14: The target length correction δL as determined for several beam drift ranges.

4.10   Computer and Electronics Deadtime

The computer deadtime is the portion of the time that the DAQ system is unable to record an event because it is busy recording another event. Scalers are used to count the total number of triggers generated for each event or trigger type. By knowing the number of events recored by the DAQ system, N_{DAQ}^i, and the total number of events fed to the DAQ, N_{Total}^i, as recorded by scalers for a particular event type (T_i where $i = 1, \cdots, 5$), one can account for the missing events and determine the computer livetime $CLT = ps_i N_{DAQ}/N_{Total}$. The computer deadtime is then defined as $\eta_{CDT} = 1.0$ - CLT where ps_i is the prescale factor for that event type.

The electronics deadtime is the portion of the time during which the triggers are missed because the hardware is busy when a second event comes in. When an event causes a trigger, the logic gate in the trigger is activated and the TDC signal stays high for a fixed time τ, which is the gate time width of the logic signal and has a value of (100 ± 20) nsec. If a second event tries to trigger and activate the gate within that time window τ, the second event will be ignored. If the event rate is R, then the probability of having n counts in a time t is given by the Poisson distribution $P(n) = (Rt)^n e^{-Rt}/n!$, and the probability distribution for the time between the events is $P(t) = Re^{-Rt}$. For small electronics deadtime, the fraction of measured events or the electronics livetime ELT is equal to the probability that the time between events will be greater than τ or:

$$ELT \ = \frac{N_{Measured}}{N_{Total}} \ = \int_{\tau}^{\infty} Re^{-Rt} \ dt \ = e^{-R\tau} \ , \qquad (4.7)$$

and the electronics deadtime is then defined as $\eta_{EDT} = 1.0$ - ELT.

The raw event rates were $\leq$ 1KHz for the left arm and $\leq$ 30KHz for the right arm, respectively, but the right arm was heavily prescaled. The computer deadtime is in the range of $(9-20)\%$ for the left arm and $(2-16)\%$ for the right arm with an

average of $\sim 10\%$ correction on both arms. The computer deadtime is well measured and known to within 1.0%. Therefore a 1.0% uncertainty in a 10% correction yields a scale uncertainty of 0.10% for both arms. Similarly, we assign a slope uncertainty of 0.10% for the left arm, and $\sim 1.0\%$ (0.10%/0.07) for the right arm when we consider the $\Delta\varepsilon$ range of 0.07. A random uncertainty in the computer deadtime of 0.0% is assigned for both arms.

The electronic deadtime is in the range of $(0.001-0.008)\%$ for the left arm with a random uncertainty, determined based on the 20% uncertainty in τ, of 0.002% (set to 0.0%), and $(0.03-0.30)\%$ for the right arm with a maximum random uncertainty of 0.06%. If we take the average random uncertainty of 0.04% for the right arm and consider the $\Delta\varepsilon$ range of 0.07, we estimate the slope uncertainty to be $0.04\%/0.07 \approx 0.50\%$. The slope uncertainty is 0.0% for the left arm. A 0.0% scale uncertainty in the electronic deadtime is assigned for both arms.

4.11   Beam Current Monitor Correction

The beam current measurement was described in detail in section 3.6. The basic technique of calibrating the beam current monitors is well documented [67, 95, 96]. The idea is to normalize the BCMs cavities to the OLO2 cavity (Unser monitor) at the injector. During a calibration run, the beam was interrupted using a Faraday cup inserted after the OLO2 cavity so that the zeros of the cavities and the Unser could be determined. The beam current was first set to 80 μA for one minute and then the Faraday cup was inserted for another minute. The beam current was then stepped down to 70 μA and the Faraday cup was inserted again for another minute. This procedure was done down to a beam current of 10 μA and then reversed up to beam current of 80 μA.

While the beam was stepped down through various currents, the EPICS informa-

tion such as the values of the upstream and downstream BCM voltage, Unser current, injector Faraday cup current, and the OLO2 current were saved to a file. The EPICS BCM constants were determined from these values as:

$$\text{constant} = \frac{< I_{OLO2} >}{< V_{cavity} > \text{- zero offset}} \, , \qquad (4.8)$$

where $< I_{OLO2} >$ and $< V_{cavity} >$ are the average value for the OLO2 current and cavity voltage, respectively. Table 4.15 summarizes the results. The zero offsets for the cavities and Unser were determined from the beam off periods when the Faraday cup was inserted and the calibration constants and the zero offsets for converting the voltage-to-frequency (V-to-F) scalers to charge were also determined to give an average current of:

$$\text{Average current} = \frac{\frac{\text{Scaler}}{\text{time}} - \text{zero offset}}{\text{constant}} \, . \qquad (4.9)$$

The values for V-to-F zero offsets and constants are listed in Table 4.16. Based on the analysis of all of the calibration runs, the gain and offset drifts were stable to within 0.1% and 0.01%, respectively. The effect of the offset drift is negligible, so a random uncertainty in the charge measurement of 0.1% is assigned for both arms. It is reported that [67] the BCMs with the Unser are calibrated at the same time as the charge monitors every 2-3 months, and the results are stable to within $\pm 0.5\%$. Therefore, a scale uncertainty in the charge measurement of 0.5% is assigned for both arms.

Constant Type	Constant Value
EPICS Upstream cavity	77.44 ± 0.04
EPICS Downstream cavity	79.08 ± 0.04

Table 4.15: The EPICS BCM calibration constants.

Constant Type	Constant Value	Constant Zero Offsets
V-to-F U1x	1331.2 ± 0.7	152.78
V-to-F U3x	4094.8 ± 2.1	163.88
V-to-F U10x	12451.7 ± 9.6	360.37
V-to-F D1x	1353.4 ± 0.7	34.63
V-to-F D3x	4190.0 ± 2.2	110.01
V-to-F D10x	13187.7 ± 10.2	307.91

Table 4.16: The V-to-F calibrations constants and offsets.

4.12 Target Boiling Correction

The LH_2 target density ρ_0 can decrease due to boiling caused by the electron beam current. In order to study the boiling effect in the LH_2, runs were taken at several beam current values using LH_2 and carbon targets. We define the normalized yield Y as the total number of events N detected in a chosen acceptance region by applying kinematics and acceptance cuts and then normalized to the effective beam charge Q_{eff} or:

$$Y = \frac{N}{Q_{eff}} \ . \tag{4.10}$$

The normalized yield as a function of current showed a linearly decreasing relationship. The deviation of the normalized yield from 1.0 over the current range represents the instability of the target density due to target boiling effect. The target density ρ was parameterized as a function of current I as:

$$\rho(I) = \rho_0(1.0 - BI) \ , \tag{4.11}$$

where $\rho_0 = \rho(I = 0)$ and B is the slope giving a target boiling correction $C_{TB} = \rho(I)/\rho_0$ as listed in Table 4.17 for the different kinematics.

Kinematics	$I(\mu A)$	$C_{TB} \pm \delta C_{TB}$	$\delta C_{TB}(relative)$ %
a and run$\leq$ 1269	30	0.9925 ± 0.0045	$\pm$ 0.60
a and run$>$ 1269	50	0.9875 ± 0.0075	$\pm$ 0.30
b	50	0.9875 ± 0.0075	$\pm$ 0.30
i-r	70	0.9825 ± 0.0105	$\pm$ 0.00

Table 4.17: The target boiling correction C_{TB} and its uncertainty δC_{TB} as determined for different kinematics. In determining $\delta C_{TB} = I\delta B$, a δB value of 1.5%/100μA is used. See text for details. Note that $\delta C_{TB}(relative)$ is the uncertainty relative to data at 70μA.

In the boiling studies, we analyze the data in two different methods. First, we plot the events/charge from scalers corrected for current-independent rate (rate of cosmic ray triggers) as a function of current. Figure 4.32 shows the results. For carbon, the slope is consistent with zero (0.32 ± 0.32)%/100μA, as it should be. For LH$_2$, the slope is (1.38 ± 0.15)%/100μA. However, there is a slight nonlinearity at lower current, possibly due to nonlinearity in the BCM calibration at very low current or uncertainty in the correction for cosmic trigger ray, so this may be a slight overestimate. This may also be a slight underestimate, since the thickness of the endcaps does not depend on current.

In the second method, we plot the yield as defined by equation (4.10) as a function of current where N is the number of the T$_3$ type tracked events. For carbon, the check is not of good quality due to poor statistics. For LH$_2$, the results yield a slope of (1.12 ± 0.65)%/100μA, but the statistics are low and so the uncertainty is large. In addition, the results are fairly cut-dependent, yielding slopes up to 3%, but with large uncertainties.

Clearly, neither test is ideal and both give lower corrections than observed by previous experiments. The scalers analysis is sensitive to the endcaps contribution and the current-independent rate. The tracked analysis is cleaner, but has low statistics. So

we take a correction of 2.5%/100μA, but apply a large uncertainty (2.5$\pm$1.5)%/100μA or (1.75$\pm$1.05)%/70μA. Therefore a scale uncertainty of 1.05% in the target boiling correction is assigned. One thing to mention is that this effect cancels out if we take the ratio of the left to the right arm cross sections, and even for the left arm alone, it is mostly a normalization uncertainty since most of the kinematics were run at the same current and at a fixed Q^2 the proton corrections do not vary much with ε.
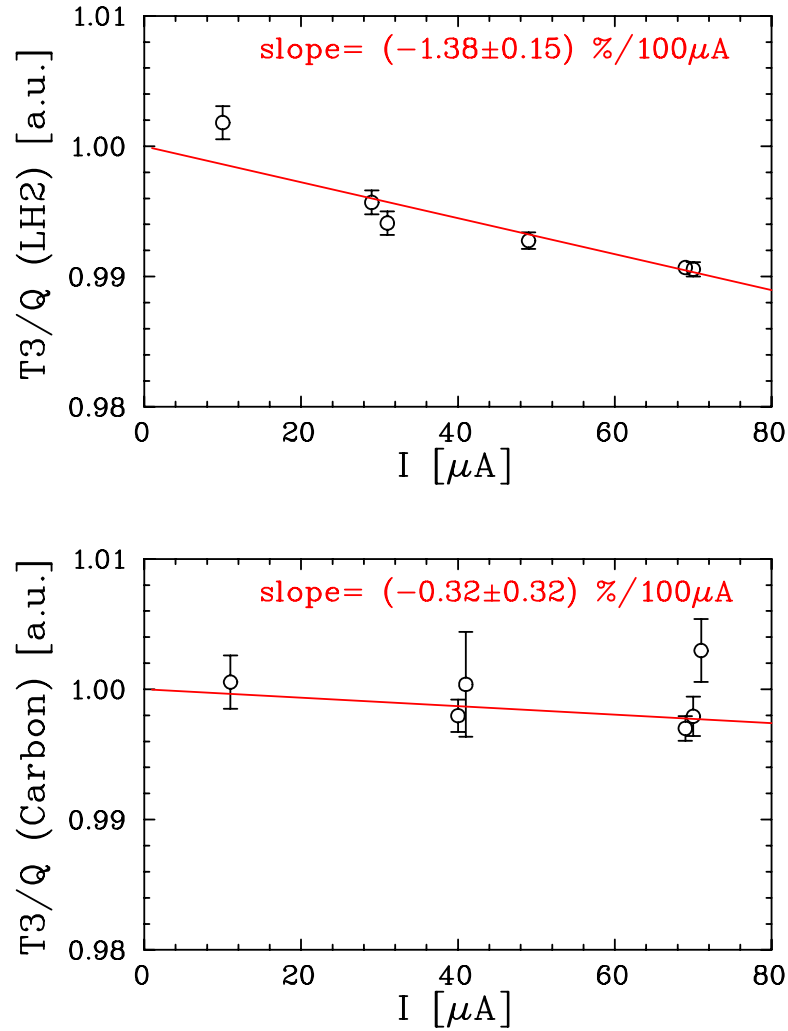
Figure 4.32: Target boiling studies. The left arm normalized yield for LH$_2$ target (top) and carbon target (bottom) as a function of current.

We check this correction by looking at kinematics a and b, where part of the data is taken at 30μA and part at 50μA. The left arm has a relatively low rate (making it more sensitive to cosmic ray rates) and has a larger contribution from the aluminum endcaps, and so we focus on the right arm to check the correction. Also, since we mainly want this correction for the left arm, it is good to have an independent check of the boiling. For the right arm data, we see a clear difference between the yield at 30 and 50μA if we do not apply the boiling correction as can be seen in Figure 4.33. The yield differs by roughly $(0.6 \pm 0.1)\%$ for a 20μA difference, yielding a boiling correction of $(3.0 \pm 0.5)\%/100\mu$A. This is consistent with the $(2.5\pm1.5)\%/100\mu$A, so we stick with the more conservative number and use the consistency at 30 and 50μA as a test of the correction. Figure 4.34 shows the yield after applying the boiling correction.

Since most of the data are taken at 70μA, we want the uncertainty relative to the data at 70μA. So we set the random uncertainty for all kinematics to 0.0% except that of kinematics a and b. We estimate the random uncertainty for kinematics a and b to be 0.45% or $1.5\%(70\mu$A - 40μA$)/100\mu$A assuming an average current of 40μA and 0.30% or $1.5\%(20\mu$A$)/100\mu$A, respectively. Furthermore, the beam was rastered to produce an ~ 2 mm $\times$ 2 mm spot with uncertainty in the raster size of $< \pm0.2$ mm which translates into a $\sim 0.1\%$ random uncertainty in the target boiling.

4.13   Summary of Systematic Uncertainties

Tables 4.18 and 4.19 summarize the systematic uncertainties for the right and left arm, respectively. The systematic uncertainties are discussed in the sections listed in these tables. The systematic uncertainty in each listed source is broken down into three types: scale, random, and slope. The contribution of each uncertainty type from all sources is then added in quadrature to form the total uncertainty in σ_R for
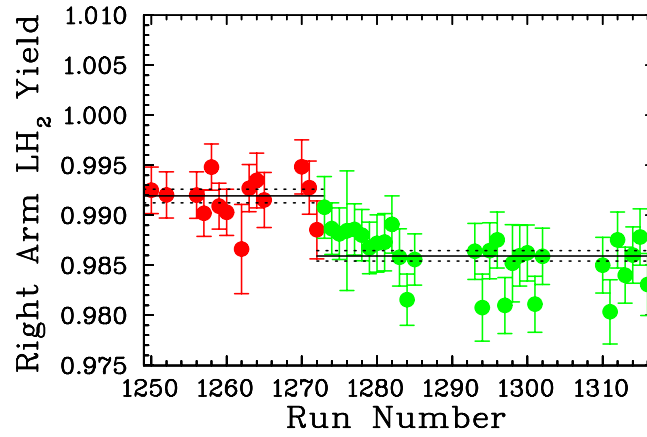
Figure 4.33: The right arm LH$_2$ yield before applying the target boiling correction for all the runs from kinematics a (1250-1285) and b (1293-1316) normalized to the yield of run 1250. The yield is shown in red(green) for runs taken at $I = 30(50)\mu$A. Runs 1272-1285 from kinematics a are taken at $I = 50\mu$A and their yield is shown in green as well. The solid black line is the average normalized yield for that current setting. The dashed black lines are the average uncertainty in the normalized yield.
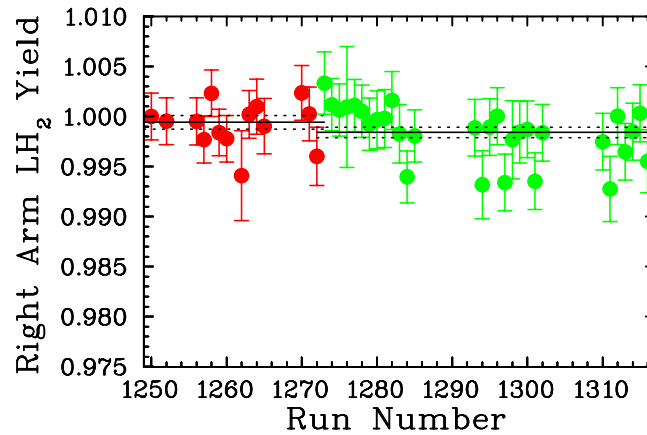
Figure 4.34: The right arm LH$_2$ yield after applying the target boiling correction for all the runs from kinematics a (1250-1285) and b (1293-1316) normalized to the yield of run 1250. The yield is shown in red(green) for runs taken at $I = 30(50)\mu$A. Runs 1272-1285 from kinematics a are taken at $I = 50\mu$A and their yield is shown in green as well. The solid black line is the average normalized yield for that current setting. The dashed black lines are the average uncertainty in the normalized yield.

that uncertainty type. Only the range on total δ_{Random} is given in these tables, while the actual value of total δ_{Random} in σ_R at each ε point is listed in Tables 5.5 and 5.6. It must be mentioned that the scale uncertainty in the pion subtraction for the left arm is 0.20% for all kinematics except those of $Q^2 = 4.10$ GeV^2 which is 0.40%. This results in a $\delta_{Slope} = 0.539\%$ for all kinematics with $Q^2 = 2.64$ and 3.20 GeV^2, and $\delta_{Slope} = 0.641\%$ for all kinematics with $Q^2 = 4.10$ GeV^2. In addition, δ_{Slope} for $Q^2 = 4.10$ GeV^2 is then scaled up by 25% to account for the $\Delta\varepsilon$ range difference among the three Q^2 points which results in a $\delta_{Slope} = 0.801\%$. See Table 4.19 for details.

157

Source	Section	Right Scale (%)	Right Random (%)	Right Slope (%)
BCM Calibration($\star$)	4.11	0.50	**0.10**	0.00
Target Boiling at 70μA($\star$)	4.12	**1.05**	0.30-0.45($\dagger a$)	0.00
Raster Size($\star$)	4.12	0.00	**0.10**	0.00
Target Length($\star$)	4.9	0.12	0.07	0.00
Electronic Deadtime	4.10	0.00	0.04	**0.50**
Computer Deadtime	4.10	0.10	0.00	**1.00**
VDC Zero-Track Inefficiency	4.5	0.00	0.00	0.00
VDC Multiple-Track Inefficiency	4.5	0.10	0.00	**0.70**
VDC Hardware Cuts	4.5.1	0.50	**0.10**	0.00
Scintillator Efficiency	4.6	0.10	0.05	0.00
PID Efficiency (β)	4.7.1	0.15	0.05	0.00
PID Efficiency (A_2)	4.7.2	0.25	0.05	0.00
PID Efficiency (A_1)	4.7.3	0.00	0.00	0.00
Pion Contamination	4.7	0.00	0.00	0.00
Proton Absorption	4.8	**1.00**	0.00	0.10
Solid Angle Cut	4.3	**2.06**	0.00	0.00
Pion Subtraction	5.7.4	0.00	0.05	0.00
Dummy Subtraction	5.7.4	0.50	0.00	0.40
ΔP Cut-Dependence	5.7.4	0.50	**0.14**	**2.00**
δ Cut-Dependence	5.7.4	0.30	**0.30**	**4.30**
0.18 mrad Angle Offset	4.4	0.20	0.02	**0.67**
0.10 mrad Angle Fluctuations	4.4	0.00	0.097-0.125($\dagger b$)	0.00
0.03% Beam Energy	3.4	0.03	0.01	0.29
0.02% Beam Energy Fluctuations	3.4	0.00	0.015-0.029($\dagger c$)	0.00
Radiative Corrections	5.6	**1.00**	**0.20**	**2.00**
		δ_{Scale}	δ_{Random}	δ_{Slope}
Total (%)		2.93	0.454-0.640	5.38

Table 4.18: Summary of the systematic uncertainties for the right arm. Numbers in bold show the biggest contribution to that uncertainty type. Sources marked with ($\star$) contribute to the uncertainty in the luminosity monitor. For ($\dagger a$), the value is 0% for all kinematics except a and b which is 0.45% and 0.30%, respectively. For ($\dagger b$), the value is applied on kinematics-by-kinematics basis as shown in Figure 4.7 and it ranges from 0.097%-0.125%. For ($\dagger c$), the value is applied on kinematics-by-kinematics basis as shown in Figure 3.11 and it ranges from 0.015%-0.029%. Since $\Delta\varepsilon \sim 0.07$ for the right arm, the slope uncertainty is much larger for the right arm.

Source	Section	Left Scale (%)	Left Random (%)	Left Slope (%)
BCM Calibration(⋆)	4.11	0.50	**0.10**	0.00
Target Boiling at 70μA(⋆)	4.12	**1.05**	0.30-0.45(†a)	0.00
Raster Size(⋆)	4.12	0.00	**0.10**	0.00
Target Length(⋆)	4.9	0.12	0.07	0.00
Electronic Deadtime	4.10	0.00	0.00	0.00
Computer Deadtime	4.10	0.10	0.00	**0.10**
VDC Zero-Track Inefficiency	4.5	0.10	0.00	0.00
VDC Multiple-Track Inefficiency	4.5	0.10	0.02	0.00
VDC Hardware Cuts	4.5.1	0.50	**0.10**	**0.25**
Scintillator Efficiency	4.6	0.10	0.05	0.00
PID Efficiency (β)	4.7.1	0.00	0.00	0.00
PID Efficiency (A_2)	4.7.2	0.00	0.00	0.00
PID Efficiency (A_1)	4.7.3	0.20	**0.10**	0.00
Pion Contamination	4.7	0.00	**0.10**	0.00
Proton Absorption	4.8	**1.00**	0.00	0.03
Solid Angle Cut	4.3	**2.06**	0.00	0.00
Pion Subtraction	5.7.4	0.00	0.15-0.30(†b)	0.20-0.40
Dummy Subtraction	5.7.4	0.50	0.00	**0.10**
ΔP Cut-Dependence	5.7.4	0.50	**0.14**	**0.20**
δ Cut-Dependence	5.7.4	0.00	0.00	0.00
0.18 mrad Angle Offset	4.4	0.13	0.01	**0.18**
0.10 mrad Angle Fluctuations	4.4	0.00	0.03-**0.10**	0.00
0.03% Beam Energy	3.4	0.13	0.02	0.07
0.02% Beam Energy Fluctuations	3.4	0.00	0.043-0.081	0.00
Radiative Corrections	5.6	**1.00**	**0.20**	**0.30**
		δ_{Scale}	δ_{Random}	δ_{Slope}
Total (%)		2.91	0.384-0.593	0.539-0.801

Table 4.19: Summay of the systematic uncertainties for the left arm. Numbers in bold show the biggest contribution to that uncertainty type. Sources marked with (⋆) contribute to the uncertainty in the luminosity monitor. For (†a), the value is 0% for all kinematics except a and b which is 0.45% and 0.30%, respectively. For (†b), the value is 0.15% for all kinematics except those of $Q^2 = 4.10$ GeV^2 which is 0.30%. The random uncertainty in the 0.10 mrad angle fluctuations and 0.02% beam energy fluctuations is applied on kinematics-by-kinematics basis as shown in Figure 4.8 and Figure 3.12, respectively.

Chapter 5 Data Analysis II: Reduced Cross Sections Extraction

5.1 Overview
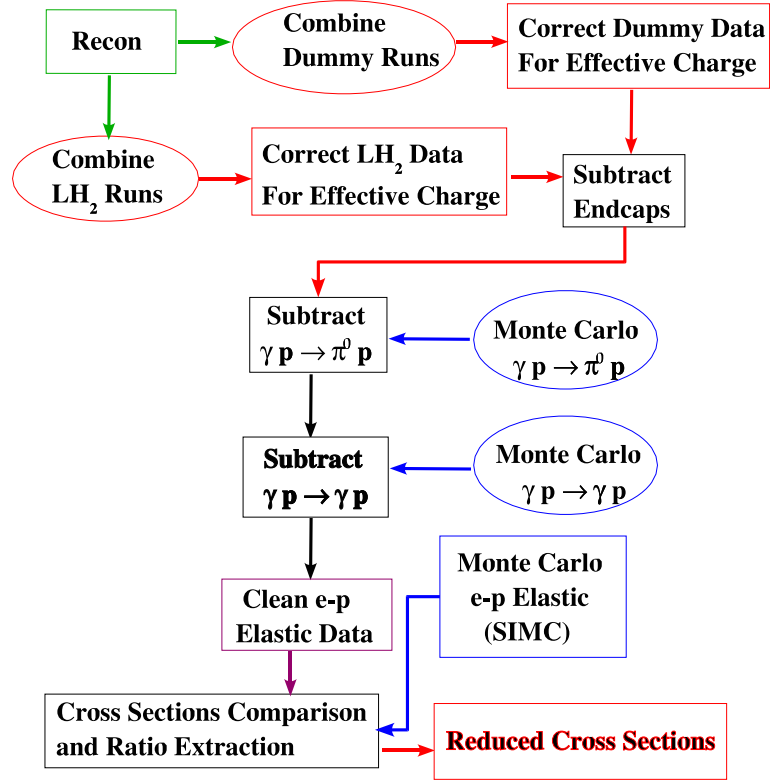
Figure 5.1: E01-001 experiment analysis flow chart.

In this chapter I will present the procedure used to extract the e-p reduced cross section σ_R. Figure 5.1 shows a flow chart of the procedure used. First, ESPACE

generates HBOOKs for a list of LH_2 and dummy target runs in a particular kinematics which are read by Recon (section 5.2). Recon applies a set of cuts and corrections on an event-by-event basis and generates a new HBOOK file for each run on the list. In addition, Recon generates the ΔP spectrum for each LH_2 and dummy run on the list. For each kinematics the ΔP spectra from all of the LH_2 and dummy runs are added separately after applying a new set of cuts to form the final ΔP spectrum for both LH_2 and dummy (section 5.3). The final ΔP spectrum for both the LH_2 and the dummy is then normalized to its total Q_{eff} (section 5.4). The final corrected dummy ΔP spectrum is subtracted from the final corrected LH_2 ΔP spectrum. Monte Carlo simulations of the $\gamma p \to \pi^0 p$ and $\gamma p \to \gamma p$ backgrounds are performed (section 5.5.2), and then normalized and subtracted from the final corrected LH_2 ΔP spectrum to produce the residual elastic e-p spectrum. The net number of the elastic e-p events is then compared to the number of elastic events in the e-p peak as simulated using the Monte Carlo simulation program SIMC (section 5.5.1) in a window in the ΔP spectrum. The reduced cross section σ_R is taken as the value of the input e-p cross section used in the simulation normalized by the ratio of number of elastic events in the data to that in the simulation (section 5.7). Finally, a linear fit of σ_R to ε gives $\tau G^2_{Mp}(Q^2)$ as the intercept and $G^2_{Ep}(Q^2)$ as the slope.

5.2   Event Reconstruction by Recon

The HBOOK file for each physics run generated by ESPACE (see section 4.2) was read using the in-house event analyzer Recon. Recon reads in the HBOOK file for a given run as Column-Wise Ntuples, applies a set of cuts on an event-by-event basis on all the physical variables saved in these Ntuples, and calculates the necessary physics quantities. A new HBOOK file for each run is then generated for the final data analysis. Table 5.2 lists the cuts applied on these physical variables. Events

that satisfy these cuts are accepted for the final data analysis.

First, a single-track event type $T_1(T_3)$ for the right(left) arm is selected. The multiplicity of a cluster of hit wires in each plane is defined as the number of hit wires in the cluster. A single-track event making an angle of 45° with the VDC surface has typically a multiplicity of 5. We require the multiplicity of each of the four planes for both VDCs to be greater than two. The Q_3 cut is applied to reject events that scrape off the exit pipe of the Q_3 quadrupole. The Q_3 cut is defined as:

$$Q_3 = \sqrt{(xfp - 2.64xpfp)^2 + (yfp - 2.64ypfp)^2} < 0.29 \ m \ , \qquad (5.1)$$

where xfp, $xpfp$, yfp, and $ypfp$ are the focal plane positions (xfp, yfp) and angles ($xpfp$, $ypfp$) variables. The Q_3 was applied to the left arm events only since there is no evidence that events were scraping off the exit pipe of the Q_3 quadrupole in the right arm spectrometer. It must be mentioned that the elastic events are far from the Q_3 edges and are not affected by the Q_3 cut. Figure 5.2 shows how the Q_3 cut was applied.

The hourglass cut (all good trajectories that make it through the HRS form an hourglass pattern ~ 69 cm before the first VDC) is then applied to remove events which come from multiple scattering inside the spectrometer and located outside the acceptance. The hourglass cut is defined as:

$$\left| yfp - 0.69ypfp + 0.005 \right| - C_1 \left| xfp - 0.69xpfp \right| \ , \qquad (5.2)$$

where C_1 has a value of 0.045(0.017) for the right(left) arm. Figure 5.3 shows how the hourglass cut is applied.

Finally cuts on the target reconstructed variables such as the momentum acceptance δ, the y-coordinate of the extended target length y_{tg}, the out-of-plane angle θ_{tg}, and the in-plane angle ϕ_{tg} are applied. Figures 5.4 and 5.5 show the target
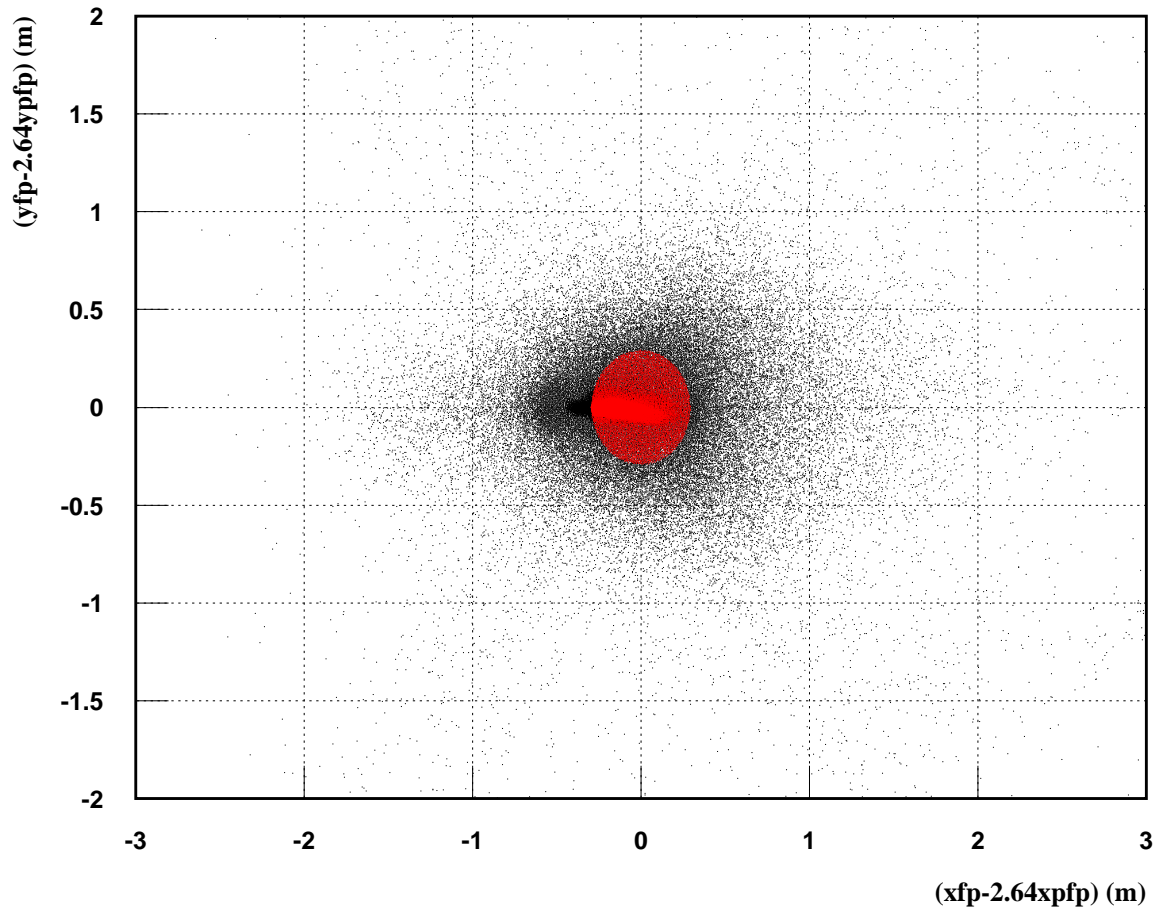
Figure 5.2: The Q_3 cut, solid red circle with radius of 0.29 m, applied to the left arm events (black) for a single run from kinematics k to reject events that were scraping off the exit pipe of the Q_3 quadrupole. Only events within the area of the solid red circle are accepted.
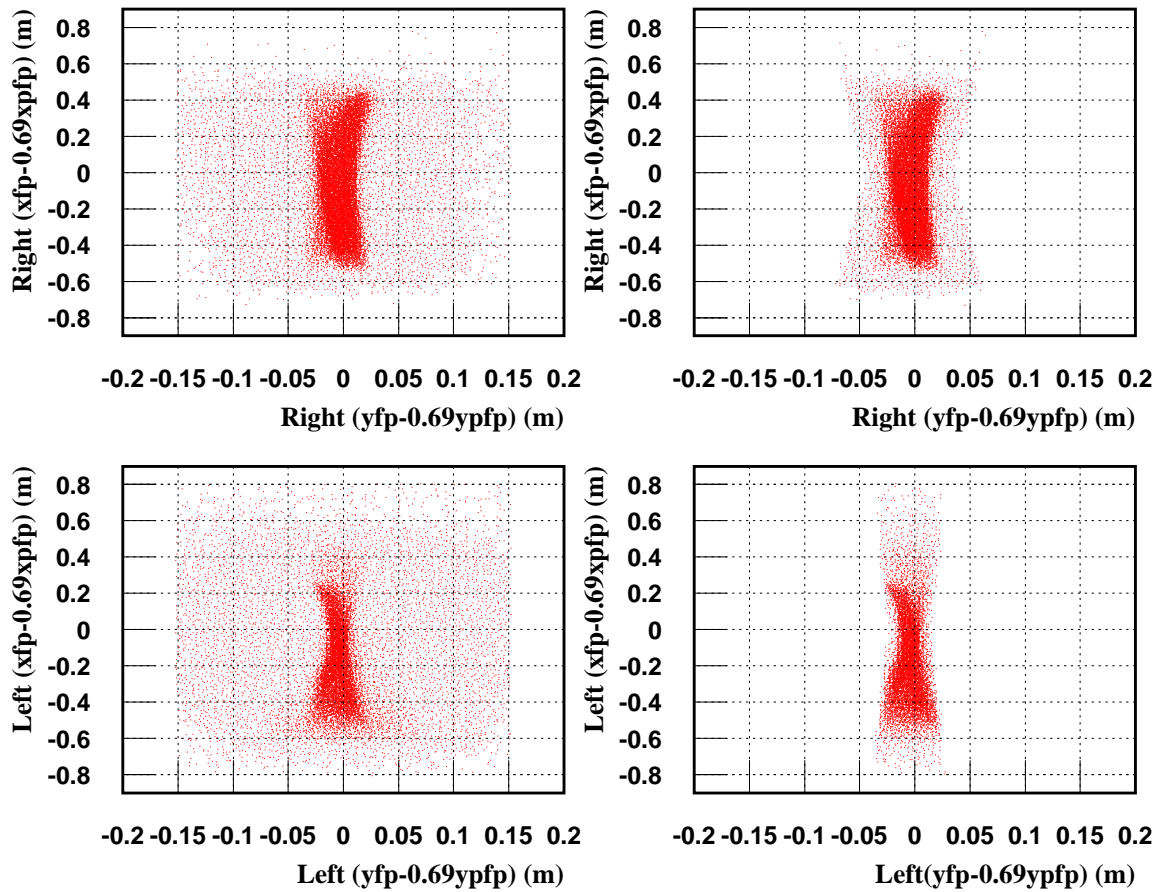
Figure 5.3: The hourglass cut applied to the right and left arms events from run 1282. The right arm events before the cut (top left) and after the cut (top right). The left arm events before the cut (bottom left) and after the cut (bottom right).

reconstructed variables after the cuts have been applied.
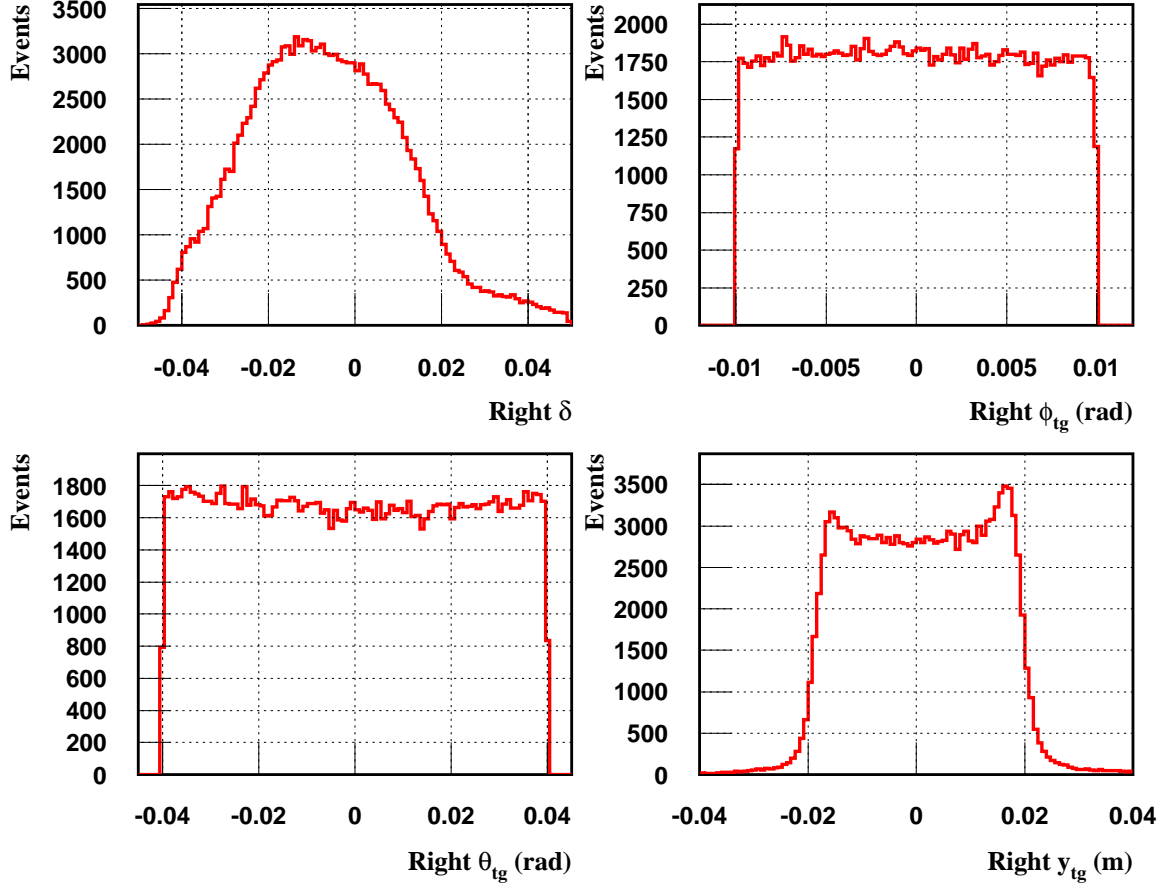
Figure 5.4: The right arm target reconstructed variables with cuts from run 1282. The right arm momentum acceptance δ (top left), in-plane angle ϕ_{tg} (top right), out-of-plane angle θ_{tg} (bottom left), and y-coordinate of the extended target length y_{tg} (bottom right).

It should be mentioned that the momentum acceptance, δ, showed an out-of-plane angle dependence on both the right and left arms, and a raster, ry, dependence on the left arm only. The momentum acceptance δ had first to be adjusted to correct for the θ_{tg} dependence for the left arm as:

$$\delta_1 = \delta_0 + 0.025\theta_{tg} + 0.250\theta_{tg}^2 \; , \tag{5.3}$$
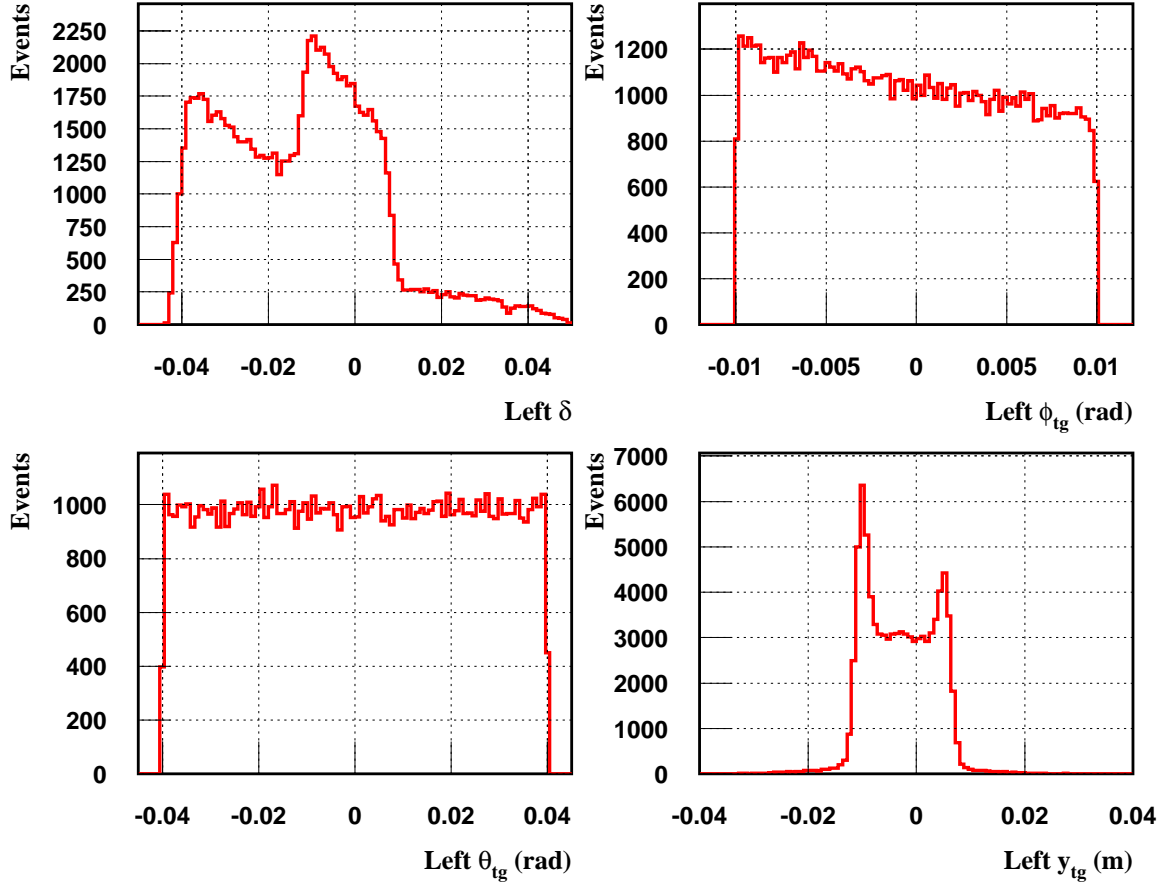
Figure 5.5: The left arm target reconstructed variables with cuts from run 1282. The left arm momentum acceptance δ (top left), in-plane angle ϕ_{tg} (top right), out-of-plane angle θ_{tg} (bottom left), and y-coordinate of the extended target length y_{tg} (bottom right).

while for the right arm:

$$\delta_1 = \delta_0 + 0.02742\theta_{tg} \ , \tag{5.4}$$

where δ_0 and δ_1 are the momentum acceptance before and after the adjustment, respectively. The raster correction was then applied as:

$$\delta_2 = \delta_1 + \text{constant} \times \text{ry} \ , \tag{5.5}$$

where ry is the raster's ADC signal (raster number 2 or rast2adc):

$$\text{ry} = 0.002\frac{(\text{rast2adc} - 1560)}{\text{raster width}} \ , \tag{5.6}$$

constant is the correction applied, and the raster width is the width of the ADC signal whose average width is 1560 and is energy dependent. Again, δ_1 and δ_2 are the momentum acceptance before and after the raster correction, respectively. Figure 5.6 shows the ΔP spectrum before and after the raster correction. Table 5.1 lists the values for the constant and raster width.

Tiefenback Energy (MeV)	constant	raster width
1912.94	0.42	-1400
2260.00	0.38	+1100
2844.71	0.00	-1000
3772.80	0.00	+1200
4702.52	0.30	-600

Table 5.1: The Tiefenback energy, constant(correction applied) and raster width needed to correct the momentum acceptance δ for the raster dependence.

In order to reconstruct ΔP, equation (3.2), the following procedure is used. The final momentum of the scattered protons $P_{measured}$ (measured using the high resolution
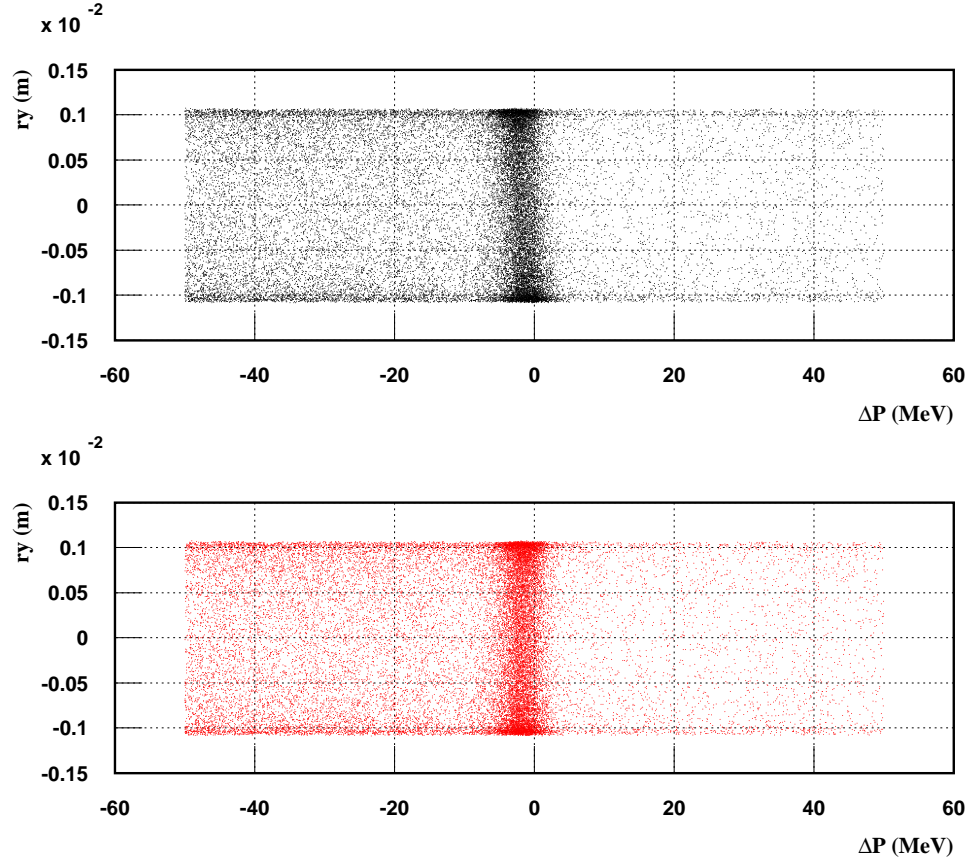
Figure 5.6: Two dimensional histogram of ΔP (x-axis) vs raster ry (y-axis). Top black: the ΔP spectrum before the correction shows a raster ry dependence as the events centered around $\Delta P = 0$ MeV are slightly tilted counter clockwise. Bottom red: the ΔP spectrum after the correction where the events are tilted clockwise (see equation (5.5)) and become mainly centered around $\Delta P = 0$ MeV.

spectrometer) is reconstructed as:

$$P_{measured} = P_{L(R)}(1 + \delta_2) \,, \tag{5.7}$$

where $P_{L(R)}$ is the central momentum setting for the left(right) arm spectrometer as listed by Table 3.1. The scattering angle of the proton is then reconstructed:

$$\cos\theta_p = \frac{\cos\theta_{R(L)} \pm \phi_{tg}\sin\theta_{R(L)}}{\sqrt{1 + \phi_{tg}^2 + \theta_{tg}^2}} \,, \tag{5.8}$$

where the plus(minus) sign is used with the right(left) arm respectively, and $\theta_{R(L)}$ is the right(left) arm spectrometer scattering angle as listed by Table 4.2. Finally, the momentum of the scattered protons $P_{calculated}(\theta_p)$, equation (3.1), is then obtained

Cut Type Applied	Left Arm Cut Value	Right Arm Cut Value
Event Type	3	1
Number of Tracks	1	1
VDC Multiplicity	Multiplicity>2	Multiplicity>2
Q_3 (m)	<0.29	-
Hourglass (m)	$<0.02\sin\theta_L+0.01$	$<0.02\sin\theta_R+0.02$
δ Momentum (%)	$-5.0<\delta<5.0$	$-5.0<\delta<5.0$
PID Aerogel ADCSUM	A_1ADCSUM<350	A_2ADCSUM<1250
PID β	-	$0.45<\beta<0.85$
Number of Clusters/VDC Plane	1	1
Minimum Number of Hits/Cluster	3	3
Maximum Number of Hits/Cluster	6	6
y_{tg} (m)	$-0.05<y_{tg}<0.05$	$-0.05<y_{tg}<0.05$
Out-of-Plane Angle (θ_{tg}) (mrad)	$-40.0<\theta_{tg}<40.0$	$-40.0<\theta_{tg}<40.0$
In-Plane Angle (ϕ_{tg}) (mrad)	$-10.0<\phi_{tg}<10.0$	$-10.0<\phi_{tg}<10.0$

Table 5.2: Cuts applied in the analysis of the E01-001 data. Cuts in the upper half of table are applied in Recon and cuts in the bottom half are applied later as discussed in section 5.3. See text for more details.

using the measured scattering angle of the proton as given by equation (5.8).

5.3   Adding Histograms

For the data analysis, the HBOOK file generated by Recon for each physics run in a given kinematics is read by a kumac file (code) written using PAW the Physics Analysis Workstation software. The PAW kumac starts by reading the run number and then loading its HBOOK file. A new set of cuts such as the PID cuts A_2 ADCSUM and β cuts for the right arm and A_1 ADCSUM cut for the left arm (to select good protons) and tracking cuts (number of clusters for each VDC's plane = 1, minimum number of hits per cluster in each VDC's plane = 3, and maximum number of hits per cluster in each VDC's plane = 6) are applied to the LH_2(dummy) ΔP ntuple of that run. See section 4.7 for the range of PID cuts used. The ΔP ntuple for LH_2 or dummy is then projected onto a histogram where a distribution of the number of counts per one MeV bin can be plotted. This procedure was done for all the LH_2 and dummy runs in that kinematics. The LH_2 and dummy ΔP histograms from all the runs are added to form the final Q_{eff} uncorrected LH_2 and dummy ΔP histogram.

The LH_2 ΔP spectrum is made of several contributions. The main contribution is from elastic $ep \rightarrow ep$ scattering which has a peak and a radiative tail. In addition there are backgrounds due to quasi-elastic and inelastic scattering in the aluminum target windows and walls and protons generated the photoreactions $\gamma p \rightarrow \pi^0 p$ and $\gamma p \rightarrow \gamma p$.

To account for the quasi-elastic contribution to the LH_2 ΔP spectrum, events scattered from the aluminum target windows were measured using an empty dummy target. The windows of the dummy target were thicker than the windows of the LH_2 target and the determination of the effective thickness of the dummy target, referred to as "dummy thickness" will be discussed is section 5.7. Figures 5.7 and 5.8 show a
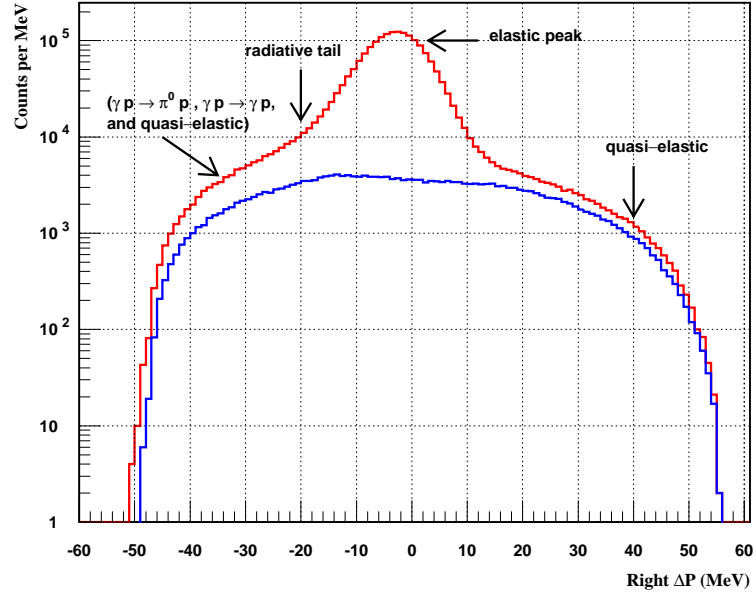
Figure 5.7: Q_{eff} uncorrected right arm ΔP spectrum for LH_2 (red) and dummy (blue) targets from kinematics b.
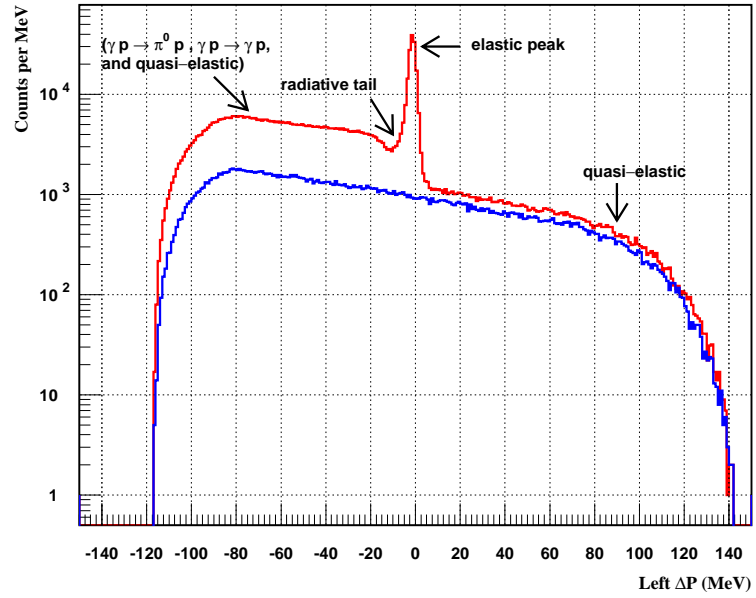
Figure 5.8: Q_{eff} uncorrected left arm ΔP spectrum for LH_2 (red) and dummy (blue) targets from kinematics b.

final Q_{eff} uncorrected ΔP spectra for the LH$_2$ and dummy targets for both the right and left arm spectrometers. The resolution of the elastic peak is dominated by the angular resolution. The right arm elastic peak has a broader width than the left arm elastic peak. This is due to the fact that at low momentum, ΔP is more sensitive to the angular resolution of the spectrometer, causing a broadening of the ΔP peak.

5.4   The Effective Charge Normalization

After adding all the LH$_2$ and all of the dummy histograms from the runs in a given kinematics, the final Q_{eff} uncorrected ΔP histogram must be divided by Q_{eff}. The effective charge as defined in section 4.1 was calculated for each LH$_2$ run using equation (4.1).

The dummy target is an empty target with thicker aluminum windows than the actual entrance and exit windows of the LH$_2$ target. In determining Q_{eff}, equation (4.1), we must correct for the effective thickness of the dummy target. The reason we use an effective thickness for the dummy target is the bremsstrahlung initiating reactions, primarily in the downstream endcap. The bremsstrahlung are different for LH$_2$ and dummy because of the different thicknesses and also the presence of the hydrogen. The dummy target spectrum is used to determine the shape of the endcaps contribution and the procedure of determining the effective dummy thickness is discussed in section 5.7. The final Q_{eff} is the sum of the effective charge from all the LH$_2$(dummy) runs, i.e., $\sum_i^{N_{run}} Q_{eff}^i$ where Q_{eff}^i is the effective charge for run number i and N_{run} is the total number of LH$_2$(dummy) runs.

The default and initial value of 4.11 for the effective dummy thickness was used to calculate Q_{eff} for the dummy data. The procedure of extracting the final effective dummy thickness used to extract the reduced cross section σ_R for each kinematics is discussed in section 5.7.2. This initial value seems to do a good job producing

the high ΔP side of the LH$_2$ spectrum which is mainly dominated by the quasi-elastic contribution from the endcaps. Figures 5.9 and 5.10 show normalized LH$_2$ and dummy ΔP spectra for the right and left arms, respectively.
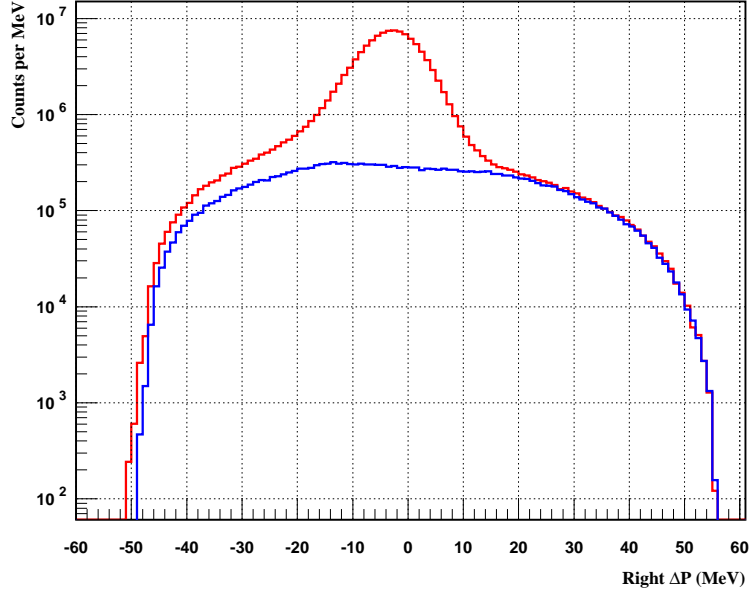
Figure 5.9: Q_{eff} corrected right arm ΔP spectrum for LH$_2$ (red) and dummy (blue) targets from kinematics b.

5.5   Monte-Carlo Simulations

5.5.1   Elastic e-p Simulations (SIMC)

The Monte Carlo simulation program SIMC is used to simulate elastic scattering for all kinematics and for both arms. The elastic e-p simulations are a crucial component of the analysis as they are used to extract the reduced cross section. SIMC was adapted from the (e,e'p) simulation program named SIMULATE that was written for SLAC experiment NE18 [63, 64], and was converted to simulate the Jefferson
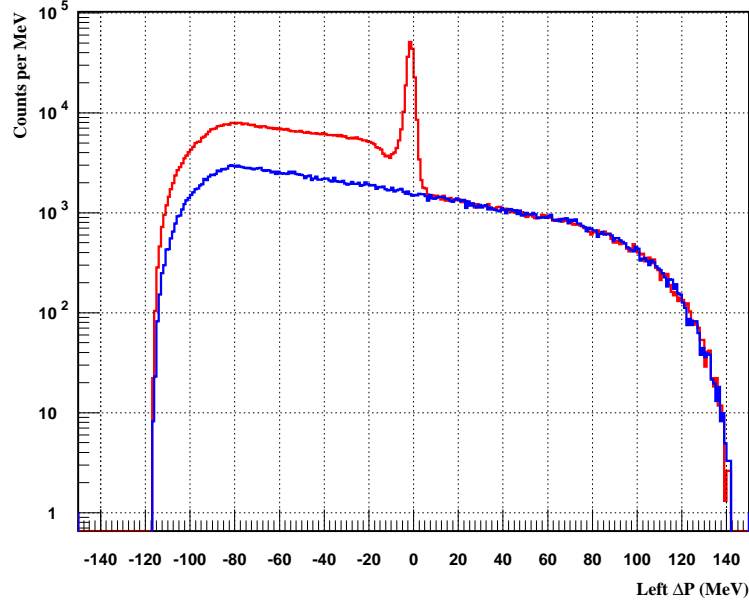
Figure 5.10: Q_{eff} corrected left arm ΔP spectrum for LH$_2$ (red) and dummy (blue) targets from kinematics b.

Lab Hall C and A spectrometers. The two main components of SIMC are the event generator, which includes the cross-section weighting and radiative corrections, and the spectrometer models. First, SIMC randomly generates the energy and position of the incident electron at the target to match the energy and spatial spread of the actual beam. In doing so, SIMC takes into account the target length and the beam raster. The beam energy is then corrected for ionization losses in the target. Moreover, SIMC randomly generates the momenta and angles of the scattered electron and proton vectors with a flat distribution over limits exceeding the actual experimental spectrometer acceptance. In our case, we generate electrons and protons in coincidence and use the Bosted cross section to weight each generated event. Having generated a basic event at the scattering vertex, SIMC allows for any or all of these events to emit real or virtual photons where the corresponding event vectors are adjusted and radiatively corrected [97]. The scattered electron and proton vectors are

transported through the target where ionization energy losses and multiple scattering in the target material, cells, and chamber are applied. Finally, only the scattered protons are transported through the spectrometers.

Transporting the protons through the spectrometer was done using the spectrometer optics models built in the Monte Carlo simulation program COSY [98]. COSY generates both the forward and backward sets of matrix elements to simulate the optical resolution of the magnetic systems in the spectrometer. Note that all the material the protons have to travel through in the spectrometer and the detector stack are included, and the multiple scattering due to all the material is calculated. However, we do not account for proton absorption in the simulations since we correct the data for that. The forward matrix elements transport the particle vectors from the entrance window of the spectrometer to its focal plane going through every major aperture in the spectrometer. SIMC assures that these particles have gone through each of these apertures by checking the acceptance of each aperture using a set of apertures cuts. These apertures include the front, middle, and back aperture of each magnetic element ($QQDQ$ configuration), the aperture of the vacuum can after the Q_3 quadrupole, the aperture of the rectangular collimator, and the aperture of each detector that was used as a fiducial cut. In addition, VDCs smearing is applied to the particle positions at the two VDCs to match those of the actual VDCs. The backward matrix elements then reconstruct or transport back the particle vectors to the target vertex where they are corrected for energy loss and multiple scattering and the elastic ΔP spectrum for a given kinematics is then reconstructed.

When comparing the shape of the elastic peak from data to that of simulations, it was obvious that the width of the elastic peak from data was broader than that of simulations. In addition, there was a clear mismatch between the shape of elastic tail from data and that of simulations. To resolve these issues, we compare the ΔP spectrum from coincidence data to that of simulations since the coincidence data

represent a pure protons sample without any background. Since the peak width is limited by the angular resolution of the spectrometer, we smear the angular resolution of the spectrometer in the simulations using a symmetric gaussian function to better fit the observed peak widths. We also apply an additional non-gaussian smearing to better match the tails. Figures 5.11 and 5.12 show the normalized LH$_2$ ΔP spectrum along with the elastic e-p simulations for the right and left arms, respectively.
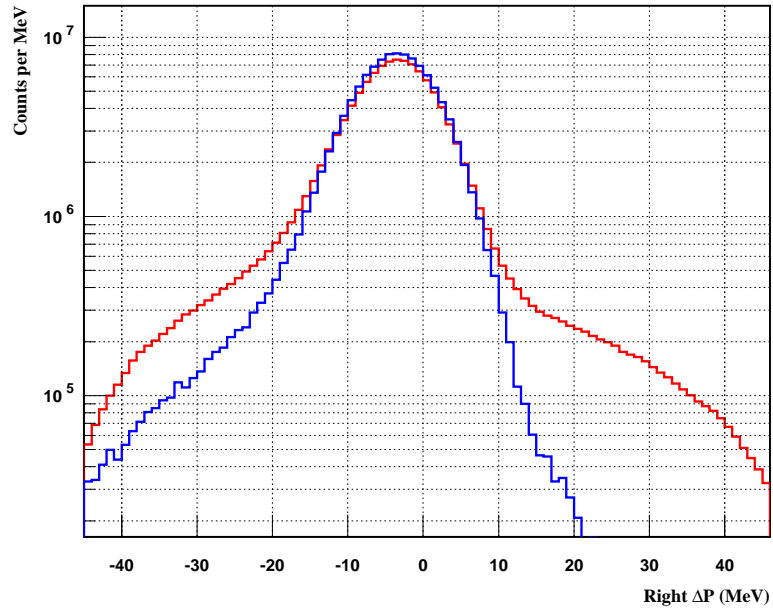
Figure 5.11: Q_{eff} corrected right arm LH$_2$ ΔP spectrum (red) and elastic e-p simulation (blue) for kinematics b.

5.5.2 $\gamma p \rightarrow \pi^0 p$ and $\gamma p \rightarrow \gamma p$ Simulations

When the electron beam passes through the target (protons in our case), electrons lose energy by radiating real photons which is known by bremsstrahlung. These real photons which impinge upon the target have a maximum energy at the beam energy. To model the ΔP spectrum for these high energy π^0 protons, we first calculate the
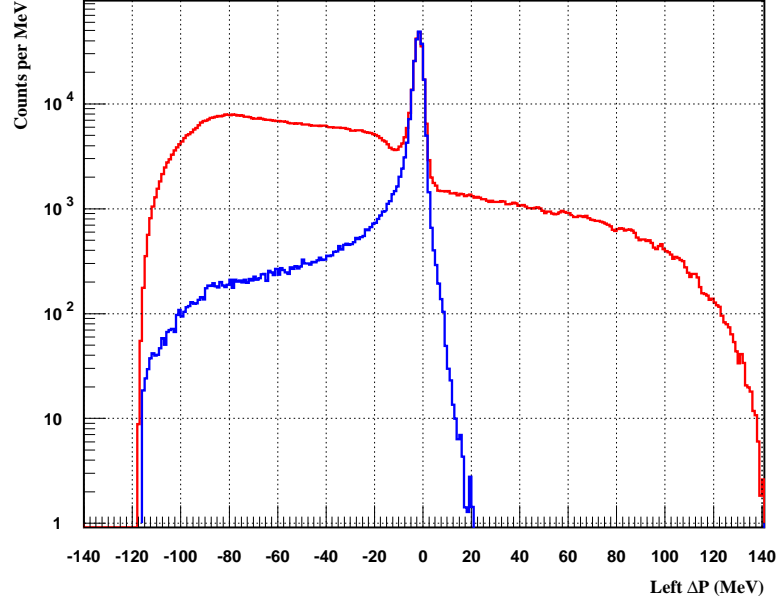
Figure 5.12: Q_{eff} corrected left arm LH$_2$ ΔP spectrum (red) and elastic e-p simulation (blue) for kinematics b.

bremsstrahlung cross section and reconstruct the E_γ spectrum for these photons [86], and then randomly generate photons according to the E_γ spectrum. The next step is to uniformly and randomly generate protons over the acceptance and this is done according to the event generation procedure discussed before. The generated event is then weighted by an s^{-7} cross section dependence, as predicted by the high energy approximation and based on the constituent counting rules or s^{-n}, forming the shape of the ΔP spectrum used for the $\gamma p \to \pi^0 p$ contribution. Note that the generated proton is transported through the spectrometer using the spectrometer optics models mentioned before. Finally, the shape of the $\gamma p \to \pi^0 p$ ΔP spectrum from simulations is normalized to that of data as discussed in section 5.7.3.

Previous experiments [99] indicated that the ratio of the $\gamma p \to \gamma p$ to the $\gamma p \to \pi^0 p$ cross sections (relative cross section) was 1-5%. We took the ratio from the original reference [99] and plotted it as a function of beam energy. Note that the beam energy

range quoted was very similar to that of the E01-001. There was a clear dependence on energy, with the ratio well fitted by $(0.92E - 1.2)\%$. Therefore, we rescaled the $\gamma p \rightarrow \pi^0 p \ \Delta P$ spectrum by $(0.92E - 1.2)\%$ to generate the Compton ΔP background. Figures 5.13 and 5.14 show the simulated ΔP spectrum for the $\gamma p \rightarrow \pi^0 p$ and $\gamma p \rightarrow \gamma p$ backgrounds for the left arm, respectively.
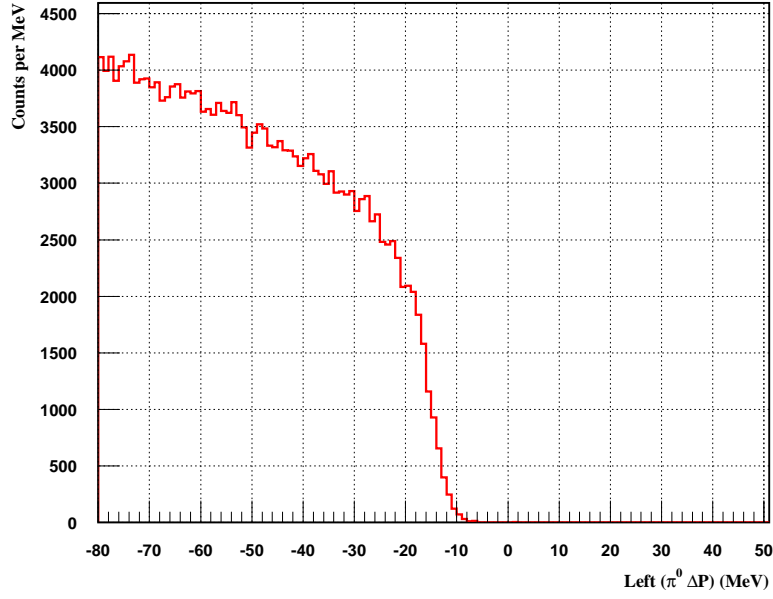
Figure 5.13: Left arm ΔP simulation for $\gamma p \rightarrow \pi^0 p$ background ($\pi^0 \Delta P$) for kinematics b.

5.6   Radiative Corrections

In this section I will start by describing the radiative corrections procedures for inclusive p(e,e')p scattering, and then discuss details of implementation for E01-001. The Lorentz invariant transition scattering amplitude equation (1.5) and hence the elastic e-p scattering differential cross section equation (1.10) were derived to lowest order in α including only the amplitude due to the exchange of a single virtual pho-
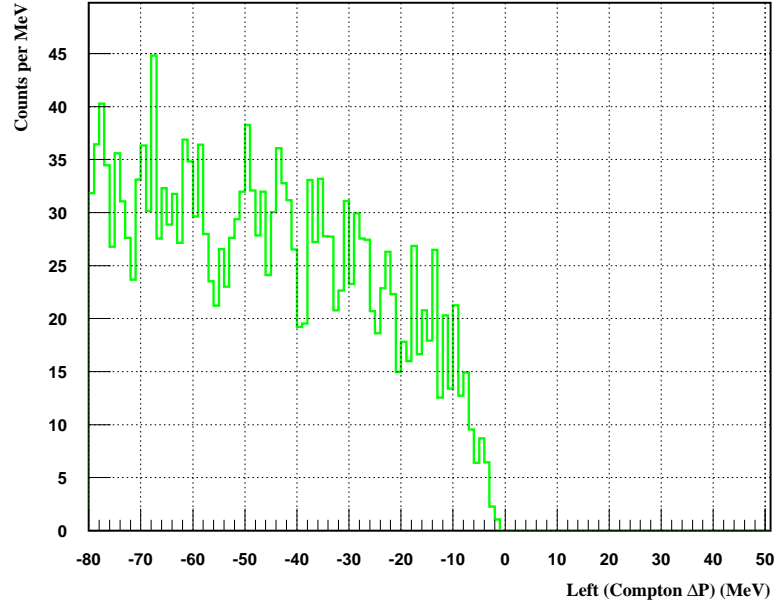
Figure 5.14: Left arm ΔP simulation for $\gamma p \to \gamma p$ background (Compton ΔP) for kinematics b.

ton between the incident electron and struck proton as shown in Figure 1.1. This is known as the Born approximation or single-photon exchange. However, in reality higher order processes in α and beyond the Born approximation also affect the cross section such as radiation of additional real and virtual photons. These processes clearly must be included. The incident electrons radiate in the presence of a nuclear field due to changes in their velocities caused by Coulomb interactions. We refer to the radiation resulting from such deceleration of the electron by bremsstrahlung or "Braking Radiation". Corrections for these higher order processes are referred to as radiative corrections. Radiative corrections are classified into internal and external radiative corrections.

- **Internal Radiative Corrections**: When the incoming and outgoing electrons interact with the Coulomb field of the nucleus involved primary in the scattering process, this results in emission and reabsorption of virtual photons and emission
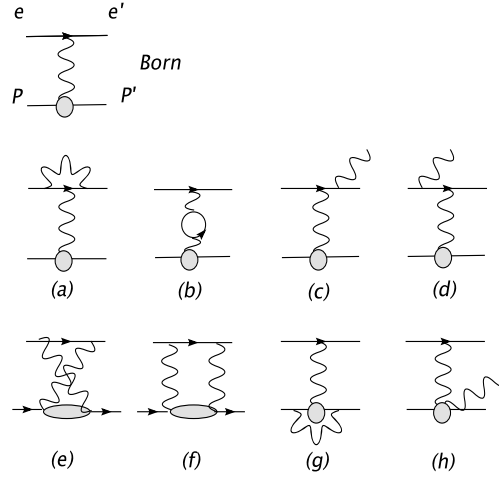
Figure 5.15: Feynman diagrams for the elastic e-p scattering including both the first-order (Born) and higher-order QCD radiative corrections (a)-(h).

of real soft photons. Figure 5.15 shows the Born term and higher-order Feynman diagrams used in the calculation of the internal radiative corrections. Note that these corrections are corrections to the principle scattering vertex itself. These internal radiative corrections are also classified into elastic radiative corrections such as vertex corrections (for both the electron and proton) Figure 5.15(a) and (g), vacuum polarization or loop diagrams Figure 5.15(b), and two-photon-exchange (TPE) Figure 5.15(e) and (f). The inelastic radiative corrections involve the emission of real photons such as internal bremsstrahlung (for either electron or proton) Figure 5.15(c), (d), and (h). Higher-order processes due to three or more photon exchange (Coulomb corrections) and emission of multiple real photons are also possible.

Corrections that involve only lepton-photon or lepton-lepton vertices (electron vertex and electron bremsstrahlung) are exactly calculable in QED. Corrections that involve photon-proton vertices (proton vertex, TPE, proton bremsstrahlung,

and Coulomb corrections) are not exactly calculable in QED and must be either estimated or measured.

- **External Radiative Corrections**: When the incoming and outgoing electrons interact with the Coulomb field of a nucleus other than the one involved in the primary scattering vertex, this also results in emission of real photons. Such radiative processes are caused by bremsstrahlung in material that the electron passes through before and after the scattering.

As we see, the radiative processes are real physical processes which depend on the target material, geometry, and kinematics of the scattering. They affect the data by modifying the cross section of the process and the kinematics (momentum, energy, and angle) of the incident electron or final state of the electron and proton. Emission of these real photons causes the detected particle's momentum to be different from the actual momentum at the scattering vertex and therefore distorts the experimental spectra. On the other hand, amplitudes involving the emission of additional virtual particles such as TPE processes affect only the magnitude of the measured cross section. The procedure for doing such radiative corrections was first derived by Schwinger [40] and later modified by Mo and Tsai [44].

The δ-function that multiplies equation (1.11) is used to assure elastic scattering in the case of the electron, that is, at a given energy E and angle θ_e, the elastic differential cross section is a δ-function in E' at $E' = E_{elastic} = E - \frac{Q^2}{2M_p}$ where E' is given by equation (1.14). See section 1.3 for more details. Bremsstrahlung radiative processes cause the elastic cross section to change from the simple δ-function (modified by finite resolution, small angle scattering, and energy spread of the beam) to an asymmetric peak with an extended tail at lower energies as shown in Figures 5.7 and 5.8 in the case of the proton. Note that this radiative tail extends down to values of ΔP where other inelastic processes such as pion production yields high energy electron, or for the case of proton detection, high energy protons generated from photoreaction $\gamma p \rightarrow \pi^0 p$ and

$\gamma p \rightarrow \gamma p$ also occur. The procedure of extracting the elastic e-p scattering reduced cross section σ_R will be discussed in section 5.7 and sub-sections therein.

To convert the measured cross section to the single-photon-exchange cross section, the Born cross section of $O(\alpha)$, we use the radiative corrections procedure of Mo and Tsai [44] as modified by Walker [7, 57] and Ent [97, 63] and implemented in the elastic e-p simulation code SIMC [63, 64]. Therefore, we write:

$$\frac{d\sigma}{d\Omega}\Big|_{Measured} = (1 + \delta_{corr})\frac{d\sigma}{d\Omega}\Big|_{Born} , \qquad (5.9)$$

where $\delta_{corr} = (\delta_{int} + \delta_{int}' + \delta_{ext})$ and δ_{int} and δ_{ext} represent the internal and external radiative corrections, respectively. The additional term δ_{int}' results from the improvements made to the internal radiative corrections by Walker. For corrections higher than $O(\alpha^3)$, we exponentiate δ_{corr} and we write:

$$\frac{d\sigma}{d\Omega}\Big|_{Measured} = e^{\delta_{corr}}\frac{d\sigma}{d\Omega}\Big|_{Born} . \qquad (5.10)$$

5.6.1 Internal Radiative Corrections δ_{int}

The internal radiative corrections δ_{int} are determined based on the modification made by Walker [7, 57] and Ent [97] to the work of Mo and Tsai [44]. They include the processes of: vacuum polarization, TPE, electron and proton vertex corrections, and internal bremsstrahlung. Note that the approximation used in equation (5.10) for higher order corrections is mainly valid only for the infrared divergent terms and the error caused by neglecting the nondivergent terms is estimated to be < 1% [100, 101, 102, 103, 104]. The contributions from vacuum polarization and electron vertex corrections are calculated exactly. However, the contributions from TPE are limited only to the infrared divergent contributions (nondivergent terms have been

neglected). Therefore, the contributions to δ_{int} can be written as:

$$\delta_{int} = \frac{-\alpha}{\pi}\left(\frac{28}{9} - \frac{13}{6}ln(\frac{Q^2}{m_e^2}) + \delta_{int.bremss.}\right) , \tag{5.11}$$

where $\delta_{int.bremss.}$ is the internal bremsstrahlung contribution and will be discussed next.

For the internal bremsstrahlung, the calculations are done under the assumption used by Tsai [39] that $\Delta E(1 + \frac{2E}{M_p}) \ll E'$ where M_p is the mass of the proton, E is the incident energy of the electron, E' is the final energy of the electron, and ΔE is the E' cutoff of the elastic peak or $\Delta E = E_{elast} - E_{cutoff}$. The resulting expression is rather lengthy and complicated. In general it has a complicated dependence on the incident energy of the electron, final energy of the electron, final energy of the proton, and ΔE. To achieve uncertainty better than 1% in the radiative corrections, corrections to this approximation were made by Walker [7, 57] as part of the improvements he made to the internal radiative corrections represented by δ_{int}'.

5.6.2 Walker's Improved Internal Radiative Corrections δ_{int}'

For a full description of the improvements made to the internal radiative corrections, the reader is referred to Walker [7, 57] where he discussed these corrections in detail. However, I will just summarize briefly these improvements. The term δ_{int}' is just an improvement on the precision to the original internal radiative correction. These improvements include correction for the $\Delta E(1 + \frac{2E}{M_p}) \ll E'$ approximation made by Tsai to the internal bremsstrahlung, inclusion of the $q\bar{q}$ and $\mu^+\mu^-$ contributions to the vacuum polarization or loop diagrams which were neglected previously, and correction for a sign error in Tsai's paper [39] for the Schwinger's correction [40] to the noninfrared divergent part of the soft photon emission cross section.

5.6.3   External Radiative Corrections δ_{ext}

The external radiative corrections δ_{ext} are determined based on the modification made by Walker [7, 57] and Ent [97] to the work of Mo and Tsai [44]. The external radiative corrections are corrections applied to the cross section due to bremsstrahlung in the target material (major contribution), spectrometer material, and the small effects of the Landau tail of the ionization energy loss spectrum [105]. When the incident electron interacts with the Coulomb field of a nucleus other than the one involved primary scattering vertex, it will emit bremsstrahlung and hence lose energy. The cross section of an electron of initial energy E that scatters elastically from a proton and has a final energy $E' = E_{elast} - \Delta E'$, when the electron is emitting bremsstrahlung photons with t_i and t_f radiation lengths of material before and after the scattering, is:

$$\frac{d^2\sigma(E,E')}{d\Omega dE'} = \left(\frac{R\Delta E'}{E}\right)^{b_i t_i}\left(\frac{R\Delta E'}{E_{elast}}\right)^{b_f t_f}\frac{1}{\Gamma(1+b_i t_i)}\frac{1}{\Gamma(1+b_f t_f)}$$
$$\times\left[\frac{d\sigma(E)}{d\Omega}\frac{b_f t_f}{\Delta E'}\phi\left(\frac{\Delta E'}{E_{elast}}\right) + \frac{d\sigma(E-R\Delta E')}{d\Omega}\frac{b_I t_I}{\Delta E'}\phi\left(\frac{R\Delta E'}{E}\right)\right], \quad (5.12)$$

where the parameter $b \sim 3/4$ [106], the parameter R represents the recoil of the proton and is $\approx \left(\frac{E}{E'}\right)^2$, and the function $\phi\left(\frac{R\Delta E'}{E}\right) = \phi\left(\frac{\omega}{E}\right)$ gives the shape of the bremsstrahlung spectrum which is normalized to one at $\frac{\omega}{E} =$ zero where ω is the lost energy of the electron after passing a thickness of t radiation lengths. The external radiative corrections δ_{ext} can be then expressed in terms of the electron cross section equation (5.12) as:

$$\delta_{ext} = ln\left(\frac{1}{\frac{d\sigma(E)}{d\Omega}}\left[LT_{corr}\int_{E_{elast}-\Delta E'}^{E_{elast}}\frac{d^2\sigma(E,E')}{d\Omega dE'}dE'\right]\right), \quad (5.13)$$

where LT_{corr} is the correction for the Landau tail as calculated from the Landau distribution [105]. Note that the integrand diverges as $\Delta E' \to$ zero due to the soft

photon bremsstrahlung spectrum. To handle this problem, the integral is usually calculated for $\Delta E' < \delta_\gamma$ where δ_γ is the soft-photon cut. When calculating δ_{ext}, one needs an accurate geometrical model of the target along with precise knowledge of the materials of which the target is made. This information is built in the elastic e-p simulation code SIMC.

5.6.4   E01-001 Specific Radiative Corrections

As mentioned before, we use the radiative corrections procedure of Mo and Tsai as modified by Walker and Ent and implemented in the elastic e-p simulation code SIMC. Full coincidence (e,e'p) simulations are performed using the prescription of Ent [97] taking into account bremsstrahlung from all three tails (bremsstrahlung from the incident electron, scattered electron, and scattered proton). The bremsstrahlung from these particles is calculated in the extended peaking approximation [97, 63]. Furthermore, only the contribution from the infrared divergent part of TPE is included.

Based on equation (1.34) and because of the factor τ that multiplies G_{Mp}^2, the cross section is dominated by G_{Mp}^2 at large Q^2. That is, σ_R in the Born approximation has only a small ε dependence at large Q^2. Therefore, understanding the ε dependence of the radiative correction δ_{corr} at large Q^2 becomes absolutely important as a few percent change in the ε slope of σ_R would have a sizable effect on $\frac{\mu_p G_{Ep}}{G_{Mp}}$.

The main ε dependence to the radiative corrections comes from the internal and external bremsstrahlung corrections (and possibly the neglected TPE terms). Bremsstrahlung corrections are usually accounted for in the conventional radiative corrections procedure used and they enter differently depending on whether the electron or proton are detected in the final state. On the other hand, several calculations in the 1950s and 1960s estimated the size of TPE to be extremely small ($\leq 1\%$) [100, 101, 102, 103, 104] and therefore was neglected in the conventional radiative corrections procedure used. An important point is that the infrared divergent part of

the TPE contribution cancels fully the corresponding infrared divergent contribution from the interference between the electron and proton bremsstrahlung. Furthermore, the finite part of TPE has always been neglected. Recently it has been found that the finite part of TPE has a significant ε dependence and it should not be neglected [16, 107, 108]. Figure 3.6 shows the radiative correction factor calculated for internal contributions only as a function of ε for $Q^2 = 2.64$ GeV^2. While the magnitude of the corrections is similar and both show an approximately linear dependence on ε, the dependence is much smaller for protons, $\sim -8\%$, than for the electron $\sim 17\%$. Note that when detecting the electron, the ε dependence of the bremsstrahlung correction exceeds the ε dependence coming from G_{Ep} which is not the case in the E01-001 experiment.

Previous Rosenbluth measurements [7, 8, 9] estimated scale and random uncertainties in the radiative corrections of $\sim 1.0\%$ and $\sim 0.60\%$, respectively. In these measurements, electrons rather than protons were detected. In our case, we assign the same scale uncertainty of 1.0% for both arms and take a 50% of the random uncertainty as quoted by the previous measurements or $\sim 0.30\%$. This is due to the fact that detecting protons will yield a smaller ε dependence bremsstrahlung correction as discussed above. We split the 0.30% uncertainty into a slope and random uncertainties with more emphasize on the slope contribution of 0.30% and random contribution of 0.20%. For the right arm, the same random uncertainty of 0.20% is assigned, while the slope uncertainty is expected to be small due to the small $\Delta\varepsilon$ range of 0.07. Note that for the left arm, the average $\Delta\varepsilon$ range of 0.70 is accounted for when the slope uncertainty is estimated. Therefore, we estimate the slope uncertainty for the right arm to be 3.0% (0.30% × 0.70/0.07) but use a smaller and more realistic figure of 2.0% since the radiative corrections are expected to be small in a such limited $\Delta\varepsilon$ range.

Finally and based on Figure 3.6, a relative $\sim 30\%$ radiative correction is needed

to bring the cross sections measured by detecting electrons and those measured by detecting protons into agreement. That is, before the radiative corrections are applied the electron and proton cross sections have an ε dependence that differs by as much as $\sim 30\%$. The extracted slope from the two measurements after the correction is applied agree to within uncertainty of 1-2%. If we assume an average uncertainty in the slope of 1.5%, this yields a fractional uncertainty in a 30% correction of 1.5%/30 = 5%. For the proton, a 5% uncertainty in a 10% ε dependence bremsstrahlung correction yields a $\sim 0.50\%$ uncertainty which is comparable to the combined 0.36% uncertainty estimated for the E01-001 measurements. It is important to mention that this is the first time a comparison between the electrons and protons measurements has been made. The excellent agreement in the extracted slope or G_{Ep}^2 from the two measurements provides a strong test of the validity of the standard radiative corrections used.

5.7 The e-p Reduced Cross Section σ_R

5.7.1 Overview

In this section the procedure for extracting σ_R is discussed. Figure 5.1 shows a flow chart of the procedure used. From Figures 5.7 and 5.8, we see that the LH$_2$ spectrum is dominated by the elastic e-p peak. In addition, there are backgrounds due to quasi-elastic scattering from the aluminum target windows and protons generated from photoreactions $\gamma p \rightarrow \pi^0 p$ and $\gamma p \rightarrow \gamma p$ that contribute to the ΔP spectrum. There is no region where only one component, the elastic peak or inelastic backgrounds, is significant. Therefore, the spectra has to be unraveled and this is done with aid of the simulated spectra but first the simulated and measured spectra have to be put on the same energy scale as will be discussed below.

5.7.2 The Effective Dummy Thickness and Endcaps Subtraction

In this section the procedure of extracting the effective dummy thickness will be discussed. We start by subtracting the Q_{eff} corrected dummy spectrum using an initial dummy thickness factor ($\frac{\text{dummy}}{\text{endcap}}$ ratio) of 4.11 from the Q_{eff} corrected LH$_2$ spectrum. Figures 5.16, 5.17, and 5.18 show this procedure for a low ε left arm spectrum, a high ε left arm spectrum, and a right arm spectrum, respectively.

The resultant LH$_2$ ΔP spectrum is then compared to that of elastic e-p simulation as generated by SIMC. The experimental e-p peak is shifted relative to that of the simulation. Therefore, we shift the position of the e-p peak from data to match that of simulation. Figures 5.19, 5.20, and 5.21 illustrate this procedure. The contribution of the $\gamma p \to \pi^0 p$ and $\gamma p \to \gamma p$ backgrounds to the LH$_2$ ΔP spectrum is the difference between the dummy subtracted LH$_2$ ΔP spectrum and elastic e-p simulation. From Figure 5.21 we see that the contribution of these backgrounds to the right arm LH$_2$ ΔP spectrum is almost negligible. The momentum acceptance of the spectrometers is $\pm 5\%$. For the higher momentum protons detected in the left arm, the momentum acceptance is great enough to be flat over the region of interest. However, for the low momentum protons detected in the right arm, the falling acceptance at the lowest ΔP results in a distortion of the spectrum at the low momentum end. This region was not used in extracting the cross sections. However, because the shape of the right arm spectrum is almost the same at all the kinematics, this distortion would only introduce a scale uncertainty in the reduced cross sections. For the left arm, Figures 5.19 and 5.20 show that the contribution of these backgrounds to the LH$_2$ ΔP spectrum is significant. As the cross sections of the π^0 protons are forward peaked, the contribution to the LH$_2$ ΔP spectrum is larger for low ε than for large ε.

After we shift the position of the e-p peak from data to match that of the simula-
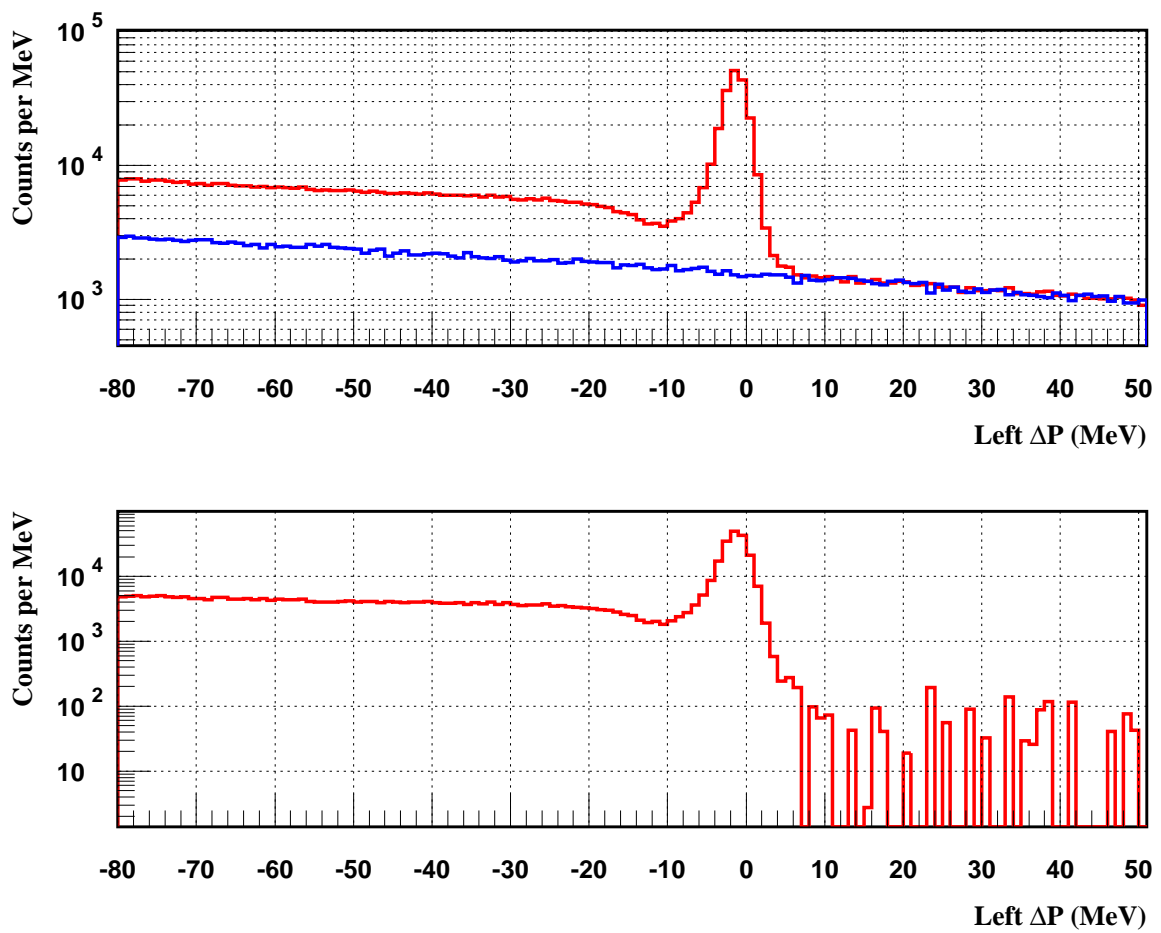
Figure 5.16: The initial left arm dummy subtraction for kinematics b (low ε). Top: the left arm LH$_2$ ΔP spectrum (red) and dummy ΔP spectrum (blue). Bottom: the dummy subtracted LH$_2$ ΔP spectrum. An initial dummy thickness factor of 4.11 was used.
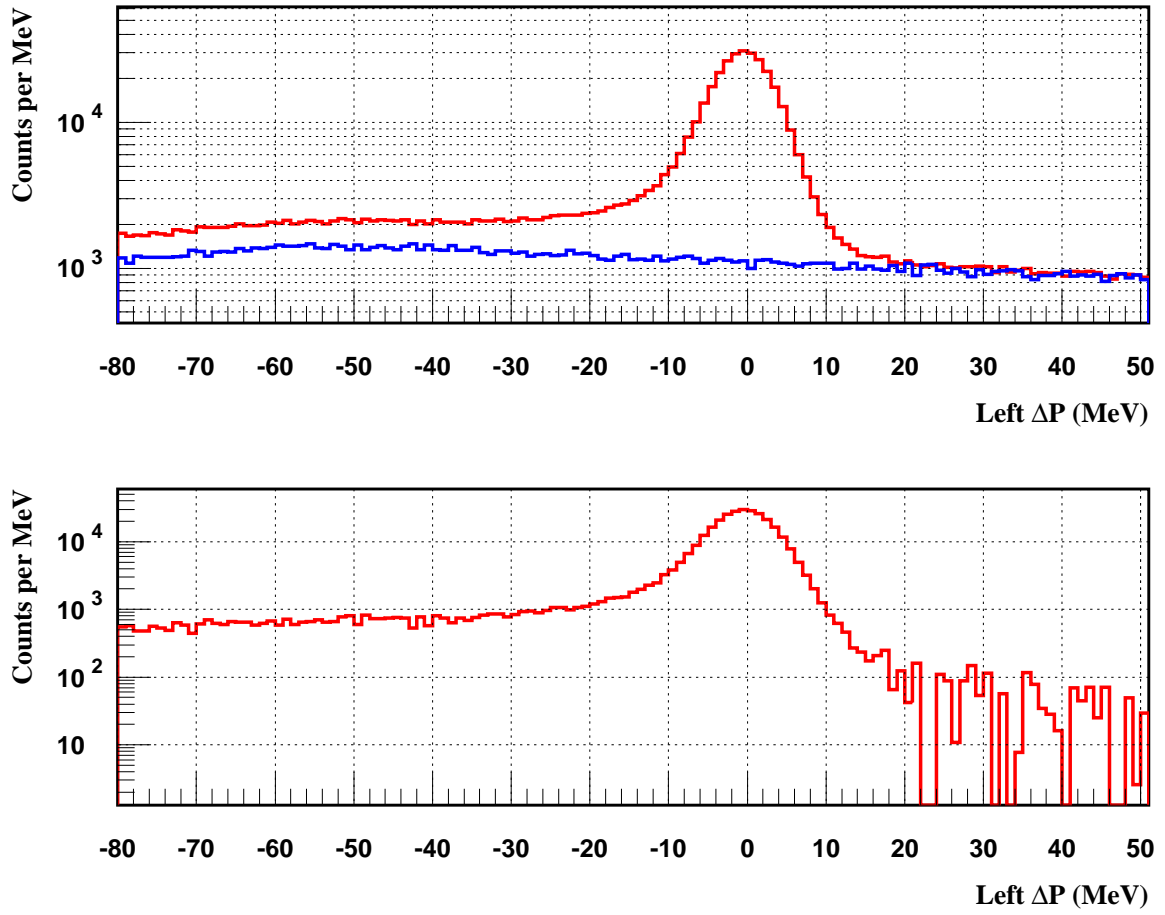
Figure 5.17: The initial left arm dummy subtraction for kinematics m (high ε). Top: the left arm LH$_2$ ΔP spectrum (red) and dummy ΔP spectrum (blue). Bottom: the dummy subtracted LH$_2$ ΔP spectrum. An initial dummy thickness factor of 4.11 was used.
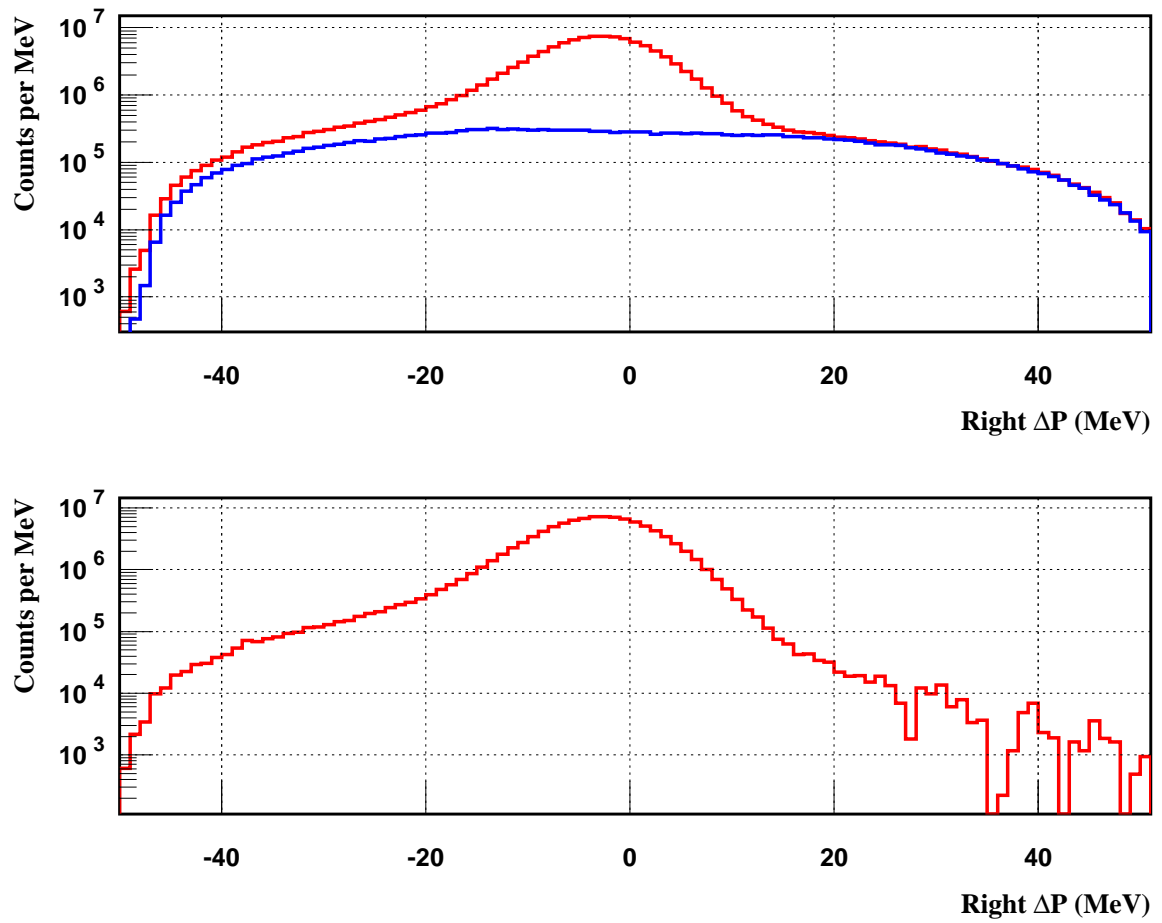
Figure 5.18: The initial right arm dummy subtraction for kinematics b. Top: the right arm LH$_2$ ΔP spectrum (red) and dummy ΔP spectrum (blue). Bottom: the dummy subtracted LH$_2$ ΔP spectrum. An initial dummy thickness factor of 4.11 was used.
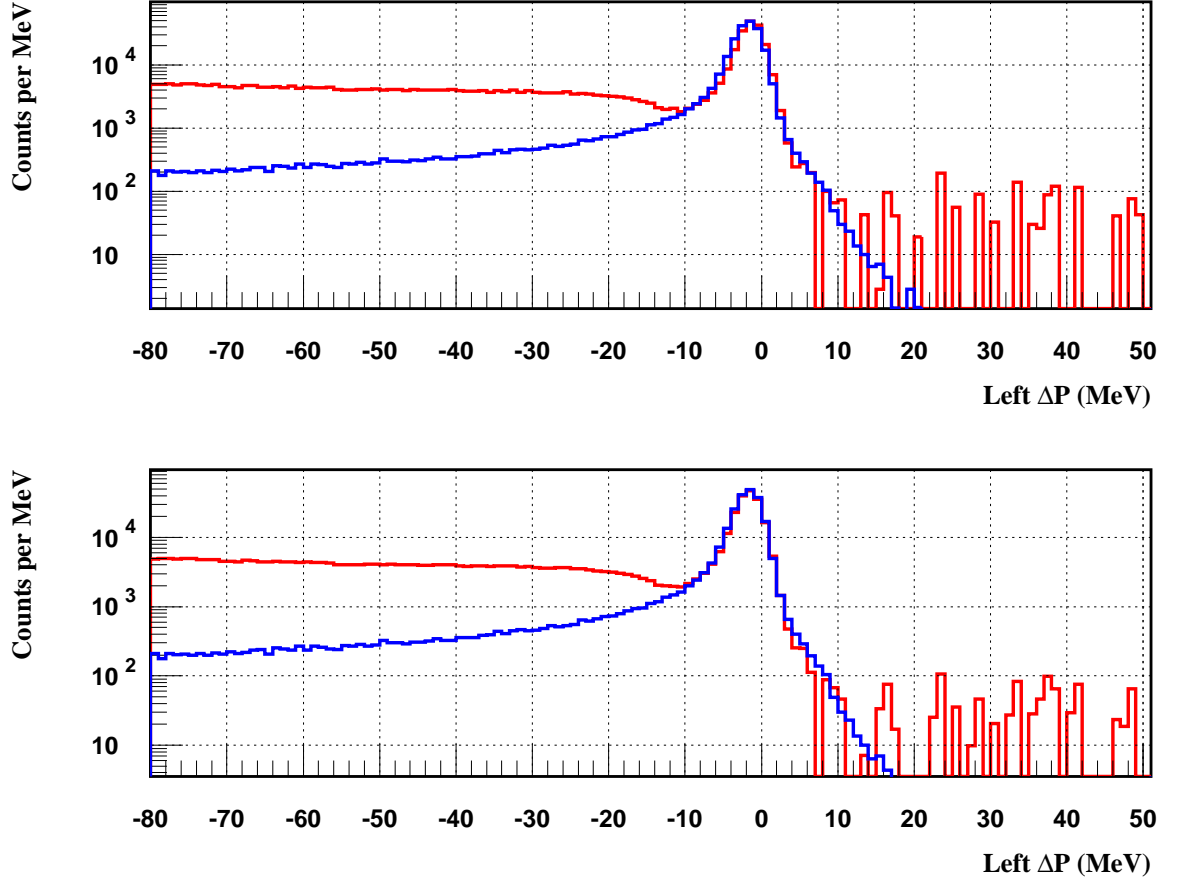
Figure 5.19: The left arm dummy subtracted LH$_2$ ΔP spectrum and elastic e-p simulation for kinematics b (low ε). Top: the left arm unshifted dummy subtracted LH$_2$ ΔP spectrum (red) and elastic e-p simulation (blue). Bottom: the left arm shifted dummy subtracted LH$_2$ ΔP spectrum (red) and elastic e-p simulation (blue). This data are from kinematics b, using the nominal incident energy and scattering angle. The final version after applying the angular shift to the scattering angle (see section 4.4) yields much smaller shift.
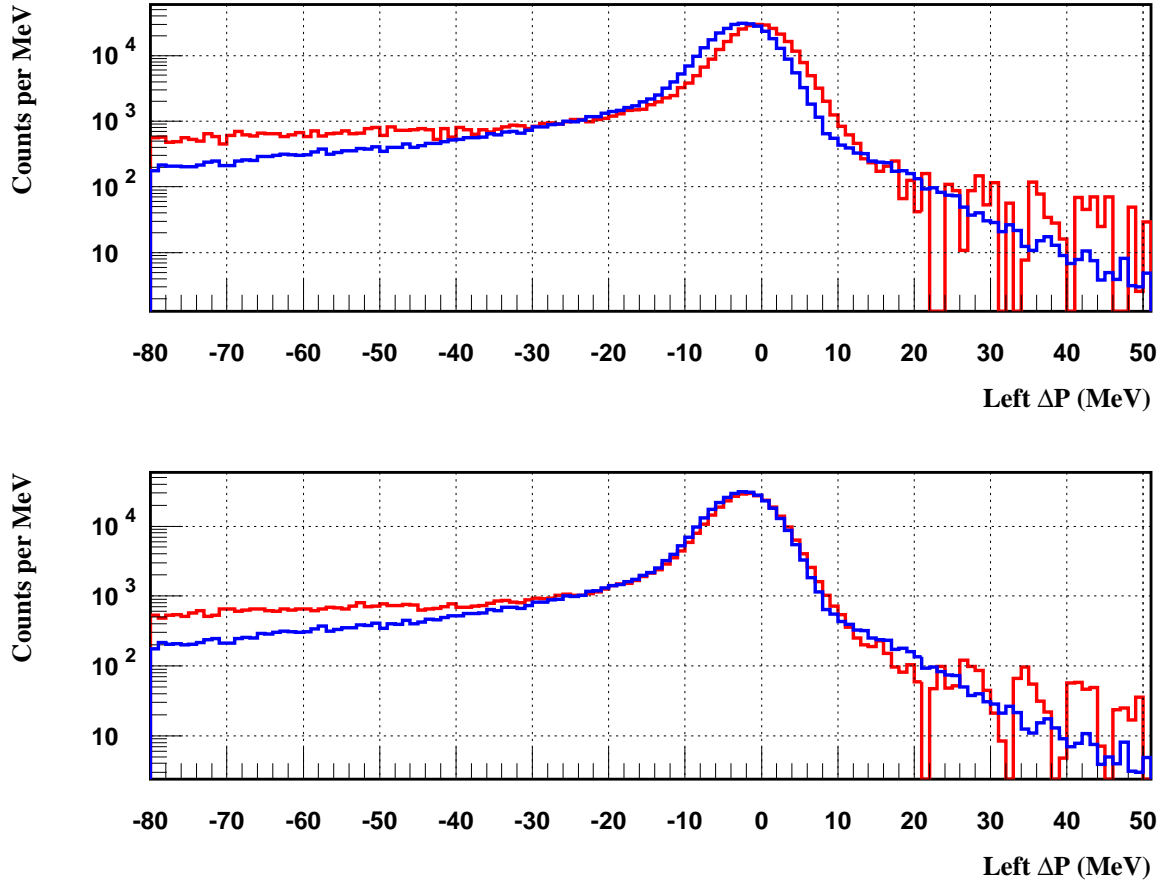
Figure 5.20: The left arm dummy subtracted LH$_2$ ΔP spectrum and elastic e-p simulation for kinematics m (high ε). Top: the left arm unshifted dummy subtracted LH$_2$ ΔP spectrum (red) and elastic e-p simulation (blue). Bottom: the left arm shifted dummy subtracted LH$_2$ ΔP spectrum (red) and elastic e-p simulation (blue). This data are from kinematics m, using the nominal incident energy and scattering angle. The final version after applying the angular shift to the scattering angle (see section 4.4) yields much smaller shift.

193
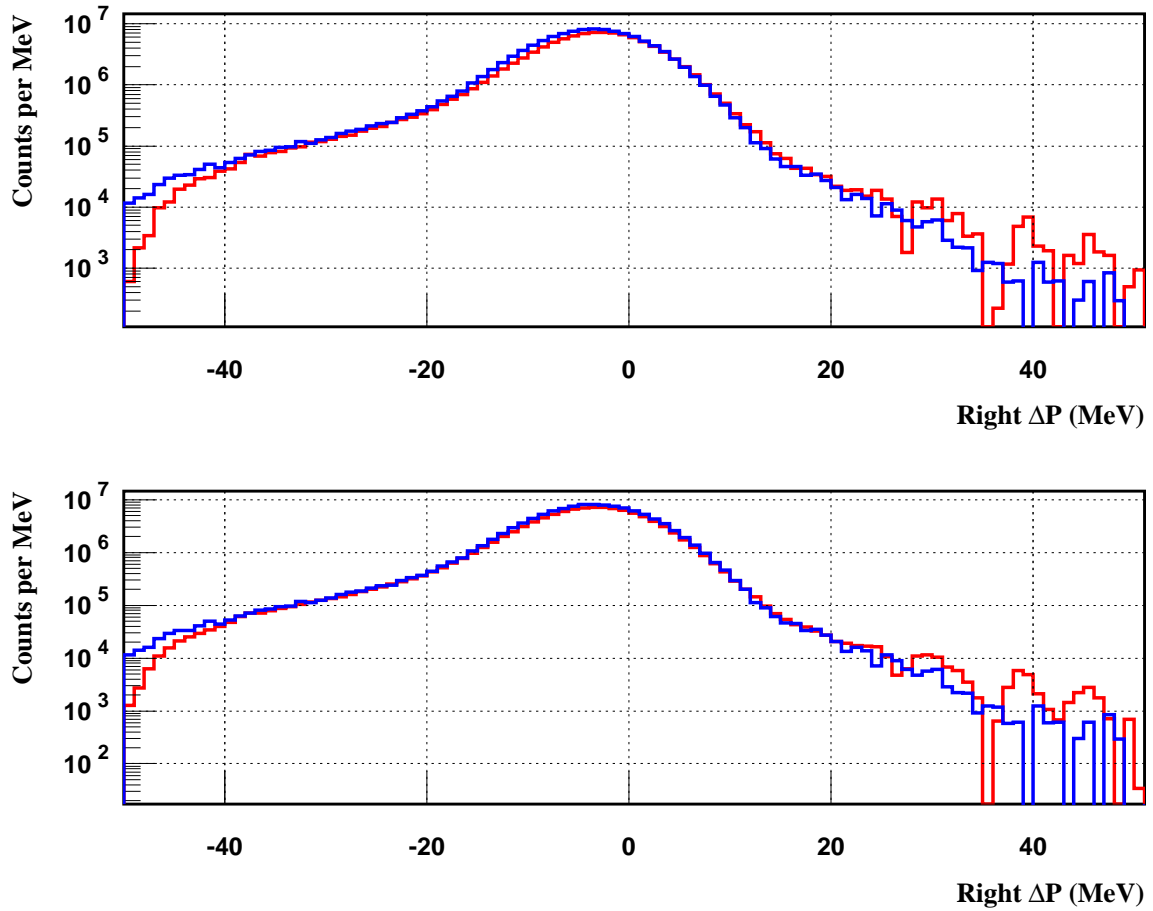
Figure 5.21: The right arm dummy subtracted LH$_2$ ΔP spectrum and elastic e-p simulation for kinematics b. Top: the right arm unshifted dummy subtracted LH$_2$ ΔP spectrum (red) and elastic e-p simulation (blue). Bottom: the right arm shifted dummy subtracted LH$_2$ ΔP spectrum (red) and elastic e-p simulation (blue). This data are from kinematics b.

tion, we compare the two ΔP spectra over a region where the elastic e-p simulation ΔP bin content is larger than 10% of that of the peak. The number of LH$_2$ events, N_{LH_2}, and number of e-p elastic, N_{e-p}, for that window is used to determine the scaling factor $\gamma_{e-p} = (N_{LH_2}/N_{e-p})$ needed to scale the elastic e-p simulation to match that of LH$_2$. Figures 5.22 and 5.23 illustrate this procedure.

Knowing that the contribution from the elastic LH$_2$ events to the LH$_2$ ΔP spectrum at large ΔP is small, the shape of the endcaps spectrum can be reliably determined by normalizing the difference between the LH$_2$ ΔP and that of the scaled elastic e-p simulation "extracted dummy" to that of the original Q_{eff} corrected dummy spectrum in the range of ΔP>30 MeV. Figures 5.24, 5.25, and 5.26 illustrate this procedure.

The number of events in the extracted dummy spectrum, $N_{extracted}$, and the number of events in the original dummy spectrum, $N_{original}$, for that window is used to determine the correction factor $\gamma_{dummy} = (N_{original}/N_{extracted})$ needed to correct the initial default value of the dummy thickness and hence define the new effective dummy thickness:

$$\text{Effective Dummy Thickness} = \frac{\text{Default Dummy Thickness}}{\gamma_{dummy}} = \frac{4.11}{\gamma_{dummy}}, \qquad (5.14)$$

which is used to correct Q_{eff} for the dummy and hence scale the dummy target spectrum for the final subtraction. The original and extracted dummy spectra are shown for both arms in the bottom right hand side plots of Figures 5.24, 5.25, and 5.26. Figure 5.27 shows the effective dummy thickness for all kinematics and for both arms. For the left arm, the effective dummy thicknesses are consistent with random fluctuation of (1-2)% from the average. The average effective dummy thickness is 0.22% thicker than the default dummy thickness used initially. For the right arm, the effective dummy thicknesses are consistent with random fluctuation of (2-3)% from the average, but the average effective dummy thickness is 5.15% less than the default
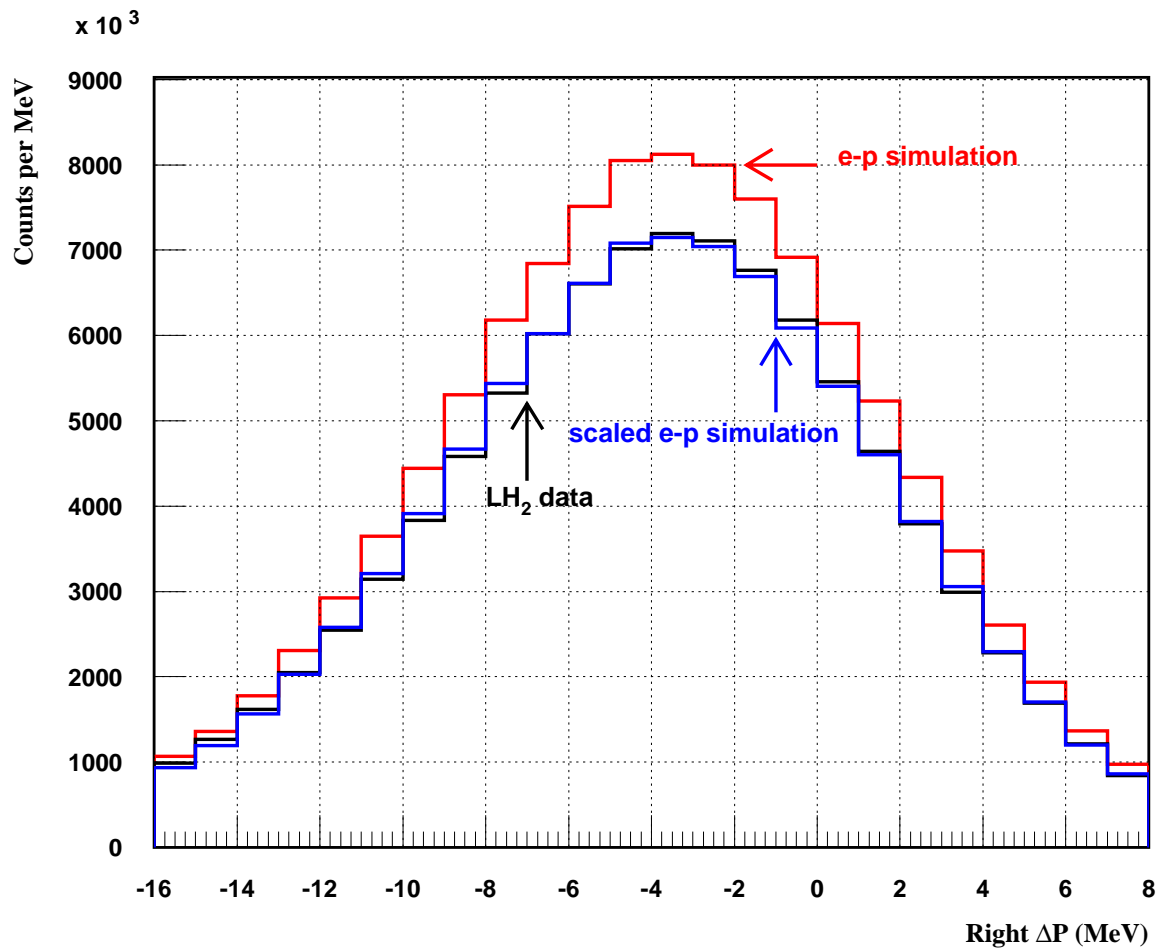
Figure 5.22: Right arm ΔP spectrum for LH_2 data (black), elastic e-p simulation (red), and scaled elastic e-p simulation (blue) for kinematics b.
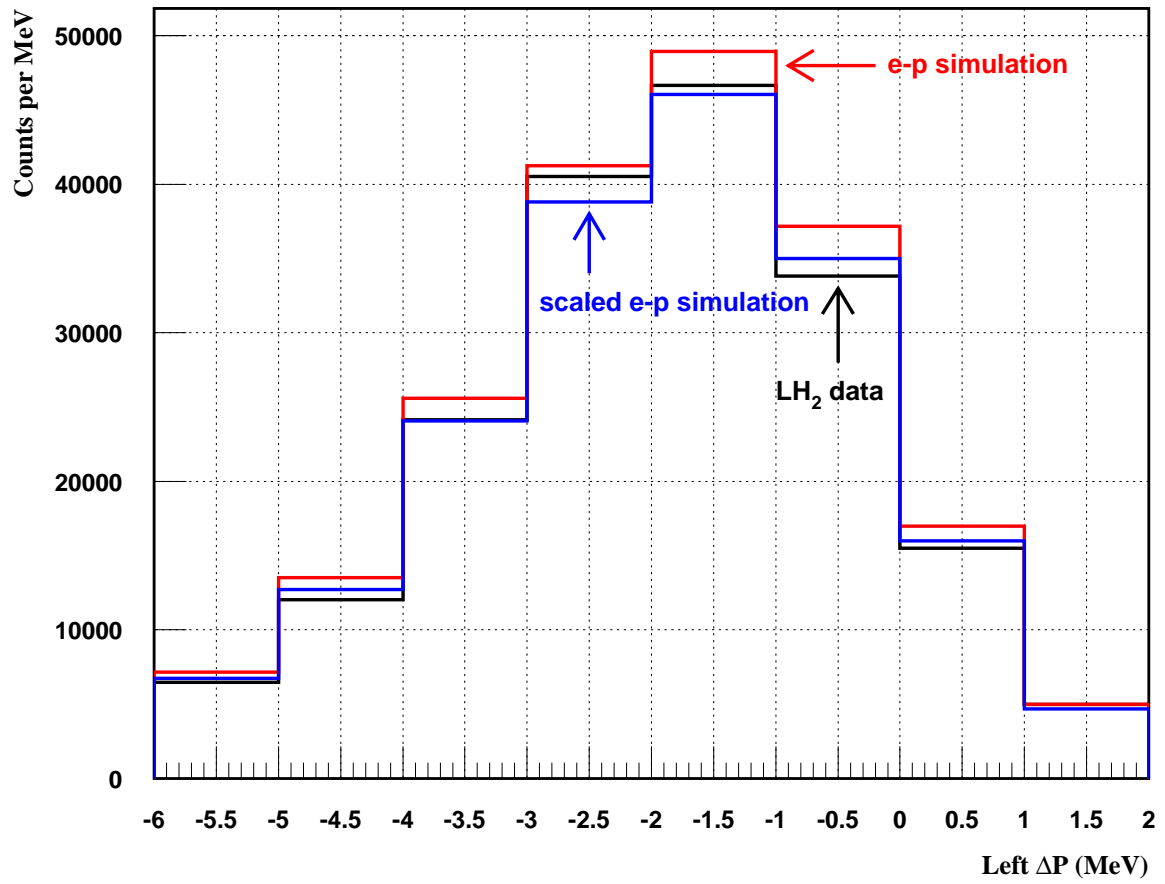
Figure 5.23: Left arm ΔP spectrum for LH$_2$ data (black), elastic e-p simulation (red), and scaled elastic e-p simulation (blue) for kinematics b.
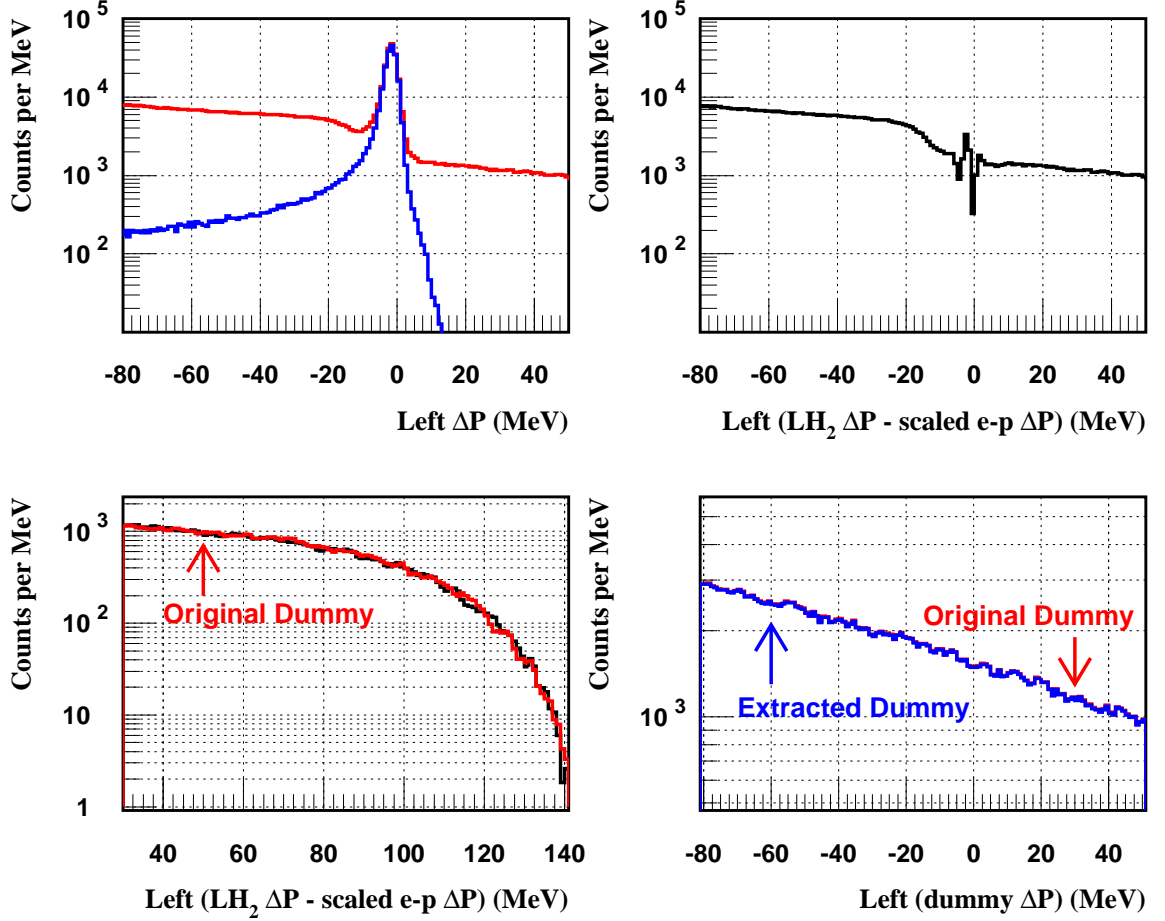
Figure 5.24: The left arm effective dummy target thickness extraction for kinematics *b*. Top left: The left arm dummy subtracted LH$_2$ ΔP spectrum (red) and scaled elastic e-p simulation (blue). Top right: the left arm dummy subtracted LH$_2$ ΔP spectrum minus scaled e-p ΔP spectrum. Bottom left: The difference between the left arm dummy subtracted LH$_2$ ΔP spectrum and scaled e-p ΔP spectrum (black) is then normalized to the left arm original dummy ΔP spectrum (red) in the range of 30-140 MeV. Bottom right: The left arm original dummy spectrum (red) and the new extracted dummy spectrum (blue).
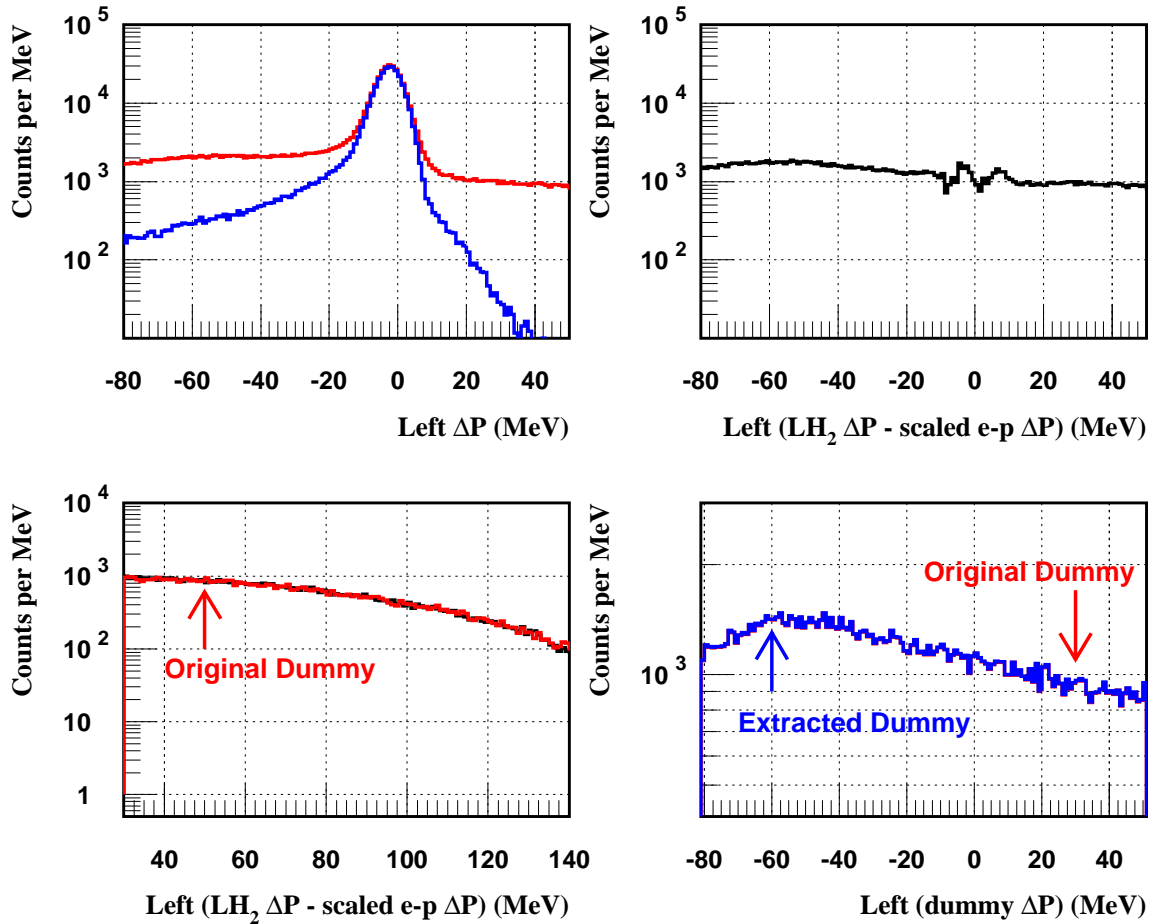
Figure 5.25: The left arm effective dummy target thickness extraction for kinematics m. Top left: The left arm dummy subtracted LH_2 ΔP spectrum (red) and scaled elastic e-p simulation (blue). Top right: the left arm dummy subtracted LH_2 ΔP spectrum minus scaled e-p ΔP spectrum. Bottom left: The difference between the left arm dummy subtracted LH_2 ΔP spectrum and scaled e-p ΔP spectrum (black) is then normalized to the left arm original dummy ΔP spectrum (red) in the range of 30-140 MeV. Bottom right: The left arm original dummy spectrum (red) and the new extracted dummy spectrum (blue).
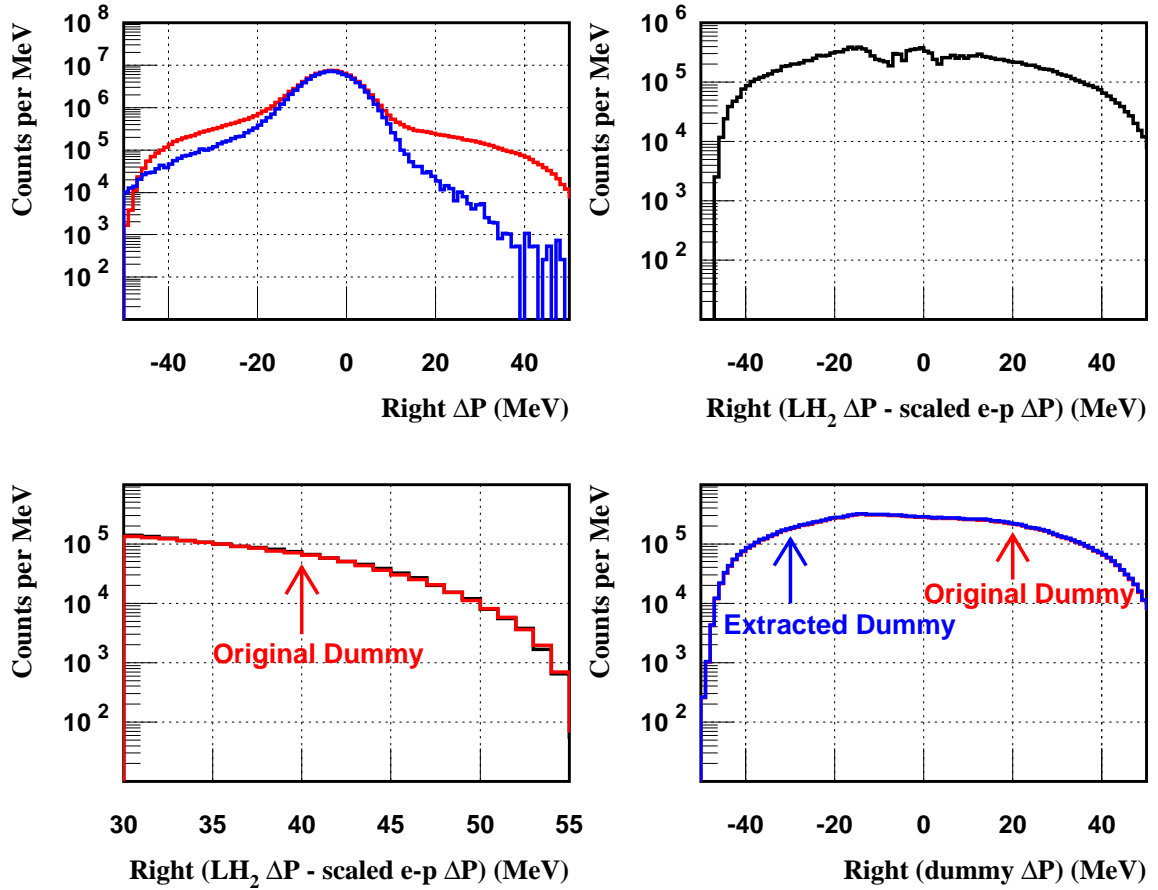
Figure 5.26: The right arm effective dummy target thickness extraction for kinematics
b. Top left: The right arm dummy subtracted LH$_2$ ΔP spectrum (red) and scaled
elastic e-p simulation (blue). Top right: the right arm dummy subtracted LH$_2$ ΔP
spectrum minus scaled e-p ΔP spectrum. Bottom left: The difference between the
right arm dummy subtracted LH$_2$ ΔP spectrum and scaled e-p ΔP spectrum (black)
is then normalized to the right arm original dummy ΔP spectrum (red) in the range
of 30-55 MeV. Bottom right: The right arm original dummy spectrum (red) and the
new extracted dummy spectrum (blue).

dummy thickness value used initially.

5.7.3   Subtracting the $\gamma p \to \pi^0 p$ and $\gamma p \to \gamma p$ Backgrounds

The next step is to subtract the protons generated from photoreactions $\gamma p \to \pi^0 p$ and $\gamma p \to \gamma p$ from the LH$_2$ ΔP spectrum. When the endcaps background and the scaled elastic e-p simulation events are subtracted from the LH$_2$ ΔP spectrum, the resultant spectrum represents the sum of the $\gamma p \to \pi^0 p$ and $\gamma p \to \gamma p$ backgrounds. For the left arm, the sum of $\gamma p \to \pi^0 p$ and $\gamma p \to \gamma p$ spectra from simulations is normalized to the (LH$_2$ - endcaps - scaled e-p simulation) spectrum in a window of -50$<$ ΔP $<$-20 MeV. The normalized simulation is then subtracted. Figures 5.28, 5.29, and 5.30 show this procedure for three representative spectra. While the uncertainty in extracting the backgrounds is larger for large ε, where the backgrounds contribution is small, even a large uncertainty in this small background yields a small uncertainty in the final extracted cross sections. The contribution of the $\gamma p \to \pi^0 p$ and $\gamma p \to \gamma p$ backgrounds to the right arm LH$_2$ spectrum is almost negligible although this contribution has a threshold that is close to the elastic peak as can be seen clearly from the bottom right hand plot of Figure 5.30. On the other hand, the contribution of the $\gamma p \to \pi^0 p$ and $\gamma p \to \gamma p$ backgrounds to the left arm LH$_2$ spectrum is much larger but with a lower threshold for the low ε case as shown in the bottom right hand plots of Figures 5.28 and 5.29. It is important to mention that for the right arm the same procedure for extracting the $\gamma p \to \pi^0 p$ and $\gamma p \to \gamma p$ backgrounds was used, and the background was found to be consistent with zero, with upper limit contribution of $<<$0.10%. Thus in the analysis, we do not make any correction for these processes and assign a 0.05% random uncertainty.

The procedure for unpealing the spectra can be iterated if necessary. However, the residual spectra after backgrounds and normalized simulated e-p are subtracted off show that this is not necessary.
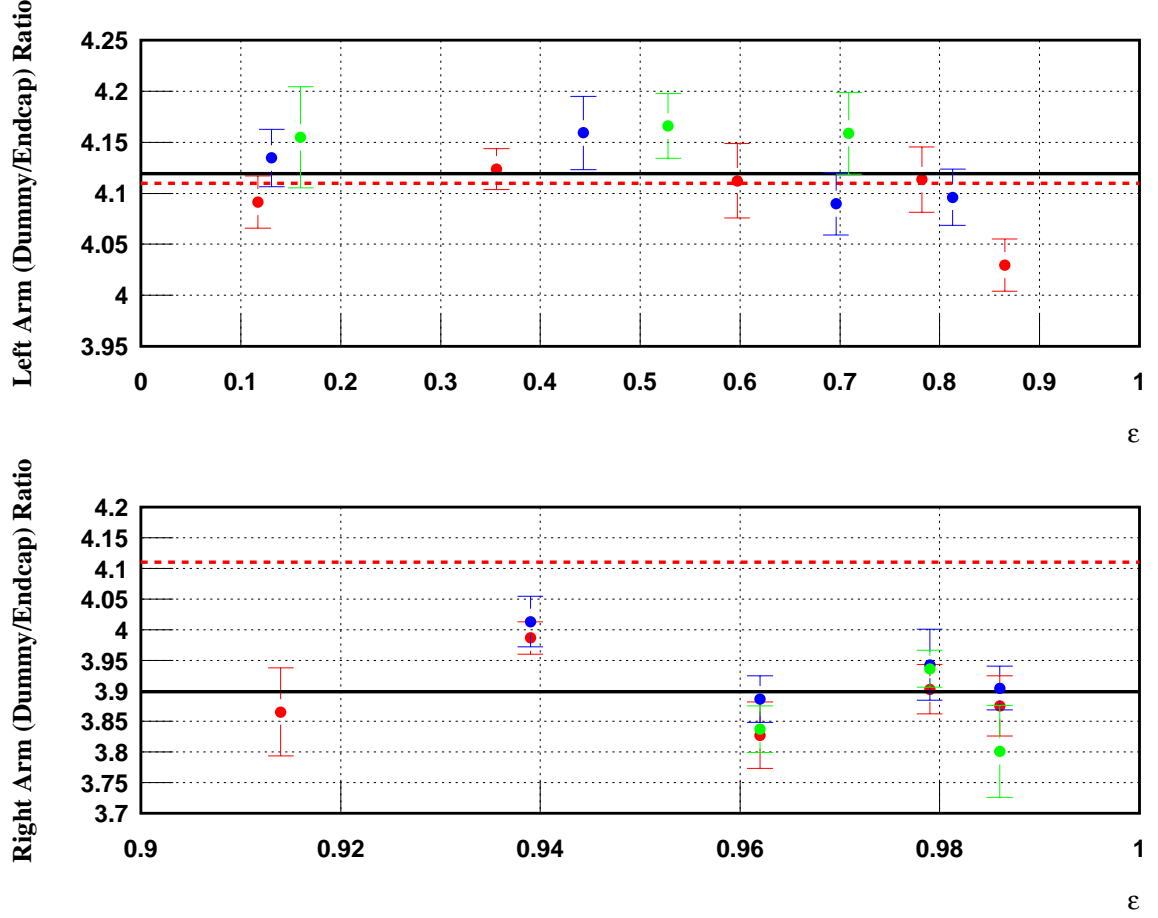
Figure 5.27: The left and right arms effective dummy thickness. Top: The left arm dummy/endcap ratio plotted as a function of increasing ε for the $Q^2 = 2.64$ GeV^2 kinematics (solid red circles), $Q^2 = 3.20$ GeV^2 kinematics (solid blue circles), and $Q^2 = 4.10$ GeV^2 kinematics (solid green circles). The solid black line is the unweighted average dummy/endcap ratio and the red dashed line is the initial default value used of 4.11. Bottom: The right arm dummy/endcap ratio plotted as a function of increasing ε for all the $Q^2 = 0.5$ GeV^2 kinematics. The same color was assigned on data so the kinematics on the right arm can be associated with their left arm counterpartner. Again, the solid black line is the average dummy/endcap ratio and the red dashed line is the initial default value used of 4.11. The uncertainty in the data is statistical only.
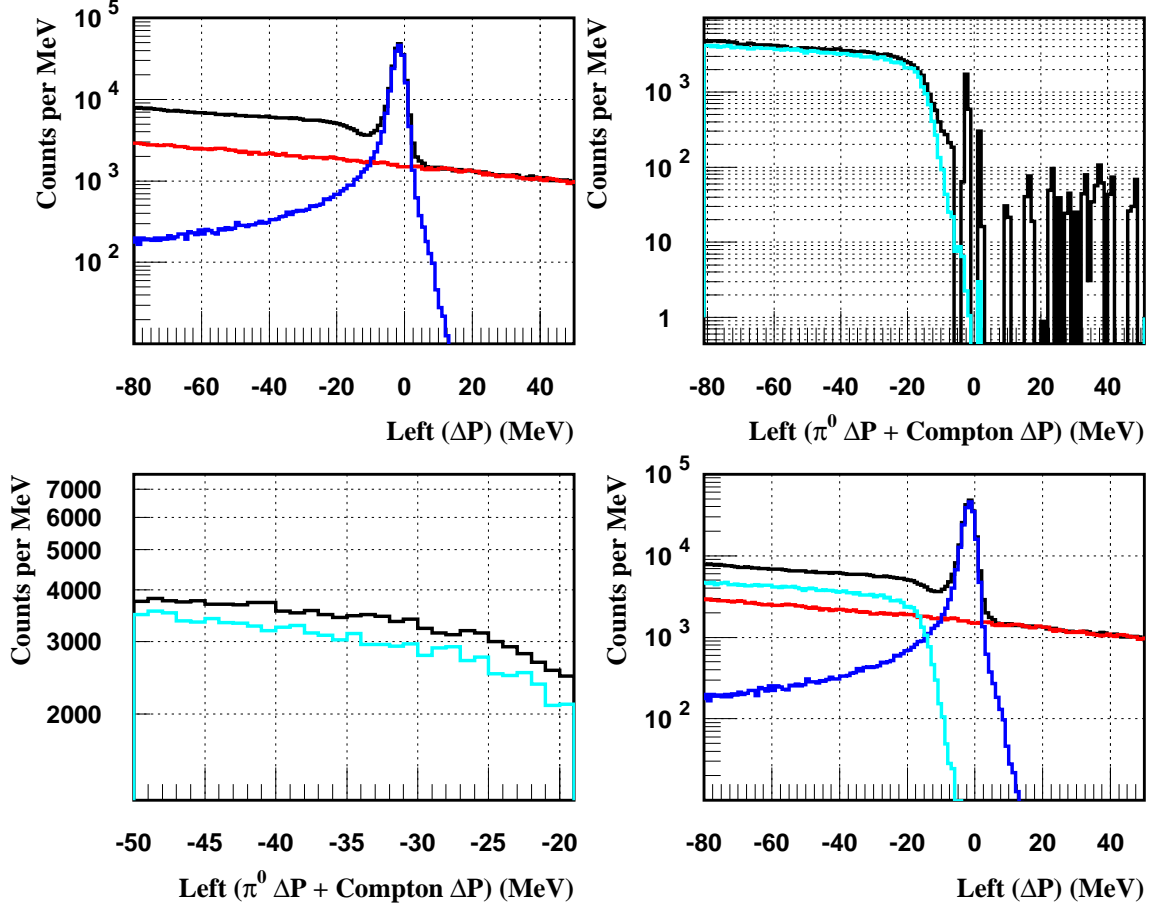
Figure 5.28: The left arm $\gamma p \rightarrow \pi^0 p$ and $\gamma p \rightarrow \gamma p$ backgrounds subtraction for kinematics b (low ε). Top left: the LH$_2$ ΔP (black), extracted dummy (red), and scaled elastic e-p simulation (blue). Top right: the sum of the $\gamma p \rightarrow \pi^0 p$ and $\gamma p \rightarrow \gamma p$ data backgrounds remaining after the subtraction of the extracted dummy and scaled elastic e-p simulation spectra from the LH$_2$ ΔP (black), and the sum of the $\gamma p \rightarrow \pi^0 p$ and $\gamma p \rightarrow \gamma p$ from simulations (cyan). Bottom left: the sum of the $\gamma p \rightarrow \pi^0 p$ and $\gamma p \rightarrow \gamma p$ as in top right above (black) and simulations (cyan) from -50 to -20 MeV. This window is used for normalization. Bottom right: the LH$_2$ ΔP (black), extracted dummy (red), scaled elastic e-p simulation (blue), and normalized sum of the $\gamma p \rightarrow \pi^0 p$ and $\gamma p \rightarrow \gamma p$ from simulations (cyan).
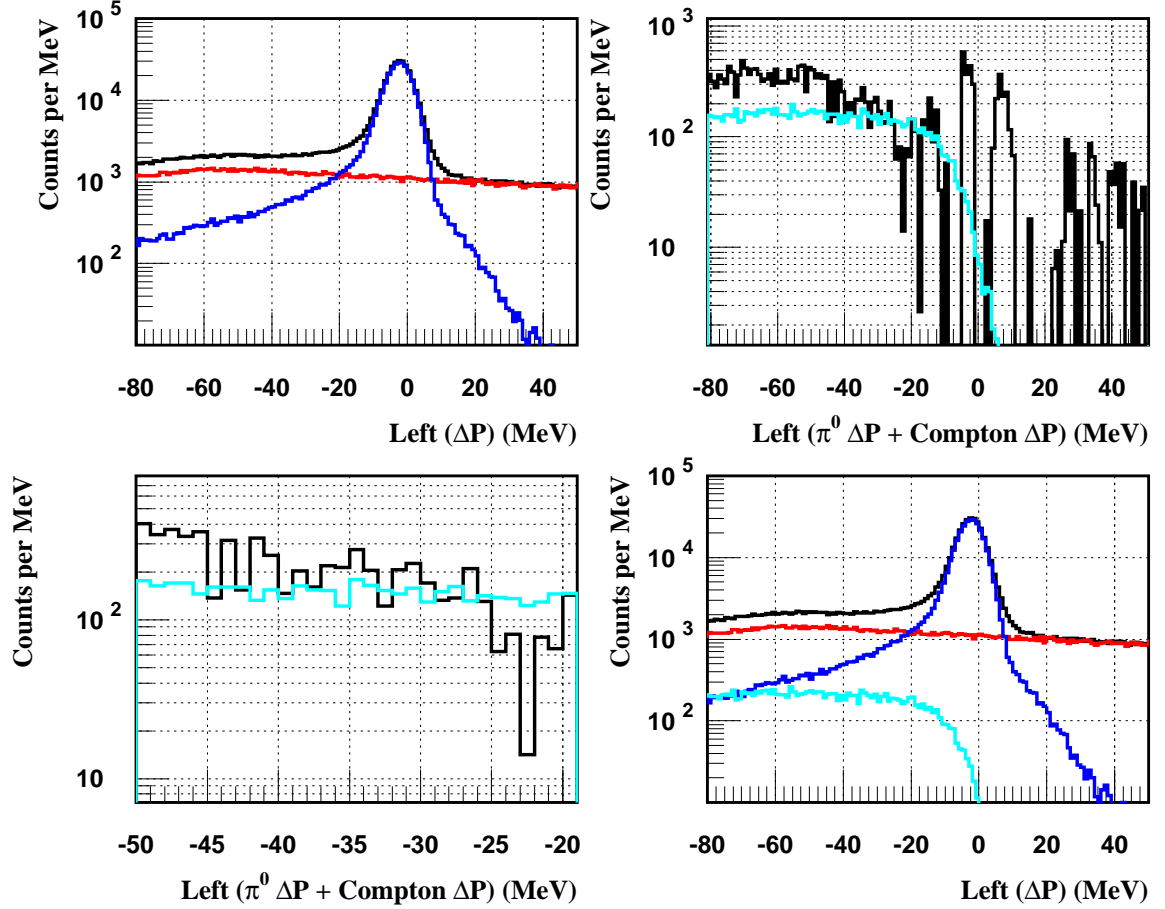
Figure 5.29: The left arm $\gamma p \to \pi^0 p$ and $\gamma p \to \gamma p$ backgrounds subtraction for kinematics m (high ε). Top left: the LH$_2$ ΔP (black), extracted dummy (red), and scaled e-p elastic simulation (blue). Top right: the sum of the $\gamma p \to \pi^0 p$ and $\gamma p \to \gamma p$ data backgrounds remaining after the subtraction of the extracted dummy and scaled e-p elastic simulation spectra from the LH$_2$ ΔP (black), and the sum of the $\gamma p \to \pi^0 p$ and $\gamma p \to \gamma p$ from simulations (cyan). Bottom left: the sum of the $\gamma p \to \pi^0 p$ and $\gamma p \to \gamma p$ as a result of the subtraction of the extracted dummy and scaled e-p elastic simulation spectra from the LH$_2$ ΔP (black) and from simulations (cyan) from -50 to -20 MeV. This window is used for normalization. Bottom right: the LH$_2$ ΔP (black), extracted dummy (red), scaled e-p elastic simulation (blue), and normalized sum of the $\gamma p \to \pi^0 p$ and $\gamma p \to \gamma p$ from simulations (cyan).

Figure 5.30: The right arm $\gamma p \to \pi^0 p$ and $\gamma p \to \gamma p$ backgrounds subtraction for kinematics b. Top left: the LH$_2$ ΔP (black), extracted dummy (red), and scaled e-p elastic simulation (blue). Top right: the sum of the $\gamma p \to \pi^0 p$ and $\gamma p \to \gamma p$ data backgrounds remaining after the subtraction of the extracted dummy and scaled e-p elastic simulation spectra from the LH$_2$ ΔP (black), and the sum of the $\gamma p \to \pi^0 p$ and $\gamma p \to \gamma p$ from simulations (cyan). Bottom left: the sum of the $\gamma p \to \pi^0 p$ and $\gamma p \to \gamma p$ as a result of the subtraction of the extracted dummy and scaled e-p elastic simulation spectra from the LH$_2$ ΔP (black) and from simulations (cyan) from -50 to -20 MeV. This window is used for normalization. Bottom right: the LH$_2$ ΔP (black), extracted dummy (red), scaled e-p elastic simulation (blue), and normalized sum of the $\gamma p \to \pi^0 p$ and $\gamma p \to \gamma p$ from simulations (cyan).

5.7.4 Extracting the Reduced Cross Section σ_R

The top left plots of Figures 5.31, 5.32, and 5.33 show the individual contributions to the ΔP spectrum for the three representative spectra. In order to extract σ_R, the ratio of elastic e-p data events to unscaled elastic e-p simulation events $R = (N_{\text{elastic-data}}/N_{e-p})$ is determined in a ΔP window around the elastic peak. In determining the range of the ΔP window used for each kinematics, the ΔP window cut was varied to simultaneously minimize the ε-dependence of the dummy and pions subtraction, as well as the elastic acceptance correction. The top right plots of Figures 5.31, 5.32, and 5.33 show the individual contributions in this ΔP window cut while the magenta solid line represents the sum of all contributions. The number of elastic events $N_{\text{elastic-data}}$ in that ΔP window is determined as:

$$N_{\text{elastic-data}} = N_{LH_2} - N_{dummy} - N_{\gamma p \to \pi^0 p} - N_{\gamma p \to \gamma p} \ . \tag{5.15}$$

Tables 5.3 and 5.4 list the range of the ΔP window used and the extracted ratio R for each kinematics for both arms. Having determined the ratio R, the unscaled elastic e-p simulation is scaled as $N_{e-p}^{new} = R \, N_{e-p}$ and then added to the remaining contributions:

$$N_{\text{total}} = N_{e-p}^{new} + N_{dummy} + N_{\gamma p \to \pi^0 p} + N_{\gamma p \to \gamma} \ , \tag{5.16}$$

to generate the sum spectrum shown which reproduces the LH$_2$ ΔP spectrum very well. The reduced cross section σ_R is taken to be the value of the reduced cross section from the Bosted fit, $\sigma_R \text{ (Bosted)}$, used in the simulation scaled by the ratio R or:

$$\sigma_R = R \, \sigma_R \text{ (Bosted)} = R \left[\tau G_{Mp}^2(Q^2) + \varepsilon G_{Ep}^2(Q^2) \right] \ , \tag{5.17}$$

where the form factors $G_{Ep}(Q^2)$ and $G_{Mp}(Q^2)$ at a given Q^2 point are determined
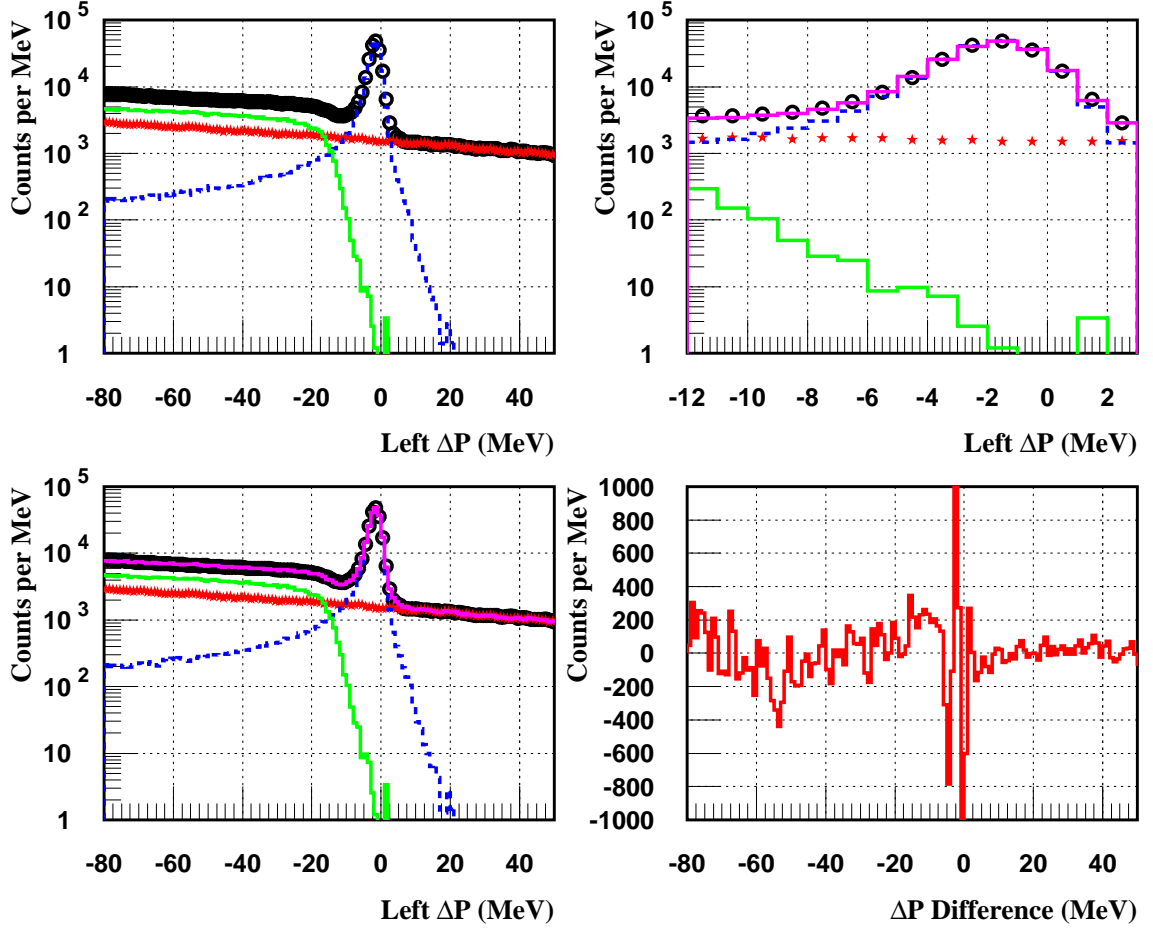
Figure 5.31: All contributions to the left arm LH$_2$ ΔP spectrum for kinematics b (low ε). Top left: the LH$_2$ ΔP data (black circles), unscaled elastic e-p simulation (blue dashed line), extracted dummy (red stars), normalized sum of the $\gamma p \rightarrow \pi^0 p$ and $\gamma p \rightarrow \gamma p$ backgrounds (solid green). Top right: the same as in Top left but for a smaller ΔP window cut to show the final ΔP window used for the final ratio extraction. The magenta line through the data is the sum of all contributions. See text for more details. Bottom left: the same as in Top right but for a larger ΔP window. Bottom right: the difference between the LH$_2$ ΔP data and the sum of all contributions.

Figure 5.32: All contributions to the left arm LH$_2$ ΔP spectrum for kinematics m (high ε). Top left: the LH$_2$ ΔP data (black circles), unscaled elastic e-p simulation (blue dashed line), extracted dummy (red stars), normalized sum of the $\gamma p \to \pi^0 p$ and $\gamma p \to \gamma p$ backgrounds (solid green). Top right: the same as in Top left but for a smaller ΔP window cut to show the final ΔP window used for the final ratio extraction. The magenta line through the data is the sum of all contributions. See text for more details. Bottom left: the same as in Top right but for a larger ΔP window. Bottom right: the difference between the LH$_2$ ΔP data and the sum of all contributions.

Figure 5.33: All contributions to the right arm LH$_2$ ΔP spectrum for kinematics b. Top left: (black circles) LH$_2$ ΔP data, (blue dashed line) unscaled elastic e-p simulation, (red stars) the modified target walls background, (solid green) the modified sum of the $\gamma p \to \pi^0 p$ and $\gamma p \to \gamma p$ backgrounds. Top right: the same as in Top left but for a smaller ΔP window cut to show the final ΔP window needed for the final ratio extraction. The magenta line through the data is the sum of all contributions. See text for more details. Bottom left: the same as in Top right but for a larger ΔP window cut. Bottom right: the difference between the LH$_2$ ΔP data and the sum of all contributions.

Q^2 (GeV^2)	Kinematics	Right ΔP Window From : To (MeV)	Right Ratio $R \pm \delta_R$
0.50	o	-19.0 : +11.0	0.9970 ± 0.0024
	a	-19.0 : +11.0	1.0021 ± 0.0020
	i	-18.0 : +12.0	0.9881 ± 0.0022
	q	-18.0 : +12.0	0.9919 ± 0.0021
	l	-18.0 : +12.0	0.9896 ± 0.0028
0.50	b	-19.0 : +11.0	1.0010 ± 0.0021
	j	-18.0 : +12.0	0.9883 ± 0.0019
	p	-18.0 : +12.0	0.9921 ± 0.0022
	m	-18.0 : +12.0	0.9884 ± 0.0026
0.50	k	-18.0 : +12.0	0.9865 ± 0.0020
	r	-18.0 : +12.0	0.9923 ± 0.0020
	n	-18.0 : +12.0	0.9838 ± 0.0029

Table 5.3: The ΔP window range used and the extracted ratio R for the right arm kinematics. The listed uncertainties in the ratios are statistical only.

Q^2 (GeV^2)	Kinematics	Left ΔP Window From : To (MeV)	Left Ratio $R \pm \delta_R$
2.64	o	-12.0 : +2.0	1.0156 ± 0.0030
	a	-12.0 : +6.0	1.0084 ± 0.0026
	i	-12.0 : +9.0	1.0054 ± 0.0033
	q	-13.0 : +11.0	1.0038 ± 0.0029
	l	-14.0 : +12.0	1.0022 ± 0.0026
3.20	b	-12.0 : +3.0	1.0236 ± 0.0036
	j	-12.0 : +8.0	1.0241 ± 0.0033
	p	-12.0 : +12.0	1.0152 ± 0.0033
	m	-14.0 : +14.0	1.0234 ± 0.0029
4.10	k	-12.0 : +5.0	1.0296 ± 0.0049
	r	-15.0 : +10.0	1.0368 ± 0.0037
	n	-17.0 : +13.0	1.0454 ± 0.0040

Table 5.4: The ΔP window range used and the extracted ratio R for the left arm kinematics. The listed uncertainties in the ratios are statistical only.

from the Bosted parameterization equations (2.2) and (2.3). Tables 5.5 and 5.6 list the reduced cross sections and their uncertainties for each kinematics for both arms. Note that the statistical uncertainty in σ_R includes the statistical uncertainty in all of the yields in equation 5.15, as well as statistical uncertainty in the extracted dummy normalization factor.

To estimate the size of the uncertainty in the dummy subtraction, we plot the ratio of N_{dummy} to N_{LH_2} events or "Dummy Subtraction" in the ΔP window cut used as a function of kinematics number and for both arms. Figures 5.34 and 5.35 show the results for the right and left arm, respectively. The dummy subtraction is a $\sim$ 10% correction for both arms and with a $\sim$ 2% slope dependence for the left arm and $\sim$ 0.5% for the right arm. We assign a 5% systematic uncertainty in the dummy subtraction correction which yields a slope uncertainty of 0.10% for the left arm and 0.36% (0.025%/0.07) for the right arm when we consider the $\Delta \varepsilon$ range of 0.07. Furthermore, a 5% uncertainty in a 10% correction yields a scale uncertainty of 0.5% for the both arms. The random uncertainty is set to 0.0% to avoid double counting the random uncertainty in the dummy subtraction since the statistical uncertainty in the effective dummy thickness as shown in Figure 5.27 is taken into account when calculating the statistical uncertainty δ_R in the ratio R for both arms. See Tables 5.3 and 5.4.

Similarly, to estimate the size of the uncertainty in the pion subtraction, we plot the ratio of $(N_{\gamma p \rightarrow \pi^0 p} + N_{\gamma p \rightarrow \gamma p})$ to N_{LH_2} events "Pion Subtraction" in the ΔP window cut used as a function of kinematics number and for both arms. Figure 5.36 shows the results for the left arm. The pion subtraction is typically a $\sim$ 0.5% correction for the left arm with a large scatter and ε dependence. We assign a $\sim$ 50% uncertainty in the pion subtraction correction or 0.25% with almost equal contribution from the slope (0.20%) and random (0.15%) uncertainties. The slope and random uncertainties are doubled for $Q^2 = 4.10$ GeV^2 to account for the larger observed ε dependence. For the

Q^2 (GeV^2)	Kinematics	ε	δ_{Stat}	δ_{Random}	δ_{σ_R}	σ_R
0.50	o	0.914	0.054E-02	0.104E-02	0.117E-02	0.22856
	a	0.939	0.046E-02	0.149E-02	0.156E-02	0.23253
	i	0.962	0.051E-02	0.106E-02	0.118E-02	0.23187
	q	0.979	0.051E-02	0.107E-02	0.119E-02	0.23468
	l	0.986	0.066E-02	0.108E-02	0.127E-02	0.23491
0.50	b	0.939	0.048E-02	0.148E-02	0.156E-02	0.23231
	j	0.962	0.045E-02	0.106E-02	0.115E-02	0.23192
	p	0.979	0.052E-02	0.107E-02	0.119E-02	0.23492
	m	0.986	0.063E-02	0.108E-02	0.125E-02	0.23462
0.50	k	0.962	0.047E-02	0.105E-02	0.115E-02	0.23150
	r	0.979	0.047E-02	0.107E-02	0.117E-02	0.23477
	n	0.986	0.070E-02	0.107E-02	0.127E-02	0.23353

Table 5.5: The elastic e-p reduced cross section σ_R for the right arm kinematics. In addition, the statistical uncertainty δ_{Stat}, random systematic uncertainty δ_{Random}, and total uncertainty δ_{σ_R} (combined δ_{Stat} and δ_{Random}) in σ_R are also given.

Q^2 (GeV^2)	Kinematics	ε	δ_{Stat}	δ_{Random}	δ_{σ_R}	σ_R
2.64	o	0.117	0.40E-04	0.51E-04	0.65E-04	0.13402E-01
	a	0.356	0.35E-04	0.82E-04	0.89E-04	0.13823E-01
	i	0.597	0.47E-04	0.55E-04	0.72E-04	0.14301E-01
	q	0.782	0.44E-04	0.57E-04	0.72E-04	0.14677E-01
	l	0.865	0.38E-04	0.58E-04	0.69E-04	0.14832E-01
3.20	b	0.131	0.30E-04	0.42E-04	0.52E-04	0.08686E-01
	j	0.443	0.29E-04	0.35E-04	0.45E-04	0.09075E-01
	p	0.696	0.30E-04	0.36E-04	0.47E-04	0.09305E-01
	m	0.813	0.27E-04	0.37E-04	0.46E-04	0.09525E-01
4.10	k	0.160	0.23E-04	0.22E-04	0.31E-04	0.04726E-01
	r	0.528	0.17E-04	0.23E-04	0.29E-04	0.04973E-01
	n	0.709	0.19E-04	0.24E-04	0.31E-04	0.05121E-01

Table 5.6: The elastic e-p reduced cross section σ_R for the left arm kinematics. In addition, the statistical uncertainty δ_{Stat}, random uncertainty δ_{Random}, and total uncertainty δ_{σ_R} (combined δ_{Stat} and δ_{Random}) in σ_R are also given.
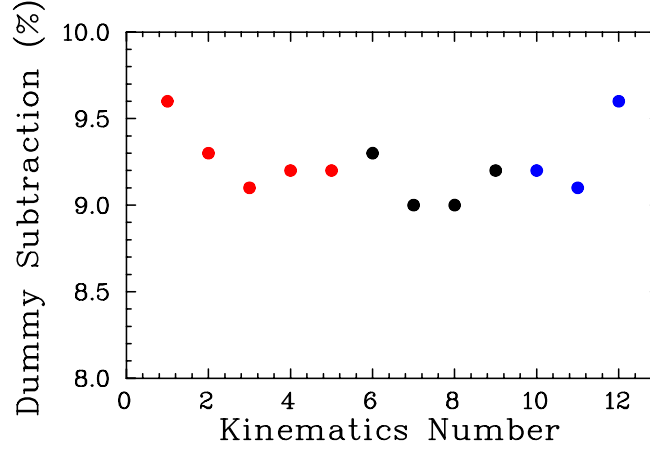
Figure 5.34: The ratio of N_{dummy} to N_{LH_2} events or "Dummy Subtraction (%)" for the right arm in the ΔP window cut used as a function of kinematics number. The points are sorted according to the kinematics of the left arm. Kinematics 1-5 correspond to $Q^2 = 2.64$ GeV^2 and shown in red, while kinematics 6-9(10-12) correspond to 3.20(4.10) GeV^2 and shown in black(blue). For each Q^2 value, the points are sorted by ε (low to high).

Figure 5.35: The ratio of N_{dummy} to N_{LH_2} events or "Dummy Subtraction (%)" for the left arm in the ΔP window cut used as a function of kinematics number. Kinematics 1-5 correspond to $Q^2 = 2.64$ GeV^2 and shown in red, while kinematics 6-9(10-12) correspond to 3.20(4.10) GeV^2 and shown in black(blue). For each Q^2 value, the points are sorted by ε (low to high).

right arm, the pion subtraction correction is set to zero and a random uncertainty of 0.05% is assigned. It is crucial to mention that when determining the ratio R for the right arm, the number of elastic events $N_{\text{elastic-data}}$ as given by equation (5.15) is now given by $N_{\text{elastic-data}} = N_{LH_2} - N_{dummy}$. This is equivalent to set the normalization factor or the π^0-factor needed to normalize the sum of $\gamma p \to \pi^0 p$ and $\gamma p \to \gamma p$ from simulations to the resultant (LH$_2$ - endcaps - scaled e-p simulation) spectrum to zero. The statistical uncertainty in the π^0-factor is taken into account when calculating the statistical uncertainty δ_R in the ratio R for the left arm. See section 5.7.3 for details.
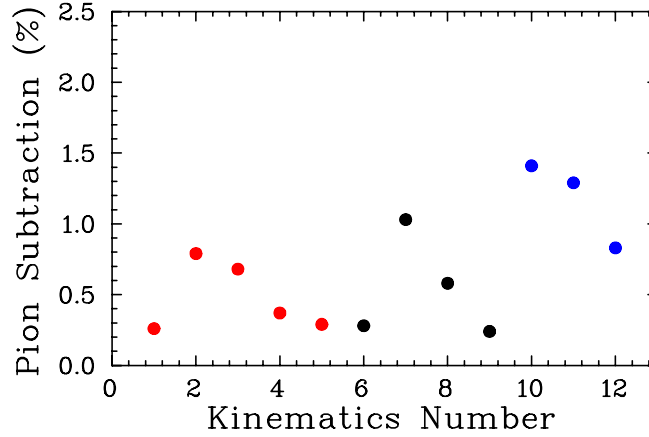
Figure 5.36: The ratio of $(N_{\gamma p \to \pi^0 p} + N_{\gamma p \to \gamma p})$ to N_{LH_2} events or "Pion Subtraction (%)" for the left arm in the ΔP window cut used as a function of kinematics number. Kinematics 1-5 correspond to $Q^2 = 2.64$ GeV^2 and shown in red, while kinematics 6-9(10-12) correspond to 3.20(4.10) GeV^2 and shown in black(blue). For each Q^2 value, the points are sorted by ε (low to high).

To estimate the uncertainty due to the ΔP cut used, we plot the percentage of the N_{e-p} events or "Elastic Peak Acceptance" within the ΔP window cut used as a function of kinematics number and for both arms. Figures 5.37 and 5.38 show the results for the right and left arm, respectively. The elastic acceptance is $\sim 85\%$ and

$\sim 95\%$ for the left and right arm, respectively. Of the 15% events lost on the left arm, $\sim 14\%$ are events lost in the radiative tail and $\sim 1\%$ are events lost in the smeared non-gaussian tails of the elastic peak. The uncertainty in the ΔP cut used due to the correction that results from the events lost in the radiative tail is accounted for in the radiative corrections uncertainties. See section 5.6 for details. The smeared non-gaussian tails are known to within $\sim 50\%$, and therefore, a 1% correction due to events lost in the non-gaussian tails yields a 0.50% scale uncertainty for the left arm. We vary the ΔP window cut used on the left arm by $\pm$ 2 MeV which changes the ratio R by $\sim 0.20\%$. The 0.20% uncertainty in R is then broken down equally as 0.14% random uncertainty and 0.14% slope uncertainty. However, if we consider the average $\Delta\varepsilon$ range of 0.70, that will modify the slope uncertainty to 0.20% (0.14%/0.70).

The right arm is more complicated than the left arm since the HRS momentum acceptance cuts off the ΔP peak. The loss due to a non-gaussian tails is $\sim 1\%$, and we take the same error estimates as for the left arm but account for the $\Delta\varepsilon$ range of 0.07 which modifies the slope uncertainty to 2.0% (0.14%/0.07).

It is crucial to realize that although the elastic peak is broadened with increasing ε for all the kinematics on the left arm, it is well within the momentum acceptance δ of the HRS and thus no elastic events are lost after applying the momentum acceptance δ cut. On the other hand, this is not the case for the right arm since the elastic peak is broader than that of the left arm and extends a bit beyond the edges of the momentum acceptance. Therefore, applying the δ cut will get rid of some elastic events. The elastic acceptance for the right arm shows a $\sim 1.5\%$ ε dependence as can be seen from Figure 5.37. Varying the δ cut changes the correction by $\sim 30\%$. Therefore, a 30% uncertainty in a 1.5% correction yields a $\sim 0.5\%$ uncertainty. However, the 30% uncertainty is not simply a scale, random, or slope uncertainty and so we break the 0.5% uncertainty equally among the scale, random, and slope uncertainties and assign a $\sim 0.30\%$ uncertainty for each. Finally, if we consider the $\Delta\varepsilon$ range of 0.07
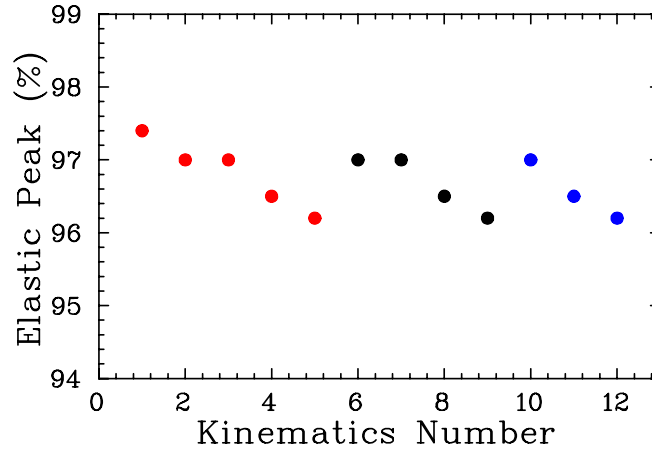
Figure 5.37: The percentage of the events or "Elastic Peak (%)" for the right arm in the ΔP window cut used as a function of kinematics number. The points are sorted according to the kinematics of the left arm. Kinematics 1-5 correspond to $Q^2 = 2.64$ GeV^2 and shown in red, while kinematics 6-9(10-12) correspond to 3.20(4.10) GeV^2 and shown in black(blue). For each Q^2 value, the points are sorted by ε (low to high).
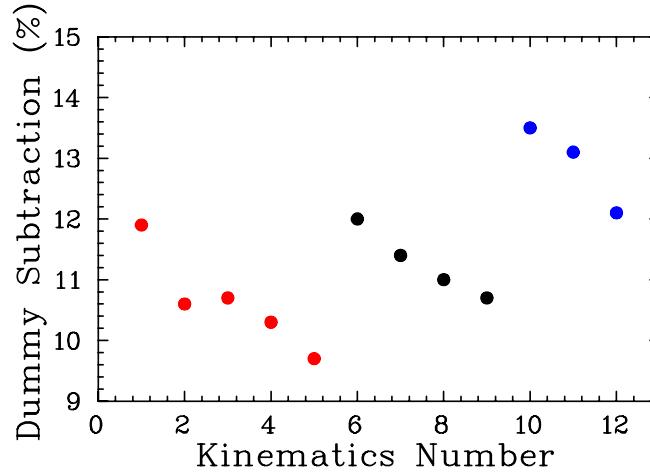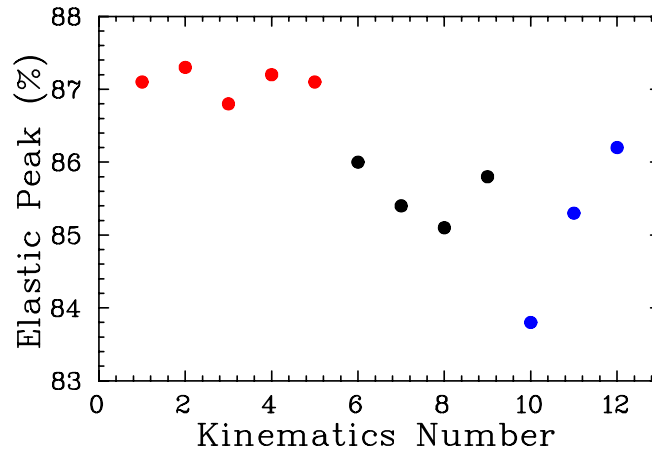

Figure 5.38: The percentage of the N_{e-p} events or "Elastic Peak %" for the left arm in the ΔP window cut used as a function of kinematics number. Kinematics 1-5 correspond to $Q^2 = 2.64$ GeV^2 and shown in red, while kinematics 6-9(10-12) correspond to 3.20(4.10) GeV^2 and shown in black(blue). For each Q^2 value, the points are sorted by ε (low to high).

for the right arm, that will modify the slope uncertainty to 4.28%.

Chapter 6   Results and Two-Photon Exchange

6.1   Overview

In this chapter I will discuss the procedure used to extract the electromagnetic form factors of the proton, G_{Ep} and G_{Mp}, and their ratio $\frac{\mu_p G_{Ep}}{G_{Mp}}$. Rosenbluth extractions of the proton form factors and their ratio using the reduced cross sections of each arm separately will be discussed. Rosenbluth extractions using the left arm reduced cross sections were recently published [109]. Initially, we planned to use the Super-Rosenbluth ratio, R_{Super}, defined as the left arm reduced cross section normalized to the right arm ratio at each kinematics point or:

$$R_{Super} = \frac{\text{Left } \sigma_R}{\text{Right } R} \; , \tag{6.1}$$

to extract the form factor ratios. Note that by using R_{Super}, we take advantage of the right arm spectrometer which served as a luminosity monitor to remove any uncertainties due to beam charge, current, target length, raster size, and target density fluctuations. See chapter 4 for a detailed discussion of the corrections and efficiencies applied to the measured beam charge, and Tables 4.18 and 4.19 for a summary of the systematic uncertainties in these corrections and efficiencies. However, we decided not to use R_{Super} to extract the form factors and their ratio since it is estimated that by dividing by the luminosity monitor, that will introduce more uncertainty in R_{Super} than it will eliminate. By looking at Table 5.5, we see that the right arm cross sections have $\sim 0.50\%$ random uncertainty, while the luminosity-related random uncertainty

is $< 0.20\%$ as can be seen from Table 4.18. Instead we use the right arm results as a consistency check of the assumed uncertainties.

The form factors and their ratio extracted from this work are discussed and compared to previous Rosenbluth extractions and recent polarization transfer results. See section 2.2 and subsections therein for a full discussion of previous Rosenbluth extractions and recent polarization transfer results. An introduction to the two-photon-exchange (TPE) and Coulomb distortion corrections as possible sources for the discrepancy between the Rosenbluth extractions and polarization transfer results is given. The linearity in the Born approximation of the Rosenbluth separation plots (L-T plots) as a function of ε is examined for this work because any deviation from linearity would provide a clear signature of the effects beyond traditional radiative corrections, and would provide information on the nonlinear component of the TPE. Finally, as the results of this work raised the interest in the physics of the TPE and Coulomb distortion corrections and laid down the foundations for new experiments aimed at measuring the size of the TPE corrections, I conclude with a brief discussion of the TPE calculations and presentations of these future experiments.

6.2 Form Factors Extraction

In this section I will describe the general procedure used to extract G_{Ep}, G_{Mp}, and $\frac{\mu_p G_{Ep}}{G_{Mp}}$ by using the reduced cross sections σ_R, as listed in Tables 5.5 and 5.6.

6.2.1 Form Factors Extraction Using σ_R (Single Arm)

Equation (1.34) defines the elastic e-p reduced cross section σ_R. A linear fit of σ_R to ε at a fixed Q^2 gives $\tau G_{Mp}^2(Q^2)$ as the intercept and $G_{Ep}^2(Q^2)$ as the slope. If the goal is to extract G_{Mp} and G_{Ep}, then a linear fit of σ_R to ε is performed using the

following form:

$$\sigma_R = \tau A^2 + B^2 \varepsilon \; , \tag{6.2}$$

where A and B are the parameters of the fit and represent G_{Mp} and G_{Ep}, and the uncertainties in A and B represent δG_{Mp} and δG_{Ep}, respectively. On the other hand, if the goal is to extract $\frac{G_{Ep}}{G_{Mp}}$, then a linear fit of σ_R to ε is performed using:

$$\sigma_R = \tau A^2 \left(1.0 + B^2 \frac{\varepsilon}{\tau} \right) \; , \tag{6.3}$$

where A and B represent G_{Mp} and $\frac{G_{Ep}}{G_{Mp}}$, and the uncertainties in A and B represent δG_{Mp} and $\delta \frac{G_{Ep}}{G_{Mp}}$, respectively. Note that the ratio $\frac{G_{Ep}}{G_{Mp}}$ and its uncertainty can be determined first by taking the ratio of the individual form factors as extracted using equation (6.2) and then propagating the (correlated) errors on G_{Ep} and G_{Mp}, however, equation (6.2) is used since it directly provides the ratio $\frac{G_{Ep}}{G_{Mp}}$ and its uncertainty.

(a) G_{Ep} and G_{Mp} Extraction Using Equation 6.2

The classification of the systematic uncertainties into scale, random, and slope uncertainties and their effects on the extracted form factors has been discussed in section 4.1. To determine the individual form factors, we start by adding in quadrature the total random uncertainty in σ_R, δ_{Random}, to the statistical uncertainty in each σ_R, δ_{Stat}, as listed in Tables 5.5 and 5.6 or:

$$\delta_{\sigma_R} = \sqrt{\delta_{Stat}^2 + \delta_{Random}^2} \; . \tag{6.4}$$

A linear fit of σ_R to ε at a fixed Q^2 using equation (6.2) yields a value of $G_{Mp} = G_{Mp}^{(1)} \pm \delta G_{Mp}^{(1)}$ and $G_{Ep} = G_{Ep}^{(1)} \pm \delta G_{Ep}^{(1)}$ where the contribution from the random uncertainty to the total uncertainty in G_{Mp} and G_{Ep} is given by $\delta G_{Mp}^{Random} = \delta G_{Mp}^{(1)}$ and $\delta G_{Ep}^{Random} = \delta G_{Ep}^{(1)}$. Figures 6.1, 6.2, 6.3, and 6.4 show such fits done at $Q^2 =$

0.50, 2.64, 3.20, and 4.10 GeV^2, respectively.

To determine the contribution of the slope uncertainty in σ_R to the total uncertainty in G_{Mp} and G_{Ep}, we vary σ_R by the uncertainties that vary linearly with ε or the total slope uncertainty, δ_{Slope}, as given at the bottom of Tables 4.18 and 4.19:

$$\sigma_R^{Slope} = \sigma_R \left(1.0 + \varepsilon \delta_{Slope} \right) , \qquad (6.5)$$

then, a linear fit of σ_R^{Slope} to ε using equation (6.2), with uncertainties in σ_R^{Slope} given by $\delta_{\sigma_R^{Slope}} = \delta_{\sigma_R}(1.0 + \varepsilon \delta_{Slope})$, yields a value of $G_{Mp} = G_{Mp}^{(2)} \pm \delta G_{Mp}^{(2)}$ and $G_{Ep} = G_{Ep}^{(2)} \pm \delta G_{Ep}^{(2)}$. Therefore, the contribution from the slope uncertainty to the total uncertainty in G_{Mp} and G_{Ep} is given by $\delta G_{Mp}^{Slope} = \left| G_{Mp}^{(1)} - G_{Mp}^{(2)} \right|$ and $\delta G_{Ep}^{Slope} = \left| G_{Ep}^{(1)} - G_{Ep}^{(2)} \right|$. Note that for the right arm we used $\delta_{\sigma_R^{Slope}} = \delta_{\sigma_R} \left(1.0 + (\varepsilon - 1.0)\delta_{Slope} \right)$ since all the measurements were taken near ε=1.0.
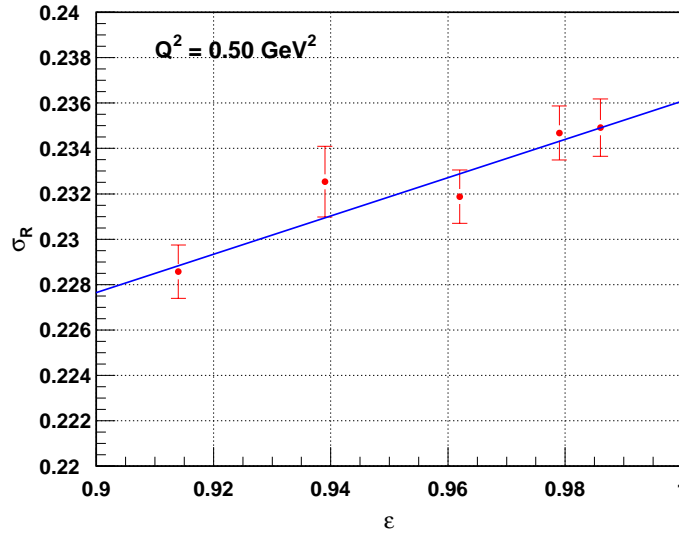
Figure 6.1: A linear fit of the right arm σ_R to ε at $Q^2 = 0.50$ GeV^2 using equation (6.2). The shown uncertainties are the combined statistical and random from equation (6.4).
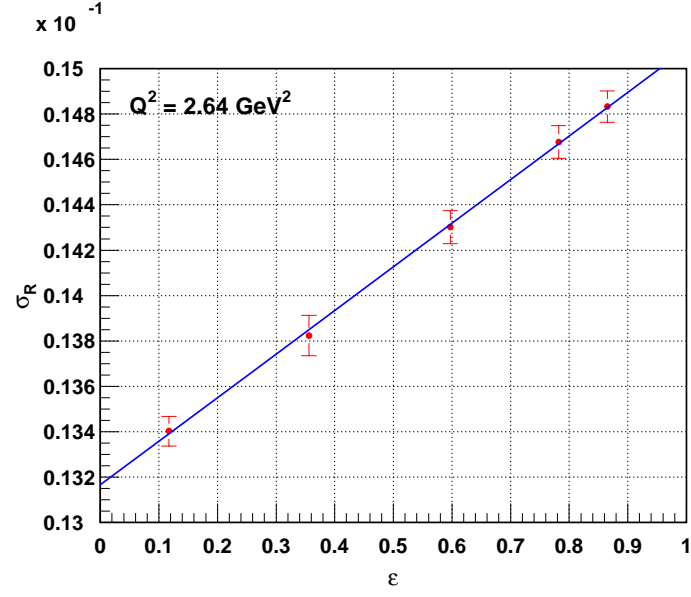
Figure 6.2: A linear fit of the left arm σ_R to ε at $Q^2 = 2.64$ GeV^2 using equation (6.2). The shown uncertainties are the combined statistical and random from equation (6.4).
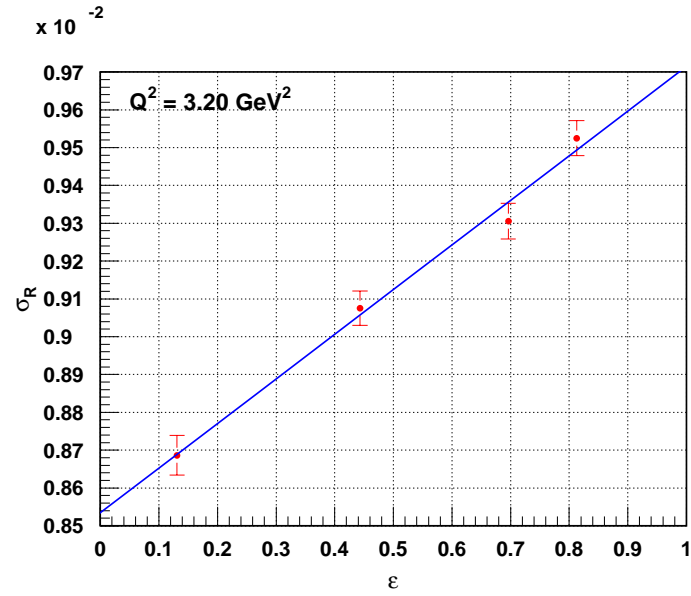
Figure 6.3: A linear fit of the left arm σ_R to ε at $Q^2 = 3.20$ GeV^2 using equation (6.2). The shown uncertainties are the combined statistical and random from equation (6.4).
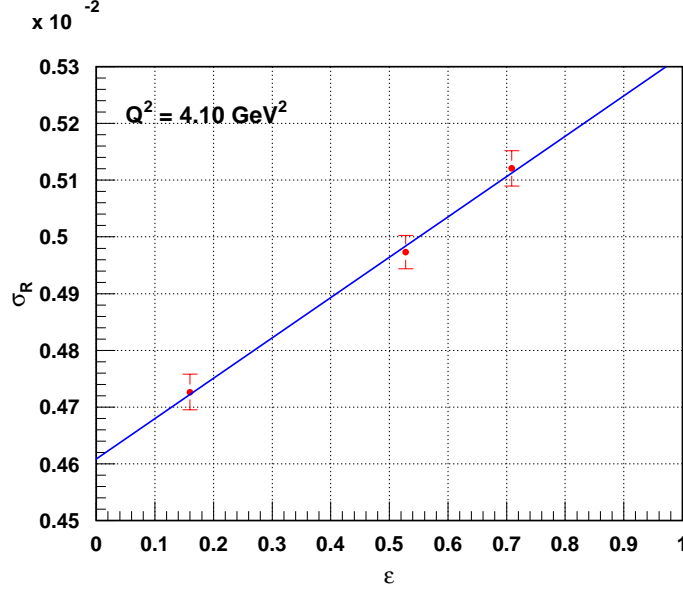
Figure 6.4: A linear fit of the left arm σ_R to ε at $Q^2 = 4.10$ GeV^2 using equation (6.2). The shown uncertainties are the combined statistical and random from equation (6.4).

Similarly, we determine the contribution of the scale uncertainty in σ_R to the total uncertainty in G_{Mp} and G_{Ep} by varying σ_R by the total scale uncertainty, δ_{Scale}, as given at the bottom of Tables 4.18 and 4.19:

$$\sigma_R^{Scale} = \sigma_R \left(1.0 + \delta_{Scale} \right) , \tag{6.6}$$

and a linear fit of σ_R^{Scale} to ε using equation (6.2), with uncertainties in σ_R^{Scale} given by $\delta_{\sigma_R^{Scale}} = \delta_{\sigma_R}(1.0 + \delta_{Scale})$, yields a value of $G_{Mp} = G_{Mp}^{(3)} \pm \delta G_{Mp}^{(3)}$ and $G_{Ep} = G_{Ep}^{(3)} \pm \delta G_{Ep}^{(3)}$. The contribution from the scale uncertainty to the total uncertainty in G_{Mp} and G_{Ep} is therefore given by $\delta G_{Mp}^{Scale} = \left| G_{Mp}^{(1)} - G_{Mp}^{(3)} \right|$ and $\delta G_{Ep}^{Scale} = \left| G_{Ep}^{(1)} - G_{Ep}^{(3)} \right|$.

Finally, G_{Mp} and G_{Ep} are given by $G_{Mp} = G_{Mp}^{(1)} \pm \delta G_{Mp}^{Total}$ and $G_{Ep} = G_{Ep}^{(1)} \pm \delta G_{Ep}^{Total}$

where δG_{Mp}^{Total} and δG_{Ep}^{Total} are given by:

$$\delta G_{Mp}^{Total} = \sqrt{(\delta G_{Mp}^{Random})^2 + (\delta G_{Mp}^{Slope})^2 + (\delta G_{Mp}^{Scale})^2} \ , \qquad (6.7)$$

and

$$\delta G_{Ep}^{Total} = \sqrt{(\delta G_{Ep}^{Random})^2 + (\delta G_{Ep}^{Slope})^2 + (\delta G_{Ep}^{Scale})^2} \ . \qquad (6.8)$$

The electric and magnetic form factors for the proton with their uncertainties were determined at $Q^2 = 0.50$, 2.64, 3.20, and 4.10 GeV^2. Tables 6.1 and 6.2 list the results.

Q^2 (GeV^2)	G_{Mp}	δG_{Mp}^{Random}	δG_{Mp}^{Slope}	δG_{Mp}^{Scale}	δG_{Mp}^{Total}	$\frac{G_{Mp}}{\mu_p G_D}$ $\pm$ $\delta(\frac{G_{Mp}}{\mu_p G_D})$
0.50	1.03340	0.06726	0.01247	0.01702	0.07049	1.07467 $\pm$ 0.07330
2.64	0.1325	0.0003466	6.988E-06	0.001913	0.001944	1.05632 $\pm$ 0.01549
3.20	0.09691	0.0003204	7.398E-06	0.001398	0.001435	1.05233 $\pm$ 0.01558
4.10	0.06291	0.0002822	4.701E-06	0.0009097	0.0009525	1.03390 $\pm$ 0.01565

Table 6.1: The magnetic form factor for the proton G_{Mp} at $Q^2 = 0.50$, 2.64, 3.20, and 4.10 GeV^2 as determined by fitting σ_R to ε using equation (6.2). In addition, the contributions from the random, slope, and scale uncertainties to the total uncertainty in G_{Mp} is also given.

Q^2 (GeV^2)	G_{Ep}	δG_{Ep}^{Random}	δG_{Ep}^{Slope}	δG_{Ep}^{Scale}	δG_{Ep}^{Total}	$\frac{G_{Ep}}{G_D}$ $\pm$ $\delta(\frac{G_{Ep}}{G_D})$
0.50	0.2906	0.03589	0.02682	0.003182	0.04492	0.8440 $\pm$ 0.1304
2.64	0.04385	0.001276	0.0009129	0.0006389	0.001694	0.9761 $\pm$ 0.03772
3.20	0.03436	0.001377	0.0007532	0.0004959	0.001646	1.04198 $\pm$ 0.04994
4.10	0.02666	0.001489	0.0007684	0.0003775	0.001718	1.2238 $\pm$ 0.07886

Table 6.2: The electric form factor for the proton G_{Ep} at $Q^2 = 0.50$, 2.64, 3.20, and 4.10 GeV^2 as determined by fitting σ_R to ε using equation (6.2). In addition, the contributions from the random, slope, and scale uncertainties to the total uncertainty in G_{Ep} is also given.

(b) G_{Mp} and $\frac{G_{Ep}}{G_{Mp}}$ Extraction Using Equation 6.3

A linear fit of σ_R to ε at a fixed Q^2 using equation (6.3) yields G_{Mp} and $\frac{G_{Ep}}{G_{Mp}}$. The same procedure outlined in subsection (a) is used with the following changes:

- $\frac{G_{Ep}}{G_{Mp}}$ replaces G_{Ep} whenever it occurs or: $G_{Ep} \rightarrow \frac{G_{Ep}}{G_{Mp}}$.

Therefore $G_{Mp} = G_{Mp}^{(1)} \pm \delta G_{Mp}^{Total}$ and $\frac{G_{Ep}}{G_{Mp}} = (\frac{G_{Ep}}{G_{Mp}})^{(1)} \pm \delta(\frac{G_{Ep}}{G_{Mp}})^{Total}$ where δG_{Mp}^{Total} and $\delta(\frac{G_{Ep}}{G_{Mp}})^{Total}$ are given by:

$$\delta G_{Mp}^{Total} = \sqrt{(\delta G_{Mp}^{Random})^2 + (\delta G_{Mp}^{Slope})^2 + (\delta G_{Mp}^{Scale})^2} \ , \qquad (6.9)$$

and

$$\delta\left(\frac{G_{Ep}}{G_{Mp}}\right)^{Total} = \sqrt{\left(\delta\left(\frac{G_{Ep}}{G_{Mp}}\right)^{Random}\right)^2 + \left(\delta\left(\frac{G_{Ep}}{G_{Mp}}\right)^{Slope}\right)^2 + \left(\delta\left(\frac{G_{Ep}}{G_{Mp}}\right)^{Scale}\right)^2}. \quad (6.10)$$

The magnetic form factor and the ratio of electric to magnetic form factor for the proton with their uncertainties were determined at $Q^2 = 0.50$, 2.64, 3.20, and 4.10 GeV^2. The results obtained for G_{Mp} are identical to those listed in Table 6.1. Table 6.3 lists the results obtained for the ratio $\frac{G_{Ep}}{G_{Mp}}$.

Q^2 (GeV^2)	$\frac{G_{Ep}}{G_{Mp}}$	$\delta\left(\frac{G_{Ep}}{G_{Mp}}\right)^{Random}$	$\delta\left(\frac{G_{Ep}}{G_{Mp}}\right)^{Slope}$	$\delta\left(\frac{G_{Ep}}{G_{Mp}}\right)^{Scale}$	$\delta\left(\frac{G_{Ep}}{G_{Mp}}\right)^{Total}$	$\frac{\mu_p G_{Ep}}{G_{Mp}} \pm \delta\left(\frac{\mu_p G_{Ep}}{G_{Mp}}\right)$
0.50	0.2803	0.05303	0.03039	0.000655	0.06112	0.7828 $\pm$ 0.1707
2.64	0.3308	0.01040	0.006930	6.202E-05	0.01249	0.9240 $\pm$ 0.03490
3.20	0.3545	0.01529	0.007770	4.100E-05	0.01715	0.9900 $\pm$ 0.04789
4.10	0.4238	0.02540	0.01222	6.601E-05	0.02819	1.1837 $\pm$ 0.07873

Table 6.3: The ratio of electric to magnetic form factor for the proton $\frac{G_{Ep}}{G_{Mp}}$ at $Q^2 = 0.50$, 2.64, 3.20, and 4.10 GeV^2 as determined by fitting σ_R to ε using equation (6.3). In addition, the contributions from the random, slope, and scale uncertainties to the total uncertainty in $\frac{G_{Ep}}{G_{Mp}}$ is also given.

6.3   Discussion of the Results

Figures 6.5 shows the world data on $\frac{\mu_p G_{Ep}}{G_{Mp}}$ ratio for the proton from previous Rosenbluth measurements along with the results of E01-001 single arm (Table 6.3). In addition, Figures 6.6 shows the $\frac{\mu_p G_{Ep}}{G_{Mp}}$ ratio from the E01-001 single arm extractions along with the results of recoil polarization. The global analysis of previous cross section data by Arrington [58] is also shown. By comparing the results of the E01-001 with those of previous Rosenbluth separations and recoil polarization measurements, we conclude that:

1. *The values of $\frac{\mu_p G_{Ep}}{G_{Mp}}$ ratio from the single arm extractions are in good agreement with the previous Rosenbluth measurements but with much smaller statistical and systematic uncertainties than the previous best measurements [8]. The total uncertainty is comparable to those of recoil polarization.*

2. *The high precision achieved in the E01-001 extractions:*

    - *Leaves little room for doubting that the values of $\frac{\mu_p G_{Ep}}{G_{Mp}}$ ratio extracted from Rosenbluth separations are inconsistent with those reported from the high-Q^2 recoil polarization measurements.*

    - *Makes it clear that the problem is not simply an experimental error in the Rosenbluth measurements or technique.*

    - *Confirms the reliability of the elastic e-p cross sections extracted from previous Rosenbluth separations.*

3. *(This point will be discussed below):*
   Provides a significant test of the validity of the commonly used radiative corrections (bremsstrahlung corrections).
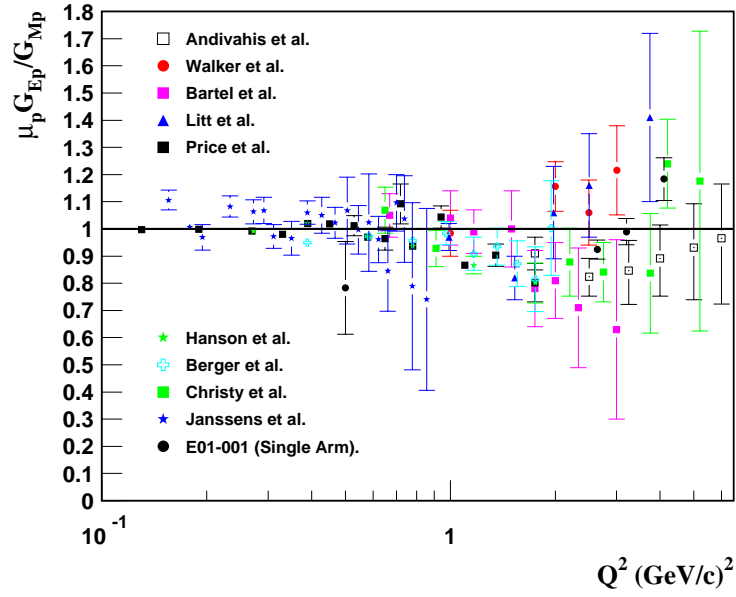
Figure 6.5: The world data of Rosenbluth separation determination of $\mu_p G_{Ep}/G_{Mp}$ ratio compared to that of E01-001 (single arm extraction) (Table 6.3).
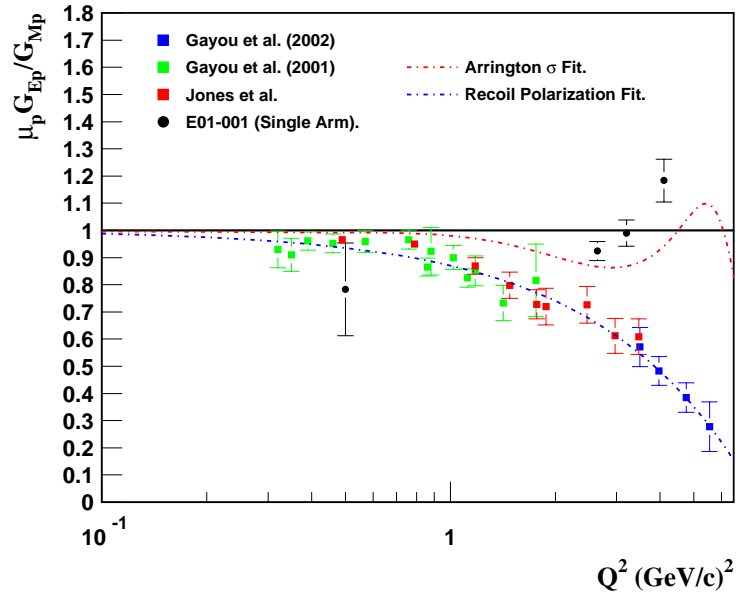
Figure 6.6: The values of $\mu_p G_{Ep}/G_{Mp}$ for the proton from E01-001 (single arm extraction) (Table 6.3) and recoil polarization.

In summary, we see that the results of the E01-001 are in agreement with the previous Rosenbluth data. The experiment provided systematic uncertainties much smaller than the best previous Rosenbluth measurements, [8], and comparable to those of the recoil polarization clearly establishing the discrepancy between the Rosenbluth separations and recoil polarization results. These results confirmed that the discrepancy is not due to experimental error in the Rosenbluth measurements and provided a strong test of the conventional radiative corrections used.

A possible source for the discrepancy is the effect of higher-order corrections to the reduced cross sections. Suggested sources for the discrepancy will be discussed in section 6.4. The reduced cross sections as defined by equation (1.34) and listed in Tables 5.5 and 5.6 are derived in the Born approximation and have been corrected for many of the higher-order radiative corrections terms. The form factors and thus their ratio have been extracted using these reduced cross sections without including fully the effects of these higher-order corrections on the reduced cross sections for consistency with previous Rosenbluth measurements.

The standard radiative correction procedure used was discussed in section 5.6. We correct the data for bremsstrahlung, vertex corrections, and loop diagrams, with almost all of the ε dependence coming from bremsstrahlung. Figure 3.6 shows the calculated radiative correction factor (internal corrections only) as a function of ε for $Q^2 = 2.64$ GeV^2. Again, while the magnitude of the corrections is similar and both show an approximately linear dependence on ε, the dependence is much smaller for protons, $\sim -8\%$, than for the electron $\sim 17\%$, and of opposite sign. Note that when detecting the electron, the ε dependence of the bremsstrahlung correction exceeds the ε dependence coming from G_{Ep} which is not the case in the E01-001 experiment.

6.4 Possible Sources for the Discrepancy

The results of the E01-001 experiment have clearly established and confirmed the discrepancy between the Rosenbluth separations and recoil polarization results. The questions that need to be answered are: why do the two techniques disagree? and which form factors are the correct ones?

As noted above, we have essentially ruled out the possibility that the discrepancy is due to an experimental error in the Rosenbluth separations measurements or technique. That confirms that previous elastic e-p cross sections are reliable which is crucial since these cross sections are used for normalization or as an input to the analysis of different experiments. In addition, reanalysis of the existing form factor data by Arrington [58], see section 2.4 for details, has confirmed that all the different data from previous Rosenbluth separations measurements are consistent. This reanalysis combined with the new results from E01-001 rule out any possibility for a bad data sets or incorrect normalization in the combined Rosenbluth analysis. **It should be noted that while the E01-001 experiment provided an independent check on previous Rosenbluth measurements there has been, to the best of my knowledge, no independent check of the high-Q^2 recoil polarization results.**

As for which form factors are the correct ones to use, again, if the cross section measurements and hence the Rosenbluth extractions are incorrect, that still will not solve the problem since the recoil polarization technique provides the ratio of G_{Ep} to G_{Mp} and not the actual values for the individual form factors. While the form factors extracted by Rosenbluth separations may possibly not represent the true form factors for the proton, they do indeed provide the correct elastic e-p cross sections and presumably provide the best parameterization when elastic cross sections are used for normalization or as an input to the analysis of different experiments.

6.4.1   Two-Photon-Exchange (TPE) Correction

The difference in the $\frac{\mu_p G_{Ep}}{G_{Mp}}$ ratio from Rosenbluth separations and recoil polarizations results can be explained by a common ε-dependent systematic error in the cross section measurements of (5-8)% [55, 58, 110]. The establishment of the discrepancy has led people to suggest that the discrepancy is due to a missing corrections in the cross section due to a higher-order processes such as two-photon-exchange (TPE). The standard radiative correction procedure used was discussed in section 5.6. Figure 5.15 shows the full contribution of the elastic and inelastic radiative corrections to the elastic e-p cross section including the first-order QED (Born) radiative corrections or single-photon-exchange. Figure 5.15 (e), crossed-box, and (f), box, are the contributions from TPE to the elastic e-p cross section which are not fully included in the standard radiative correction procedures. See [111, 16, 107] for details. **It is believed that inclusion of TPE contributions may remove the discrepancy**.

If we assume that the discrepancy is in fact due to TPE and the recoil polarization results are approximately correct, then the $\frac{\mu_p G_{Ep}}{G_{Mp}}$ ratio becomes small enough as Q^2 gets large (note the smaller slope predicated by recoil polarization) that the ε dependence of the reduced cross section is dominated by TPE. Figures 6.7 and 6.8 show the contribution of the TPE, $\Delta_{2\gamma}$, to ε dependence of the L-T plots at Q^2 = 2.64 and 4.10 GeV^2, respectively. At large Q^2 where G_{Ep} is suppressed and the reduced cross section in the Born approximation has almost no ε dependence, the discrepancy implies cross section difference of 5-10%. In this region, almost all of the ε dependence would come from TPE and the ε dependence of the reduced cross section will represent the full contributions of TPE.

The high precision provided by the E01-001 experiment on σ_R and hence on $\frac{\mu_p G_{Ep}}{G_{Mp}}$ is of great importance as it constitutes a precise measurement of the discrepancy between the Rosenbluth separations and recoil polarization results, thus allowing for a precise test as to whether TPE effects can
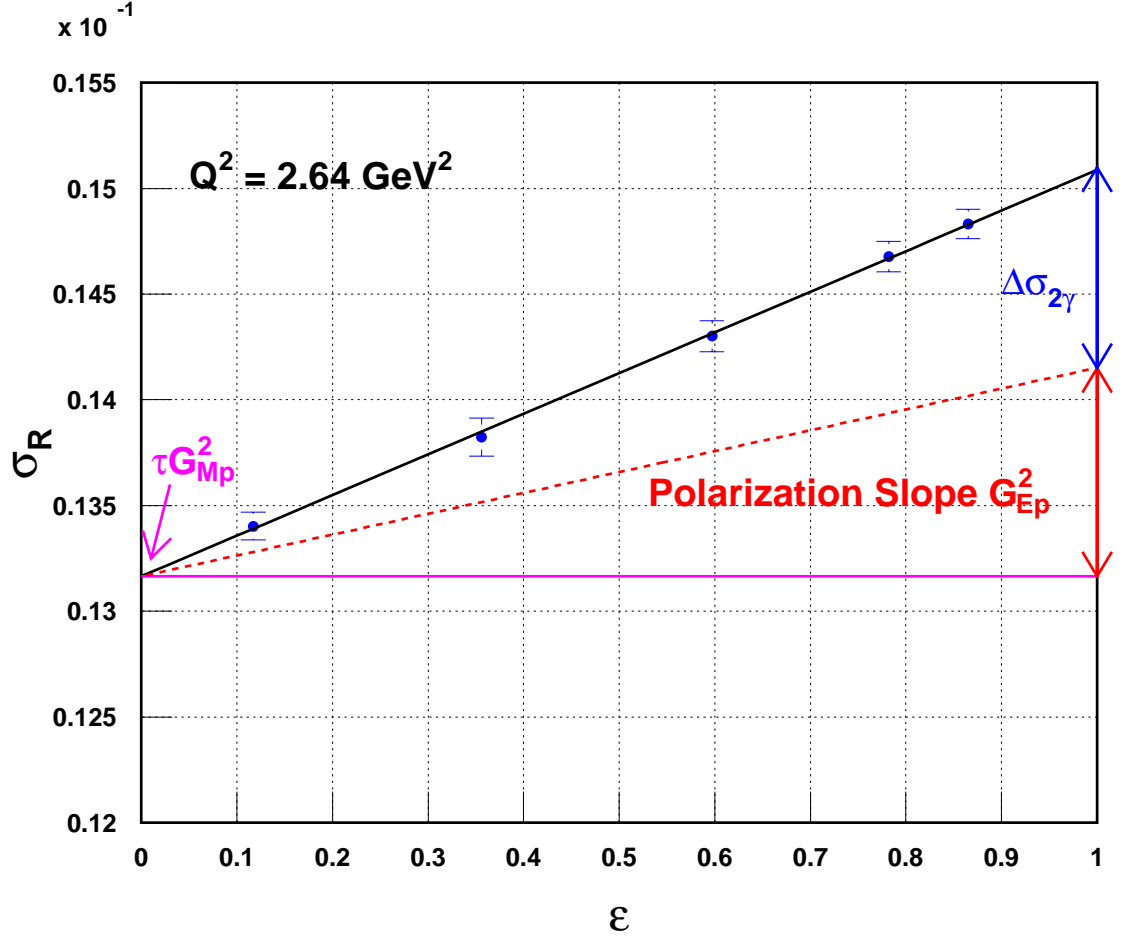
Figure 6.7: The ε dependence of the reduced cross section at $Q^2 = 2.64$ GeV^2 as measured in the E01-001 experiment (blue solid circles), and as predicted from the recoil polarization (red dashed line). The black solid line is a linear fit to the data. If the recoil polarization results represent the true form factors (note the smaller slope or G_{Ep}^2 predicted by the recoil polarization and shown in red double arrow), then TPE or $\Delta\sigma_{2\gamma}$ shown as blue double arrow will yield roughly about half of the ε dependence at $Q^2 = 2.64$ GeV^2.
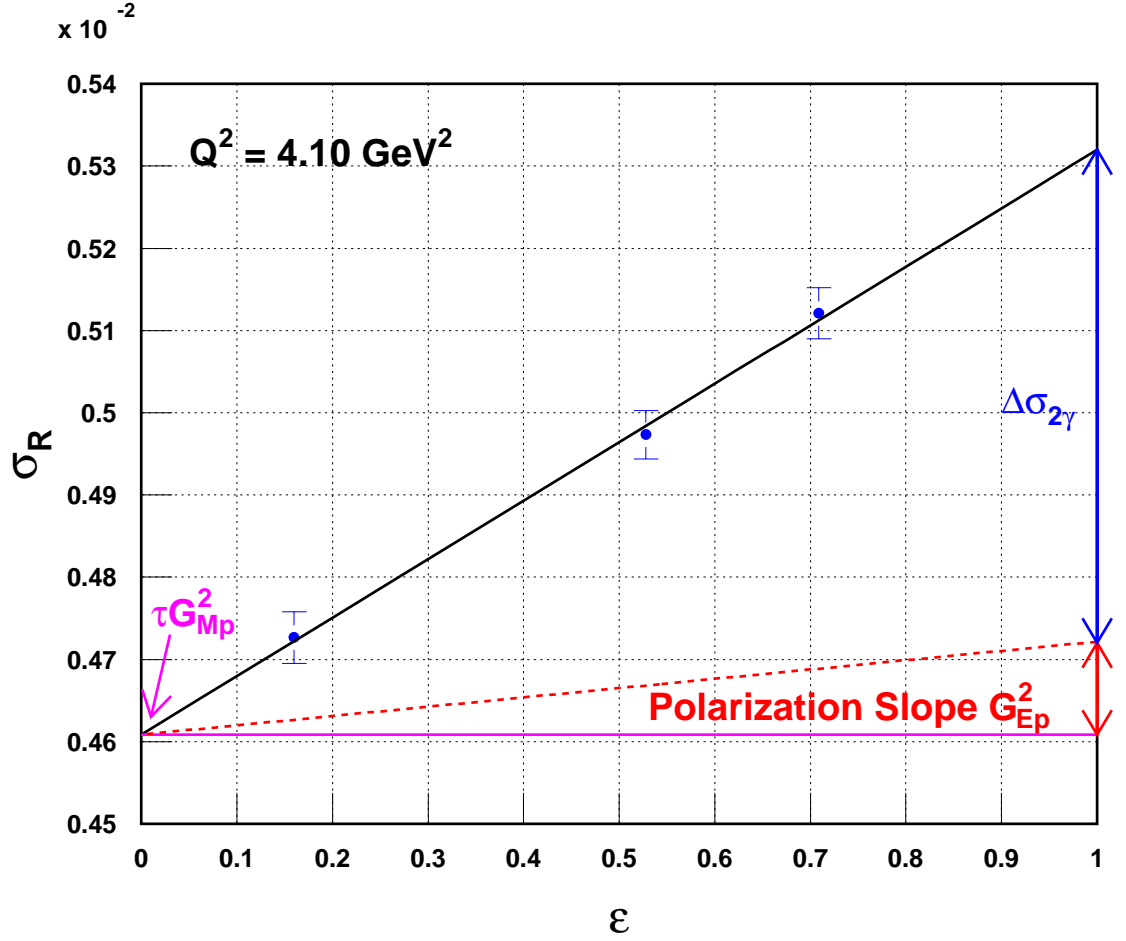
Figure 6.8: The ε dependence of the reduced cross section at $Q^2 = 4.10$ GeV^2 as measured in the E01-001 experiment (blue solid circles), and as predicted from the recoil polarization (red dashed line). The black solid line is a linear fit to the data. If the recoil polarization results represent the true form factors (note the smaller slope or G_{Ep}^2 predicted by the recoil polarization and shown in red double arrow), then TPE or $\Delta\sigma_{2\gamma}$ shown as blue double arrow will yield about 85% of the ε dependence at 4.10 GeV^2.

explain the difference between Rosenbluth and recoil polarization measurements. The reduced cross section in the Born approximation varies linearly with ε. Therefore, at low Q^2 where G_{Ep} contributes most, any deviation from linearity would have to come from higher-order terms that are not included in the standard radiative correction procedures. Such deviation from linearity would provide a clean signature of TPE and would provide information about the nonlinear component of TPE. If the TPE correction is to explain the discrepancy, it would have to introduce (5-8)% ε-dependent correction to the cross sections. Such correction would have to be roughly linear since large nonlinearities are not observed.

An important point to emphasize is that **the standard radiative corrections have an ε dependence that is comparable to the slope brought about by the form factors, (see Figure 3.6)**. In addition, if missing radiative correction terms are the reason for such discrepancy, then the form factors extracted from Rosenbluth separations and to lesser extent those from recoil polarization do not represent the true form factors for the proton since we are not correctly isolating the single-photon-exchange process. Therefore, it is absolutely crucial to understand the radiative corrections and in particular higher-order processes such as TPE theoretically and experimentally before we can be confident in our knowledge of the proton form factors.

Several calculations in the 1950s and 1960s tried to estimate the size of the TPE contributions to the unpolarized elastic e-p cross sections [100, 101, 102, 103, 104]. While some calculations used only the proton intermediate state [104], other included the excited intermediate states of the proton as well [100, 101, 102, 103]. The TPE corrections estimated from these calculations were extremely small ($\leq 1\%$) and were not included in the standard radiative correction procedures.

Motivated in part by the results of the E01-001 experiment, the interest in the physics of TPE and Coulomb distortion corrections and their impact on electron scattering observables has recently risen both experimentally and theoretically. In

addition, the results of the E01-001 experiment have laid down the foundation for new experiments aimed at measuring the size of the TPE corrections (to be discussed in section 6.5). All of the new calculations have predicted a nonlinearities in the ε dependence of TPE. A brief description of these recent calculations will be given below. In addition, their effect on the $\frac{\mu_p G_{Ep}}{G_{Mp}}$ ratio from the E01-001 extractions will be examined where possible.

6.4.2 Recent Calculations of the TPE Corrections

- ***Calculation by Blunden, Melnitchouk, and Tjon et al. [16]:***

This is a low energy hadronic model that takes into account the proton intermediate state and neglects excited intermediate states. It includes only the elastic contributions to the TPE correction or the box and crossed-box diagrams shown in Figure 5.15 (f) and (e), respectively. Their initial calculations yielded an ε dependence of $\sim 2\%$ with small nonlinearities at small ε and insignificant Q^2 dependence. These corrections became larger with the inclusion of an improved form factors [107]. Figure 6.9 shows the effect of such a calculation on the ratio $\frac{\mu_p G_{Ep}}{G_{Mp}}$ extracted from the E01-001 experiment. In addition, the effect of Coulomb correction by Sick and Arrington [17] (see section 6.4.3 for details) is also shown. While the discrepancy is largely resolved for $Q^2 = 2\text{-}3$ GeV^2, this calculation fails to resolve the discrepancy for $Q^2 > 3$ GeV^2. Recently, the authors have included the Δ resonance as an intermediate excited state to their elastic box and crossed-box calculations of TPE corrections [108]. The Δ contribution is smaller in magnitude than the contribution when the proton is in the intermediate state with a small modification to the ε dependence of the TPE corrections.

Figure 6.9: The $\mu_p G_{Ep}/G_{Mp}$ ratio for the proton from the E01-001 experiment (red open circles) and recoil polarization (black open diamonds). The E01-001 $\mu_p G_{Ep}/G_{Mp}$ corrected for TPE correction by Blunden et al [16] (blue solid circles). The E01-001 $\mu_p G_{Ep}/G_{Mp}$ ratio corrected for TPE correction by Blunden et al including the Coulomb correction by Sick and Arrington [17] (green crosses).

- ***Calculation by Chen et al. [18]:***

This is a high energy model at the quark-parton level. It calculates the TPE correction using a generalized parton distribution (GPD) for the quark distribution to describe the emission and re-absorption of the partons by the nucleon as shown in Figures 6.10 (the dominant contribution) and 6.11. For large Q^2, the calculation shows a significant ε dependence and nonlinearity to the correction with a weak Q^2 dependence. Since this is a high energy model, it is not expected to be valid at low Q^2 values. Figure 6.12 shows the effect of such a calculation on the $\frac{\mu_p G_{Ep}}{G_{Mp}}$ ratio from the E01-001 experiment. In addition, the effect of Coulomb correction by Sick and Arrington is also shown. Their correction predicts $\sim 50\%$ of what is needed to fully resolve the discrepancy. Their recent result [112] also shows the model dependence

due to the use of different GPDs. Using a different GPD model can significantly enlarge their corrections.
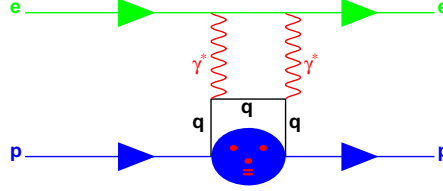
Figure 6.10: Feynman diagram known as the handbag diagram used for the partonic calculation of TPE contribution to elastic e-p scattering by Chen et al [18]. The electron (green) interacts with the proton via two virtual photons (red), while the proton (blue) shown as solid line and circle to represent the proton GPDs emits quark (black) which interacts with the two virtual photons. The quark gets re-absorbed again by the proton.
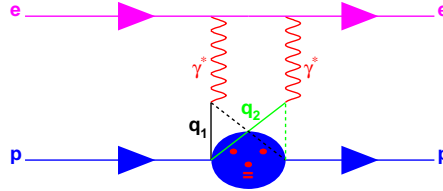
Figure 6.11: Feynman diagram known as the cat's ears diagram used for the partonic calculation of TPE contribution to elastic e-p scattering by Chen et al [18]. The electron (magenta) interacts with the proton via two virtual photons (red), while the proton (blue) shown as solid line and circle to represent the proton GPDs emits two quarks q_1 and q_2 (black and green solid lines) which interact with the two virtual photons. The two quarks get re-absorbed again by the proton (black and green dashed lines).
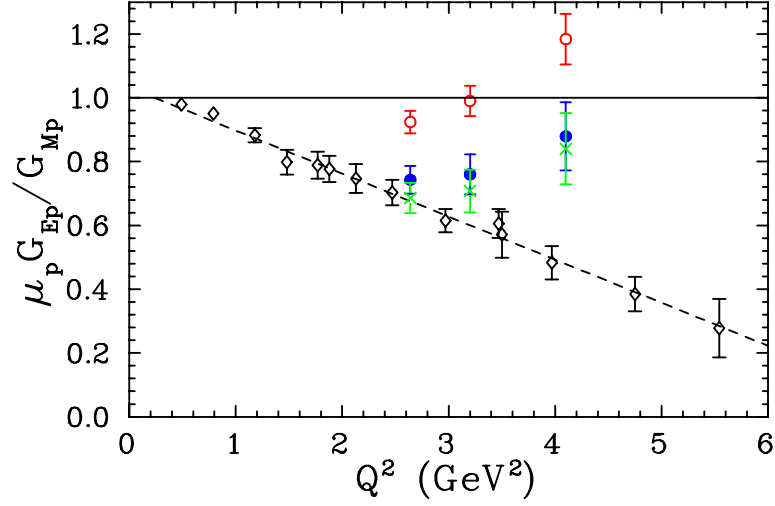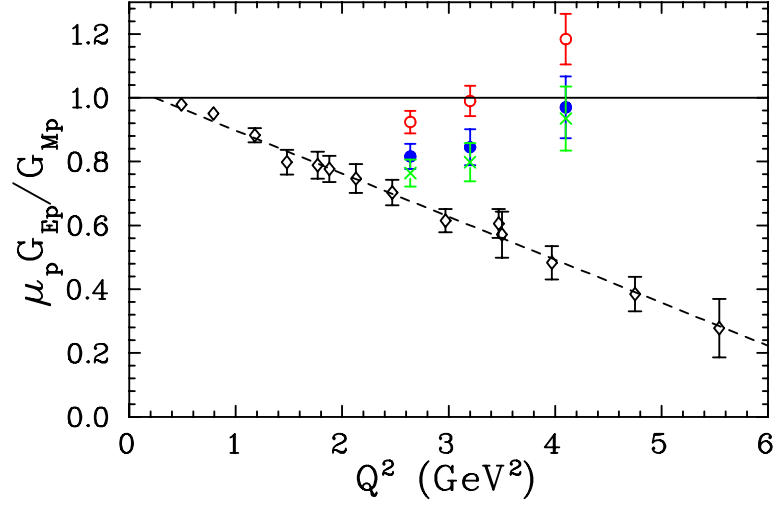
Figure 6.12: The $\mu_p G_{Ep}/G_{Mp}$ ratio for the proton from the E01-001 experiment (red open circles) and recoil polarization (black open diamonds). The E01-001 $\mu_p G_{Ep}/G_{Mp}$ ratio corrected for TPE correction by Chen et al [18] (blue solid circles). The E01-001 $\mu_p G_{Ep}/G_{Mp}$ ratio corrected for TPE correction by Chen et al including the Coulomb correction by Sick and Arrington (green crosses).

- *Calculation by Afanasev et al. [113]:*

This calculation is done at the quark-parton level in the double logarithm approximation. This calculation predicts only the ε and Q^2 dependence but not the overall magnitude, and therefore cannot be applied as a correction to the data without additional assumptions. In addition, this calculation yields large nonlinearities at large ε where the ε dependence of the TPE corrections behaves in the opposite direction to that of Blunden [16].

- *Predictions by Rekalo and Tomasi-Gustafsson et al. [114]:*

This work predicts the TPE correction based on symmetry arguments. The results show large nonlinearities at large ε. They predict that TPE corrections should

depend on $x = \sqrt{1+\varepsilon}/\sqrt{1-\varepsilon}$, but do not calculate the size or Q^2 dependence. Their calculation predicts a similar ε dependence to that of Afanasev [112].

Clearly, if TPE explains the discrepancy it must be due to an ε dependence modification of the reduced cross sections and thus the overestimate of G_{Ep} in the Rosenbluth separations. But this is not the whole story since TPE can have an effect on G_{Mp} as well. Most of the previously described calculations predicated that the largest effect on the cross section would occur at small ε. This would reduce σ_R at $\varepsilon = 0.0$ (τG_{Mp}^2) by 3-5% at large Q^2 with small Q^2 dependence. Therefore, it is crucial to know the exact ε dependence of the TPE correction and in particular the size of the nonlinearity as $\varepsilon \to 0$ in order to extract an accurate value of G_{Mp}.

6.4.3 Multiple Soft Photon Exchange (Coulomb Distortion)

It has been reported that inclusion of the Coulomb distortion to the elastic e-p cross section can slightly reduce the discrepancy between the Rosenbluth separations and recoil polarization results [115, 17]. Higinbotham [115] evaluated the effect in the Effective Momentum Approximation (EMA) where the incident electron with energy E approaches the nucleus is accelerated due to its Coulomb interaction with the nucleus. Consequently, the four momentum transfer Q gets modified and the nucleus is probed at a slightly larger Q, Q_{Modified}:

$$Q_{\text{Modified}} = Q\left(1 + \frac{3}{2}\frac{Z\alpha\hbar c}{R_{eq}E}\right) , \qquad (6.11)$$

where R_{eq} is the hard sphere equivalent radius of the proton. Therefore, Q_{Modified} will affect the reduced cross sections such as it will raise up the reduced cross sections more at low ε values than at high ε. This in turn will reduce the Rosenbluth extracted

slope, G_{Ep}^2, and hence lower the form factors ratio. The Coulomb distortion correction to the elastic e-p cross section exhibits a small ε dependence of 0.5% which is $\sim$ 10% of the effect needed to bring the Rosenbluth and recoil polarization results into agreement.

The Coulomb distortion and in particular the effect of the proton charge on the ingoing and outgoing electron waves has been examined using the second order Born approximation based on the approach used in electron-deuteron scattering [17]. Such distortions have usually been ignored for $Z = 1$, but have a significant effect on the proton rms radius. An exponential charge distribution for the proton was assumed for the calculation using the fact that $G_{Ep} \sim G_D$ where G_D is the dipole form factor. The Coulomb distortion correction to the elastic e-p cross section exhibits an ε dependence of (1.0-2.5)% and behaves approximately like $\frac{1}{Q^2}$. The correction is maximum near $Q^2 = 1$ GeV^2 and then begins to decrease by increasing Q^2. The Coulomb distortion explains a portion of the discrepancy but is a smaller effect than TPE. At large Q^2, G_{Ep} is suppressed and the effect of the Coulomb distortion on G_{Ep} is larger than one might expect.

6.4.4   Search For Nonlinearities

Due to the linearity of the reduced cross section with ε in the Born approximation, any deviation from linearity would have to come from higher-order terms that are not included in the standard radiative correction procedures. At low Q^2, such a nonlinearity would provide a clean signature of TPE and give information about the nonlinear component of TPE. To search for a deviation from linearity in the reduced cross section, we fit the measured cross sections to a second-order degree polynomial of the form:

$$\sigma_R = P_0 \left(1 + P_1 \varepsilon + P_2 \varepsilon^2 \right) , \tag{6.12}$$

where P_2 is the curvature parameter and provides a simple measure of the size of the nonlinear term relative to the cross section at $\varepsilon = 0.0$. The uncertainty in P_2, δP_2, sets a limit on the ε^2 term. Figures 6.13 and 6.14 show such fit done for the SLAC NE11 [8], and E01-001 experiments at $Q^2 = 2.50$ and 2.64 GeV^2, respectively. In addition, the value of the extracted P_2 and δP_2 are also shown. We would like to compare the value of δP_2 from the two experiments at $Q^2 = 2.64$ GeV^2, however, since SLAC NE11 did not take any measurements at this Q^2, we had to compare to the closest Q^2 available which is $Q^2 = 2.50$ GeV^2. For the SLAC NE11, we get $P_2 = 0.0031$ with $\delta P_2 = \pm 0.12$, while the E01-001 yields $P_2 = 0.0154$ with $\delta P_2 = \pm 0.0445$ which is clearly a much better limit on P_2. Moreover, as $\varepsilon \to 0$, the variation of P_0 between the linear and quadratic fits can help estimate an upper limit on the TPE contribution to $\delta(\tau G_{Mp}^2)$.
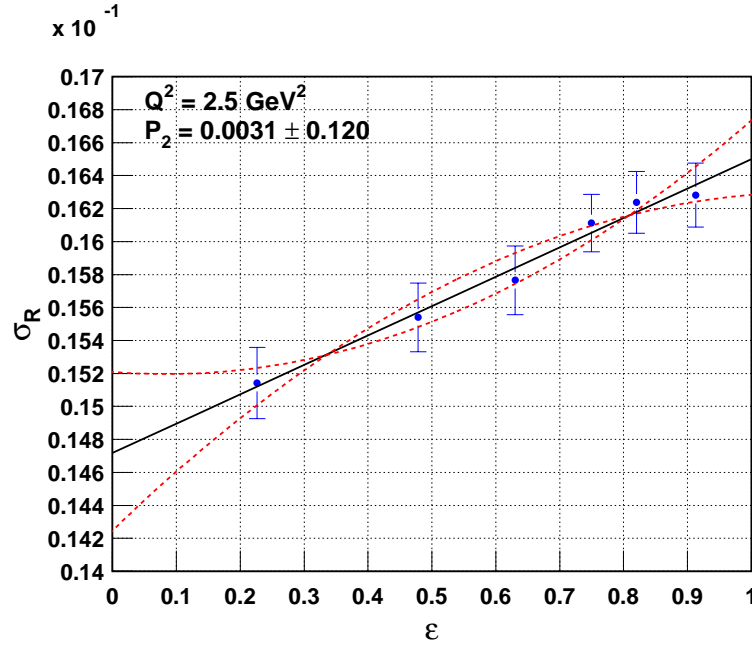
Figure 6.13: Search for nonlinearity in the SLAC NE11 σ_R at $Q^2 = 2.50$ GeV^2. The solid black line is the linear fit, while the dashed red lines are quadratic fits with $P_2 = \pm\, 0.120$.
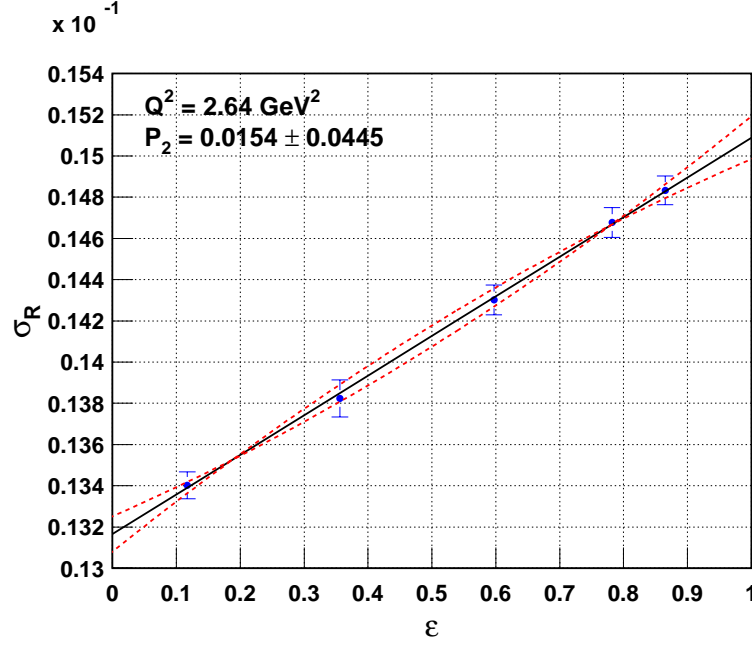
Figure 6.14: Search for nonlinearity in the E01-001 σ_R at $Q^2 = 2.64$ GeV^2. The solid black line is the linear fit, while the dashed red lines are quadratic fits with $P_2 = \pm$ 0.0445.

The E01-001 experiment provides lower uncertainty in τG_{Mp}^2 than SLAC NE11 which is the best previous Rosenbluth measurements. Similar analysis was done at other Q^2 values for the E01-001 experiment. Table 6.4 lists the results.

In order to be fully sensitive to nonlinearity that occurs at low ε, measurements of the reduced cross section must be made at very low ε. In fact, for an improved measurement of nonlinearities, it is crucial that one covers the maximum possible ε range at both the low and high ε values, and to take enough ε points in the linear region to work as a baseline for deviations from linearity since most of TPE calculations predicted that nonlinearities are likely to appear as $\varepsilon \to 0$ or $\varepsilon \to 1$.

Parameter	NE11 Q^2=2.50 GeV^2	E01-001 Q^2=2.64 GeV^2	E01-001 Q^2=3.20 GeV^2	E01-001 Q^2=4.10 GeV^2
P_2	0.003	0.015	0.013	0.057
δP_2	± 0.120	± 0.044	± 0.056	± 0.12
$\delta(\tau G_{Mp}^2)$ (%)	3.27	0.87	1.10	2.19

Table 6.4: The curvature parameter P_2, its uncertainty δP_2, and the uncertainty in τG_{Mp}^2 or $\delta(\tau G_{Mp}^2)$ as extracted for the SLAC NE11 experiment at $Q^2 = 2.50$ GeV^2 and for the E01-001 experiment at $Q^2 = 2.64$, 3.20, and 4.10 GeV^2 .

6.5 Future Experiments and TPE

6.5.1 Introduction

It has been pointed out previously that the results of the E01-001 experiment have clearly established and confirmed the discrepancy between the Rosenbluth separations and recoil polarization results. Consequently, the E01-001 results have laid down the foundation for new experiments aimed at measuring the size of the TPE corrections at Jefferson Lab.

Based on the formalism of Guichon and Vanderhaeghen [110], which provides the connection between the cross section and polarization observables and goes beyond the Born approximation, the e-p cross section and the recoil polarization results can be expressed in terms of three generalized form factors or amplitudes, $\tilde{G}_{Ep}$, $\tilde{G}_{Mp}$, and $\tilde{F}_3$ which are complex functions that depend on both Q^2 and ε:

$$P_t = -\sqrt{\frac{2\varepsilon(1-\varepsilon)}{\tau}} \frac{|\tilde{G}_{Mp}|^2}{\sigma_R} \left(R + Y_{2\gamma} \right) , \qquad (6.13)$$

$$P_l = \sqrt{(1+\varepsilon)(1-\varepsilon)} \frac{|\tilde{G}_{Mp}|^2}{\sigma_R} \left(1 + \frac{2\varepsilon}{1+\varepsilon} Y_{2\gamma} \right) , \qquad (6.14)$$

$$\frac{\sigma_R}{|\tilde{G}_{Mp}|^2} = 1 + \frac{\varepsilon}{\tau} R^2 + 2\varepsilon \left(1 + \frac{R}{\tau} \right) Y_{2\gamma} , \qquad (6.15)$$

where σ_R is the reduced e-p cross section, $Y_{2\gamma}$ is a dimensionless variable replacing $\tilde{F}_3$ as it will be discussed below, and R is given by:

$$R = \frac{|\tilde{G}_{Ep}|}{|\tilde{G}_{Mp}|} \ . \tag{6.16}$$

Note that in the Born approximation, these amplitudes are real and depend only on Q^2 or: $\tilde{G}_{Ep} \rightarrow G_{Ep}$, $\tilde{G}_{Mp} \rightarrow G_{Mp}$, and $\tilde{F}_3 \rightarrow$ zero. In order to separate the Born and higher order corrections, the generalized form factors are broken into the Born and TPE contributions or:

$$\tilde{G}_{Ep}(\varepsilon, Q^2) = G_{Ep}(Q^2) + \Delta G_{Ep}(\varepsilon, Q^2) \ , \tag{6.17}$$

$$\tilde{G}_{Mp}(\varepsilon, Q^2) = G_{Mp}(Q^2) + \Delta G_{Mp}(\varepsilon, Q^2) \ , \tag{6.18}$$

$$\tilde{F}_3(\varepsilon, Q^2) = \tilde{F}_3(\varepsilon, Q^2) \ . \tag{6.19}$$

Therefore and following [110], we can replace $\tilde{F}_3$ with a dimensionless variable $Y_{2\gamma}$:

$$Y_{2\gamma} = \text{Re}\left(\frac{\nu \tilde{F}_3(\varepsilon, Q^2)}{M_p^2 |\tilde{G}_{Mp}|}\right) \ , \tag{6.20}$$

where $\nu = M_p^2 \sqrt{(1+\varepsilon)/(1-\varepsilon)}\sqrt{\tau(1+\tau)}$. That way we have the two real Born amplitudes or G_{Ep} and G_{Mp}, and three two-photon amplitudes or ΔG_{Ep}, ΔG_{Mp}, and $Y_{2\gamma}$. Note that ΔG_{Ep} and ΔG_{Mp} are complex and expected to be small compared to the Born amplitudes. They interfere with the Born amplitudes, which are real and much larger, so the imaginary part of two-photon amplitudes should be negligible. Therefore, the imaginary part of the two-photon amplitudes will be dropped and $\tilde{G}_{Ep}$ and $\tilde{G}_{Mp}$ will refer to the real part of the amplitudes.

In the generalized formalism, and if the TPE contributions are ε-independent, the measured ratio of the form factors can be written in terms of these generalized form

factors for the recoil polarization as:

$$R_{\mathrm{Pol}} = \frac{\tilde{G}_{Ep}}{\tilde{G}_{Mp}} + \left(1 - \frac{2\varepsilon}{1+\varepsilon}\frac{\tilde{G}_{Ep}}{\tilde{G}_{Mp}}\right)Y_{2\gamma} \ , \qquad (6.21)$$

and for the Rosenbluth separations (L-T) as:

$$R_{\mathrm{L\text{-}T}}^2 = (\frac{\tilde{G}_{Ep}}{\tilde{G}_{Mp}})^2 + 2\left(\tau + \frac{\tilde{G}_{Ep}}{\tilde{G}_{Mp}}\right)Y_{2\gamma} \ . \qquad (6.22)$$

From equations (6.21) and (6.22) we see that only the $Y_{2\gamma}$ term leads to a difference between the Rosenbluth separations and recoil polarization form factor ratio and such difference is proportional to $Y_{2\gamma}$.

6.5.2 Experiment E04-019

Experiment E04-019 [116] will measure the ε dependence of the recoil polarization extractions of $\frac{G_{Ep}}{G_{Mp}}$. The recoil polarization will be measured using the big Focal Plane Polarimeter (FPP) in Hall C and it will be done at a fixed Q^2 value of 3.20 GeV^2. The value $Q^2 = 3.20$ GeV^2 is chosen to overlap the high-precision cross section measurements of the Super-Rosenbluth E01-001 experiment. Measurements will be taken at 4 ε points and the kinematics are chosen to be the same as those in the Super-Rosenbluth experiment so that the high-precision cross sections measured by the Super-Rosenbluth experiment can be used in the analysis. Based on equations (6.13), (6.14), and (6.15) and by using the measured values of $\frac{P_t}{P_l}$, and σ_R at a given ε point, one can solve for $\tilde{G}_{Mp}$, $Y_{2\gamma}$, and R. Note that because the E04-019 experiment will measure the ε dependence and not the size of $Y_{2\gamma}$, it will not by itself provide sufficient information to correct the recoil polarization for TPE effects. Experiment E04-019 is scheduled to run along with the coming Hall C experiment G_E^p–III of JLAB in 2006.

6.5.3 Experiment E05-017

Experiment E05-017 [117] is a high-precision Rosenbluth separation measurement similar to the Super-Rosenbluth E01-001 experiment where protons will be detected with an improved precision. It aims to mapping the ε and Q^2 dependence of TPE contributions to the elastic e-p cross section by providing high-precision Rosenbluth separations for $1 \leq Q^2 \leq 6$ GeV^2 by taking more ε and Q^2 points over a wide range. Such high precision measurements will allow for precise extraction of TPE effects from the difference between Rosenbluth and recoil polarization measurements. Moreover, it will make improved measurements of any nonlinearities in the ε dependence of the cross sections than those reported in this work. By providing improved Rosenbluth separations measurements of $\frac{\mu_p G_{Ep}}{G_{Mp}}$, E05-017 will determine the Q^2 dependence of TPE. The overall goal is to increase the precision on $\frac{\mu_p G_{Ep}}{G_{Mp}}$ by a factor of 2-3 over the entire Q^2 range compared to a global Rosenbluth extractions which will allow for precise comparison with the recoil polarization results. Experiment E05-017 is approved to run in Hall C of JLAB.

6.5.4 Experiment E04-116

Experiment E04-116 [118] we will measure the ε dependence of the charge asymmetry $R = \frac{\sigma(e^+)}{\sigma(e^-)}$, where $\sigma(e^+)$ and $\sigma(e^-)$ are the elastic cross sections of positron- and electron-proton scattering, respectively. Such measurements will allow for direct determination of TPE contribution to the elastic e-p scattering cross section and will be done for $0.5 \leq Q^2 \leq 2.0$ and $0.1 \leq \varepsilon \leq 0.9$.

The crucial point here is that the radiative corrections can be classified into two categories: those whose their sign depends on the charge of the incident lepton, and those whose their sign does not depend on the charge of the incident lepton. The standard radiative corrections are all independent of the sign of the lepton except for the interference term between the electron(positron) bremsstrahlung and proton

bremsstrahlung that is regularized by the infrared term from TPE. In other words, the standard radiative corrections developed by Mo and Tsai [44] include only the infrared divergent contributions from TPE diagrams, which necessarily cancel the infrared divergent contributions from the interference term between electron and proton bremsstrahlung, and neglect contributions from multiple soft photons exchange (Coulomb corrections).

The relation of R to TPE and hence to the elastic e-p scattering cross section is given below: The amplitude of the elastic e-p scattering up to α^2 including only amplitudes that contribute to the charge asymmetry can be written as:

$$A_{ep \rightarrow ep} = e_e e_p A_{Born} + e_e^2 e_p A_{e-bremsst} + e_e e_p^2 A_{p-bremsst} + e_e^2 e_p^2 A_{2\gamma} \ , \qquad (6.23)$$

where $e_e(e_p)$ is the charge of the electron(proton) and the amplitudes A_{Born}, $A_{e-bremsst}$, $A_{p-bremsst}$, and $A_{2\gamma}$ are the Born(single-photon exchange), electron-bremsstrahlung, proton-bremsstrahlung, and two-photon exchange amplitudes, respectively. By squaring equation (6.23) and keeping only corrections up to α that have odd powers of electron charge, we get:

$$|A_{ep \rightarrow ep}|^2 = e_e^2 e_p^2 \left(|A_{Born}|^2 + 2 e_e e_p A_{Born} Re(A_{2\gamma}^{\star}) + 2 e_e e_p Re(A_{e-bremsst} A_{p-bremsst}^{\star}) \right) \ , \qquad (6.24)$$

where Re stands for the real part of the amplitude.

The term $2 e_e e_p Re(A_{e-bremsst} A_{p-bremsst}^{\star})$ in equation (6.24) describes the interference between the electron and proton bremsstrahlung and its infrared divergence contribution cancels exactly the corresponding infrared divergence contribution from $2 e_e e_p A_{Born} Re(A_{2\gamma}^{\star})$. Therefore, after correcting the elastic e-p scattering cross section for this interference term, the only radiative correction that leads to a charge asymmetry would have to come from TPE. The effects of TPE and Coulomb corrections have the opposite sign for electrons and positrons or $\sigma(e^{\pm}) = \sigma_{Born}(1 \mp \delta_{2\gamma})$ where $\delta_{2\gamma}$

is the TPE correction yielding a charge asymmetry $R = \frac{\sigma(e^+)}{\sigma(e^-)} \approx 1 - 2\delta_{2\gamma}$. By plotting R as a function of ε, any deviation of R from 1.0 is a model-independent measure of TPE in elastic e-p scattering. Experiment E04-116 will run in Hall B of JLAB. It is approved for engineering run to check backgrounds with secondary beam.

A similar e^+-e^- comparison is proposed to run at VEPP-3. The experiment will measure the ratio $R = \frac{\sigma(e^+)}{\sigma(e^-)}$ at low ε and moderate Q^2, where no precision data exist. For more details, the experiment is described in reference [119].

Chapter 7   Summary and Conclusion

High precision measurements of the elastic e-p scattering cross sections were made at the Hall A of the Thomas Jefferson National Accelerator Facility. The Super-Rosenbluth experiment E01-001 ran in May 2002 where an unpolarized electron beam from the Continuous Electron Beam Accelerator Facility in the range of $1.912 \leq E \leq 4.702$ GeV was used and directed on a 4-cm-long unpolarized liquid-hydrogen target. Protons were detected, in contrast to previous measurements where the scattered electrons were detected, to dramatically decrease any ε dependence systematic uncertainties and corrections. The left arm spectrometer was used to measure three Q^2 points of 2.64, 3.20, and 4.10 GeV^2. Simultaneously, measurements at $Q^2 = 0.5$ GeV^2 were carried out using the right arm spectrometer which served as a luminosity monitor to remove any uncertainties due to beam charge, current, and target density fluctuations. A total of 12 ε points (5 ε points for $Q^2 = 2.64$ GeV^2, 4 ε points for $Q^2 = 3.20$ GeV^2, and 3 ε points for $Q^2 = 4.10$ GeV^2) were measured covering an angular range of $12.52^o < \theta_L < 38.26^o$ for the left arm, while the right arm was at $Q^2 = 0.5$ GeV^2, and used to simultaneously measure 5 ε points covering an angular range of $58.29^o < \theta_R < 64.98^o$, allowing for high precision L-T separation of the proton electric and magnetic form factors and hence their ratio $\frac{\mu_p G_{Ep}}{G_{Mp}}$. The measured cross sections were corrected for internal and external radiative corrections using updated procedure based on Mo and Tsai [44, 7, 97]. The absolute uncertainty (scale uncertainty) in the measured cross sections is approximately 3% for both arms and with relative uncertainties, random and slope, below 1% for the left arm, and below 1% random and 6% slope for the right arm. The extracted form factors, $\frac{G_{Ep}}{G_D}$ and $\frac{G_{Mp}}{\mu_p G_D}$, were determined for the left arm at the three Q^2 points to 4%-7% and 1.5%, respectively.

Moreover, the ratio $\frac{\mu_p G_{Ep}}{G_{Mp}}$ was determined at the three Q^2 points to 4%-7%, and found to approximate form factor scaling or $\frac{\mu_p G_{Ep}}{G_{Mp}} \approx 1.0$.

The results of this work are in agreement with the previous Rosenbluth data and inconsistent with the high-Q^2 recoil polarization results. The E01-001 experiment provided systematic uncertainties much smaller than the best previous Rosenbluth measurements [8], and comparable to those of the recoil polarization, clearly establishing the discrepancy between the Rosenbluth separations and recoil polarization results. Furthermore, the high precision of the results confirmed that the discrepancy is not an experimental error in the Rosenbluth measurements or technique, confirmed the reliability of the elastic e-p scattering cross sections extracted from previous Rosenbluth separations, provided a strong test of the conventional radiative corrections used, and constituted a precise measurement of the discrepancy.

A possible source for the discrepancy is the effect of a missing correction to the reduced cross sections due to two-photon exchange (TPE) corrections. Therefore, it is absolutely crucial to understand the radiative corrections and in particular higher-order processes such as TPE theoretically and experimentally before we can be confident in our knowledge of the proton form factors. Consequently, and motivated by the results of the E01-001 experiment, the interest in the physics of TPE and Coulomb distortion corrections and their impact on electron scattering observables has risen experimentally and theoretically. In addition, the results of the E01-001 experiment have laid down the foundation for new experiments aimed at measuring the size of the TPE corrections.

"I have noticed that nobody writes a book in his day, but is certain to declare on the morrow, that if this were to be altered it would be better, if this were to be added it would be more desirable, if this were to be moved forward it would be preferable and if this were to be omitted it

would be more pleasing. This saying is one of the wisest maxims and it is evidence that the whole human race is seized by imperfection."

— Al-Imad Al-Asfahani (Al-Katib), 1125-1200 A.D.: A historian and one of the major writers. He accompanied Salah Al-Din Al-Ayyubi (Saladin) and recorded his history.

Bibliography

[1] T. Janssens, R. Hofstadter, E. B. Huges, and M. R. Yearian, Phys. Rev. **142**, 922 (1966).

[2] J. Litt *et al.*, Phys. Lett. B **31**, 40 (1970).

[3] L. E. Price *et al.*, Phys. Rev. D **4**, 45 (1971).

[4] C. Berger *et al.*, Phys. Lett. B **35**, 87 (1971).

[5] W. Bartel *et al.*, Nucl. Phys. B **58**, 429 (1973).

[6] F. Borkowski *et al.*, Nucl. Phys. B **93**, 461 (1975).

[7] R. C. Walker *et al.*, Phys. Rev. D **49**, 5671 (1994).

[8] L. Andivahis *et al.*, Phys. Rev. D **50**, 5491 (1994).

[9] M. E. Christy *et al.*, Phys. Rev. C **70**, 015206 (2004).

[10] M. J. Alguard, Phys. Rev. Lett. **37**, 1258 (1976).

[11] B. D. Milbrath *et al.*, Phys. Rev. Lett. **80**, 452 (1998).

[12] M. K. Jones *et al.*, Phys. Rev. Lett. **84**, 1398 (2000).

[13] T. Pospischil *et al.*, Eur. Phys. J. **A12**, 125 (2001).

[14] O. Gayou *et al.*, Phys. Rev. C **64**, 038202 (2001).

[15] O. Gayou *et al.*, Phys. Rev. Lett. **88**, 092301 (2002).

[16] P. G. Blunden, W. Melnitchouk, and J. A. Tjon, Phys. Rev. Lett. **91**, 142304 (2003).

[17] J. Arrington and I. Sick, Phys. Rev. C **70**, 028203 (2004).

[18] Y. C. Chen *et al.*, Phys. Rev. Lett. **93**, 122301 (2004).

[19] F. Halzen and A. D. Martin, *"Quarks and Leptons"*: An Introductory Course in Modern Particle Physics, John Wiley and Sons, Inc., New York (1984).

[20] S. J. Brodsky and G. Farrar, Phys. Rev. Lett. **31**, 1153 (1973).

[21] S. J. Brodsky and G. Farrar, Phys. Rev. D **11**, 1309 (1975).

[22] G. Höhler, Nucl. Phys. B **114**, 505 (1976).

[23] M. Gari and W. Krümpelmann, Phys. Lett. B **173**, 10 (1986).

[24] G. P. Lepage and S. J. Brodsky, Phys. Rev. Lett. **43**, 545 (1979).

[25] G. P. Lepage and S. J. Brodsky, Phys. Rev. D **22**, 2157 (1980).

[26] P. E. Bosted, Phys. Rev. C **51**, 409 (1995).

[27] E. J. Brash, A. Kozlov, S. Li, and G. M. Huber, Phys. Rev. C **65**, 051001(R) (2002).

[28] J. J. Murphy, Y. M. Shin, and D. M. Skopik, Phys. Rev. C **9**, 2125 (1974).

[29] K. M. Hanson, Phys. Rev. D **8**, 753 (1973).

[30] A. F. Sill *et al.*, Phys. Rev. D **48**, 29 (1993).

[31] D. H. Perkins, *"Introduction to High Energy Physics"*, Addison-Wesley Publishing Company (1987).

[32] R. G. Sachs, Phys. Rev. **126**, 2256 (1962).

[33] M. N. Rosenbluth, Phys. Rev. **79**, 615 (1950).

[34] N. Dombey, Rev. Mod. Phys. **41**, 236 (1969).

[35] A. I. Akheizer and M. P. Rekalo, Sov. J. Part. Nucl. **4**, 236 (1974).

[36] R. G. Arnold, C. E. Carlson, and F. Gross, Phys. Rev. C **23**, 363 (1981).

[37] L. Bimbot, Nucl. Phys. A **684**, 513 (2001).

[38] R. Hofstadter, Ann. Rev. Nucl. Part. Sci. **7**, 231 (1957).

[39] Y. S. Tsai, Phys. Rev. **122**, 1898 (1961).

[40] J. Schwinger, Phys. Rev. **76**, 790 (1949).

[41] H. A. Bethe and J. Ashkin, *"Experimental Nuclear Physics"*, 272, (1953).

[42] L. Eyges, Phys. Rev. **76**, 264 (1949).

[43] M. Goitein *et al.*, Phys. Rev. D **1**, 2449 (1970).

[44] L. W. Mo and Y.-S. Tsai, Rev. Mod. Phys. **41**, 205 (1969).

[45] N. Meister and D. Yennie, Phys. Rev. **130**, 1210 (1963).

[46] W. Bartel *et al.*, Phys. Rev. Lett. **17**, 608 (1966).

[47] W. Heitler, *"The Quantum Theory of Radiation"*, 378, (1954).

[48] P. N. Kirk *et al.*, Phys. Rev. D **8**, 63 (1973).

[49] S. Stein *et al.*, Phys. Rev. D **12**, 1884 (1975).

[50] P. E. Bosted *et al.*, Phys. Rev. C **42**, 38 (1990).

[51] S. Rock *et al.*, Phys. Rev. D **46**, 24 (1992).

[52] R. G. Arnold *et al.*, Phys. Rev. Lett. **57**, 174 (1986).

[53] A. V. Afanasev, Phys. Lett. B **514**, 269 (2001).

[54] D. Dutta *et al.*, Phys. Rev. C **68**, 064603 (2003).

[55] J. Arrington, Phys. Rev. C **69**, 022201(R) (2004).

[56] H. Budd, A. Bodek, and J. Arrington, arXiv: hep-ex/0308005, 2005.

[57] R. C. Walker, Ph.D. thesis, California Institute of Technology, 1989.

[58] J. Arrington, Phys. Rev. C **68**, 034325 (2003).

[59] I. Niculescu, Ph.D. thesis, Hampton University, 1999.

[60] G. G. Simon, C. Schmitt, F. Borkowski, and V. H. Walther, Nucl. Phys. A **333**, 381 (1980).

[61] W. Bartel *et al.*, Phys. Lett. B **25**, 242 (1967).

[62] W. Albrecht *et al.*, Phys. Rev. Lett. **17**, 1192 (1966).

[63] N. C. R. Makins, Ph.D. thesis, Massachusettes Institute of Technology, 1994.

[64] T. G. O'Neill, Ph.D. thesis, California Institute of Technology, 1994.

[65] The Thomas Jefferson National Accelerator Facility, Newport New, VA, USA. http://www.jlab.org.

[66] D. Marchand, Ph.D. thesis, Université Blaise Pascal, Clermont-Ferrand, France, 1997.

[67] J. Alcorn *et al.*, Nucl. Instrum. Meth. **A522**, 294 (2004).

[68] http://hallaweb.jlab.org/equipment/beam.html.

[69] O. Ravel, Ph.D. thesis, Université Blaise Pascal, Clermont-Ferrand, France, 1997.

[70] X. Zheng, Ph.D. thesis, Massachusettes Institute of Technology, 2002.

[71] http://hallaweb.jlab.org/equipment/targets.html.

[72] http://hallaweb.jlab.org/equipment/HRS.htm.

[73] http://hallaweb.jlab.org/equipment/detectors/detectors.html.

[74] K. G. Fissum *et al.*, Nucl. Instrum. Meth. **A474**, 108 (2001).

[75] http://hallaweb.jlab.org/equipment/acquisition.html.

[76] M. Iodice *et al.*, Nucl. Instrum. Meth. **A411**, 223 (1998).

[77] M. Coman, M.S. thesis, Florida International University, 2000.

[78] B. Wojtsekhowski *et al.*, High performance threshold aerogel counters, Nucl. Instr. and Meth., to be submitted.

[79] CODA: http://coda.jlab.org, Hall A operations Manual, 2000; Hall A operations Manual Archive.

[80] EPICS: http://www.jlab.org/accel/documents/epics_doc.html.

[81] E. Offerman, ESPACE, User's Guide, http://hallaweb.jlab.org/espace/docs.html.

[82] HBOOK: Reference Manual, CERN Program Library Long Writeup Y250, Version 4.22, 1994.

[83] http://paw.web.cern.ch/paw/.

[84] N. Liyanage, http://hallaweb.jlab.org/publications/Technotes/technote.html#2002, JLAB-TN-02-012.

[85] http://hallaweb.jlab.org/news/minutes/collimator-distance.html.

[86] E. C. Schulte, Ph.D. thesis, University of Illinois at Urbana-Champaign, 2002.

[87] L. Zhu, Ph.D. thesis, Massachusettes Institute of Technology, 2004.

[88] M. K. Jones, private communication.

[89] J. R. Arrington, private communication.

[90] K. Hagiwara *et al.*, Phys. Rev. **D66**, 010001 (2002).

[91] S. Eidelman *et al.*, Phys. Lett. **B592**, 1 (2004).

[92] D. Meekins, private communication.

[93] D. Meekins, Current Hall A Target Configuration, April 25, 2002, http://www.jlab.org/~xiaochao/e01001/halla_current_config2.html.

[94] X. Zheng, private communication.

[95] X. Zheng, BCM Calibration for E01-001: www.jlab.org/~xiaochao/e01001/.

[96] M. Jones, BCM Calibration: http://www.jlab.org/~jones/e01-020/.

[97] R. Ent *et al.*, Phys. Rev. C **64**, 054610 (2001).

[98] M. Berz, COSY Infinity Version 7 Reference Manual, NSCL Technical Report MSUCL-977, Michigan State University, 1995.

[99] M. A. Shupe *et al.*, Phys. Rev. D **19**, 1921 (1979).

[100] S. D. Drell and M. Ruderman, Phys. Rev. **106**, 561 (1957).

[101] S. D. Drell and S. Fubini, Phys. Rev. **113**, 741 (1959).

[102] N. R. Werthammer and M. A. Ruderman, Phys. Rev. **123**, 1005 (1961).

[103] G. K. Greenhut, Phys. Rev. **184**, 1860 (1969).

[104] R. R. Lewis, Phys. Rev. **102**, 537 (1956).

[105] L. Landau, Journal of Phys **VIII**, 201 (1944).

[106] Y. S. Tsai, Rev. Mod . Phys **46**, 815 (1974).

[107] P. G. Blunden, W. Melnitchouk, and J. A. Tjon, Two-photon exchange in elastic electron nucleon scattering, arXiv: nucl-th/0506039, 2005.

[108] S. Kondratyuk, P. G. Blunden, W. Melnitchouk, and J. A. Tjon, Delta resonance contribution to two-photon exchange in electron proton scattering, arXiv: nucl-th/0506026, 2005.

[109] I. A. Qattan *et al.*, Phys. Rev. Lett. **94**, 142301 (2005).

[110] P. A. M. Guichon and M. Vanderhaeghen, Phys. Rev. Lett. **91**, 142303 (2003).

[111] L. C. Maximon and J. A. Tjon, Phys. Rev. C **62**, 054320 (2000).

[112] A. V. Afanasev *et al.*, The two-photon exchange contribution to elastic electron nucleon scattering at large momentum transfer, arXiv: hep-ph/0502013, 2005.

[113] A. Afanasev, S. Brodsky, and C. Carlson, presented at the DNP Meeting, Tuscon, AZ, Oct. 2003.

[114] M. P. Rekalo and E. Tomasi-Gustafsson, Eur. Phys. J. **A22**, 119 (2004).

[115] D. Higinbotham, JLab Report JLAB-PHY-03-116, (unpublished).

[116] R. Gilman *et al.*, Jefferson lab experiment E04-019.

[117] J. Arrington *et al.*, Jefferson lab experiment E05-017.

[118] W. Brooks *et al.*, Jefferson lab experiment E04-116.

[119] J. Arrington *et al.*, Proposal for positron measurement at VEPP-3.